amU
Aix Marseille Université

NNT : 0000AIXM0000

THÈSE DE DOCTORAT

Soutenue à Aix-Marseille Université
le 11 décembre 2025 par

Carine SADAKA

Constraints on the meteorite flux to Earth over the last 2 million years

Discipline
Sciences de l'environnement

Spécialité
Géosciences

École doctorale
ED 251 – Sciences de l'environnement

Laboratoire/Partenaires de recherche
CEREGE

Composition du jury

Beda HOFMANN — Rapporteur
Chargé de recherche – Naturhistorisches Museum Bern

Steven GODERIS — Rapporteur
Professeur des universités – Vrije Universiteit Brussel

Kees WELTEN — Examinateur
Chargé de recherche – University of California

Evelyn FÜRI — Présidente du jury
Directrice de recherche – CRPG, Nancy

Katherine JOY — Examinatrice
Professeur des universités – University of Manchester

Pierre VERNAZZA — Examinateur
Chargé de recherche– Aix-Marseille Université

Jérôme GATTACCECA — Directeur de thèse
Directeur de recherche– CEREGE

Affidavit

I, undersigned, Carine Sadaka, hereby declare that the work presented in this manuscript is my own work, carried out under the scientific supervision of Jérôme Gattacceca, in accordance with the principles of honesty, integrity and responsibility inherent to the research mission. The research work and the writing of this manuscript have been carried out in compliance with both the French national charter for Research Integrity and the Aix-Marseille University charter on the fight against plagiarism.

This work has not been submitted previously either in this country or in another country in the same or in a similar version to any other examination body.

Place Aix-en-Provence, France, date 15 octobre 2025

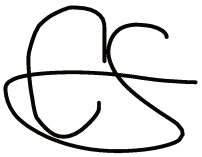

Cette œuvre est mise à disposition selon les termes de la Licence Creative Commons Attribution - Pas d'Utilisation Commerciale - Pas de Modification 4.0 International.

Liste de publications et/ou brevets et participation aux conférences

1) Liste des publications et/ou brevet [1] réalisées dans le cadre du projet de thèse :

   1. **(Publié)** Sadaka, C., Gattacceca, J., Gounelle, M., Roskosz, M., Lagain, A., Tartese, R., Bonal, L., Maurel, C., Martinez, R. and Valenzuela, M. (2025), Systematic meteorite collection in the Catalina Dense Collection area (Chile): Description and statistics. Meteorit Planet Sci, 60: 308-323. https://doi.org/10.1111/maps.14307

   2. **(Publié)** Sadaka, C., Gattacceca, J., Dumas, F., Braucher, R., ASTER Team, Leya, I., Tauseef, M., Blard, P.-H., Bekaert, D., Füri, E., Zimmermann, L., Lagain, A., Devillepoix, H.A.R. and Gounelle, M. (2026), Terrestrial ages of meteorites from the Atacama Desert (Chile) and insights into the past meteorite flux to Earth. Meteorit Planet Sci. https://doi.org/10.1111/maps.70125

   3. **(En préparation)** Sadaka, C., J. Gattacceca, F. Dumas, et al. 2025. In Prep. "Description of the Calama Area Meteorite Collection (Atacama Desert, Chile)". Article in preparation for submission in *Meteoritics & Planetary Science*.

2) Participation aux conférences[2] et écoles d'été au cours de la période de thèse :

   Conférences internationales

   1. (Présentation orale) Sadaka C, Gattacceca J, Dumas F, Kuzina D, Braucher R & Gounelle M (2023) « Constraining the Meteorite Flux on Earth during the Last 2 Ma ». http://doi.org/10.7185/gold2023.19263. ***Goldschmidt Conference***, 2023, Lyon, France

   2. (Présentation orale) C. Sadaka, J. Gattacceca, F. Dumas1, R. Braucher, M. Gounelle, M. Valenzuela, L. Bonal, J. Eschrig, L. Folco, K. Joy, A. Musolino, M. Roskosz, R. Tartèse, and ASTER Team. « The dense and old Catalina meteorite collection, Atacama Desert, Chile ». ***Meteoritical Society Annual Meeting***, 2024, Brussels, Belgium

   3. (Poster) Sadaka, C.; Gattacceca, J.; Braucher, R.; Dumas, F.; Gounelle, M.; Vernazza, P.; ASTER Team. «Atacama Desert meteorite collections: Insight into

[1] Cette liste comprend les articles publiés, les articles soumis à publication et les articles en préparation ainsi que les livres, chapitres de livre et/ou toutes formes de valorisation des résultats des travaux propres à la discipline du projet de thèse. La référence aux publications doit suivre les règles standards de bibliographie et doit être conforme à la charte des publications d'AMU.

[2] Le terme « conférence » est générique. Il désigne à la fois « conférence », « congrès », « workshop », « colloques », « rencontres nationales et/ou internationales » … etc.

Indiquer si vous avez fait une présentation orale ou sous forme de poster.

the past meteorite flux. » ***Lunar and Planetary Science Conference***, 2025, The Woodlands, TX/Virtual. Virtual Poster

Conférences nationales et workshops

1. (Présentation orale) C. Sadaka, J. Gattacceca, F. Dumas, D. Kuzina, R. Braucher, M. Gounelle, ASTER Team. Constraining the Meteorite Flux on Earth during the Last 2 Ma. ***Congrès EDSE*** 2023, Marseille
2. Colloque du projet des sciences participatives FRIPON / Vigie-Ciel 2023, Paris
3. Colloque du projet des sciences participatives FRIPON / Vigie-Ciel 2025, Paris

Écoles d'hiver/d'été et formations :

4. Formation : Nucléides Cosmogéniques, octobre 2022, Laboratoire National des Nucléides Cosmogéniques, Aix-en-Provence
5. École des Houches 'Small bodies of the Solar System and their link with extraterrestrial samples', février 2024, PNP, Les Houches
6. Summer school 'Sample Returns', organized by the Origins Institute, juin 2024, Institut Origins, Observatoire de Haute Provence (OHP)

Résumé

La Terre est continuellement bombardée par des objets extraterrestres de tailles et d'origines variées. Parmi eux, les météorites, dont la taille varie entre quelques centimètres et plusieurs mètres, survivent à l'entrée atmosphérique et atteignent la surface terrestre. Les météorites offrent des informations uniques sur la composition et l'évolution du Système solaire. Les déserts chauds sont particulièrement propices à leur conservation et leur collecte, grâce à leur climat aride et à la stabilité de leurs surfaces. Le désert d'Atacama, au Chili, se distingue par une aridité extrême et une stabilité de surface à long terme, qui ont permis l'accumulation des collections de météorites les plus anciennes et les plus denses au monde. Ces conditions offrent la possibilité d'étudier le flux de météorites sur Terre sur des échelles de temps non accessibles ailleurs. Par exemple, la collection d'El Médano présente un âge terrestre moyen de 710 000 ans. Des données préliminaires suggèrent aussi des variations dans la composition du flux de météorites au cours du temps, notamment une augmentation significative des chondrites H par rapport aux chondrites L entre 500 000 et 1 million d'années.

Cette thèse a pour objectif d'étudier l'intensité et la composition du flux de météorite au cours des deux derniers millions d'années, ainsi que ses éventuelles variations temporelles. Elle s'appuie sur deux régions distinctes dans le désert d'Atacama : la première dans la zone dense de collection de Catalina (DCA de Catalina) située à environ 60 km de la DCA d'El Médano, et la deuxième un ensemble de zones situés plus au nord et regroupées sous le nom de « zone de Calama » (dans les DCAs de Calama, Chug Chug et Sierra Gorda), à environ 270 km d'El Médano.

Dans la zone de Catalina, des recherches systématiques menées à pied sur 6,80 km² ont permis de collecter 1 599 météorites, constituant la « Collection Systématique de Catalina » (CSC). Il s'agit de la plus forte densité de météorites recensée dans un désert chaud, dépassant celle d'El Médano, et confirmant la richesse exceptionnelle en météorites de la Dépression Centrale de l'Atacama.

Les âges terrestres ont été déterminés à partir des concentrations du nucléide cosmogénique ^{36}Cl dans la phase métallique de 51 météorites non appariées issues de la CSC et de 49 météorites provenant de la zone de Calama, par spectrométrie de masse par accélérateur. Les résultats montrent que la CSC constitue la collection de météorites la plus ancienne identifiée à ce jour. En combinant ces âges aux densités au sol, il a été possible d'estimer le flux de météorites au cours des deux derniers millions d'années.

Les données d'El Médano et de Catalina ont ensuite été combinées pour étudier l'évolution de la composition du flux, en particulier la diminution récente de la proportion de chondrites H. Cette tendance n'est pas reproduite par les modèles d'évolution du flux de météoroïdes provenant des principales régions sources de chondrites H.

Enfin, les âges d’exposition aux rayons cosmiques ont été mesurés sur un sous-ensemble de météorites de l’Atacama, par mesure du gaz rare néon. La combinaison des âges terrestres et des âges d'exposition permet d’estimer les âges d’éjection de ces objets depuis leurs astéroïdes parents, apportant ainsi de nouvelles contraintes sur les processus dynamiques et collisionnels susceptibles d’avoir modifié la nature du flux de météorites sur Terre au cours des deux derniers millions d’années.

Mots clés : météorites, chondrites ordinaires, désert d’Atacama, nucléides cosmogéniques, âge terrestre, flux de météorites, âge d’exposition, ceinture d’astéroïdes

Abstract

The Earth is continuously bombarded by extraterrestrial objects of various sizes and origins. Among them, meteorites, centimeter- to meter-sized fragments that survive atmospheric entry, provide invaluable insights into the composition and evolution of the Solar System. Hot deserts are particularly favorable for meteorite recovery due to their arid climates and stable geomorphological conditions. The Atacama Desert, renowned for its extreme aridity and long-term surface stability, hosts some of the densest and oldest meteorite collections in the world. These unique collections enable the study of the meteorite flux over longer timescales than in any other hot desert. Previous studies, notably on the El Médano collection, have highlighted the potential of this region for studying the past meteorite flux and suggested temporal variations in meteorite composition, including an increase in H chondrite abundance relative to L chondrites between 0.5 and 1 million years ago.

The main goal of this thesis is to investigate the intensity and composition of the meteorite flux to Earth over the last two million years using distinct Atacama Desert collections. The study focuses on two independent areas: the Catalina Dense Collection Area (DCA) and the Calama, Chug Chug, and Sierra Gorda DCAs—collectively referred to as the "Calama area", located approximately 60 km and 270 km from El Médano, respectively.

In the Catalina DCA, systematic on-foot search campaigns covering 6.80 km² yielded 1599 meteorites, forming the "Catalina Systematic Collection" (CSC). This represents the highest meteorite density recorded in any hot desert, even surpassing that of the neighboring El Médano DCA, and confirms that the Central Depression of the Atacama Desert hosts the densest meteorite collections among arid regions.

To assess the spatial extent of the old terrestrial ages of the Atacama meteorites, terrestrial ages were measured for a random subset of 51 unpaired meteorites from the CSC and 49 unpaired meteorites from the Calama area based on the concentration of the cosmogenic nuclide ^{36}Cl in the metallic phase using Accelerator Mass Spectrometry. Results reveal that the CSC is the oldest known meteorite collection to date, exceeding the average terrestrial age previously determined for the El Médano collection. By combining terrestrial ages with recovery densities, we reconstructed the meteorite flux over the past two million years.

We then combined the terrestrial age datasets from El Médano and Catalina to investigate long-term changes in the composition of the meteorite flux. Notably, we notice a decline in H chondrite abundance over time and discuss this trend in the context of dynamical models of meteoroid delivery from the main H chondrite source regions.

Finally, we determined cosmic-ray exposure (CRE) ages for a subset of Atacama H chondrites using noble gas neon measurements. By combining CRE and terrestrial ages, we constrain the ejection ages of meteorites from their parent bodies. This approach provides new

constraints on the dynamical and collisional processes that may have shaped the temporal variations in H and L chondrite abundances over the last two million years.

Keywords: meteorites, ordinary chondrites, Atacama Desert, cosmogenic nuclides, terrestrial ages, past meteorite flux, CRE ages, asteroid belt

Résumé détaillé

Les météorites sont des fragments d'astéroïdes, de la Lune ou de planètes, qui ont survécu à leur traversée de l'atmosphère terrestre et atteint la surface de la Terre. Leur étude apporte des informations essentielles sur l'origine et l'évolution du Système solaire, puisqu'elles renferment des matériaux témoignant à la fois de la formation de la nébuleuse solaire et des processus de différentiation et d'évolution planétaire qui ont suivi.

À ce jour, plus de 77 000 météorites sont recensées dans la Meteoritical Bulletin DataBase (MBDB ; https://www.lpi.usra.edu/meteor/), dont environ 400 météorites martiennes et 750 lunaires, tandis qu'environ 99% proviennent d'astéroïdes provenant de la ceinture principale entre les orbites de Mars et Jupiter. Les chondrites ordinaires, comprenant les groupes H, L, et LL, sont les plus abondantes sur Terre et représentent environ 78% des chutes observées dans le monde.

Au-delà de leur nature fascinante, les météorites ont une valeur scientifique inégalable. Les chondrites, météorites non différenciées, sont parmi les matériaux les plus primitifs du Système solaire. Elles contiennent notamment les solides les plus vieux du Système solaire, datant de la formation de la nébuleuse solaire, et sont ainsi témoins de l'évolution de cette dernière. Les météorites différenciées, quant à elles, proviennent des noyaux, manteaux ou croûtes de corps planétaires ou d'astéroïdes différenciés. Leur étude renseigne ainsi sur la formation et la différentiation planétaire.

Depuis plusieurs décennies, des milliers de météorites ont été collectées, principalement dans les régions désertiques. En Antarctique, le climat froid et sec, associé aux processus glaciaires qui concentrent les météorites dans les zones de glace bleue, a permis la collecte de plusieurs dizaines de milliers de spécimens. Les déserts chauds (Afrique du Nord, péninsule Arabique, Nullarbor en Australie, Roosevelt County aux États-Unis, désert d'Atacama au Chili) sont également caractérisés par des conditions topographiques et climatiques favorables à la préservation et la collecte des météorites en vue des précipitations moindres et des taux d'érosion relativement faibles. Contrairement à l'Antarctique, où les dynamiques glaciaires concentrent les météorites et compliquent l'estimation des densités et de l'appariement, les déserts chauds agissent comme des surfaces d'accumulation passives, avec un transport latéral négligeable.

Le désert d'Atacama, situé au nord du Chili, est le désert non polaire le plus aride au monde. Bordé par l'océan Pacifique à l'ouest et la cordillère des Andes à l'est, il s'étend sur une superficie de 105 000 km². Le cœur hyperaride du désert reçoit moins de 4 mm de précipitations par an. Cette aridité extrême s'est installée depuis au moins 3 millions d'années, conférant ainsi à cette région une stabilité géomorphologique et climatique unique au monde.

Ces conditions favorisent la préservation à long terme des météorites sur des périodes significativement plus longues que les autres environnements désertiques. En effet, la

Dépression Centrale du désert d'Atacama abrite les collections de météorites les plus denses et les plus anciennes parmi les déserts chauds, notamment la collection d'El Médano précédemment étudiée, avec une densité exceptionnellement élevée et un âge terrestre moyen autour de 710 ka.

Dans ce contexte, cette thèse vise à exploiter le potentiel unique du désert d'Atacama avec pour objectifs principaux :

- Caractériser en détail une collection systématique de météorites dans la Dense Collection Area (DCA) de Catalina, au cœur de la Dépression Centrale hyperaride
- Vérifier l'étendue spatiale des fortes densités et des âges terrestres anciens mis en évidence à El Médano en comparant avec l'une étude systématique dans la DCA de Catalina ainsi qu'une seconde zone indépendante, la zone de Calama située plus au nord dans un contexte légèrement plus humide et avec une géomorphologie plus active
- Reconstituer l'intensité du flux passé de météorites sur les deux derniers millions d'années et évaluer la variabilité temporelle de la composition du flux (notamment l'abondance relative de chondrites H)
- Combiner les âges terrestres (en ^{36}Cl) avec les âges d'exposition cosmique (en ^{21}Ne) pour contraindre les âges d'éjection depuis les corps parents et en déduire des contraintes sur l'évolution dynamique et collisionnelle de la ceinture d'astéroïdes.

Dans la zone de Catalina, des recherches systématiques à pied ont été menée sur une surface de 6,80 km². Elle a permis de collecter 1599 météorites, formant la Catalina Systematic Collection (CSC). Cette approche systématique est fondamentale, car elle permet d'estimer des densités réelles et comparables entre zones, contrairement aux collectes aléatoires. La CSC présente la densité la plus élevée jamais mesurée dans un désert chaud, dépassant celle d'El Médano.

La classification des météorites est basée sur l'analyse pétrographique (microscopie optique), magnétique (mesure de la susceptibilité magnétique) et géochimique (composition des minéraux par microsonde électronique). Dans la CSC, parmi les 457 météorites de masse supérieure à 20 g, on trouve 96 % de chondrites ordinaires, 3 % de mésosiderites, une eucrite et une météorite de fer. L'absence de chondrites carbonées dans la CSC est probablement due à leur fragilité élevée face à l'abrasion causée par le vent. Pour obtenir une valeur robuste de la densité, il est nécessaire d'avoir une estimation de l'appariement (lorsque deux fragments appartiennent à la même météorite initiale). Pour cela, nous adoptons une approche probabiliste en utilisant un modèle mathématique précédemment développé, que nous avons adapté à la CSC. Ce modèle repose sur la comparaison des propriétés pétrographiques, magnétiques, minéralogiques des fragments et leur répartition à la surface. Cette approche a été complétée par une analyse spatiale de clusters basée sur les distances entre les fragments.

La densité brute de la CSC est de 235 météorites par km² (67 par km² pour les météorites > 20 g). Après correction de différents biais, la densité réelle est estimée à 71 météorites >20 g par km². Cette densité élevée est probablement liée à vieil âge terrestre de la CSC, ce qui expliquerait aussi l'absence de chondrites carbonées dans la collection, vu leur fragilité. Cette

longue période d'accumulation est liée à l'hyperaridité à long terme et la stabilité de surface du désert d'Atacama, conditions qui persistent depuis plusieurs millions d'années. La densité en météorites de la CSC est ainsi nettement supérieure à celle des autres déserts chauds comme le désert du Sahara, le désert d'Arabie, le Nullarbor en Australie, ou les déserts du sud-ouest des États-Unis.

De plus, les météorites du CSC sont en moyenne moins altérées que celles d'autres déserts chauds, malgré la longue période d'accumulation. Le rapport de chondrite H sur chondrite L du CSC est plus élevé que celui des autres déserts chauds, de l'Antarctique et des chutes, mais proche du rapport de la collection d'El Médano, reflétant potentiellement des variations dans la composition du flux passé de météorite sur Terre.

La détermination des âges terrestres (temps de résidence d'une météorite à la surface depuis sa chute sur Terre) et des âges d'exposition aux rayons cosmiques (âges CRE qui reflète la durée du trajet dans l'espace interplanétaire du météoroïde) est basée sur la mesure des nucléides cosmogéniques produits par l'interaction des rayons cosmiques avec les minéraux constituants les météorites au cours de la traversée dans l'espace interplanétaire.

Les âges terrestres ont été déterminés à partir des concentrations en ^{36}Cl mesurées dans la phase métallique des météorites par spectrométrie de masse par accélérateur (AMS). Le ^{36}Cl, un radionucléide avec une demi-vie de 301 000 ans, permet ainsi de dater des météorites jusqu'à ~3 Ma. Les âges CRE sont, quant à eux, déduits à partir du néon (^{21}Ne), un gaz rare stable mesuré par spectrométrie de gaz. Il renseigne sur la durée passée par le météoroïde dans l'espace et permet ainsi de vérifier que ce dernier avait bien atteint sa concentration à saturation en ^{36}Cl avant sa chute sur Terre.

Cette double approche fournit deux contraintes essentielles :

- Les âges terrestres, combinées aux densités mesurées, permettent d'estimer le flux de météorites moyen au cours du temps
- La combinaison des âges terrestres et d'exposition permet d'estimer les âges d'éjection depuis la ceinture d'astéroïdes, apportant des contraintes sur la dynamique de transfert des météoroïdes vers la Terre

Dans la CSC, les âges terrestres ont été mesurés sur 51 météorites non appariées et atteignent une moyenne d'environ 1 Ma (médiane 750 ka), avec des valeurs maximales dépassant 2 Ma. Ces âges confirment la stabilité exceptionnelle des surfaces de l'Atacama. Le flux de météorites moyen au cours des deux derniers millions d'années est estimé à 69 ± 8 météorites > 20 g par km² par million d'années. Cette valeur est cohérente avec les estimations à plus court terme issues des collections antarctiques, sahariennes et des chutes observées.

En ce qui concerne la zone de Calama, la zone « productive », définie comme la surface claire à contexte géomorphologique favorable, s'étend sur environ 550 km². Dans cette zone, 1 206 météorites ont été collectées par des chercheurs de météorites privés, soit une densité moyenne de 2,2 météorites par km², beaucoup plus faible que celle mesurée par nous-mêmes par une recherche systématique sur une zone de 2,5 km^2 (37 météorites par km²). Cette différence illustre l'efficacité des collectes systématiques. En extrapolant cette densité

systématique à l'ensemble de la zone productive, celle-ci pourrait encore abriter près de 20 000 météorites non découvertes. Un contraste encore plus marqué avait été observé dans la zone de Catalina, où la densité obtenue par recherches systématiques était 118 fois plus élevée que celle des collectes aléatoires. Ces résultats confirment que les prospections systématiques sont indispensables pour établir des densités représentatives et comparables entre régions, et estimer le flux de météorites vers la Terre.

Dans la Calama Systematic Collection (CASC), nous avons classé l'ensemble des météorites de masse >5 g, ainsi qu'un sous-échantillon de 10 météorites <5 g, soit un total de 59 échantillons. À l'exception de deux météorites (Calama 058, une chondrite carbonée CR2, et Calama 800, une enstatite chondrite EL4b-an), toutes les autres appartiennent aux chondrites ordinaires, réparties entre H5, H6, L5 et L6, avec également une brèche H5-6, une LL3, une LL5 et deux LL7. La CASC confirme donc la nette prédominance des chondrites ordinaires dans les collections de l'Atacama, tout en montrant que des types plus rares, bien que minoritaires, peuvent être préservés sur ces surfaces.

Par ailleurs, les âges d'exposition mesurés sur des carbonates de surface dans la zone de Calama (jusqu'à 1,35 Ma) confirment que la surface est stable, mais plus jeune que celle d'El Médano, où des âges d'exposition supérieurs à 6 Ma ont été mesurés. Ces résultats sont cohérents avec les conditions plus dynamiques et légèrement plus humides qui caractérisent la région de Calama, comparé aux zones de la Dépression Centrale de l'Atacama.

Malgré ces différences régionales, les âges terrestres mesurés dans la CASC sont remarquablement élevés pour un désert chaud. L'âge moyen est de 533 ka, avec une médiane de 331 ka, des valeurs nettement supérieures à celles rapportées pour les autres déserts chauds du globe. À titre de comparaison, les collections d'Oman et d'Arabie Saoudite présentent des âges compris entre 10 et 25 ka (moyenne : 20 ± 12 ka), celles du désert de Lut en Iran entre 10 et 30 ka, celles du Nullarbor en Australie autour de 19 ± 13 ka, celles du Sahara entre 0 et 35 ka, et celles de Roosevelt County (Nouveau-Mexique, USA) entre 7 et >44 ka. La zone de Calama se distingue donc par des âges terrestres bien plus anciens, qui rejoignent les tendances observées à Catalina et El Médano, confirmant l'exceptionnelle capacité du désert d'Atacama à préserver les météorites sur le long terme.

L'analyse des âges terrestres des collections combinées de Catalina et El Médano révèle des variations de la composition du flux : la proportion de chondrites H présente un pic marqué entre 1,2 et 0,4 Ma, suivi d'un déclin vers les valeurs actuelles. Cette tendance n'est pas expliquée par les modèles dynamiques actuels, qui prédisent une proportion constante.

Les âges d'exposition (CRE) ont été déduites des mesures de ^{21}Ne sur 33 chondrites H qui ont un âge terrestre >0.5 Ma et provenant des collections systématiques de Catalina et El Médano. Ces âges varient de 1,6 à 47 Ma (moyenne 10,6 Ma ; médiane 3,8 Ma), en accord avec les données de la littérature.

En combinant les âges terrestres avec les âges CRE des chondrites H, nous pouvons déterminer les âges d'éjection des météorites depuis leurs corps parent. Leur distribution reflète un pic à 5–7 Ma, associé aux contributions des familles Karin et Koronis$_2$. Un pic supplémentaire vers 3 Ma, non décrit dans la littérature, pourrait indiquer la contribution d'une

petite famille astéroïdale non détectée, liée à un événement collisionnel ponctuel. Notre base de données des âges d'éjections des chondrites H reste encore limitée en termes de nombres d'échantillons, mais elle a renforcé la vision que le flux de météorite est dominé par des collisions stochastiques et soulève la possibilité de la présence d'évènements collisionnel non détecté par les modèles dynamiques actuels, et qui ont pu influencer le flux de météorites au cours des derniers millions d'années.

En conclusion, cette thèse met en évidence le rôle unique du désert d'Atacama dans la préservation exceptionnelle des météorites. La zone de Catalina fournit la collection systématique la plus dense et la plus ancienne, permettant de reconstruire le flux de météorites sur les deux derniers millions d'années. La zone de Calama, située à environ 270 km de Catalina et dans un contexte environnemental légèrement différent, confirme que ces densités et ces âges exceptionnels ne se limitent pas à la Dépression Centrale, mais s'étendent à l'échelle régionale.

Grâce à la combinaison d'analyses de densité, d'âges terrestres (^{36}Cl) et d'âges d'exposition cosmique (^{21}Ne), nous avons pu reconstituer l'intensité et la composition du flux de météorites au cours des deux derniers millions d'années. Nos résultats indiquent une stabilité globale de l'intensité du flux, mais révèlent également des variations compositionnelles importantes, probablement liées à des événements collisionnels ponctuels dans la ceinture d'astéroïdes. L'Atacama apparaît ainsi comme un site unique pour explorer les liens entre dynamique astéroïdale et flux de météorites sur Terre sur des échelles intermédiaires (10^5–10^6 ans), inaccessibles ailleurs.

To the memory of my beloved father.

Remerciements

Writing a thesis is not an easy task, but I think I left the most difficult part for the end. There are so many people I would like to thank, and I don't know where to start, where to stop, or in which language to write.

First, I would like to thank **all members of the jury** for accepting to be part of this and for taking the time to read and evaluate my thesis. My gratitude goes also to the two members of my committee, **Lydie Bonal** and **Julie Aleman**.

These past three years have been highly enriching, both scientifically and personally, and one thing I have learned is that science cannot be done alone. I had the chance to work, collaborate, discuss, and meet many people who each taught me something.

To the one who taught me the most, who trusted me and believed in me, who organized field missions to the Atacama Desert twice in a row just for me, to my supervisor, **Jérôme Gattacceca**, you have all my gratitude. I enjoyed every part of working alongside you. Thank you for being kind, supportive, available, and overall, an amazing scientist and human being. Sorry for defending on a Thursday, I know it's football day!

I would like to thank everyone at **CEREGE**, who accompanied me throughout this journey and made life easier.

From the Planéto team, thank you to: **Clara**, since day one, an amazing person and researcher I look up to; **Anthony**, for all the discussions on asteroids and statistical models, your help and contribution to my papers and manuscript, the good times spent in the field in the Atacama Desert; **Yoann, Minoru, Pierre, Valéry, François**, un grand merci.

Merci à **Julien L.** pour toutes les sections polies durant ces trois ans (et ce n'est pas fini !). Merci à **Françoise** pour sa gentillesse et ses bons gâteaux (sans gluten et sans lactose !).

Merci à la **Direction du CEREGE** et à toutes les personnes de l'administration, en particulier **Noémie Garron** et **Patricia Rieux**.

Un immense merci à **Aix-Marseille Université** et l'**ED251,** qui ont financé ma thèse, ainsi qu'à **Isabelle Hammad** pour sa réactivité et tout ce qu'elle fait pour les doctorants.

Un très très grand merci à l'équipe **ASTER**, pour leur travail, leur gentillesse, et toutes les mesures de chlore !

Je remercie tous les **doctorants et postdocs (et autres postes) du CEREGE** partis ou toujours là: **Mary, Julie, Naïs, Guillaume, Amazigh, Anthony, Claire, David, Didier, Camille, Elise, Floriane, Lou, Perrine, Julien**… pour les discussions et les bons moments partagés.

Et les Koolkidz : **Charlotte, Nicolas, Vincent, Virgil, Louisa, Houda, Lilas, Morgane, Ellyn, Lounis, Paul B., Yohan, Daniel…** Merci à **Florian** d'avoir fait ton stage de M2 avec moi, merci pour les météorites classées, le métal extrait, et les mesures de chlore faites.

Merci du fond du cœur à **Abraham, Youssef, Oumaima, Mélanie, Pauuuuuul, Hugooo et Cécile**, votre amitié m'a beaucoup aidée ces dernières années.

I am deeply grateful to **Ingo Leya** for allowing me to do noble gas measurements at the University of Bern and for everything I learned during and after this experience, and, of course,

I would like to thank **Tauseef,** who helped me with the measurements and made me feel welcome in a new city.

Un grand merci à **David Bekaert, Pierre-Henry Blard, et Evelyn Füri** pour leur aide dans les mesures de néon au CRPG.

Je remercie chaleureusement les personnes qui étaient présentes sur le terrain en Atacama en novembre 2023: **Matthieu Gouenelle, Mathieu Roskosz, Lydie Bonal, Pierre-Marie Zanetta, Alexandre Corgne, Lionel Vacher, et Lunaaaa.** Je tiens également à remercier toutes les personnes qui ont participé à toutes les missions de collectes des météorites sur lesquelles j'ai travaillé.

I am eternally grateful to have met these four girls, who have become family. You are the best part of this PhD, I can't imagine how I would have done it without you, my sisters **Nour, Medhavi, Maureen, and Anna**. Thank you for the laughs, cries, (inside) jokes, adventures, travels, help, advice, bumpy bus rides, brief running sessions, (very) late lunches… some days you were my sole motivation. You have been there through it all, the good and the bad, and for that, you have my infinite gratitude, I will always cherish these moments spent with you.

Un merci astronomique à mon copain, **Pierre**, pour ta présence, tes conseils, ton aide avec les codes Python, mon Git, mes repos… pour la musique que tu partages avec moi et qui m'aide au quotidien. Merci de m'avoir supportée, même dans les moments les plus difficiles, et surtout pendant la rédaction (de l'intro).

À mes très chers amis, qui eux aussi font ou ont déjà fait une thèse: **Elio, Christelle, Antoine, Michelle, Batoul, Gaëlle, Elias, Bosko…** et aussi ceux qui ne font pas de thèse: **Marwa**, **Sarah, Joelle, Sally, Mariam…**

À ma famille et mes amis au Liban, je leur dois beaucoup, même de loin. **Maman**, merci d'avoir supporté mes appels en sortant du labo, mes moments de joie, de stress, de fatigue, de pleurs... Merci à mon frère **Mickel** (qui m'a toujours poussée et me conduit à l'aéroport en supportant mes pleurs) et ma sœur jumelle**, Maryline** (qui ne me ressemble pas du tout). Un immense merci à ma grande famille, ma mamie, mes tantes, mes oncles, et tous mes cousins et cousines, il y aurait de quoi remplir l'amphi ! Vous avez toujours cru en moi, et pour cela je suis très reconnaissante. J'espère vous rendre fiers de moi.

En espérant n'avoir oublié personne, encore merci à tous.

P.S. No meteorites were harmed during this PhD...only cut, crushed, dissolved, leached, bombarded by high-speed electrons, and occasionaly degassed.

Table of Contents

Affidavit *3*

Liste de publications et/ou brevets et participation aux conférences *5*

Résumé *7*

Abstract *9*

Résumé détaillé *11*

Remerciements *17*

Table of Contents *19*

List of Figures *23*

List of Tables *27*

List of Abbreviations and Units **29**

1. Introduction *32*

1.1. The Solar System **32**

1.1.1. Formation of the Solar System 32

1.1.2. Components of the Solar System 36

1.2. Asteroids and the Main Asteroid Belt **40**

1.2.1. Asteroid classification 40

1.2.2. Asteroid families 42

1.2.3. Structure of the Main Asteroid Belt 44

1.3. How does extraterrestrial material reach us? **46**

1.3.1. Thermal forces 46

1.3.2. Resonances and gravitational effects 49

1.3.3. Implications of the Yarkovsky effect 50

1.4. Meteorites **51**

1.4.1. Definitions and importance 51

1.4.2. Meteorite classification 52

1.4.3. Formation of meteorites in the Solar System 55

1.4.4. Secondary processes 56

1.4.5. Focus on ordinary chondrites 58

1.5. Cosmogenic nuclides in meteorites **70**

1.5.1. Production pathways and types 70

1.5.2. Applications 71

2. Chapter 2 ..... *76*

2.1. Introduction **76**

2.2. Article summary **79**

2.3. Article **80**

2.4. Conclusion 97

3. Chapter 3 100

3.1. Introduction 100

3.1.1. Flux of extraterrestrial material to Earth 100

3.1.2. Terrestrial ages 102

3.1.3. Accelerator Mass Spectrometry 103

3.1.4. Chlorine-36 104

3.2. Article summary 106

3.3. Article 106

3.4. Conclusion 206

4. Chapter 4 209

4.1. Introduction 209

4.2. Article 209

4.3. Conclusion 246

5. Chapter 5 251

5.1. Introduction 251

5.2. Methods 255

5.3. Results and discussion 255

5.3.1. Neon isotopic compositions 255

5.3.2. Cosmic-ray exposure ages and ejection ages 256

5.4. Conclusion 259

5.5. Chapter supplementary 260

6. Chapter 6 268

6.1. Conclusions 268

6.1.1. Meteorite density 268

6.1.2. Terrestrial ages and past meteorite flux 268

6.1.3. Composition of the meteorite flux 269

6.1.4. Cosmic-ray exposure ages and ejection histories 269

6.2. Side projects 269

6.3. Perspectives 270

6.3.1. On the future of hot desert meteorite collections 270

6.3.2. Towards confirming the 3 Ma peak in H chondrite ejection ages 271

6.3.3. Comparing meteorite and micrometeorite flux records 271

Bibliography 273

Appendices 290

A. Detailed protocol of ^{36}Cl extraction from meteorite samples 290

B. Uncertainty on terrestrial age 294

C. Uncertainty on H chondrite relative abundance 295

D. Repositories and projects..... 296

E. Additional terrestrial ages..... 297

F. Additional neon analysis and CRE ages..... 298

List of Figures

Figure 1.1. Hubble image of a compact star-forming region in the Cygnus constellation (3300 light-years away). A young massive star is surrounded by a molecular cloud. Credit: NASA & ESA 33
Figure 1.2. Schematic view of the small-body populations in the Solar System, including the Main Asteroid Belt, Kuiper Belt, and Oort Cloud. Sizes and distances are not to scale. (CREDIT ESA; acknowledgement: work performed by ATG under contract to ESA). 34
Figure 1.3. Evolution of the Solar System through dynamical models (The Grand Tack and The Nice model). From DeMeo and Carry (2014). 36
Figure 1.4. (a) Schematic of an elliptical orbit showing the semimajor axis a and semiminor axis b (b) Inclination i of a planar orbit with respect to a reference plane X and periapsis (c) Ascending (Ω) and descending node (d) argument of periapsis $\boldsymbol{\omega}$. Credit: https://github.com/bryanwweber/orbital-mechanics-notes. 39
Figure 1.5. Mosaics of Bennu (left) and Vesta (right) (NASA/JPL-Caltech/UCLA/MPS/DLR/IDA). 40
Figure 1.6. The Bus–DeMeo spectral taxonomy of asteroids showing reflectance spectra for each class (in the 0.45–2.45 μm wavelength range; from DeMeo et al. (2009). 41
Figure 1.7. (a) Present-day structure of the main reservoirs in the Solar System. (b) Primordial structure of the protoplanetary disk. From Vernazza and Beck (2017). 42
Figure 1.8. Structure of the Main Asteroid Belt showing the inner (blue), middle (orange), and outer (green) main belt, separated by the Kirkwood Gaps caused by the mean-motion resonances (3 :1, 5 :2, 7:3, 2 :1). Based on Alan Chamberlain, JPL/Caltech. 45
Figure 1.9. Major asteroid families and resonances in the main asteroid belt. From (DeMeo and Carry 2014) 46
Figure 1.10. Schematic illustration of the two components of the Yarkovsky effect (a) The diurnal Yarkovsky effect (b) The seasonal Yarkovsky effect. From Bottke et al., (2006). 48
Figure 1.11. Explicative scheme of the YORP effect from Bottke et al. (2006). 49
Figure 1.12. Image captured by the Italian Space Agency's LICIACube a few minutes after DART collided with Dimorphos on Sept. 26, 2022. Credit: ASI/NASA 49
Figure 1.13. Undifferentiated vs differentiated bodies. 52
Figure 1.14. Meteorite classification scheme. Based on (Weisberg et al. 2006) and Rubin and Ma (2021). 54
Figure 1.15. Representation of the NC-CC-CI trichotomy. From (Hopp et al. 2022). 55
Figure 1.16. Summary plot of the heliocentric distances and times of formation of different meteorite types in the early Solar System. From Desch et al. (2018). 56
Figure 1.17. Different chondrules in El Médano 520 (LL3.15) under reflected light. 59
Figure 1.18. Fayalite vs ferrosilite content in ordinary chondrites (n = 5701). Data from MBDB. 60
Figure 1.19. Different degrees of metamorphism in H chondrites seen under reflected light (Catalina 580–H3, Catalina 958–H4, Catalina 789–H5, Catalina 799–H6), showing progressive

equilibration of silicates and growth of metal and sulfide grains with increasing petrologic type. 62
Figure 1.20. Reflected-light images illustrating different degrees of weathering in ordinary chondrites. (a) Catalina 799–H6 W1: fresh sample showing abundant metal (bright white) and sulfide grains (pale salmon) (b) Calama 650–L6 W3: heavily weathered sample showing extensive replacement of metal and sulfide grains by Fe- oxyhydroxides (light grey) and the development of alteration veins. 63
Figure 1.21. Magnetic susceptibility (log χ) as a function of the weathering grade for H (filled) and L (open) chondrites. From Rochette et al. (2008). 65
Figure 1.22. Onion shell (with increasing petrographic grade T3–T6) and rubble pile structures. After Wilkison et al. (2002). 67
Figure 1.23. Distribution of cosmic-ray exposure ages of H, L, and LL chondrites. From Eugster (2003). 68
Figure 1.24. Zodical light (white light on the right), induced by the zodiacal cloud, along with the Milky Way on the left, in the Paranal sky taken by ESO's Very Large Telescope (VLT) at Paranal Observatory in Chile. Credit: Y. Beletsky (LCO)/ESO. 70
Figure 1.25. Evolution of the radioactive (black) and stable (green) nuclide content in meteorites. The dashed vertical red line represents the time of the fall of the meteorite on Earth. Cosmic ray exposure (CRE) age corresponds to the time spent by the meteoroid in the interplanetary medium before reaching Earth (orange dashed double arrow), while the terrestrial age corresponds to the time spent by the meteorite on Earth (gray dashed double arrow). The age of ejection of the meteoroid from the parent asteroid is the sum of the terrestrial age and the cosmic ray exposure age. 72
Figure 2.1. Number of meteorites from Antarctica, Northwest Africa, South America, and Asia reported in the last 11 Meteoritical Bulletins, with each bulletin corresponding to a civil year phased with civil years, with MB102 reporting meteorites approved by the Nomenclature Committee in 2013 and so on. From The Meteoritical Bulletin, no. 113; Gattacceca et al. (2025). 76
Figure 2.2.Search campaigns for meteorites in Antarctica (upper), Tunisian Sahara (middle), and the Atacama Desert (bottom)..... 78
Figure 2.3. Illustration of the concept of pairing. Background generated with AI. 80
Figure 3.1. Accelerator Mass Spectrometer at the ASTER facility in CEREGE (Aix-en-Provence, France). Credit: ASTER, LN2C laboratory..... 103
Figure 5.1. Schematic illustration of the different ages of a meteorite. The ejection age is the sum of the cosmic-ray exposure age (duration of exposure to cosmic rays in the interplanetary medium) and the terrestrial age (residence time on Earth). 251
Figure 5.2. Distribution of cosmic-ray exposure ages of ordinary chondrites (H, L, and LL). Distinct peaks reflect major collisional events in the asteroid belt (From Eugster 2003). 252
Figure 5.3. Abundance of different meteorite groups in the NEO vs meteorite falls populations and the difference between the two. Data from Brož, Vernazza, Marsset, DeMeo, et al. (2024b). 254
Figure 5.4. 20Ne/22Ne as a function of 21Ne/22Ne of H chondrites 33 (and replicas; n=39) from the Catalina Systematic Collection and the El Médano Systematic Collection. Also shown is the atmospheric component with 20Ne/22Ne = 9.80 and 21Ne/22Ne = 0.02904 (Ozima and Podosek 2002), and the cosmogenic component range (Dalcher et al. 2013; Leya and Masarik 2009)..... 256

Figure 5.5. Distribution of cosmic-ray exposure (CRE) ages for H chondrites compiled from (Graf and Marti 1995), shown alongside CRE ages of H chondrites from the Atacama Desert determined in this study (n = 33). 257
Figure 5.6. Distribution of cosmic-ray exposure (CRE) ages for H chondrites compiled from (Graf and Marti 1995), shown alongside ejection ages of H chondrites from the Atacama Desert with terrestrial ages > 0.5 Ma (this study, n = 33). 257
Figure 5.7. Ejection age as a function of the terrestrial age of the 33 H chondrites measured in this study from Catalina and El Médano collections, along with error bars. The dashed lines represent the main clusters of ejection ages: the ~3 Ma peak (red), the 5.8 Ma peak associated with the Karin cluster (green), and the 7.6 Ma peak linked to Koronis2 cluster (purple). 258
Figure 5.8. Distribution of ejection ages H chondrites with terrestrial age >0.5 Ma (n = 33). Error bars are uncertainties for a Poisson distribution (√N for N meteorites in a bin). 259
Figure 5.9. Extraction line and gas spectrometer for gas measurements at CRPG, Nancy. 260
Figure 5.10. Extraction line and gas spectrometer at the University of Bern, Switzerland. 260

List of Tables

Table 1.1. Main petrological and chemical changes with increasing petrologic type of ordinary chondrites. Adapted from Van Schmus and Wood (1967). 61
Table 1.2.Main cosmogenic nuclides commonly used in meteorite studies, with half-lives and target elements (Eugster et al. 2006). 71
Table 5.1. Neon isotopic compositions, cosmogenic components, and Cosmic-Ray Exposure (CRE) ages of Atacama meteorites measured in this study. 261
Table 5.2. Terrestrial ages, cosmic-ray exposure (CRE) ages, and ejection ages of H chondrites from the Atacama Desert (n = 33). 264

Table A. 1. Terrestrial ages of three mesosiderites from the Catalina Systematic Collection. 297
Table A. 2. Neon isotopic compositions, cosmogenic components, and Cosmic-Ray Exposure (CRE) ages of meteorites from the Calama area. 298

List of Abbreviations and Units

Institutions and Laboratories

ASTER – Accélérateur pour les Sciences de la Terre, Environnement, Risques (CEREGE)

CEREGE – Centre de Recherche et d'Enseignement des Géosciences de l'Environnement (Aix-en-Provence, France)

CRPG – Centre de Recherches Pétrographiques et Géochimique (Nancy, France)

ESA – European Space Agency

NASA – National Aeronautics and Space Administration (United States)

Atacama Meteorite Collections and Laboratories

CAC – Calama Area Collection

CASC – Calama Area Systematic Collection

CSC – Catalina Systematic Collection (Atacama Desert)

DCA – Dense Collection Area

EMSC – El Médano Systematic Collection (Atacama Desert)

General abbreviations and symbols

AMS – Accelerator Mass Spectrometry

AU – Astronomical Unit

Atm. – Atmospheric

CAI – Calcium-Aluminium-rich Inclusion

En – Enstatite ($MgSiO_3$) component of pyroxene

Fa – Fayalite (Fe_2SiO_4)

Fs – Ferrosilite ($FeSiO_3$)

H, L, LL – Ordinary chondrite groups (high, low, and low-low iron content)

ICP-OES – Inductively Coupled Plasma–Optical Emission Spectrometry

Ma / ka – Ages in millions / thousands of years before present

Myr / kyr – Time durations in millions / thousands of years

NEA / NEO – Near-Earth Asteroid / Near-Earth Object

OC – Ordinary Chondrite

Wo – Wollastonite ($CaSiO_3$)

YORP effect – Yarkovsky–O'Keefe–Radzievskii–Paddack effect

± – Uncertainty (one standard deviation)

Chapter one

Introduction

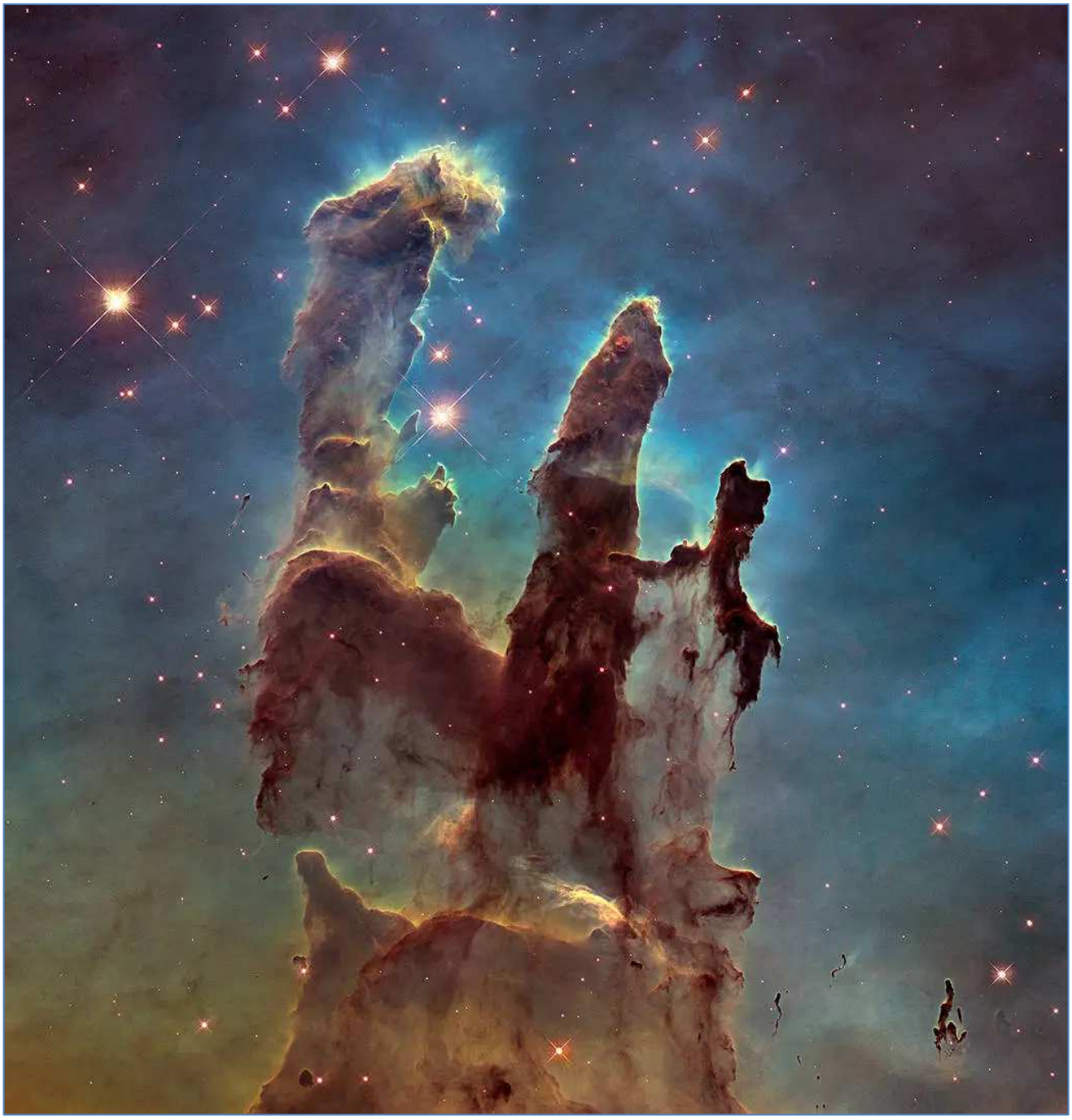

We've always defined ourselves by the ability to overcome the impossible. And we count these moments. These moments when we dare to aim higher, to break barriers, to reach for the stars, to make the unknown known.

Cooper – Interstellar

1. Introduction

1.1. The Solar System

Since the dawn of time, humans have gazed at the night sky, fascinated by the darkness of the universe and the luminous dots hanging above our heads, seeking to understand what surrounds us. How was it created? How did it evolve? How did the universe reach its current state?

Thanks to significant conceptual and technological advances, many questions have been answered, though an astronomical amount remains open. One way to explore our universe is to look up to the sky or simply go to space. But what if we looked down to study what is up there? What if these dark rocks called ***meteorites,*** we find lying on the ground, can tell us much more than we think about the Solar System around us?

1.1.1. Formation of the Solar System

The Solar System formed 4.57 billion years ago from the gravitational collapse of a rotating molecular cloud of gas and dust known as the solar nebula, forming a dense core in which a central protostar developed, surrounded by a rotating protoplanetary disk. The disk's rotation was maintained through conservation of angular momentum.

Around 100 thousand to 1 million years after collapse, once the protostar's core reached ~10 million K, hydrogen fusion into helium began, marking the birth of the Sun as a main-sequence star[3]. During this early phase, refractory inclusions[4] and chondrules[5] formed in the nebula. Calcium-Aluminium-rich inclusions (CAIs) are the oldest dated solids in the Solar System, with ages of 4567.30 ± 0.16 Ma (Connelly et al. 2012), later refined to 4568.7 Ma (Piralla et al. 2023). Chondrule formation followed within a few million years.

By approximately 3–5 Myr after CAI formation, strong solar winds and radiation pressure from the young Sun had dispersed most of the remaining nebular gas and dust, leaving behind the building blocks of planets.

[3] Longest and most stable phase in a star's life cycle, during which hydrogen fusion into helium occurs in its core, which is in hydrostatic equilibrium.

[4] Submillimeter- to centimeter-sized objects found in chondritic meteorites, rich in refractory elements such as Ca, Al, and Ti. They are classified into two main types: calcium-aluminum-rich inclusions (CAIs) and amoeboid olivine aggregates (AOAs).

[5] Micrometer- to millimeter-sized molten silicate spherules formed by rapid melting and cooling of dust



Figure 1.1. Hubble image of a compact star-forming region in the Cygnus constellation (3300 light-years away). A young massive star is surrounded by a molecular cloud. Credit: NASA & ESA

Once the protoplanetary disk dissipated, gravitational accretion[6] and dynamical evolution led to the formation of our Solar System as we know it today, which consists of the Sun and eight planets (Mercury, Venus, Earth, Mars, Jupiter, Saturn, Uranus, and Neptune), along with dwarf planets, natural satellites, comets, asteroids, and dust particles.

The distinction between planets and dwarf planets was established by the International Astronomical Union (IAU) in 2006. A dwarf planet is defined as a body that orbits the Sun, is not a satellite of another body, is massive enough to have reached hydrostatic equilibrium[7] (i.e., nearly spherical shape), but has not cleared its orbital neighborhood, unlike planets. There are currently five recognized dwarf planets in the Solar System: Ceres, Pluto, Eris, Haumea, and Makemake.

Objects that are neither planets, dwarf planets, nor satellites are classified as small Solar System bodies. They include asteroids (except Ceres), comets, Trojans, Centaurs, and most trans-Neptunian objects[8]. Asteroids have irregular shapes, are smaller than planets and dwarf planets, and have not cleared their orbital neighborhood. Examples include Vesta, Pallas, and Eos.

[6] Process by which solid bodies grow through gravitational attraction and accumulation of surrounding gas, dust, or solids, leading to the formation of larger objects such as planetesimals and planets

[7] The state in which an object's self-gravity is strong enough to overcome material strength, shaping the body into a sphere (or oblate spheroid: sphere flattened at the poles and enlarged at the equator due to rotation)

[8] Except dwarf planets such as Pluto and Haumea

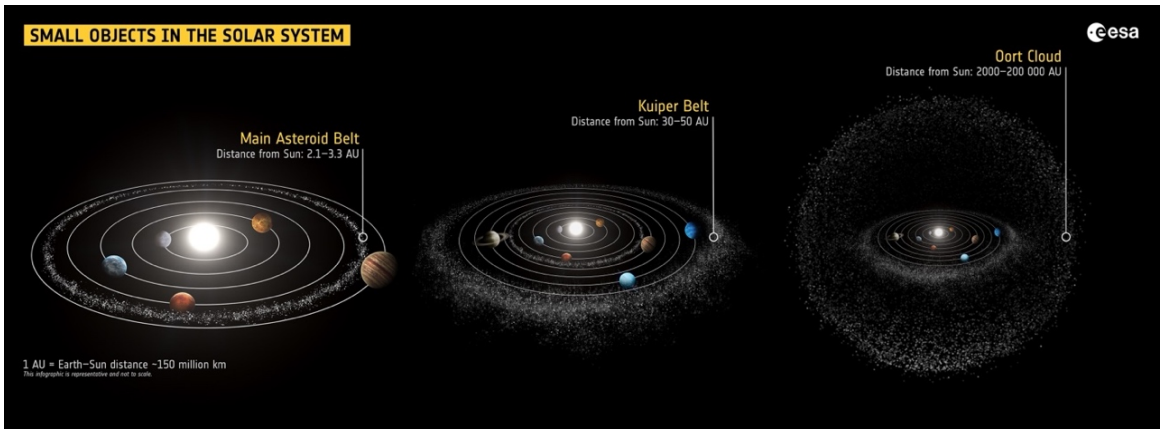

Figure 1.2. Schematic view of the small-body populations in the Solar System, including the Main Asteroid Belt, Kuiper Belt, and Oort Cloud. Sizes and distances are not to scale. (CREDIT ESA; acknowledgement: work performed by ATG under contract to ESA).

The main concentrations of small bodies in the Solar System include (Figure 1.2):

- Near-Earth Objects (NEOs): Asteroids and comets with orbits that bring them close to Earth (within 1.3 AU[9] of the Sun). They mainly originate from the Main Asteroid Belt
- Main Asteroid Belt: A dense, ring-shaped region of asteroids between 2.1 and 3.3 AU, between the orbits of Mars and Jupiter. It includes millions of objects, from the dwarf planet Ceres to kilometer- to m-sized asteroids
- Trojan asteroids: Populations of asteroids that share an orbit of a planet, clustered around the stable L4 and L5 Lagrange points[10], respectively 60° ahead and behind the planet. The largest and most studied population are the Jupiter Trojans, but smaller Trojan groups also exist for Neptune, Mars, Earth and Uranus.
- Kuiper Belt: A region beyond the orbit of Neptune, between 30 and 50 AU, estimated to be 20–200 times more massive than the Main Asteroid Belt. It includes Pluto, Haumea, Makemake and many smaller icy bodies. It is the main reservoir of short-period comets.[11]
- Scattered Disk: A dynamically outer excited extension of the Kuiper Belt, populated by highly inclined and eccentric objects strongly disturbed by Neptune's gravity, such as Eris
- Oort Cloud: A distant, spherical shell of icy bodies extending from about 2000 to 200000 AU. It likely includes billions of comets and is the main source of long-period comets.[12]

[9] Astronomical Unit: Earth–Sun distance where 1 AU= 149 597 870 700 m (IAU Resolution B2, XXVIII General Assembly of International Astronomical Union, Beijing, 31 August 2012)

[10] Lagrange points are positions of gravitational equilibrium where a small-mass object can remain stable under the combined gravitational influence of two massive orbiting bodies. There are five Lagrange points (L1–L5).

[11] Comets with periods <200 years (https://science.nasa.gov/solar-system/comets/facts/)

[12] Comets with orbital periods > 200 years, up to 30 million years. (https://science.nasa.gov/solar-system/comets/facts/)

Several models have been proposed to explain the present-day structure of the Solar System, suggesting that giant planets migrated from their original positions due to interactions with the protoplanetary disk, and later with planetesimals[13].

The Grand Tack model (Walsh et al. 2011) suggests that Jupiter, initially at ~3.5 AU near the snow line[14], migrated inward through the gas disk to ~1.5 AU before going backwards ("tacking") due to interaction with Saturn, strongly influencing the early structure of the Solar System (Figure 1.3). This migration induced strong radial mixing of planetesimals, scattering materials both inward and outward, and depleting solids inside 1 AU. This model explains the small mass of Mars and the depletion of the primordial asteroid belt, which was later replenished by a mixture of bodies from both the inner and outer Solar System.

The Nice model (Tsiganis et al. 2005; Gomes et al. 2005) describes a later phase of orbital instability among the giant planets, occurring after the dispersal of the gas disk. This instability induced significant rearrangements of small body populations, including the dispersal of the primordial Kuiper Belt, formation of the Oort Cloud, capture of the Trojan asteroids, and additional mass loss from the main belt (Figure 1.3). Together, these events are thought to have ejected more than 99.9% of the original planetesimal population from the Solar System .

[13] Solid bodies that represent the intermediate stage between dust grains and planets, later forming planetary embryos.

[14] The snow line is the distance from the protostar of a solar nebula beyond which temperatures are low enough for volatile compounds such as water, methane, and ammonia, to condense into solid grains, subsequently allowing their condensation into planetesimals.

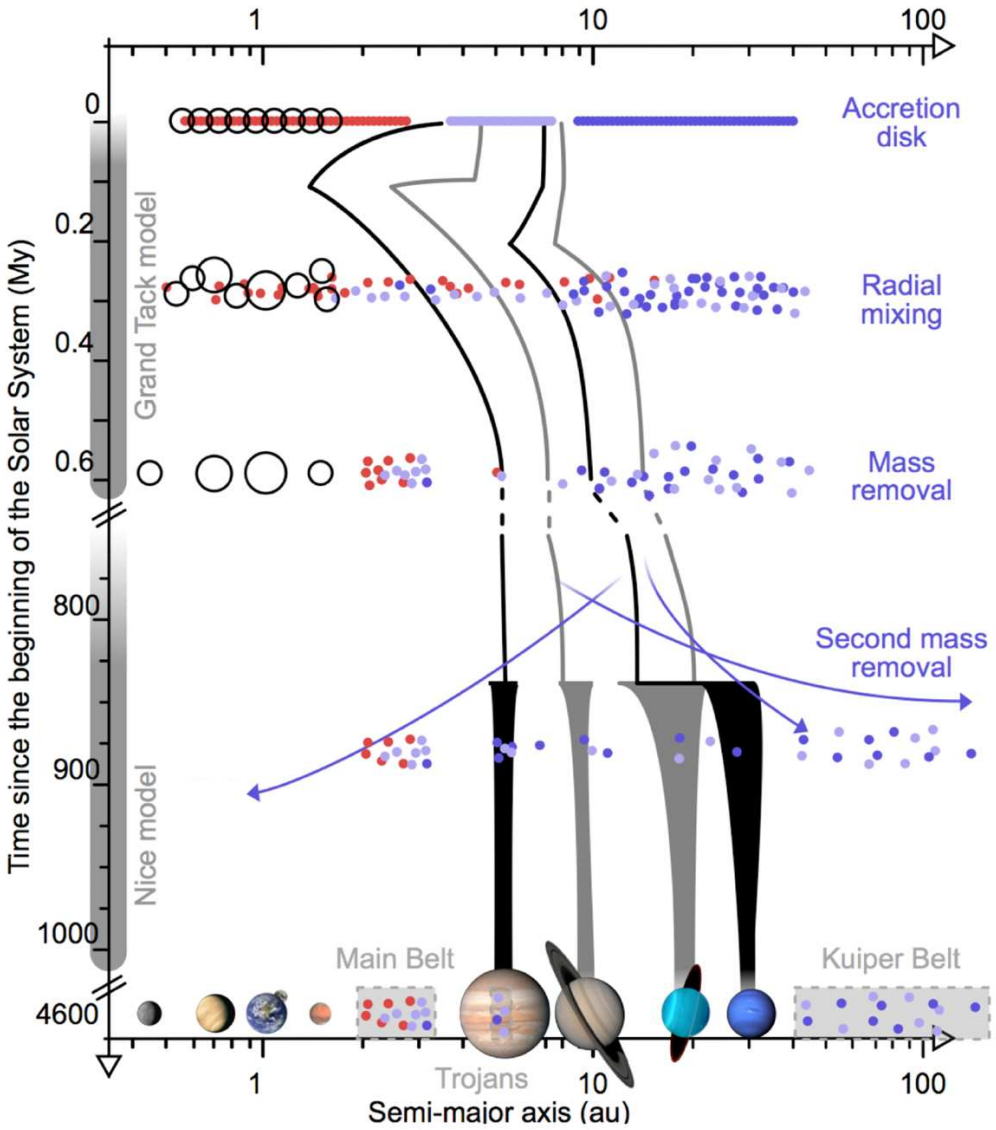

Figure 1.3. Evolution of the Solar System through dynamical models (The Grand Tack and The Nice model). From DeMeo and Carry (2014).

1.1.2. Components of the Solar System

1.1.2.1. Definitions

I will begin this section with some necessary definitions (Rubin and Ma 2021).

- ***Meteorite***: A natural solid object originating from a parent body such as a planet, asteroid, moon, or comet, that was ejected into interplanetary space and later survived passage through a planetary atmosphere to reach the surface as a rock larger than 2 mm in size.
- ***Micrometeorite:*** A very small meteorite, ranging in size from a few μm to 1 mm.
- ***Meteoroid***: A natural solid object with size up to 1 m, moving in the interplanetary space.

- ***Dust* grain**: A particle larger than a molecule and <1 μm in size. Aggregates of dust particles (1 μm to 1 mm) constitute micrometeoroids or meteoroids.
- ***Interplanetary Dust Particles (IDPs):*** Micrometer-sized extraterrestrial grains (<1 μm to a few tens of μm), mainly from cometary and asteroidal debris, a fraction of which reach Earth's surface.
- ***Asteroid***: A natural sub-planetary object between 1 m and 1000 km in diameter, orbiting a star. The upper limit corresponds approximately to the diameter of Ceres (946 km). Bodies >400 km are generally rounded by gravity (hydrostatic equilibrium) and may be classified as planets or dwarf planets.
- ***Comet***: A natural volatile-rich solid body at least 1 m in size, orbiting a star, and which displays outgassing (coma and tail) upon close encounter with the star. Kuiper Belt Objects (KBOs) and trans-Neptunian Objects (TNOs) are sources of short-period comets with periods ≤ 200 years, while Oort Cloud objects produce long-period comets (with some periods up to >1 million years). TNOs and Oort Cloud objects remain outside the inner Solar System. Extinct comets that degassed their volatile supply because of several close encounters with the Sun are still considered as comets.
- ***Planet***: A celestial body orbiting a star, massive enough so that gravity shaped it into a spheroid (hydrostatic equilibrium) and cleared its orbital neighborhood of comparable-sized objects. Diameters are in the ~200–300,000 km size range.
- ***Dwarf planet***: A celestial body orbiting a star, massive enough for its self-gravity to give it a nearly spherical shape (typically with a mean diameter >400 km) but has not cleared its orbital neighborhood of other comparably sized objects.
- ***Moon*** (natural satellite): A body at least 1 km in diameter, orbiting a larger planet, dwarf planet, asteroid, comet, or substellar object[15].
- ***Meteor***: The luminous phenomenon produced when a solid object enters a planetary atmosphere at high velocity (generally 11–72 km/s on Earth, Abe 2008).
- ***Meteor shower***: An event that occurs dust grains or larger particles, mainly from comets (rarely from asteroids), encounter Earth's orbit and producing numerous meteors. A famous example includes the Perseids originating from Comet 109P/Swift–Tuttle.
- ***Meteorite shower***: The fall of multiple meteorite fragments, typically caused by the fragmentation a of meteoroid upon atmospheric entry. The fragments usually fall within an elongated strewn field, orientated along the trajectory of the meteoroid. Famous examples include Pultusk (H5, Warsaw, Poland, 180 000 fragments, ~250 kg) and the Jiddat al Harasis (JaH) 073 (L6, ~3500 fragments over ~20 × 6 km, Oman; (Wimmer et al. 2022).
- ***Pairs***: Meteorite samples identified as fragments of the same original meteorite fall. In some cases, two or more fragments can belong to the same meteorite that fragmented in the atmosphere or on the ground, these are known as paired samples. Pairing is based

[15] A body whose mass is below the threshold of hydrogen fusion in its core (~0.072 solar masses; Chabrier and Baraffe 2000).

on mineralogical, petrographic, magnetic, and geochemical properties, as well as terrestrial ages and cosmic-ray exposure ages.

- ***Fusion crust***: Thin (<1 mm) melt rock layer formed on a meteorite's surface during atmospheric passage.
- ***Mineral***: A naturally occurring, mostly inorganic, homogenous solid with an ordered atomic arrangement and a well-defined chemical composition (sometimes variable in case of impurities). Mineral examples include feldspar and halite. There are currently 6174 approved minerals[16], of which 430 found in meteorites (Rubin and Ma 2021).
- ***Rock:*** A naturally occurring solid aggregate of one or more minerals. Meteorites include all three rock types: igneous, sedimentary, and metamorphic.
- ***Breccia:*** A rock composed of angular clasts of rock or mineral fragments cemented by a finer-grained or glassy matrix. Types include monomict (single lithology), dimict (two lithologies), polymict (more than two lithologies), or genomict (consisting of clasts of a single rock type but with different metamorphic grades (Bischoff et al. 2006).
- ***Cosmogenic nuclides:*** Isotopes produced by interactions of cosmic rays with matter, including stable nuclides (e.g., ^{21}Ne) and radionuclides (e.g., ^{14}C, ^{36}Cl, ^{26}Al, ^{10}Be).
- ***Terrestrial age:*** The time spent by the meteorite on the Earth's surface after its fall.
- ***Cosmic-ray exposure (CRE) age:*** time spent by a meteoroid in the interplanetary space after excavation from its parent body before falling to Earth.

1.1.2.2. Basic concepts in orbital dynamics

Before discussing dynamical evolution, I will start with the following necessary definitions:

- Spin: Rotation of a body around its own axis.
- Orbit (or orbital revolution): Curved trajectory of a body around a central, more massive body under gravitational influence.
- Orbital period (P): Time required for an orbiting body to complete one revolution around the central body.
- Node: Intersection point of an orbit with the reference plane. The ascending node is where the body goes northward (from south to north), and the descending node is where it moves southward (from north to south).
- Periapsis: Point in an orbit where the body is closest to the central object.

Orbital parameters are defined by several properties (Figure 1.4)[17]:

[16] https://www.mindat.org/minerals.php

[17] For explanations and 3D figures, refer to: https://orbital-mechanics.space/classical-orbital-elements/classical-orbital-elements.html

- Semimajor axis (a): Half the longest diameter of an orbital ellipse, defines the size of the orbit.
- Eccentricity (e): Measure of the orbital shape, describing the deviation of a trajectory from a perfect circle; $e = 0$: circular orbit, $0 < e < 1$: elliptical orbit, $e = 1$: parabolic trajectory, $e > 1$: hyperbolic trajectory.
- Inclination (i): Tilt of the orbital plane relative to the reference plane, measured in degrees (0 –180°).
- Longitude of the ascending node (Ω): Angle in the reference plane that defines the direction of the ascending node (the point where the body crosses northward through the plane).
- Argument of periapsis ($\boldsymbol{\omega}$): Angle between the ascending node and the orbit's periapsis, in the orbital plane.
- True anomaly ($\boldsymbol{\nu}$): Angle between the periapsis and the current position of the body along its orbit. It specifies the body's position at a given instant.
- Mean anomaly (M): Angular measure of the body's orbital position assuming uniform motion. It is used to calculate the true anomaly.
- Mean motion (n): Average angular velocity of the orbiting body, expressed as an angle per unit time.

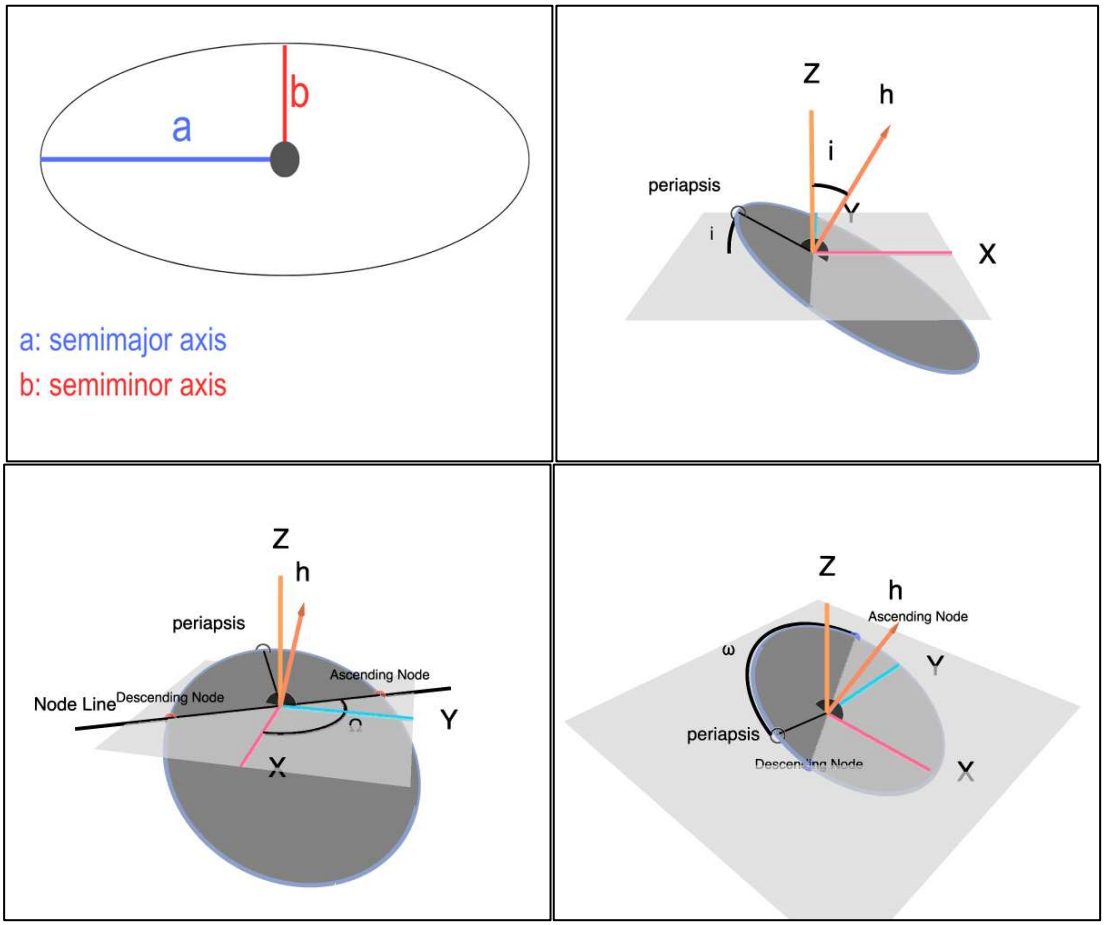

Figure 1.4. (a) Schematic of an elliptical orbit showing the semimajor axis a and semiminor axis b (b) Inclination i of a planar orbit with respect to a reference plane X and periapsis (c) Ascending (Ω)

and descending node (d) argument of periapsis ω. Credit: https://github.com/bryanwweber/orbital-mechanics-notes.

1.2. Asteroids and the Main Asteroid Belt

1.2.1. Asteroid classification

The Main Asteroid Belt, located between the orbits of Mars and Jupiter, is populated by over a million asteroids larger than 1 km in diameter. As of July 2025, more than 1.34 million asteroids have been identified in the belt (IAU Minor Planet Center, 2025[18]), although many asteroids <1 km remain undetected. The largest object is (1) Ceres (946 km in diameter), followed by (4) Vesta, (2) Pallas, and (10) Hygiea. Around 230 asteroids have diameters ≥100 km (Vernazza et al. 2021).

Asteroids are rocky bodies orbiting the Sun mainly within the Main Asteroid Belt and rotating in the same direction as the planets. They were formed by accretion of the first solids, thus recording the conditions of the formation and evolution of the Solar System. Their heavily cratered surfaces and generally higher eccentricities and inclinations relative to planets, testify to the importance of collisions in shaping their dynamical history. Fragmentation has played a major role since most asteroids are rubble piles, which are gravitational aggregates of fragments resulting from the catastrophic disruption of larger parent bodies. What we observe today are therefore millions of small bodies, which are thought to be remnants of only ~150–250 original planetesimals (e.g., Delbo et al. 2017; Gattacceca et al. 2020).

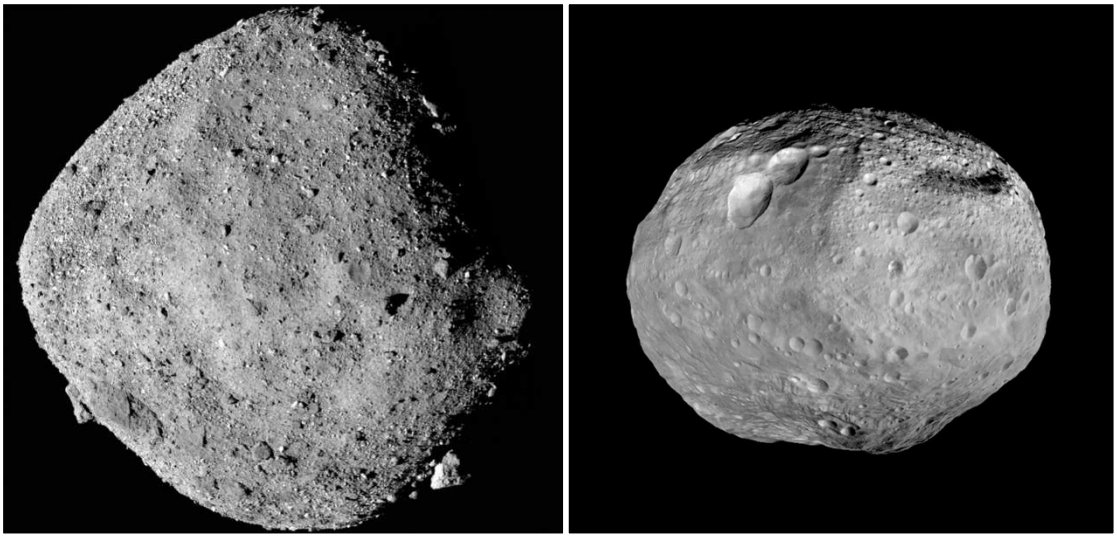

Figure 1.5. Mosaics of Bennu (left) and Vesta (right) (NASA/JPL-Caltech/UCLA/MPS/DLR/IDA).

Asteroid classification is primarily based on their chemical composition, determined from spectral properties and albedo (i.e., surface reflectivity). The most widely used system is the Bus-DeMeo taxonomy (DeMeo et al. 2009), which classifies asteroids based on their reflectance[19] spectra in the visible and near-infrared wavelengths (Figure 1.6). This taxonomy

[18] https://www.minorplanetcenter.net/mpc/summary

[19] Reflectance measures the fraction of reflected sunlight emitted by an asteroid's surface. It provides information on the composition and mineralogy of an asteroid.

divides asteroids into three major complexes (S-complex, C-complex, and X-complex), and nine classes (A, D, K, L, O, Q, R, T, and V), for a total of 25 distinct spectral classes (Burbine et al. 2024).

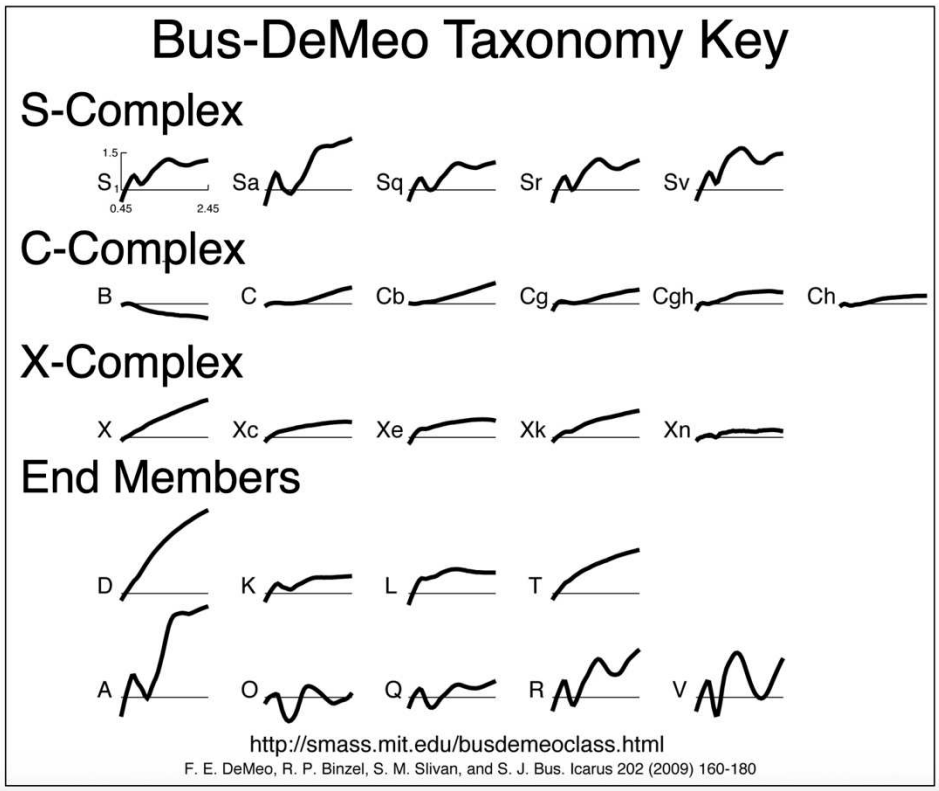

Figure 1.6. The Bus–DeMeo spectral taxonomy of asteroids showing reflectance spectra for each class (in the 0.45–2.45 μm wavelength range; from DeMeo et al. (2009).

The Main Asteroid Belt is dominated by C-type asteroids (75% in number and ~60% in mass), which are dark, carbon- and water-rich bodies similar in composition to carbonaceous chondrites and are mainly located in the middle and outer belt. S-type asteroids (~17% in number and 8% in mass), more abundant in the inner main belt, are rich in silicates (olivine and pyroxene) with minor metallic iron and are commonly linked to ordinary chondrites (Vernazza and Beck 2017; DeMeo and Carry 2014). The remaining population includes the X-complex, subdivided into M-types (metallic), E-types (enstatite-rich), and P-types (dark and primitive) asteroids, as well as minor types with rarer compositions (Burbine et al. 2024).

How can this compositional diversity of material in the asteroid belt be explained? The present-day asteroid belt contains only a tiny fraction of the mass of the Solar System (~3% of the mass of the Moon; (Pitjeva and Pitjev 2018), not substantial enough to form a planet. This mass deficit is the consequence of Jupiter's strong gravitational perturbations, which excited planetesimal orbits, further inhibiting accretion. Furthermore, these perturbations enhanced collisional fragmentation through high-velocity impacts.

In addition, planetary migration strongly shaped the composition of the main belt. Dynamical models of early Solar System evolution also show that, during the early migration of the giant planets, a significant number of carbonaceous asteroids were implanted from

beyond Jupiter's orbit (Figure 1.7; e.g., Walsh et al. 2011; Morbidelli et al. 2015; Desch et al. 2018). According to the Grand Tack model, the inward migration of Jupiter first caused a depletion of the primordial belt, followed by its outward migration that replenished the belt with a mixture of bodies from both the inner (between 1 and 3 AU) and the outer belt (beyond the giant planets) (Walsh et al. 2011; Vernazza and Beck 2017). This scenario explains both the current low mass and the radial mixing of the asteroid belt, specifically, the dominance of anhydrous S-type asteroids in the inner belt and the prominence of hydrated C-type asteroids in the outer belt, consistent with the dichotomy between non-carbonaceous and carbonaceous reservoirs (See Section 1.4.3).

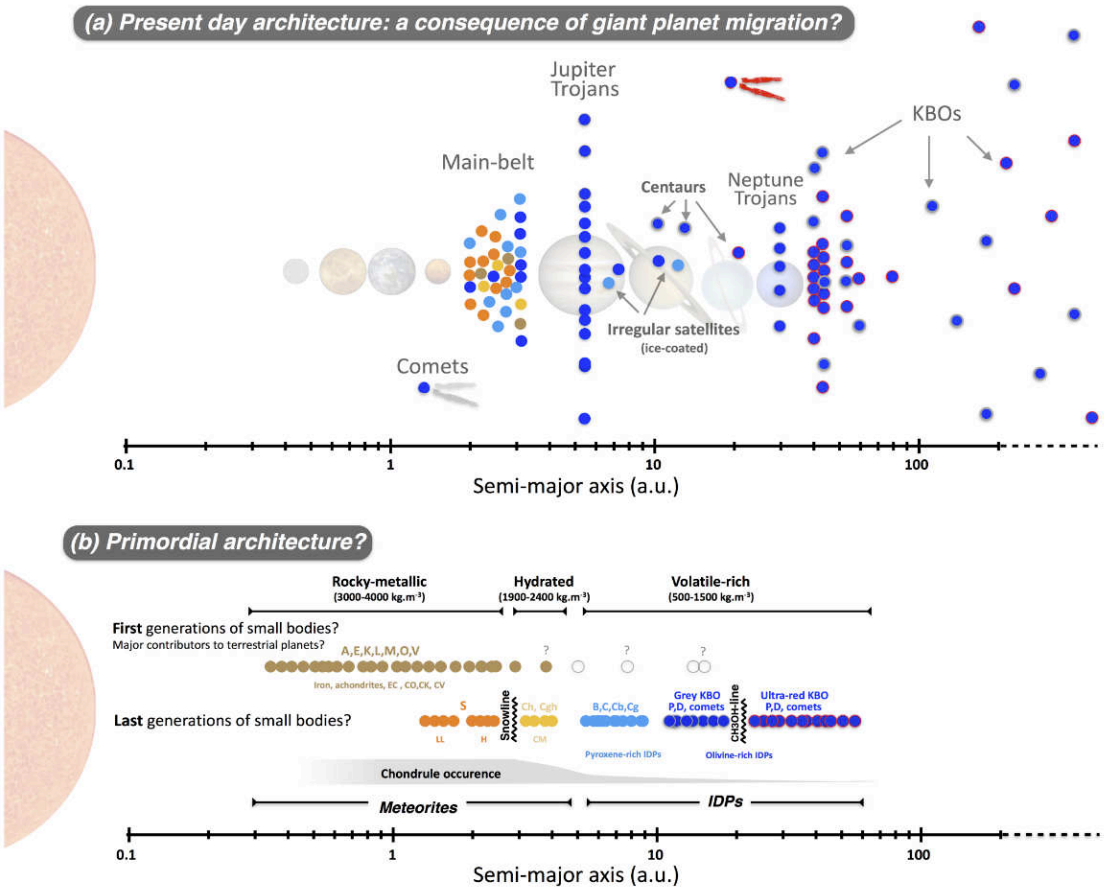

Figure 1.7. (a) Present-day structure of the main reservoirs in the Solar System. (b) Primordial structure of the protoplanetary disk. From Vernazza and Beck (2017).

1.2.2. Asteroid families

1.2.2.1. Formation

Asteroid families are formed through the catastrophic collisional disruption[20] of a large asteroid (the parent body), generally by impact with a smaller projectile. The Vesta family, however, derived from a major cratering event rather than complete breakup. Family members share similar proper orbital elements (semimajor axis *a*, eccentricity *e*,

[20] A high-energy impact between asteroids that completely shatters the parent body into many fragments, rather than just causing cratering or partial breakup

and drouarinclination *i;* see Section 1.1.2.2) and often exhibit spectral similarities consistent with a common origin. Modern asteroid surveys, such as WISE/NEOWISE (Masiero et al. 2013), indicate that this similarity among asteroid family members remains true even for the smallest fragments (Nesvorný et al. 2015).

In such disruptions, numerous fragments are ejected with escape velocities much smaller than their orbital velocity around the Sun, initially forming a tight cluster (Michel et al. 2015). Some fragments reaccumulate into rubble-pile aggregates that interact gravitationally with their neighbors. The outcome depends strongly on the parent body's properties, particularly the internal porosity.

Jupiter's strong gravitational perturbations play a key role in shaping the asteroid belt, acting like that disturbing neighbor who shakes the whole neighborhood up. Indeed, resonances with Jupiter destabilize orbits, increase collisional velocities, therefore increasing fragmentation and the formation of new asteroid families (Nesvorný et al. 2015).

Immediately after breakup, fragments remain clustered in orbital space, sharing similar perihelia, longitudes of node, and mean anomalies. Over time, family members gradually disperse as a result of:

- Keplerian shear: Small differences in semimajor axis cause slight differential orbital periods, stretching families along their orbits.
- Differential precession: Each asteroid slowly rotates over time due to small gravitational perturbations from planets, mainly Jupiter and Saturn. But because bodies have different precession rates, their orbital orientations gradually diverge.

Long-term dispersal is further amplified by the Yarkovsky effect which alters semimajor axes, as well as by planetary resonances, both mean-motion and secular resonances, that increase eccentricities or inclinations and may even eject members entirely (see Section 1.3). Additionally, close encounters with large asteroids such as Ceres can also disrupt family orbits. Despite this spreading, families remain detectable even after hundreds of millions to billions of years (Nesvorný et al. 2015).

1.2.2.2. Identification

Asteroid families are identified as clusters in the space of proper orbital elements: the proper semimajor axis (a_P), proper eccentricity (e_P), and proper inclination (i_P), which describe the size, shape, and tilt of orbits. Numerical algorithms, such as the Hierarchical Clustering Method (or HCM), are commonly used for this purpose (Nesvorný et al. 2005). These dynamical groupings combined with compositional data, establish common parent origin. Exceptions include interlopers, which are objects that share orbital elements with a family but differ spectrally, revealing unrelated origins. For example, a C-type family containing an S-type asteroid.

1.2.2.3. Spectral properties and ages

The taxonomic classification of asteroid families is mainly based on their physical properties derived from observational measurements mainly reflectance spectra and albedo (Nesvorný et al. 2015). Family members typically show similar spectral and albedo features, implying a common origin and generally undifferentiated interiors. However, some heterogeneity may occur due to variations in the parent body's internal structure or from the effects of space weathering[21].

Asteroid family ages range from very young (<1 million years) to ancient (>1 billions of years); Brož et al. 2024). The age of a family is determined through two different dynamical modeling techniques, depending on the timing of the family-forming collision (Nesvorný et al. 2005).

Both approaches are fundamentally based on the progressive dispersion of family members from their common origin under the influence of gravitational and non-gravitational forces ; Spoto et al. 2015). For young families (<10 Ma), age are determined using backward numerical integration of member orbits to the point of angular convergence of the nodes and perihelia (e.g., Koronis$_2$ family at 7.5 Ma; Brož et al. 2024). For older families, ages are derived by modeling their Yarkovsky-induced dispersion in semimajor axis, which produces a V-shape in size-orbit space (Spoto et al. 2015). Finally, for the oldest and most evolved families, collisional modeling of their size-frequency distributions provides age estimates (Spoto et al. 2015).

1.2.3. Structure of the Main Asteroid Belt

The Main Asteroid Belt is divided into three regions, separated by dynamically unstable zones associated with resonances with Jupiter (DeMeo and Carry 2014). The most prominent occur at 2.5 AU (3:1 resonance) and 2.8 AU (5:2 resonance), which separate the belt into inner, middle, and outer regions (Figure 1.8).

[21] Weathering that occurs to a body subjected to the outer space environment, especially bodies lacking atmospheres. Processes include collisions of galactic and solar cosmic rays, irradiation, implantation and sputtering from solar wind particles, and bombardment by different sizes of meteorites and micrometeorites. Space weathering alters the physical and optical properties of the surface of the objects affected.

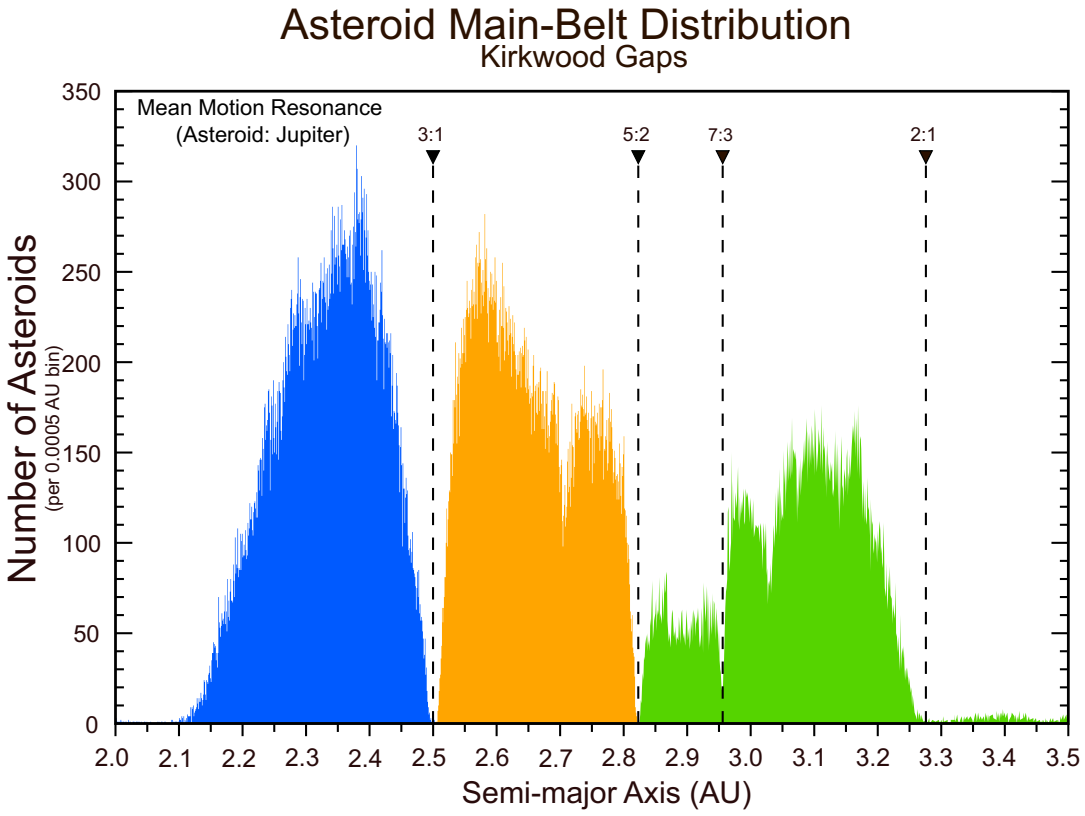

Figure 1.8. Structure of the Main Asteroid Belt showing the inner (blue), middle (orange), and outer (green) main belt, separated by the Kirkwood Gaps caused by the mean-motion resonances (3 :1, 5 :2, 7:3, 2 :1). Based on Alan Chamberlain, JPL/Caltech.

The inner belt (2.1–2.5 AU) is dominated by S-type asteroids (stony), the middle belt (2.5–2.8 AU) is composed of a mix of S- and C-type asteroids (carbonaceous), and the outer belt (2.8–3.3 au) includes primarily C-type and D-type asteroids, representing more primitive materials.

The most prominent asteroid families include the Flora, Vesta, Massalia, Polana, Hertha, Eunomia, Gefion, Koronis, Eos, etc. families (Figure 1.9). The main belt also hosts several underpopulated regions, known as Kirkwood gaps, induced by orbital resonances with Jupiter. For example, the 3 :1 resonance at 2.5 AU destabilizes orbits, efficiently removing asteroids from that zone (see Section 1.3.2).

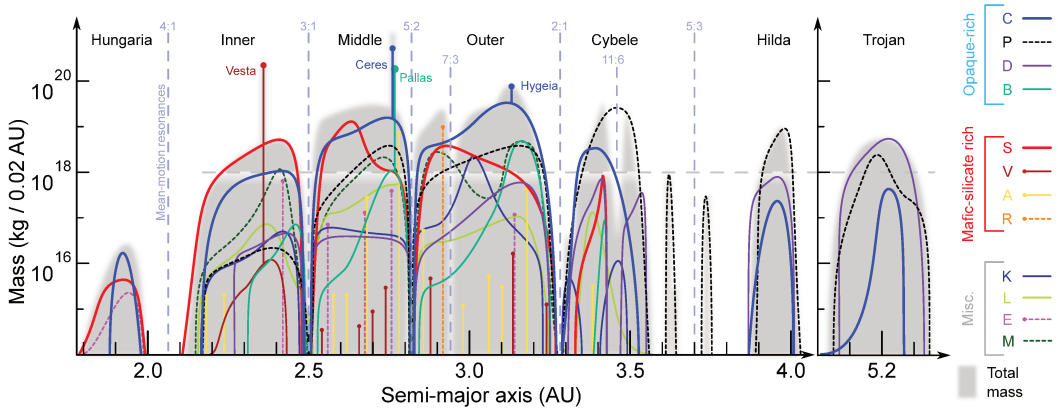

Figure 1.9. Major asteroid families and resonances in the main asteroid belt. From (DeMeo and Carry 2014) .

1.3. How does extraterrestrial material reach us?

Earth receives extraterrestrial material across a wide range of sizes, from micrometer-sized dust to centimeter–meter scale meteoroids, and up to kilometer-sized asteroids. In terms of mass flux, the smallest particles (~1 µm–5 mm) are dominant, with the frequency of larger objects decreasing sharply with size (Rojas et al. 2021; Fénisse et al. 2025).

The transfer of this material to Earth is controlled by a combination of collisional, dynamical, and orbital processes differing according to particle size (Rubin 2018; Bottke 2000; Bottke et al. 2015; Morbidelli and Vokrouhlický 2003). Collisions induce the fragmentation of parent asteroids, producing smaller fragments that evolve dynamically until they reach powerful resonances that inject them into planet-crossing orbits. For this to be possible, several non-gravitational forces play a key role in altering their trajectories.

1.3.1. Thermal forces

1.3.1.1. Poynting-Robertson drag

Micrometer- to millimeter-sized particles (IDPs and micrometeorites) are influenced by the Poynting-Robertson drag. This effect results from the anisotropic reemission of absorbed solar energy. This drag removes the angular momentum of particles and slowly shrinks their orbital semimajor axes, causing the particles to spiral inward towards the Sun, and eventually intersect Earth's orbit (Wyatt and Whipple 1950).

The efficiency of the Poynting-Robertson drag is approximated as $t = 7.0 \times 10^5 \times \rho \times r \times d^2$; where t is the time in years, ρ is the bulk density in $kg.m^{-3}$, r the particle radius in meters, and d is the heliocentric distance in AU (Wyatt and Whipple 1950).

This expression shows that the effect is strongly size dependent. For example, a 1 cm particle takes roughly 10^4 times longer than a 1 μm particle to spiral inward towards the Sun (Rubin 2018). In detail, for a 1 mm grain at 3 AU, it would take ~20 million years to spiral into the Sun, or ~18 million years to reach the Earth's orbit.

The Poynting-Robertson drag is therefore a major mechanism in delivering micrometer- to millimeter-sized dust and micrometeorites towards Earth.

1.3.1.2. Yarkovsky effect

The Yarkovsky effect is a non-gravitational thermal force acting on rotating bodies due to anisotropic reemission of absorbed solar radiation. This force is most effective for objects in the 1 cm to 100 m size range. It is a major contributor to the transport of material from the Main Asteroid Belt to Earth (Farinella et al. 1998). In detail, small bodies absorb sunlight at visible wavelengths and reradiate the energy as heat in the infrared. Because of thermal inertia[22], this reradiation is delayed relative to absorption and is influenced by the object's rotation. The resulting anisotropy produces a tiny net recoil force. Over long timescales (10^5 –10^6 years), this force gradually shifts orbital parameters, specially the semimajor axis.

The Yarkovsky effect has two variants: the diurnal one due to the rotational motion and the seasonal one due to the orbital motion (Bottke 2000; Bottke et al. 2006; Vokrouhlický et al. 2015). Both components are illustrated in Figure 1.10.

1- Diurnal effect: driven by the day/night heating cycles, strongest when the spin axis is perpendicular to the orbital plane.

   - For prograde rotators (spinning in the same direction as the orbit), thermal emission increases the semimajor axis, causing the body to spiral outward.
   - For retrograde rotators (spinning in the opposite direction to the orbit), the semimajor axis decreases, causing the body to spiral inward.
   - The strength of the diurnal effect depends on the object's rotation rate, the direction of spin, and the thermal properties.

2- Seasonal effect: driven by changes in solar heating as the body moves along its orbit. It is strongest when the spin axis lies in the orbital plane.

   - Unlike the diurnal component, this effect always acts as a drag, causing the body to spiral inward, regardless of spin direction.

[22] Thermal inertia is the measure of how quickly a material's temperature changes when it is heated or cooled. In other words, it represents the resistance of a material to temperature change.

- It is a direct consequence of the lag in reradiation of the heat, so that the maximum recoil occurs after the object has moved in its orbit, resulting in a force opposite to its motion.
- This lag is analogous to the Earth's temperature lag, where afternoons are warmer than noon (diurnal lag), and July and August are hotter than June (seasonal lag).
- Its magnitude depends on both the distance from the Sun, rotation period, and obliquity.

Over long timescales, these small effects can cause significant orbital drifts. A concrete example is the detection of Yarkovsky effect on the asteroid (6489) Golevka through radar observations (Chesley et al. 2003).

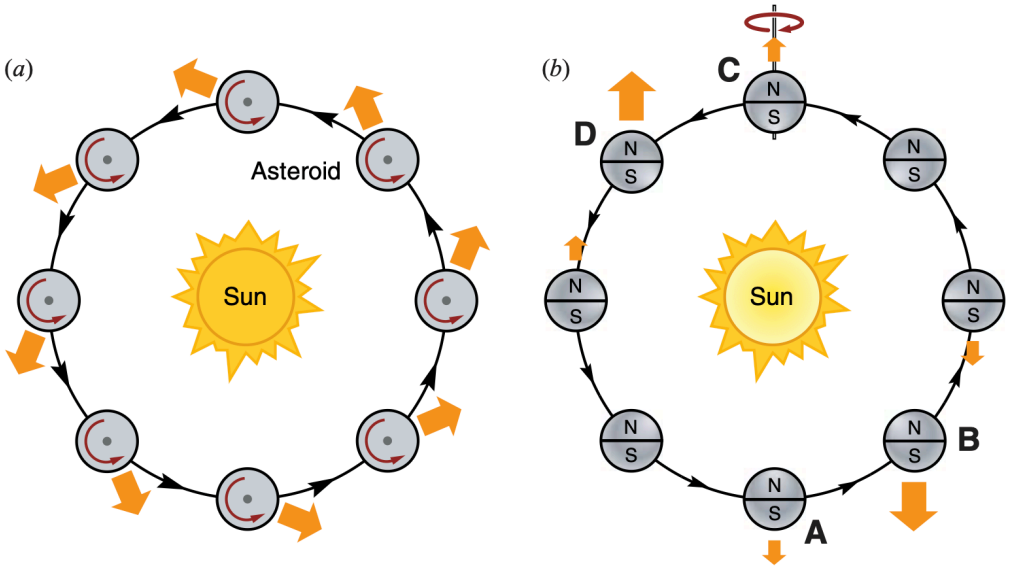

Figure 1.10. Schematic illustration of the two components of the Yarkovsky effect (a) The diurnal Yarkovsky effect (b) The seasonal Yarkovsky effect. From Bottke et al., (2006).

1.3.1.3. YORP effect

The Yarkovsky-O'Keefe-Radzievskii-Paddack (YORP) effect is a torque[23] induced by the asymmetric reflection and reemission of sunlight from irregularly shaped asteroids (Rubincam 2000). Its strength depends on the body's shape, size, spin orientation, and distance from the Sun. Over long timescales, these torques accumulate and can control the long-term evolution of asteroid spin vectors, thus indirectly controlling the Yarkovsky effect. Irregular asteroids experience uneven reradiation that can either spin them up or slow them down, while also affecting their obliquities (Figure 1.11).

[23] Rotational force that changes an object's spin rate or the orientation of its rotation axis.

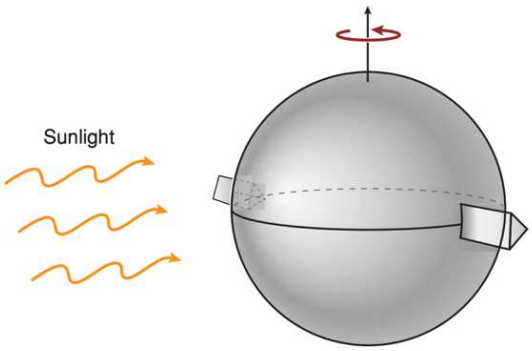

Figure 1.11. Explicative scheme of the YORP effect from Bottke et al. (2006).

Over millions of years, the YORP effect can gradually increase an asteroid's spin rate until it can no longer hold itself together, causing it either to break apart or shed material from its equator. The ejected material may reaccumulate nearby, creating a small satellite and thus forming a binary system (Bottke et al. 2006). An example is the asteroid (65803) Didymos and its moon Didymorphos targeted by NASA's DART mission in 2022 (Madeira et al. 2023), shown in Figure 1.12.

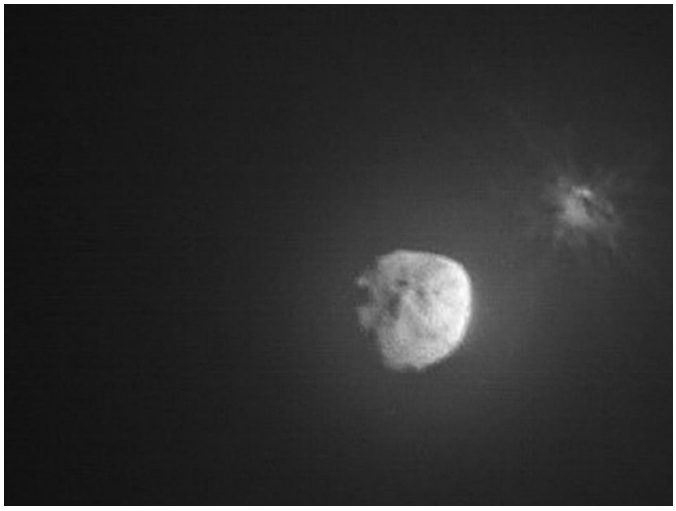

Figure 1.12. Image captured by the Italian Space Agency's LICIACube a few minutes after DART collided with Dimorphos on Sept. 26, 2022. Credit: ASI/NASA

1.3.2. Resonances and gravitational effects

In celestial mechanics, a resonance occurs when the orbital motions of two bodies are commensurate (i.e., proportionate), so that their orbital periods are in a simple integer ratio. This synchronization causes repeated gravitational perturbations that can either stabilize or destabilize the orbit of the smaller body over long timescales (Nesvorný et al. 2002; Gallardo 2018).

Two major resonance types shape the asteroid belt:

1- The Mean-Motion Resonances (MMRs):

- Occur when the orbital period of an asteroid is a simple fraction of that of a planet.
- For example, in the 3:1 resonance with Jupiter, an asteroid goes around the Sun three times for every orbit of Jupiter.
- Each time the asteroid and Jupiter align, Jupiter's gravity gives a small periodic "kick" at the same orbital phase, gradually increasing the asteroid's eccentricity until it crosses Mars' or Earth's orbit.
- The Kirkwood gaps within the asteroid belt represent depleted regions caused by strong MMRs with Jupiter (notably the 3:1, 4:1, and 5:2 resonances) (Figure 1.8).

2- Secular Resonances

- Occur when the precession rate[24] of an asteroid's perihelion or node matches with that of a planet.
- Over millions of years, the asteroid's eccentricity or inclination increases, ultimately driving bodies into planet-crossing orbits.
- A major example is the ν6 secular resonance with Saturn, located at the inner edge of the asteroid belt (near 2.1 AU), which represents one of the main sources of Earth-crossing asteroids.

In short, thermal forces can slowly bring meteoroids into resonance zones, notably the ν6 secular resonance and 3:1 mean-motion resonance, where their orbits become destabilized, and they are subsequently injected into Earth-crossing trajectories (Gladman et al. 1997; Vokrouhlický et al. 2015; Vokrouhlický and Farinella 2000).

Large bodies (kilometer- to multi-kilometer sized) are primarily influenced by gravitational interactions and resonances while thermal effects are negligible, making their transfer to Earth relatively rare (Minton and Malhotra 2010; Carruba 2003).

1.3.3. Implications of the Yarkovsky effect

The Yarkovsky effect slowly delivers material to strong resonances inside the main belt. As these bodies approach a main belt escape hatch, they can be transported into planet-crossing orbits, eventually reaching Earth. During their transfer through the interplanetary space, they are bombarded by cosmic rays, which produce cosmogenic nuclides used to estimate cosmic-ray exposure[25] (CRE) ages of meteorites. The delivery timescales are consistent with CRE ages of meteorites, with most iron meteorites exhibiting CRE ages shorter than ~1.5 Ga, and stony meteorites shorter than ~120 Ma (Eugster 2003; Herzog 2007).

Meter-sized meteoroids drift in semimajor axis at rates of about ± (0.01–0.001) AU per Myr due to Yarkovsky effect, with the direction (inward or outward) depending on spin orientation,

[24] Precession rate is the slow rotation of the orbit's orientation in space.
[25] Time spent by the meteoroid in the interplanetary space when it is exposed to cosmic rays, from excavation from its parent body until arrival on Earth

and speed depending on the thermal conductivity K[26] of the surface, spin rate, and thermal inertia.

1. Low thermal conductivity (K =~0.0001 W/m/K, porous and/or dusty surfaces): the drift is fast, allowing meteoroids to overcome weak resonances, and spiral inward or outward until reaching a major resonance (3:1 with Jupiter or $\nu 6$ with Saturn), which they will not be able to escape. Along the way, they may be trapped in weak resonances temporarily, which changes their eccentricity and inclination, while the semimajor axis remains fixed. Nondestructive collisions can reset spin and reverse drift direction, making the journey more chaotic. Thus, meteoroids reach strong resonances relatively quickly, often in a chaotic path shaped by spin changes and resonance crossings.

2. High thermal conductivity (K > 0.1 W/m/K, bare rock surfaces): the drift is slow, implying that meter-sized meteoroids often get disrupted before ever reaching resonance. The meteoroids that eventually make it to resonances are usually fresh fragments from ongoing collisional cascades. Over time, multiple generations of disruption and drift allow some outliers of the family to eventually reach powerful resonances before being destroyed. In this case, resonances are not fed by long-lived meteoroids, but by a steady reservoir of fragments continuously supplied by asteroid families.

In summary, the Yarkovsky effect, combined with orbital resonances, is the primary mechanism by which meter-sized meteoroids are transported from the main belt into the near-Earth space, ultimately supplying the majority of meteorites that fall to Earth (Bottke et al. 2006; Vokrouhlický and Farinella 2000).

1.4. Meteorites

1.4.1. Definitions and importance

Meteorites are fragments of asteroids, planets, or the Moon that survive atmospheric entry and reach the Earth's surface. Currently, more than 77 000 meteorites have been catalogued in the Meteoritical Bulletin Database (https://www.lpi.usra.edu/meteor/), including ~400 Martian meteorites and ~750 lunar meteorites, while ~99% originate from asteroids.

Beyond their fascinating nature and spectacular atmospheric entries, meteorites represent tangible samples from the Solar System that can be manipulated and analyzed in laboratories. Chondrites, the most primitive meteorites, contain the oldest objects of the Solar System, CAIs, dated back to the early formation of the Solar System, making them witnesses of the early evolution of the solar nebula. In contrast, differentiated meteorites, originate from cores,

[26] Thermal conductivity: measures how well the heat flows through the material.

mantles and crusts of differentiated bodies such as planets and asteroids (Figure 1.13). These samples provide information on planetary formation and differentiation processes.

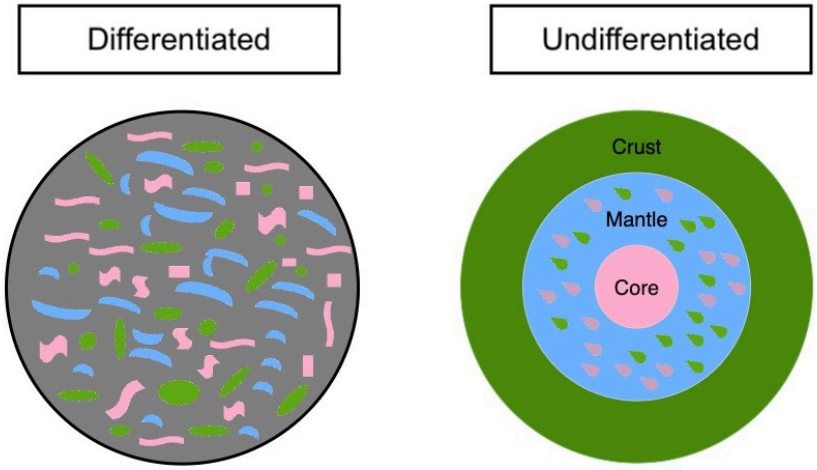

Figure 1.13. Undifferentiated vs differentiated bodies.

In addition, meteorites exhibit various features that record secondary processes on parent asteroids. For instance, shock features in meteorites record collisional processes that shaped the planets and asteroids, while some carbonaceous chondrites contain hydrated minerals and organics, mandatory components for the emergence of life, making them key to understand the origin of life on Earth, but also the presence of extraterrestrial life outside our planet. Furthermore, terrestrial ages of meteorites tell us about the frequency of meteorite falls to Earth, improving our understanding of the impact hazard and the delivery mechanisms to Earth.

Besides their scientific value, meteorites have played an important role in human societies. Before the emergence of iron smelting, meteoritic iron was the only available source of metallic iron used to design tools and ornaments. The most famous example is the dagger of Tutankhamun in Egypt (Comelli et al. 2016) and Inuit harpoons and knives in Greenland made from the Cape York meteorite (Svensson et al. 2021; Buchwald 2001). In addition, the Widmanstätten patterns in iron meteorites have inspired both metallurgy and art.

Moreover, events like the Chelyabinsk fall in 2013 reminded humans of the potential threats from near-Earth objects, emphasizing the importance of planetary defense and raising public awareness. Meteorites are also an educational tool that ignites the interest of children and adults, through exhibited specimens in museums and universities. Finally, meteorites also have an economic importance through meteorite hunting and trade, especially in deserts, where samples are collected and sold or donated to museums and research institutions across the globe. Though, this raises ethical questions of culture heritage and private ownership.

1.4.2. Meteorite classification

The first distinction to be made in meteorite classification is between a meteorite fall and a find. A meteorite is qualified as a 'fall' if its entry was associated with an observed fall (whether with the naked eye or through radars, cameras, or satellites) and the specimen was recovered shortly after the fall. A meteorite 'find' is a sample that has been found at the surface without being observed to fall.

A meteorite is usually named after the place it has been found in (town, city, county, or mountain, lake, river, valley, island). If several meteorites were found in the same place, numbers are added after the name[27], which is the case for desert finds in dense collection areas (DCAs), e.g., Frontier Mountain 84001 (Antarctica), Dhofar 155 (Oman), Catalina 500 (Atacama Desert, Chile).

Meteorite classification is mainly based on petrographic, magnetic, geochemical, and mineralogical properties (Weisberg et al. 2006; Rubin and Ma 2021a), which divides them into three major families: chondrites (differentiated), achondrites (differentiated) and primitive achondrites (Figure 1.14):

1- Chondrites: Undifferentiated stony meteorites that did not experience large-scale melting or differentiation. They consist of µm- to mm-sized igneous silicate spherules (chondrules), refractory inclusions (CAIs and Ameboid Olivine Aggregates; AOAs), and a fine-grained matrix (consisting of amorphous and crystalline silicates, oxides, sulfides, carbonates, Fe-Ni metal, and organic matter, depending on the secondary processes on the parent body, i.e., thermal metamorphism and aqueous alteration). They represent the building blocks of planets.

   Chondrites are divided into three main classes:

   - Ordinary chondrites (H, L, LL): the most common class on Earth, with up to ~78% of observed falls (MBDB, as of September 2025)
   - Carbonaceous chondrites (CI, CM, CO, CV, CK, CR, CH, CB, CL): rare ~4% of falls, volatile- and organic-rich meteorites
   - Enstatite chondrites (EH and EL): highly reduced samples

   Other types include Kakangari (K) and Rumuruti (R) chondrites.

2- Achondrites: Differentiated meteorites originating from parent bodies that were large enough to have undergone differentiation (formation of core, mantle, and crust structure through melting and segregation; Figure 1.13). They are igneous or metamorphic in texture. Major groups include:

   - Martian meteorites: (shergottites, nakhlites, chassignites and orthopyroxenites) ejected from Mars through impacts.
   - HED (howardites, eucrites, diogenites) meteorites: most likely originate from asteroid (4) Vesta in the inner asteroid belt.

[27] Full guidelines on meteorite nomenclature can be found here: https://www.lpi.usra.edu/meteor/docs/nc-guidelines.pdf

- Lunar meteorites: originate from the Mon's surface and can be divided into three mai categories: anorthositic or feldspathic, basaltic or gabbroic, and mixed or polymict breccias.
- Iron meteorites: consist mainly of Fe-Ni metal. Magmatic irons originate from planetary cores, while non-magmatic irons consist of mixtures of metal and silicate residues produced by impact processes (Goldstein et al. 2009).
- Stony irons: pallasites and mesosiderites made of metal and silicate in approximately similar abundances, representing mixtures of core and mantle materials.
- Aubrites: enstatite achondrites, most are breccias with igneous and impact-melted clasts, with highly reduced minerals.
- Angrites: igneous rocks of basaltic composition with distinctive mineralogy.

3- Primitive achondrites: intermediate between chondrites and achondrites, show evidence of limited partial melting and recrystallization but with chondritic chemical signatures. They provide insight into the earliest stages of planetary differentiation. Major groups include: ureilites, acapulcoites and lodranites, brachinites, and winonaites.

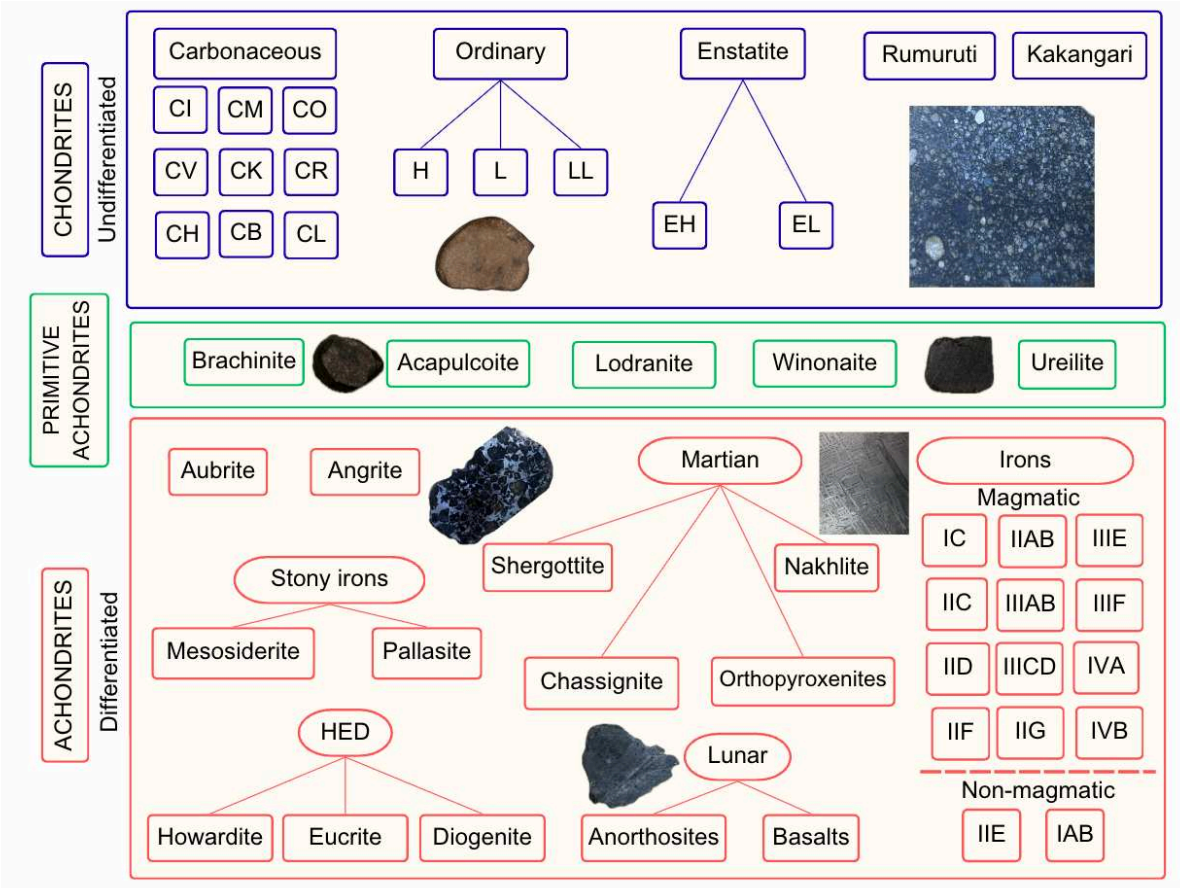

Figure 1.14. Meteorite classification scheme. Based on (Weisberg et al. 2006) and Rubin and Ma (2021).

Meteorites are subdivided into classes, clans, groups, and subgroups. Meteorites belonging to the same group have similar compositional, textural and mineralogical properties that vary only slightly within a limited range, consistent with the hypothesis of a common origin from a

single parent body (Weisberg et al. 2006; Rubin and Ma 2021b; Scott and Krot 2003). However, for achondrites, the link between meteorite group and parent body differs. For example, Martian meteorites include several groups despite originating from a single parent body, while HED meteorites represent various lithologies (howardites, eucrites, diogenites) from the asteroid (4) Vesta.

1.4.3. Formation of meteorites in the Solar System

The compositional and geochemical diversity among meteorite groups (mainly nucleosynthetic isotopic anomalies[28]) reflects their formation at different locations and times within the early Solar System (Warren 2011). This diversity is dictated by the fundamental division of the protoplanetary disk into two isotopically distinct reservoirs that remained isolated for several million years due to the early formation of Jupiter: the inner, non-carbonaceous (NC) reservoir and the outer, carbonaceous (CC) reservoir. This NC-CC isotopic dichotomy is observed across several elements (e.g., Ti, Cr, Ni, Fe) and exhibits a clear gap between NC and CC compositions, pointing toward two genetically distinct reservoirs (e.g., (Warren 2011; Desch et al. 2018; Kruijer et al. 2019; Kleine et al. 2020). The most plausible explanation is the early rapid formation of Jupiter's core, which created a gap in the protoplanetary disk and acted as a barrier inhibiting radial mixing (Desch et al. 2018).

Recently, new isotopic measurements, especially of Fe and Ni, revealed evidence for a potential third reservoir linked to CI chondrites and returned samples from the C-type asteroids Ryugu and Bennu. These materials display isotopic signatures distinct from both NC and CC reservoirs, leading to the emergence of an NC-CC-CI trichotomy (Figure 1.15) (Nesvorny et al. 2023; Hopp et al. 2022; Gattacceca et al. 2025). Dynamical models predict the formation of CI-like bodies farther out in the disk at around 15–25 AU, near the ice giants, followed by subsequent inward scattering and implantation into the asteroid belt by giant planet migration (Nesvorny et al. 2023).

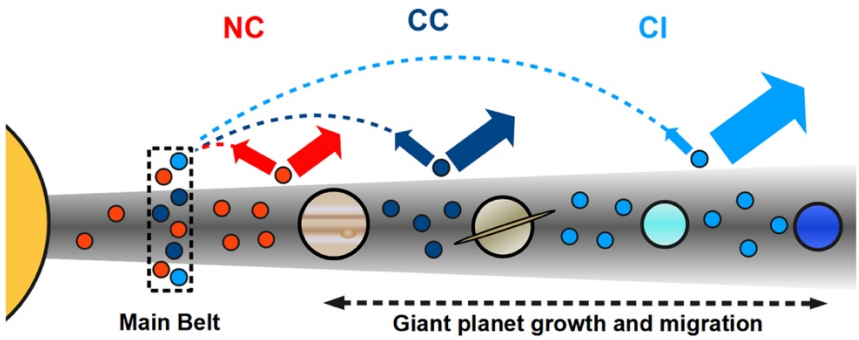

Figure 1.15. Representation of the NC-CC-CI trichotomy. From (Hopp et al. 2022).

Nonetheless, this trichotomy scenario is still debated, with Spitzer et al. (2024) arguing that a distinct CI reservoir is not required to explain such isotopic anomalies. Instead, they suggest

[28] An isotopic anomaly is a deviation of an isotopic ratio from a terrestrial reference standard. Nucleosynthetic isotope anomalies are small deviations (~ppm) in stable isotope ratios that derive from the heterogeneous distribution of presolar material in the early protoplanetary disk, rather than from mass-dependent fractionation processes (e.g., Dauphas & Schauble, 2016).

that all CC groups formed from a common outer solar system dust reservoir, with variable accretion efficiencies of small metal grains, rather than separate formation regions.

In summary, by combining geochemical signatures, mineralogy, spectroscopy and dynamical models, a clearer picture of meteorite formation has been established. Non-carbonaceous meteorites (ordinary chondrites, enstatite chondrites, R-chondrites, and most stony achondrites) likely formed in the inner disk, inside Jupiter's orbit, while carbonaceous meteorites (carbonaceous chondrites) formed in the outer disk, beyond Jupiter's orbit, and were later implanted inward due to planet migration (Figure 1.16). CI-like bodies, potentially representing a third isotopic reservoir, probably formed farther out in the protoplanetary disk before being injected during the migration of giant planets.

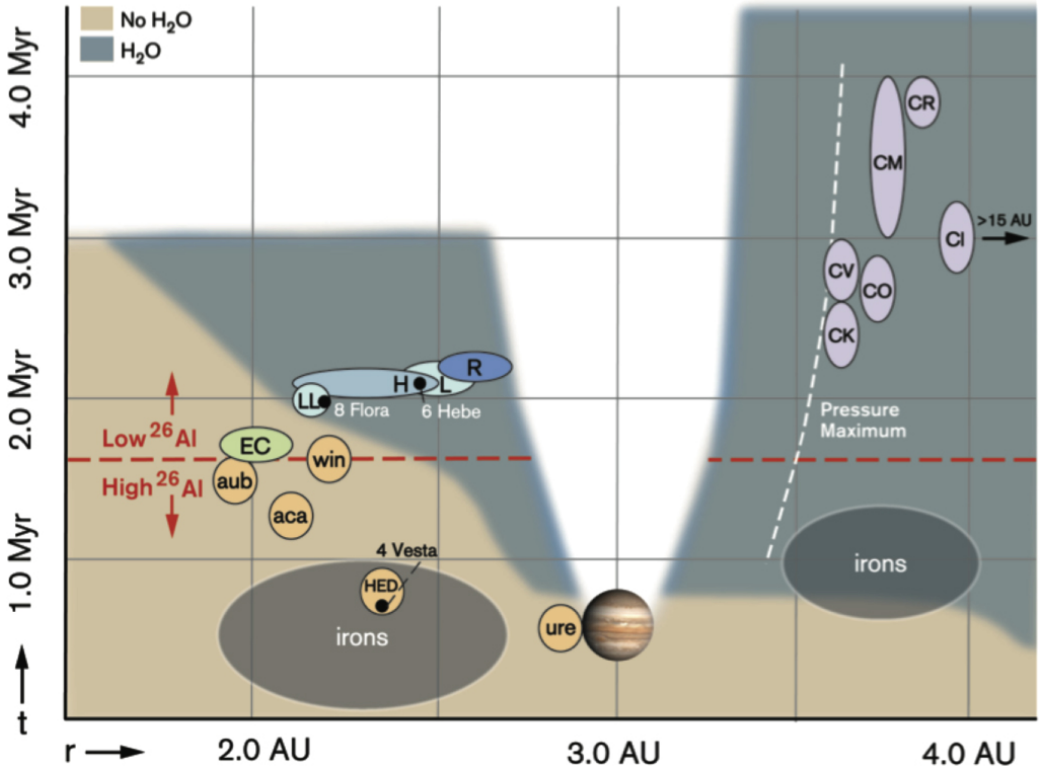

Figure 1.16. Summary plot of the heliocentric distances and times of formation of different meteorite types in the early Solar System. From Desch et al. (2018).

1.4.4. Secondary processes

Most meteorites have undergone parent body secondary processes, including thermal metamorphism, shock metamorphism, and aqueous alteration at different degrees. These processes partly alter the original signatures but provide essential records of parent-body processes.

1.4.4.1. Thermal metamorphism

Thermal metamorphism represents the alteration of mineralogical and textural properties due to heating on the parent body, mainly through radioactive decay of short-lived nuclides such as ^{26}Al (half-life 717 kyr) or, to a lesser extent, collisional heating (Rubin and Ma 2021).

Van Schmus and Wood (1967) introduced the concept of "petrologic type" to describe the degree of thermal metamorphism in chondrites. It consists of a scale ranging from type 1 to type 6, with type 3 being the least metamorphosed and type 6 the most metamorphosed. A type 7 was later introduced for even more metamorphosed samples (Tait et al. 2014). This scale is based on chemical, mineralogical, and textural properties.

Type 3 chondrites are further subdivided into subtypes 3.0 to 3.9 (Sears et al. 1980), and consist mainly of chondrules and chondrule fragments, opaque minerals (mainly kamacite and taenite), sulfides (troilite), embedded in a fine-grained matrix.

With increasing metamorphism from type 3 to type 6, progressive modifications include: increasing recrystallization, loss of volatile components, crystallization of secondary feldspar and removal of chondrule glassy mesostasis, increasing homogeneity in the composition of mineral grains, crystallization of secondary Ca-pyroxene grains, increasing abundance of phosphate, crystallization of secondary chromite grains, and coarsening of kamacite and troilite grains.

1.4.4.2. Aqueous alteration

Most carbonaceous chondrites (especially CI, CM, and CR), and to a lesser extent some non-carbonaceous groups (e.g., type 3 ordinary chondrites; Grossman and Brearley 2005), have been affected by aqueous alteration on their parent asteroids. Primary planetesimals were progressively heated through the radioactive decay of short-lived radionuclides, such as ^{26}Al. This heating produced liquid water from the melting of the ice incorporated in bodies that accreted beyond the snow line. Through water-rock interactions, primary minerals (silicates, metal, sulfides) were transformed into secondary phyllosilicates, oxides, sulfides, and carbonates (Rubin and Ma 2021). Whether alteration began before or after accretion remains debated, though most evidence supports parent-body processes (Suttle and Folco 2020; Lee et al. 2025). This process is particularly common in carbonaceous chondrites which are thought to have formed beyond the snow line (Figure 1.16). The degree of aqueous alteration is one of the major criteria for the classification of carbonaceous chondrites (Weisberg et al. 2006). On the petrographic scale of Van Schmus and Wood, types 3–1 reflect increasing degrees of aqueous alteration. Type 1 chondrites reflect the highest degrees of aqueous alteration: primary silicates are completely transformed, opaque matrix is composed of secondary phyllosilicates, chondrule glass is absent, and veins are replaced by secondary carbonates and sulfates. Type 2 chondrites exhibit moderate alteration characterized by an opaque matrix mainly made of phyllosilicates, oxysulfates, and hydrated oxides, along with partial alteration of primary chondrule glass. Type 3 chondrites are the least altered with an opaque matrix composed mostly of olivine, sulfides, and metal, and the preservation of primary glass within chondrules (McSween 1979).

1.4.4.3. Shock metamorphism

Shock metamorphism, induced by impacts on meteorite parent bodies, is reflected in the transformation and deformation of minerals.

Shock processes affect optical extinction features, enhance the development of planar fractures in silicate minerals, and can induce whole rock recrystallisation, melting, and the formation of high-pressure mineral phases, such as the transformation of plagioclase into maskelynite. Other shock processes include brecciation, shearing, and impact melting, which can induce formation of metal-troilite mixtures, shock veins and melt pockets, as well as new high-temperature and high-pressure phases such as ringwoodite (Stöffler et al. 1991; 2018; Rubin and Ma 2021).

1.4.5. Focus on ordinary chondrites

Ordinary chondrites (OCs) are by far the most abundant meteorites in world collections, with ~84% of officially documented meteorites in the Meteoritical Bulletin DataBase (as of September 2025). They are called 'ordinary' and are the most common, but it does not mean they are not worthy to study. Their high abundance makes them particularly valuable: it allows to study the meteorite flux on Earth and explore the thermal and collisional history of their parent bodies, as well as effects of terrestrial weathering on meteorites.

1.4.5.1. Main minerals and components

The main components of ordinary chondrites are:

- Chondrules: the most abundant components in chondrites (Figure 1.17), with type-3 OC including 65–75 vol% of chondrules. Chondrules range in size from ~0.25 µm to ~5 cm in diameter and are divided into five main textural types (Rubin and Ma 2021a): Porphyritic, Barred Olivine, Radial Pyroxene, Cryptocrystalline, Granular olivine-pyroxene. Chemically, chondrules are divided into Type I (low-FeO) and Type II (high-FeO) based on FeO content in silicates (Grossman and Brearley 2005).

- Matrix: fine-grained and silicate-rich material surrounding chondrules, usually composed of olivine, pyroxene, Fe-Ni metal, and sulfides.

- Opaque phases: Mainly metallic Fe-Ni (kamacite, taenite) and troilite, along with minor chromite with minor accessory ilmenite and rutile, rarely magnetite. Variations in the abundance and composition of opaque phases reflect different oxidation states among H, L and LL chondrites.

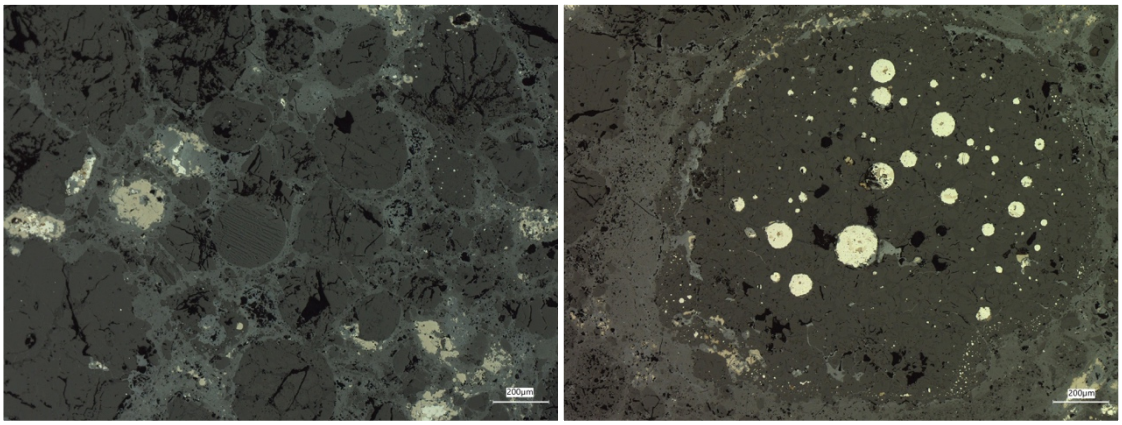

Figure 1.17. Different chondrules in El Médano 520 (LL3.15) under reflected light.

Ordinary chondrites are divided into three groups based of their bulk iron and metallic Fe content:

- H chondrites: high total Fe
- L chondrites: low total Fe
- LL chondrites: lowest metallic Fe and lowest total Fe

The classifications H/L or L/LL can be encountered. They are used when a meteorite's characteristics are ambiguous and fall between two groups. Pourkhorsandi et al. (2022) suggested the existence of an intermediate group between H and L chondrites with the (HL) designation (e.g., Famenin meteorite; H/L3). Other groups have been suggested such as the HH chonrite group (Wasson, 2017) or the F chondrite group (Kirby et al., 2025).

The primary distinction between H, L, and LL chondrites is based on the fayalite content in olivine and ferrosilite content in low-Ca pyroxene, since each group is characterized by a specific range (Figure 1.18).

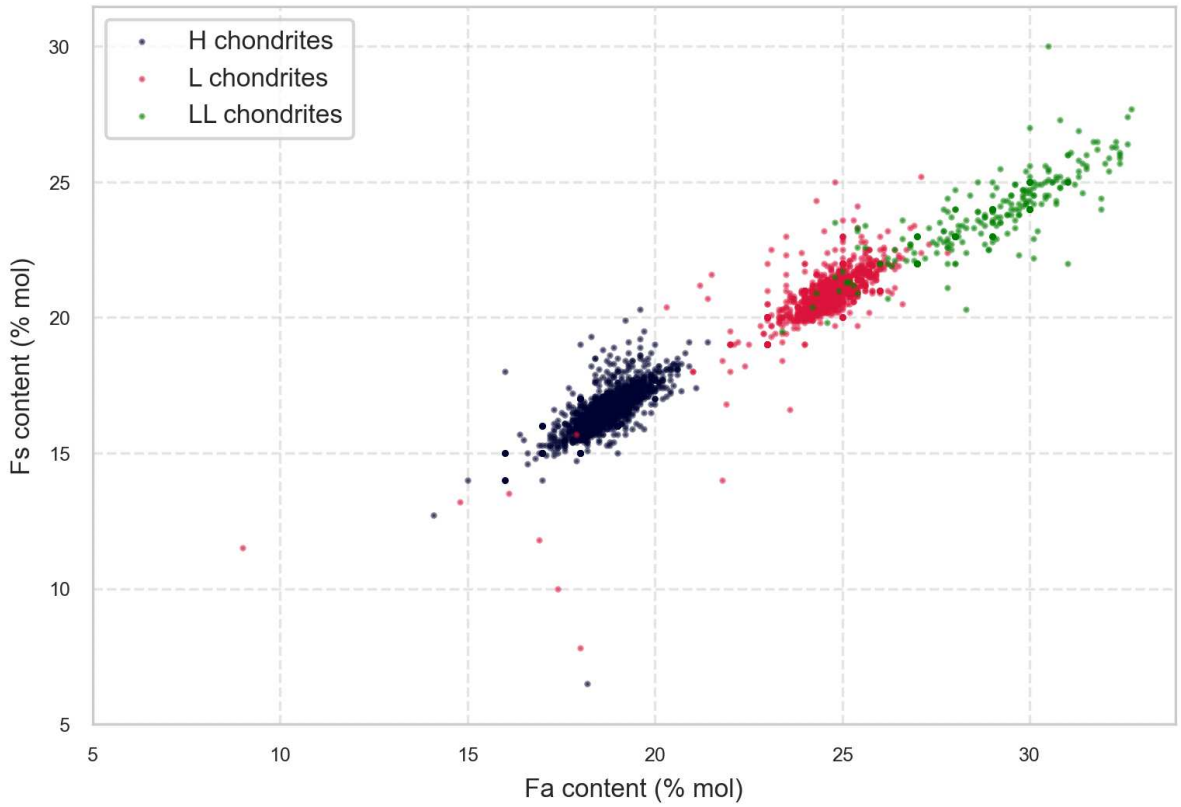

Figure 1.18. Ferrosilite vs fayalite content in ordinary chondrites (n = 5701). Data from MBDB.

Magnetic susceptibility (expressed as logχ; where χ in units of 10^{-9} m^3/kg) reflects the magnetization induced in the ferromagnetic phases (mainly Fe-Ni metal, magnetite, pyrrhotite) under a weak applied magnetic field (Rochette et al. 2003). The measurement of magnetic susceptibility allows a rapid and nondestructive classification of meteorites, especially for ordinary chondrites (Folco et al. 2006; Rochette et al. 2003). This classification is particularly useful for type 3 ordinary chondrites whose silicate grains display highly heterogeneous compositions. However, terrestrial weathering can significantly lower magnetic susceptibility values, with the progressive oxidation of metallic phases and transformation of oxides into oxyhydroxides, so that the weathering grade must be taken into account in the magnetic classification of meteorites (see Figure 1.21).

1.4.5.2. Sub-classifications of ordinary chondrites

a. Petrologic types

As seen above, Van Schmus and Wood (1967) proposed a classification scheme that combined metamorphic changes with bulk compositions and assigned petrologic types 3 through 6 for ordinary chondrites, with the most primitive being type 3, while the remaining types reflect increasing metamorphic grade through types 4—6 (Figure 1.19). The original classification system did not include a type 7, but a 7 designation was later introduced for chondrites with no relict chondrules as a result of complete metamorphism (Tait et al. 2014). Table 1.1 summarizes the main metamorphic changes recognized by observations and analyses.

Criterion	Petrologic Type			
	3	4	5	6
Homogeneity (% mean deviation)	pyroxene ≥5% olivine ≥5%	<5% to homogeneous	homogeneous	
Low-Ca pyroxene	predominately monoclinic	>20% monoclinic	<20% monoclinic	orthorhombic
Feldspar	minor primary	secondary, grains <2μm	secondary, grains 2-50μm	secondary, >50μm grains
Chondrule glass	clear, isotropic	devitrified	absent	
Matrix	opaque to transparent	transparent microcrystalline	recrystallized	
Chondrule-matrix boundary	sharply defined		moderately diffuse	diffuse

Table 1.1. Main petrological and chemical changes with increasing petrologic type of ordinary chondrites. Adapted from Van Schmus and Wood (1967).

Subtypes 3.0–3.9 have been introduced to provide a finer subdivision of unequilibrated OCs (Sears et al. 1980). The main methods used to distinguish between subtypes are thermoluminescence (Sears et al. 1980), heterogeneity of silicate composition (Sears et al. 1992), Raman spectroscopy (Bonal et al. 2016), and Cr_2O_3 concentration in ferroan olivine (Grossman and Brearley 2005).

Some meteorites can include clasts of other petrologic types that are related to the host rock. These are called “cognate breccias”. All clasts and the matrix share the same parent body and mostly the same lithological origin. They usually reflect impact mixing and regolith processes, not inter-asteroidal transfer of material (Bischoff et al. 2006) (e.g., H5-6 Catalina 599; H3-6 Catalina 825).

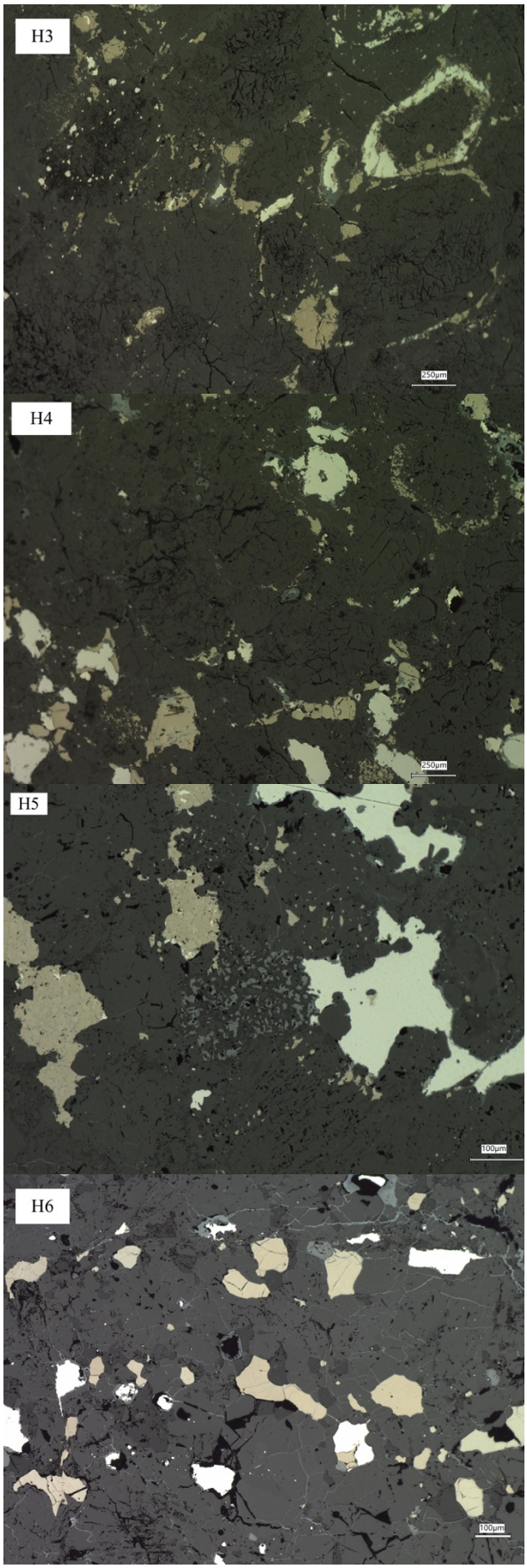

Figure 1.19. Different degrees of metamorphism in H chondrites seen under reflected light (Catalina 580–H3, Catalina 958–H4, Catalina 789–H5, Catalina 799–H6), showing progressive equilibration of silicates and growth of metal and sulfide grains with increasing petrologic type.

b. Terrestrial weathering

Once on Earth, meteorites are exposed to weathering agents (water, wind, air) causing alteration of primary mineral phases. A thin red coating, due to oxidation of metallic Fe from atmospheric water appears.

Meteorite finds are particularly prone to alteration, where metallic Fe-Ni and sulfide grains are progressively replaced by oxyhydroxides (Figure 1.20). Weathering is quantified on a scale ranging from W0 (fresh) to W6 (strongly weathered), based on oxidation percentages and petrographic changes (Table 1.2) (Wlotzka 1993; Zurfluh et al. 2016).

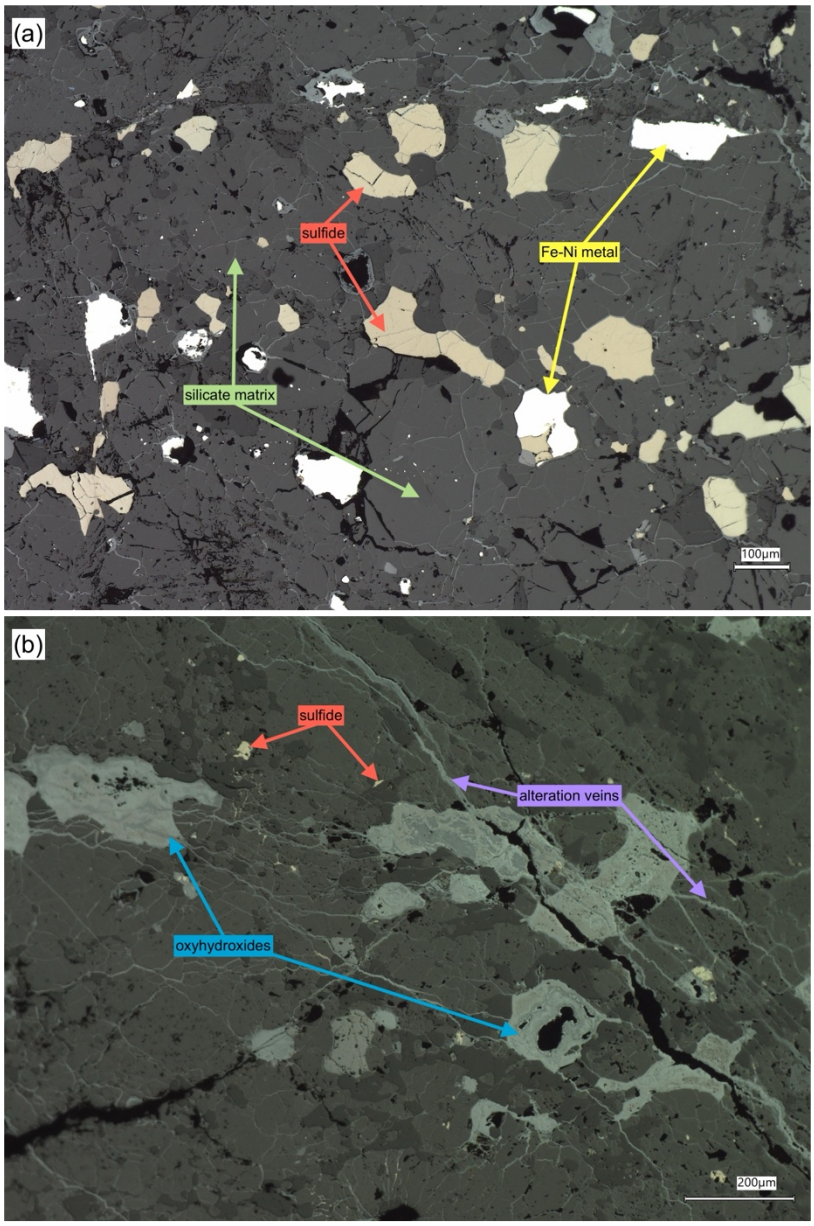

Figure 1.20. Reflected-light images illustrating different degrees of weathering in ordinary chondrites. (a) Catalina 799–H6 W1: fresh sample showing abundant metal (bright white) and sulfide grains (pale salmon) (b) Calama 650–L6 W3: heavily weathered sample showing extensive replacement of metal and sulfide grains by Fe- oxyhydroxides (light grey) and the development of alteration veins.

Weathering Grade	Metal oxidation (%)	Troilite oxidation (%)	Petrographical observations
W0	0	0	Fresh; metal and sulfides unaltered
W1	<20	≥0	Thin oxide rims on metal/troilite; minor oxide veins
W2	20–60	<20	Moderate metal oxidation; presence of pervasive oxide veins
W3	>60	<20	Heavy oxidation of metal; troilite showing minor oxidation
W4	>95	>95	Nearly complete replacement of metal and most troilite by oxides/hydroxides
W5	100	100	Total oxidation of metal and troilite, major alteration of silicates, mainly olivine
W6	100	100	Strong replacement of silicates by clay minerals and oxides; highly weathered rock

Table 1.2. Weathering grade features in ordinary chondrites. Adapted from (Wlotzka 1993; Zurfluh et al. 2016).

Magnetic susceptibility is affected by weathering since it reduces the fraction of metal phases in samples, thus magnetic susceptibility decreases with increasing weathering grade (Figure 1.21), so that some chondrites cannot be distinguished using magnetic susceptibility. For meteorites with a weathering grade >W4, metal alteration is too important, and magnetic susceptibility cannot be used for classification.

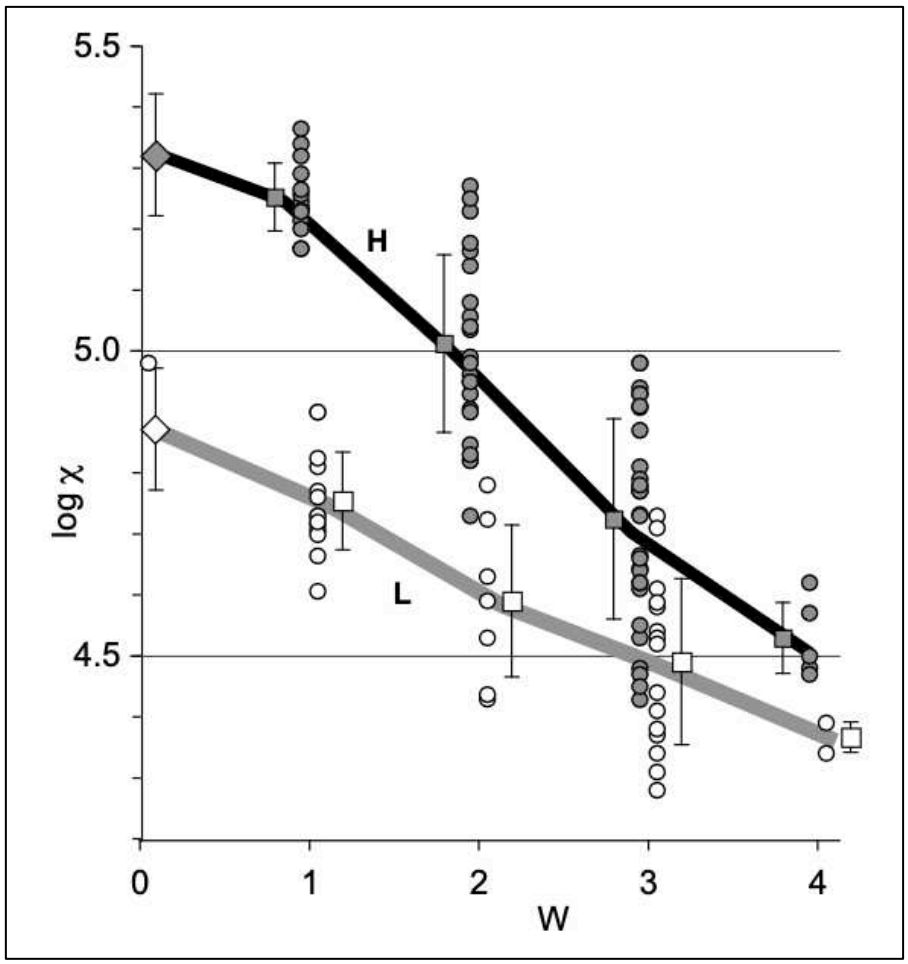

Figure 1.21. Magnetic susceptibility (log χ) as a function of the weathering grade for H (filled) and L (open) chondrites. From Rochette et al. (2008).

c. Shock stage

Shock in ordinary chondrites can induce the development of several features (Stöffler et al. 1991; Rubin and Ma 2021a):

- Extinction and fracture in common silicate minerals (e.g., undulose extinction in olivine)
- large metal-troilite nodules (up to ~3 cm maximum)
- metal-sulfide rounded nodules (metal-sulfide melts and silicate melts are immiscible)
- shock veins formed of metallic Fe-Ni with or without troilite (<1 to >100 μm thick)
- silicate darkening: shock-induced process that increases the opacity of silicates minerals because of trails of metallic Fe-Ni and troilite blebs within fractures of silicate grains, producing "black chondrites" (e.g., Catalina 545).

Stöffler et al. (1991) introduced a shock stage scale ranging from S1 (unshocked) to S6 (highly shocked), reflecting increasing metamorphism with increasing pressure and temperature. This scale was later refined by Stöffler et al. (2018).

1.4.5.3. Origin of ordinary chondrites

a. Thermal structure of parent bodies: onion shell or "salad mix"?

The thermal history of ordinary chondrites parent bodies is a very heated (pun intended) debate (Vernazza et al. 2014; 2015; Lucas et al. 2020; Li et al. 2025). Two primary models have been suggested to explain their thermal structure: the onion shell model and the fragmentation-reassembly model.

1. The onion shell model states that, following accretion, OCs parent bodies were internally heated mainly through the decay of the short-lived radionuclide ^{26}Al, before cooling gradually by conduction towards the surface. This induced the formation of a concentric thermal structure, with the most metamorphosed material (type 6) at the center, followed by successive shells of less metamorphosed material (types 5 and 4), and unmetamorphosed type 3 material near the surface (Figure 1.22) (Hellmann et al. 2019; Edwards and Blackburn 2020). High temperature thermochronometers strongly support this model. For example, Hf-W systematics studies (e.g., Kleine et al. 2008) showed an inverse correlation between petrographic types with cooling rates and ages with (type 6 chondrites have younger ages and slower cooling rates).

2. The fragmentation-reassembly model proposes that the OC parent bodies initially developed an onion shell structure which was later altered by catastrophic collisions, most likely during or shortly after peak metamorphism (Lucas et al. 2020). The resulting hot fragments subsequently cooled and reaccreted quickly into rubble-pile asteroids (Figure 1.22). Supporting evidence for this scenario come from various observations, of which the fact that OC meteorites commonly display shock metamorphism and brecciation features resulting from hypervelocity collisions on their parent bodies (Stöffler et al. 1991; Bischoff et al. 2006).

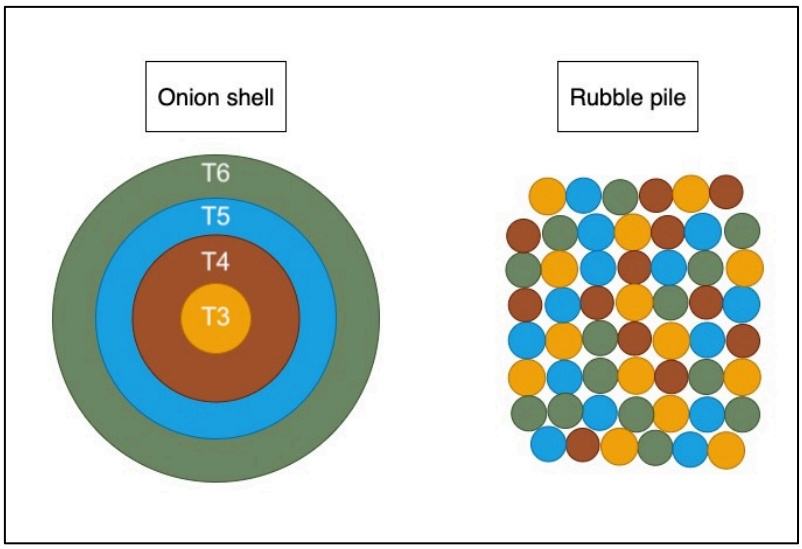

Figure 1.22. Onion shell (with increasing petrographic grade T3–T6) and rubble pile structures. After Wilkison et al. (2002).

Specifically, for H chondrites, radiometric ages evidenced an onion-shell cooling structure produced from heating due to ^{26}Al decay in H chondrites (e.g., Trieloff et al. 2003; Kleine et al. 2008) through metallographic studies of cooling rates (i.e., Pb–Pb, Ar–Ar, Hf–Wf, etc.). Later studies of thermal histories through mineral thermometry (silicates and oxides) (Wlotzka 2005), compositional profiles of minerals (Ganguly et al. 2013), and metallographic cooling rates combined with shock effects show no clear systematic trend with petrologic type, suggesting that early impacts disrupted the parent body during cooling, inducing mixing in the materials from various depths and thus producing the diverse cooling histories recorded in H chondrites. In L chondrites, shock ages and fossil meteorite studies strongly support a catastrophic disruption scenario at ~470 Ma (e.g., Korochantseva et al. 2007; Weirich et al. 2012). Finally, through studies of LL-like asteroid Itokawa returned samples, it has been concluded that the parent body of LL chondrites was 20–50 km in radius and accreted 1.9–2.2. Myr after CAI formation (Nakamura et al., 2011). Recently, Terada et al. (2018) suggested that a potential catastrophic event occurred ~1.4 Ga on the LL chondrite parent body. Studies of LL7 chondrites (Li et al. 2025) suggest that they formed through additional heat provided by impacts, to already hot types 5 and 6 material, which was then excavated and reburied, producing a two-stage cooling history. This process is also thought to have happened in other ordinary chondrite groups (Li et al. 2025).

In summary, the most consistent scenario for the thermal evolution of OCs parent bodies is a complex history with, first, a radiogenic heating phase that induced the formation of an onion shell structure due to ^{26}Al heating, as recorded by high temperature thermochronometers. This structure was later disrupted by major impact events, tens of millions of years after CAI formation (Hellmann et al. 2019). The resulting fragments reaccreted then, thus forming heterogeneous cooling histories recorded by lower-temperature systems (Scott et al. 2014; Lucas et al. 2020).

b. Ordinary chondrites parent bodies: S-type asteroids?

Cosmic-ray exposure (CRE) ages of meteorites reveal a broad range with distinct peaks (Figure 1.23), generally interpreted as fragments resulting from the same family-forming collisional event on their parent body (Eugster 2003; Herzog 2007).

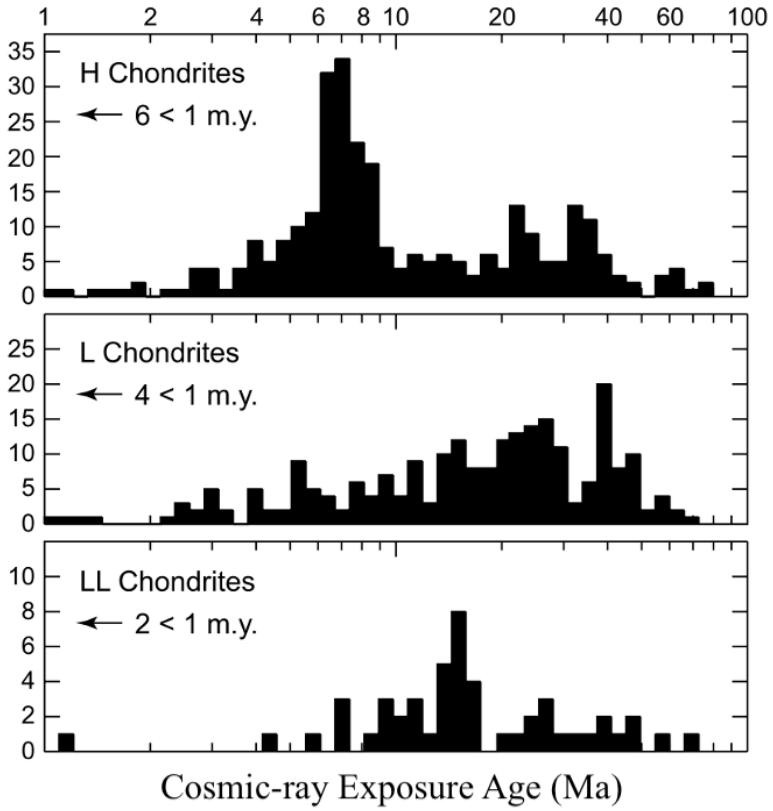

Figure 1.23. Distribution of cosmic-ray exposure ages of H, L, and LL chondrites. From Eugster (2003).

However, linking meteorite samples to asteroid families is challenging, despite major progress in recent years, especially with the increasing number of detected asteroids. Asteroids are usually detected through visible and infrared spectrometry and/or photometry as seen in Section 1.2. The most widely used method to link meteorites with parent bodies is by comparing meteorite and asteroid optical reflectance spectra (Burbine 2016). There are currently between 100–150 distinct parent bodies detected in the asteroid belt (DeMeo et al. 2015).

Early studies suggested S-type asteroids to be at the origin of ordinary chondrites (Chapman and Salisbury 1973; Gaffey et al. 1993), however, there were some discrepancies between S-type asteroids spectra and those of ordinary chondrites, known as the ordinary chondrite paradox. These differences are now attributed to space weathering since they alter the physical, chemical, and optical properties of asteroidal surfaces through bombardment by micrometeorites and irradiation by solar wind particles (Brunetto et al. 2006; Vernazza et al. 2009) .

Space missions have confirmed this link, with the Hayabusa mission launched in 2003 to the S-type asteroid (25143) Itokawa. In-situ measurements and laboratory analysis on returned

Itokawa particles indicated that the Itokawa asteroid has an LL chondrite-like composition, confirming that S-type asteroids are parent bodies of ordinary chondrites. In addition, these analyses confirmed the effect of space weathering on asteroid spectra, explaining the mismatch between OCs and S-type asteroids (Vernazza et al. 2014; Brož et al. 2024b).

In the following subsections, I will present the proposed parent asteroid family of each ordinary chondrite group.

1) H chondrites

H chondrites with a CRE ages ~7 Ma most likely originate from the Koronis family, located just beyond the 5:2 resonance in the main belt. The Koronis family was suggested as a source of H chondrites (Vernazza et al. 2014) using similarities in the shape of reflectance spectra and the young age of the family. For example, the asteroid (243) Ida was visited by NASA's Galileo spacecraft in 1993 and belongs to the Koronis family.

The Koronis family consist of several subfamilies. First, the Karin cluster, with an estimated dynamical age at 5.75 ± 0.05 Ma (Nesvorný et al. 2002; Carruba et al. 2020). Another cluster is the Koronis_2 subfamily derived from a cratering event on Koronis itself with an age of 10 ± 5 Ma (Carruba et al. 2020), later refined by (Brož et al. 2024b) at 7.6 ± 0.2 Ma and suggesting it as the main source of the observed peak of CRE age of H chondrites at ~7 Myr. Finally, the Koronis_3 subfamily is a more dispersed and older group with an age <120 Myr (Brož et al. 2024a).

2) L chondrites

The Massalia family (2.41 AU, i=1.4°) displays strong mineralogical affinity with L chondrites (Marsset et al. 2024) and has an estimated age of ~450 ± 50 Ma, consistent with the ~470 Ma L-chondrite breakup event. This family is thought to have formed through a cratering event on (20) Massalia with relatively low ejection velocities (~44 m/s) and still provides material to Earth as suggested by the associated 1.4° dust band[29]. In contrast, Jenniskens and Devillepoix (2025) favor the Hertha family (2.42 AU, i = 2.4°) as the main source of L chondrites on Earth, since the Hertha family spectra is intermediate between H and LL spectra. While this is broadly consistent with an L-like composition, it does not exactly match L-chondrite spectra. Its dynamical age is debated in the 242–761 Ma range but is less accurate. However, the major breakup of (135) Hertha induced higher ejection velocities of ~285 m/s, which caused a large dispersal of fragments, better explaining the exceptional L-chondrite flux at 470 Ma (Jenniskens and Devillepoix 2025).

While both families could be plausible candidates as L-chondrites parent body, further evidence need to be constrained to identify the contribution of each family to the delivery of L chondrites to Earth.

[29] The zodiacal cloud is a diffuse disk of dust in the inner solar system, produced mainly by asteroid collisions and comet activity; it is observed from Earth as the faint zodiacal light along the ecliptic before dawn or after dusk.



Figure 1.24. Zodical light (white light on the right), induced by the zodiacal cloud, along with the Milky Way on the left, in the Paranal sky taken at the site of ESO's Very Large Telescope (VLT) at Paranal Observatory in Chile. Credit: Y. Beletsky (LCO)/ESO.

3) LL chondrites

LL chondrites are associated with the Flora family (~2.20 AU), which is characterized by LL-type spectra (Vernazza et al. 2008). Several Flora asteroids have been visited by spacecrafts (notably Gaspra, Annafrank, Dinkinesh). Studies of the Hayabusa mission returned samples from the asteroid Itokawa display mineralogical and chemical characteristics with metamorphosed LL chondrites, in particular LL5, giving further evidence for the Flora family as the origin of LL chondrites (Nakamura et al. 2011). Overall, the Flora family is considered as the most plausibly dominant reservoir of LL chondrites, with minor contributions from nearby families such as the Baptistina or Iris families (Jenniskens and Devillepoix 2025).

1.5. Cosmogenic nuclides in meteorites

1.5.1. Production pathways and types

In the interplanetary space, meteoroids are continuously exposed to energetic particles originating from three main sources (Eugster et al. 2006; Herzog and Caffee 2014):

- Galactic Cosmic Rays (GCRs): highly energetic protons and heavy ions that originate from outside the Solar System. They are the dominant source of cosmogenic nuclides in meteorites.
- Energetic solar-flare particles

- Solar wind particles (SW): low-energy ions implanted at the surface of meteoroids

The most prominent pathway for cosmogenic nuclide production in meteoroids is spallation reactions caused by high-energy GCRs. In brief, primary GCR protons and α particles (with energies of hundreds of MeV to GeV) collide with target elements (Mg, Al, Si, Fe, Ca, etc.), inducing nuclei fragmentation and producing cascades of secondary particles, particularly neutrons. These neutrons can penetrate deeper and cause additional nuclear reactions at different energies (fast, epithermal, thermal). As a result, cosmogenic nuclides are produced at the surface, but also within the interior of a meteoroid, depending on its size and the shielding depth of the analyzed sample, but also on the bulk chemical composition of the meteoroid (i.e., abundance of target elements) (e.g., Eugster et al., 2006; Leya and Masarik, 2009; Dalcher et al., 2013).

Cosmogenic nuclides produced in meteoroids can be divided into two categories (418):

- Stable isotopes: they accumulate linearly with time in the interplanetary space (e.g., noble gases ^{3}He, ^{21}Ne, ^{38}Ar)
- Radioactive isotopes: they are simultaneously produced and lost by radioactive decay, until reaching equilibrium (e.g., ^{10}Be, ^{26}Al, ^{36}Cl, ^{14}C, etc.)

Table 1.3 provides details on the most commonly used nuclides in meteorites.

Nuclide	Half-life (yr)	Main Targets
^{3}He, ^{4}He	Stable	O, Mg, Si, Fe
^{10}Be	1.51×10^{6}	O, Mg, Si, Fe
^{14}C	5730	O, Mg, Si, Fe
^{20}Ne, ^{21}Ne, ^{22}Ne	Stable	Mg, Al, Si, Fe
^{26}Al	7.17×10^{5}	Si, Al, Fe
^{36}Ar, ^{38}Ar	Stable	Fe, Ca, K
^{36}Cl	3.01×10^{5}	Fe, Ca, K
^{41}Ca	1.034×10^{5}	Ca, Fe

Table 1.2.Main cosmogenic nuclides commonly used in meteorite studies, with half-lives and target elements (Eugster et al. 2006).

1.5.2. Applications

1.5.2.1. Meteorite chronology

Cosmogenic nuclides are used as chronometers (Figure 1.25) to reconstruct:

- Cosmic-ray exposure (CRE) ages: the time a meteoroid spent in space after ejection from its parent body.
- Terrestrial ages: the time a meteorite has resided on Earth's surface since its fall, constrained from the decay of radioactive nuclides.
- Ejection ages: obtained by combining CRE and terrestrial ages, representing the time elapsed between excavation from the parent body and recovery on Earth.

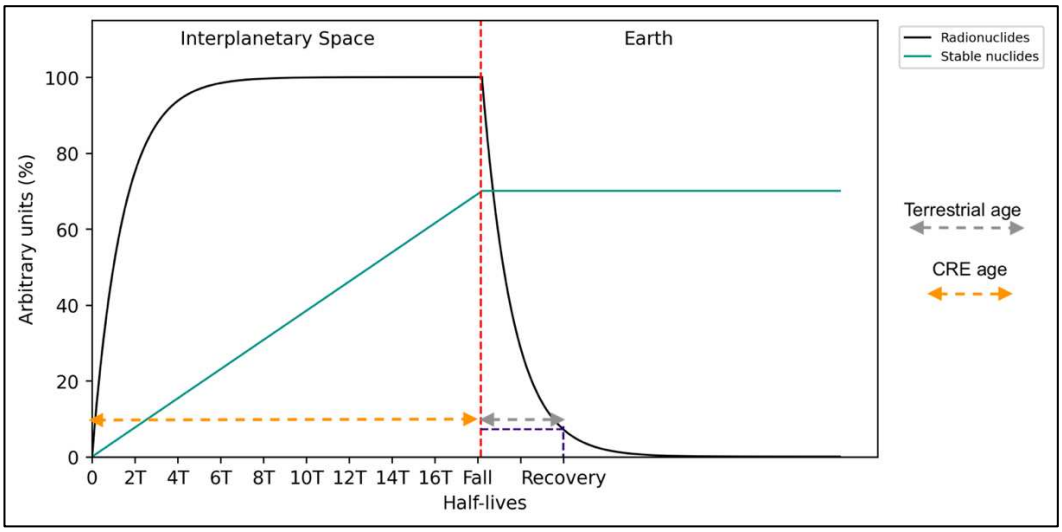

Figure 1.25. Evolution of the radioactive (black) and stable (green) nuclide content in meteorites. The dashed vertical red line represents the time of the fall of the meteorite on Earth. Cosmic ray exposure (CRE) age corresponds to the time spent by the meteoroid in the interplanetary medium before reaching Earth (orange dashed double arrow), while the terrestrial age corresponds to the time spent by the meteorite on Earth (gray dashed double arrow). The age of ejection of the meteoroid from the parent asteroid is the sum of the terrestrial age and the cosmic ray exposure age.

Beyond dating, cosmogenic nuclides also record complex irradiation histories, including multiple exposure stages (Herzog et al. 2007; Herzog et al. 2006). Combining such data across many meteorites enables reconstruction of parent-body processes such as major collisional events or long-term survival of meteoroids in space.

1.5.2.2. Shielding and pre-atmospheric size

Upon atmospheric entry, meteorite undergo fragmentation and ablation to different degrees, so that knowing the size of the meteoroid in space cannot be inferred form the recovered mass at the surface. For simplicity, meteorites are assumed a spherical shape with a radius expressed in gram per cm^2. Sample depth and meteoroid size can be inferred using the combined measurement of the cosmogenic $^{22}Ne/^{21}Ne$ ratio and a radionuclide, for example (Eugster et al. 2006).

To conclude this subsection, cosmogenic nuclides are an important part of this thesis. Using ^{36}Cl terrestrial ages (Chapters 3 and 4), in ordinary chondrites from the Atacama Desert, it is possible to reconstruct the past meteorite flux to Earth over the last 2 Myr. Moreover, by combining terrestrial ages with ^{21}Ne-based CRE ages, we constrain ejection ages (Chapter 5), providing preliminary insights into the collisional and dynamical evolution of asteroids in the Main Asteroid Belt and their contribution to supplying extraterrestrial material to Earth.

Chapter two

Catalina Systematic Collection, Atacama Desert, Chile: statistics, classification, pairing, and density



Une nappe tendue sous un pommier ne peut recevoir que des pommes, une nappe tendue sous les étoiles ne peut recevoir que des poussières d'astres […]

Terre des Hommes – Antoine de Saint-Expupéry (1939)

Chapter summary

2.1. Introduction **76**

2.2. Article summary **79**

2.3. Article **80**

2.4. Conclusion **97**

2. Chapter 2

2.1. Introduction

As seen in the previous chapter, meteorites hold a high scientific importance for understanding the origin and evolution of the Solar System. The past decades have been fruitful in terms of meteorite recovery, particularly in desert regions such as Antarctica, Northwest Africa (NWA), Asia (Oman, Iran, Saudi Arabia), and South America (mainly the Atacama Desert) (Figure 2.1)

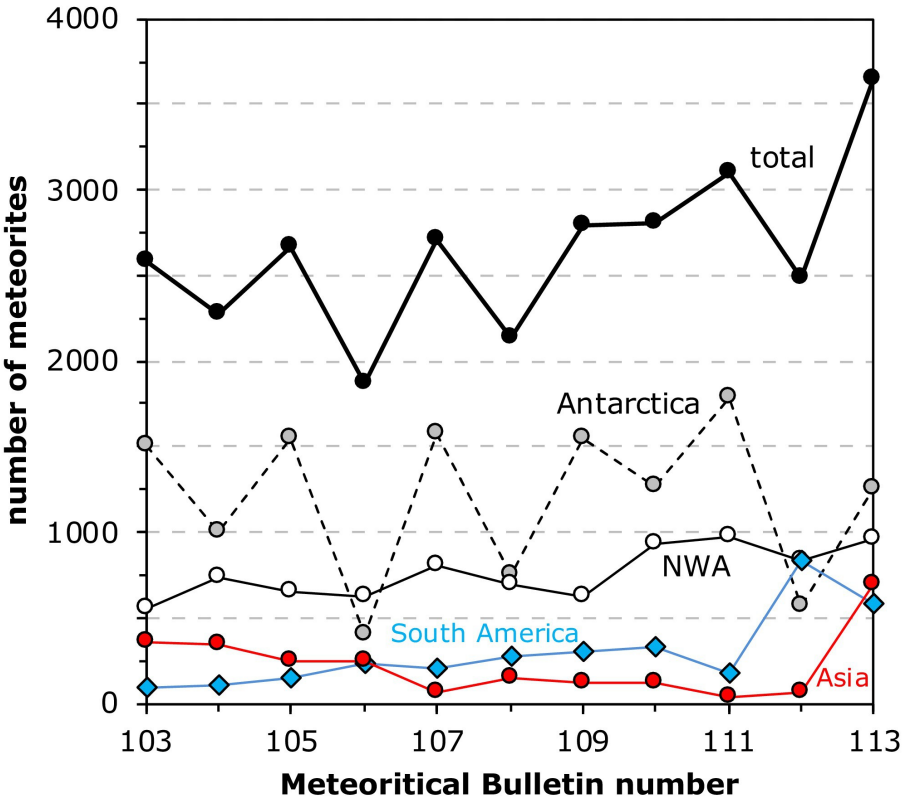

Figure 2.1. Number of meteorites from Antarctica, Northwest Africa, South America, and Asia reported in the last 11 Meteoritical Bulletins, with each meteoritical bulletin number corresponding to a civil year, with MB102 reporting meteorites approved by the Nomenclature Committee in 2013 and so on. From The Meteoritical Bulletin, no. 113; Gattacceca et al. (2025).

Antarctica represents the most productive region for meteorite recovery on Earth, accounting for ~59% of all meteorites in world collections (Meteoritical Bulletin Database, MBDB, as of September 2025). This high recovery rate is linked to the cold and dry climate, which reduces chemical and physical weathering, thus better preserving meteorites. In addition, the color contrast between the white ice/snow and the dark meteorites covered by fusion crust makes meteorite recognition easier. Most importantly, the concentration of meteorites in blue-ice stranding zones, where ice flow movements bring them to the surface, leads to high concentrations of meteorites at the surface (Yoshida 2010; Zekollari et al. 2019). While ice

flow, ablation, and localized trapping maximize recovery, they, however, also complicate density estimations and pairing assessment (Harvey 2003).

In contrast, hot deserts act as passive accumulation surfaces with negligible lateral transport, providing more suitable contexts for field collections. Large numbers of meteorites have been recovered in these regions, mainly the North African desert (Aboulahris et al. 2019; Belhai 2023; Bischoff and Geiger 1995; Schlüter et al. 2002), the Arabian Peninsula (Hofmann and Gnos 2025; Hofmann et al. 2018; Pourkhorsandi et al. 2019), Nullarbor Plain in Australia (Benedix et al. 1999; Jull et al. 2010), Roosevelt County in the United States (Zolensky et al. 1990), and the Atacama Desert in Chile (Hutzler et al. 2016; Gattacceca et al. 2011a; Pinto et al. 2024).

The Atacama Desert, located in northern Chile, is the driest nonpolar desert ("hot desert") in the world. It is bordered by the Pacific Ocean to the west and the Andes Mountains[30] to the east, covering a total surface of 105000 km^2. The most prominent characteristic of the Atacama is the lack of precipitation, with a hyperarid core receiving less than 4 mm of rainfall per year (Azua-Bustos et al. 2018). The Atacama Desert is also considered as the oldest desert on Earth, with hyperaridity established several million years ago (Dunai et al. 2005).

The region's exceptional atmospheric conditions, with high altitudes, rare cloud cover, dry air, and minimum light pollution and radio interference, has rendered it one of the main sites for telescopic observations. The Atacama Desert hosts the most important telescopes in the world, including the Very Large Telescope (Paranal Observatory) and the ALMA international radio observatory (Llano de Chajnantor Observatory). The hyperarid landscapes are also used as a Mars analog by NASA to test instruments for space missions.

[30] Andes Mountains are the most extended continental mountain range in the world, 8900 km long and 200–700 km wide.



Figure 2.2.Search campaigns for meteorites in Antarctica (upper), Tunisian Sahara (middle), and the Atacama Desert (bottom).

Given its hyperaridity, surface stability, and relatively flat topography, the Atacama holds favorable conditions for long-term preservation and recovery of meteorites. Indeed, many

studies revealed extremely high densities exceeding 200 meteorites per km^2 (Gattacceca et al. 2011a; Hutzler et al. 2016; Pinto et al. 2024), making the Atacama Desert the densest region among hot deserts.

In this chapter, I present a detailed study of the Catalina Systematic Collection in the Central Depression of the Atacama Desert, focusing on recovery, classification, pairing, and density estimation. For more details on Analytical procedure and calculation, refer to Appendices A, B, C.

2.2. Article summary

We studied a hot desert meteorite collection from the Central Depression of the Atacama Desert, located in the Catalina Dense Collection Area (DCA). The Catalina Systematic Collection (CSC) was assembled through several systematic on-foot search campaigns throughout four different field campaigns.

We present details on the recovery method and the meteorite classification, which was based on petrography, magnetic properties, and mineral compositions using microscope observations and electron microprobe analysis. We adapted the pairing model of Hutzler et al. (2016), which calculates a likelihood of two fragments belonging to the same meteorite fall by comparing petrographic, magnetic, and geochemical characteristics, also taking into account the distance between two fragments. We also evaluate pairing using a cluster analysis algorithm based on the spatial distribution of the recovered meteorites. This study includes a statistical overview of the meteorite density, classification, and pairing. We present details on the spatial distribution, mass distribution, weathering grade, group and type statistics, and density estimations.

We recovered a total number of 1599 meteorites across a continuous area of 6.80 km^2, yielding a meteorite density of 235 meteorites per km^2, a density significantly higher than in other hot deserts such as the Sahara Desert, Arabian Desert, Nullarbor Desert in Australia, or deserts in Southwest USA.

We classified all 457 meteorites with masses greater than 20 g, 96% of which are ordinary chondrites, along with 3% mesosiderites, one iron meteorite, and one eucrite. The lack of carbonaceous chondrites can be explained by the fact that these fragile meteorites are highly prone to alteration by abrasion. After pairing and recovery biases corrections, the meteorite density is 71 meteorites >20 g per km^2.

This high density confirms that the Atacama Desert is the densest region among hot deserts in terms of meteorites. This is due to the long-standing surface stability and hyperaridity of the Atacama Desert, suggesting old terrestrial ages for the CSC meteorite collection.

Studied meteorites from the CSC exhibit on average lower chemical weathering than other hot desert collections, despite the long accumulation period. The H/L ratio in the CSC is higher than that of Antarctica, other hot deserts, and fall collections, potentially reflecting temporal changes in the composition of the meteorite flux over the past million years.

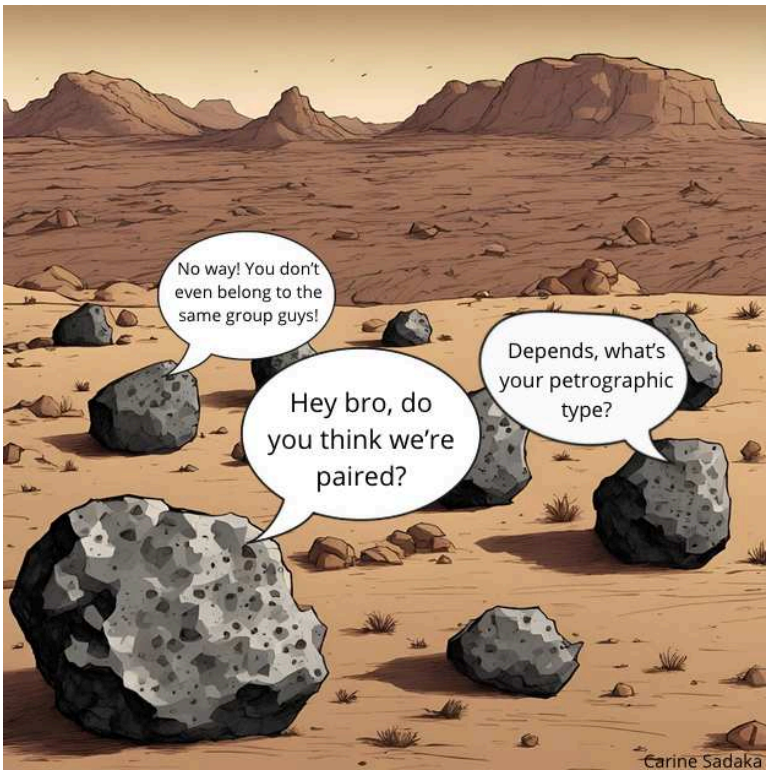

Figure 2.3. Illustration of the concept of pairing. Background generated with AI.

2.3. Article

Article published in *Meteoritics & Planetary Science* (January 2025). Sadaka, C., Gattacceca, J., Gounelle, M., Roskosz, M., Lagain, A., Tartese, R., Bonal, L., Maurel, C., Martinez, R. and Valenzuela, M. (2025), Systematic meteorite collection in the Catalina Dense Collection area (Chile): Description and statistics. Meteorit Planet Sci, 60: 308-323. https://doi.org/10.1111/maps.14307

Check for updates

The Meteoritical Society

Meteoritics & Planetary Science 1–16 (2025)
doi: 10.1111/maps.14307

Systematic meteorite collection in the Catalina Dense Collection area (Chile): Description and statistics

Carine SADAKA[1]*, Jérôme GATTACCECA[1], Matthieu GOUNELLE[2], Mathieu ROSKOSZ[2], Anthony LAGAIN[1,3,4], Romain TARTESE[5], Lydie BONAL[6], Clara MAUREL[1], Rodrigo MARTINEZ[7], and Millarca VALENZUELA[8,9]

[1]Aix-Marseille Université, CNRS, IRD, INRAE, CEREGE, Aix-en-Provence, France
[2]Muséum National d'Histoire Naturelle, Institut de minéralogie, de physique des matériaux et de cosmochimie—UMR7590, Paris, France
[3]Aix-Marseille Université, Institut ORIGINES, Marseille, France
[4]Space Science and Technology Centre, School of Earth and Planetary Sciences, Curtin University, Perth, Western Australia, Australia
[5]Department of Earth and Environmental Sciences, The University of Manchester, Manchester, UK
[6]Institut de Planétologie et d'Astrophysique, Université Grenoble Alpes, Grenoble, France
[7]Museo del Meteorito, San Pedro de Atacama, Chile
[8]Universidad Católica del Norte, Antofagasta, Chile
[9]Center of Astrophysics and Associated Technologies CATA, Santiago, Chile

***Correspondence**
Carine Sadaka, Aix-Marseille Université, CNRS, IRD, INRAE, CEREGE, Aix-en-Provence, France.
Email: sadaka@cerege.fr

(Received 15 July 2024; revision accepted 30 December 2024)

Abstract–We present the outcome of search campaigns conducted in the Catalina Dense Collection area (DCA) located in the central depression of the Atacama Desert, Chile. The "Catalina Systematic Collection" (CSC) was assembled through systematic on-foot searches, resulting in a total of 1599 meteorites, before pairing, collected over a surface of 6.80 km^2. This yielded a recovery density of 235 meteorites per km^2 (67 meteorites >20 g per km^2), making it the densest among hot deserts, even higher than the neighboring El Médano DCA collection. This confirms that the central depression of the Atacama Desert holds the highest meteorite density among hot deserts. We classified 457 meteorites weighing more than 20 g. After correcting for various recovery biases, we estimated a true meteorite density on the ground of 131 meteorites per km^2 for meteorites >20 g before pairing. Using a probabilistic approach, we calculated an average pairing likelihood, yielding 71 meteorites >20 g per km^2 after pairing. This high density is likely linked to an old age of the CSC, which would also explain the absence of carbonaceous chondrites, as they are more prone to alteration by abrasion. This long meteorite accumulation period is related to the long-term hyper-aridity and surface stability of the Atacama Desert, which have persisted for several million years. Meteorites from the CSC show less chemical weathering on average than in other hot deserts, despite the long accumulation period. The H/L ratio in the CSC is higher than in meteorites from other hot deserts, Antarctica, and falls, but similar to the El Médano collection, potentially reflecting variations in the composition of the meteorite flux over the past Myr.

© 2025 The Author(s). *Meteoritics & Planetary Science* published by Wiley Periodicals LLC on behalf of The Meteoritical Society.
This is an open access article under the terms of the Creative Commons Attribution License, which permits use, distribution and reproduction in any medium, provided the original work is properly cited.

INTRODUCTION

Deserts are the most productive places on Earth for meteorite recovery. This is mainly due to the dry conditions and low erosion, which allow the accumulation and preservation of meteorites over long time scales. During the past decades, tens of thousands of meteorites have been recovered in deserts. While the cold desert of Antarctica accounts for the majority of meteorite finds with around 60% of officially recognized meteorites (Meteoritical Bulletin Database, MBDB, https://www.lpi.usra.edu/meteor/, as of December 2024), hot deserts, such as the Arabian Desert (Hofmann et al., 2018; Hofmann & Gnos, 2024), the Sahara Desert (Aboulahris et al., 2019; Belhai, 2023), deserts in Southwest USA (Zolensky et al., 1990), the Atacama Desert (Gattacceca et al., 2011; Pinto et al., 2024), and the Nullarbor Desert (Benedix et al., 1999; Devillepoix et al., 2022), account for around 35% of classified meteorites. Contrary to the Antarctic case where meteorites are concentrated by glacial processes (Zekollari et al., 2019), the high meteorite densities in hot deserts result from the passive accumulation of meteorites with time. Therefore, besides being an invaluable source of meteorites, hot desert meteorite collections allow assessing the stability of the collection surface, estimating the meteorite flux to the Earth and its possible variations over different time scales (Drouard et al., 2019; Zolensky et al., 1990, 2006), and investigating the rate and effects of terrestrial weathering on meteorites (Al-Kathiri et al., 2005; Pourkhorsandi et al., 2019; Zurfluh et al., 2016).

The Atacama Desert, located in Northern Chile, stands out among hot deserts due to its exceptionally arid and stable climatic conditions. Previous studies indicated that the Atacama Desert is home to the densest hot desert meteorite collections in the world, with up to more than 100 meteorites per km^2 (Gattacceca et al., 2011; Hutzler et al., 2016). In contrast, meteorite densities in other hot deserts are much lower, with about 0.1–1 meteorite per km^2 in the Sahara and 0.57–7.3 meteorites per km^2 in the Arabian Desert (Hofmann et al., 2018; Hofmann & Gnos, 2024). As of today, more than 3700 meteorites from Chile have been listed in the MBDB, most of which have been recovered from DCAs located in the Atacama Desert (Pinto et al., 2024). Furthermore, the Atacama Desert is also a valuable site for collecting micrometeorites, adding another layer of scientific interest to this area (Van Ginneken et al., 2024).

In this study, we focus on the Catalina DCA located in the central depression of the Atacama Desert, extending from 25°18′S to 24°54′S latitude and 70°00′W to 69°30′W longitude. We carried out exhaustive on-foot systematic searches on a single continuous zone during five field campaigns. A total of 1599 meteorites were recovered over an area of 6.80 km^2, which is notably higher than any previous systematic study in the Atacama Desert. We call this meteorite collection the Catalina Systematic Collection (CSC). In this work, we present the geological and geomorphological description of the collection area, as well as the statistical properties of the CSC in terms of classification, mass distribution, weathering, pairing, and meteorite density.

GEOLOGY, GEOMORPHOLOGY, CLIMATE

The Atacama Desert, nestled between the Pacific Ocean and the Andes, is composed of five main geological units: the Coastal Range, the Central Depression, the pre-Andean Range, the Altiplano, and the Western Cordillera. Known as the oldest and driest hot desert in the world (Clarke, 2006), it is characterized by an arid to hyper-arid climate. In the hyper-arid zone, the average annual precipitation does not exceed 5 mm $year^{-1}$ (Pfeiffer et al., 2021). The exact age of the onset of the Atacama Desert's aridity remains debated but falls in the 3–25 Ma range (Clarke, 2006; Dunai et al., 2005). This aridity results from a combination of several factors. To the West, the coastal current and the Southeast Pacific anticyclone reduce the advection of Pacific water vapor inland, while to the East, the Central Andes act as a barrier (rain shadow effect), preventing the advection of water vapor from Amazonia to the continental interior (Houston & Hartley, 2003). Due to this long-standing hyper-aridity, some surfaces of the Atacama Desert have not been significantly eroded for millions of years.

In the following, we focus on the central depression where our study area is located. The central depression is an approximately 50 km-wide longitudinal continental basin located West of the Main Cordillera. Its average elevation is around 1000 m in the west and between 2000 and 3000 m in the east. The central depression includes Paleogene–Neogene alluvial, fluvial, and evaporitic sediments, primarily from the Precordillera and Western Cordillera, scattered with thick volcanic ignimbrites (Carretier et al., 2018). The central depression is characterized by low chemical weathering and lacks any fluvial system. It hosts the most productive areas in terms of meteorite recovery, compared to other morphological units (Pinto et al., 2024). The Catalina DCA, in the heart of the central depression, is characterized by a hyper-arid climate with an average annual air temperature range of ~16°C and an average annual cumulative precipitation of ~5 mm $year^{-1}$, recorded between 2001 and 2021 (Pinto et al., 2024).

The CSC area encompasses one main geological formation (Espinoza et al., 2011): the Augusta Victoria Formation (Campanian–Maastrichtian) that includes biotite- and sanidine-bearing rhyolitic pyroclastic rocks.

19455100, 0, Downloaded from https://onlinelibrary.wiley.com/doi/10.1111/maps.14307 by Cnu Marseille Ap-Hm/Aix-Marseille Universite Direction Du Scd, Wiley Online Library on [13/01/2025]. See the Terms and Conditions (https://onlinelibrary.wiley.com/terms-and-conditions) on Wiley Online Library for rules of use; OA articles are governed by the applicable Creative Commons License

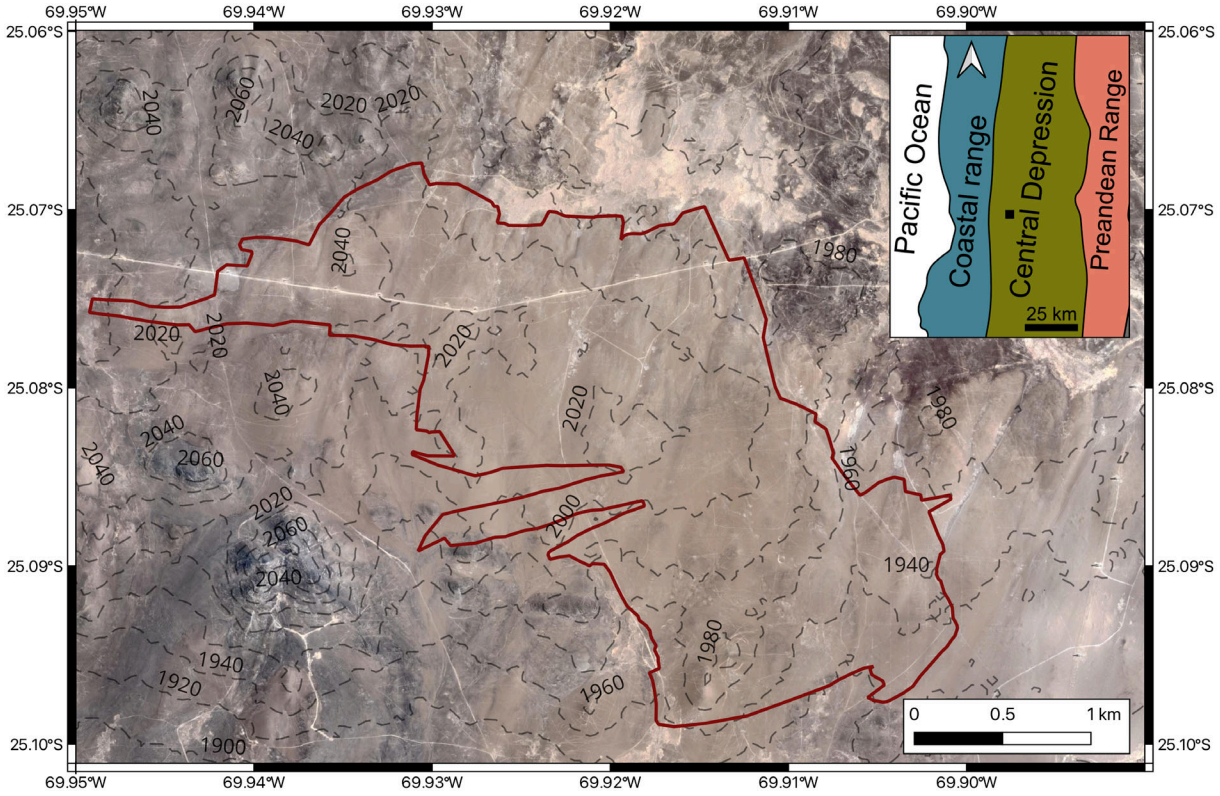

FIGURE 1. Satellite image of the investigated area. The CSC area is outlined in red. Altitude contours are in meters. The insert shows a map of the three main geological units in Northern Chile, with the study area marked by a black square. Google Earth Image.

Outside the searched zone, other formations surround the CSC, of which basaltic and andesitic–basaltic amygdaloidal lavas from the La Negra Formation (middle Jurassic–upper Jurassic), as well as monzodiorites, quartz-bearing monzodiorites, and pyroxene monzonites that are part of the late lower cretaceous Cerro del Pingo plutonic group, and finally, alluvial deposits from upper Miocene–pliocene comprised of poorly stratified gravels with intercalations of coarse sand and silt, some of which contain nitrates (Espinoza et al., 2011).

The CSC area features flat plains with gentle slopes. The surfaces are largely composed of a few centimeters of non-consolidated materials (mostly gravels of igneous rocks) overlying a caliche layer consisting of anhydrite, nitrate, and iodine-rich salts (Tapia et al., 2018). The search area described in this work is a single continuous zone, centered at 25°04′S latitude and 69°55′W longitude, with an altitude range between 1903 and 2054 m above sea level (average altitude of 2046 m), and an average slope of 2° (Figure 1). Despite the presence of numerous volcanic rocks at the surface, the gentle topography and light-colored surface (Figure 2a) make the investigated area very favorable for meteorite recovery.

METHODS

Meteorite Recovery

In this study, the collection of meteorites in the Catalina DCA was performed on foot, focusing on a continuous zone on the western side of the DCA. Searches consisted of walking in straight lines at a distance of 8 m from each other, effectively scanning a 4-m area on each side of each searcher. Great care was taken to inspect the surface in a systematic way. For each meteorite found, the GPS coordinates and the distance from the walking line were noted. These samples were collected during five dedicated search campaigns organized by CEREGE (Aix-en-Provence, France) in collaboration with MNHN (Museum national d'Histoire naturelle de Paris, France), the Universidad Catolica del Norte (Antofagasta, Chile), and the Universidad Austral (Valdivia, Chile) in 2017, 2019, 2022, 2023, and 2024. An additional 101 samples were collected by Rodrigo Martínez from Museo del Meteorito (San Pedro de Atacama, Chile). We classified all meteorites with a mass above 20 g, for a total of 457 meteorites. We also

19455100, 0, Downloaded from https://onlinelibrary.wiley.com/doi/10.1111/maps.14307 by Cnu Marseille Aix-Hm/Aix-Marseille Universite Direction Du Scd, Wiley Online Library on [13/01/2025]. See the Terms and Conditions (https://onlinelibrary.wiley.com/terms-and-conditions) on Wiley Online Library for rules of use; OA articles are governed by the applicable Creative Commons License

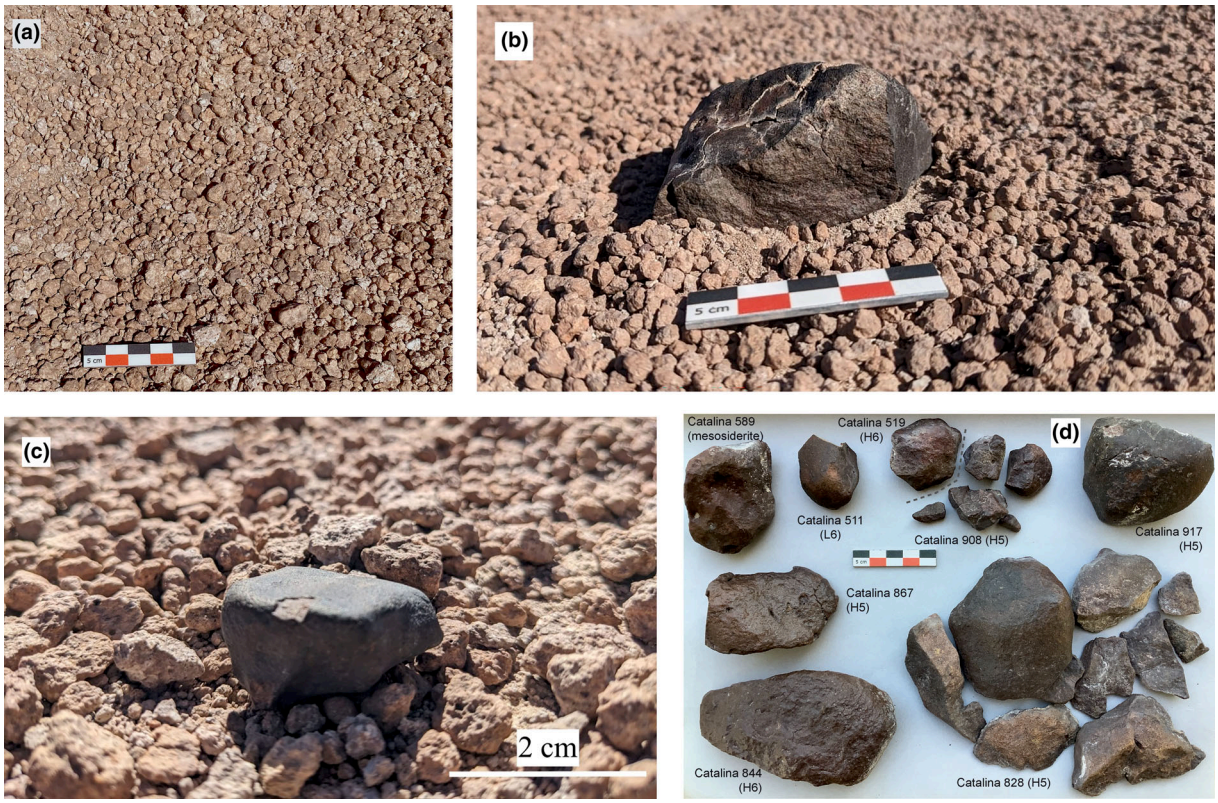

FIGURE 2. (a) Typical surface of the studied zone in the Catalina DCA with a gravel-covered surface. (b) Catalina 827 (LL5, 293 g) in situ. (c) Catalina 905 (L6, 21 g) in situ. (d) Photograph of several Catalina meteorites from the CSC.

classified 65 meteorites weighing less than 20 g, selected based on their unusual aspect or magnetic susceptibility. They include four mesosiderites (Catalina 621, Catalina 629, Catalina 927, Catalina 928), one LL7 (Catalina 462), one L3 (Catalina 570), and one winonaite (Catalina 700). All meteorites classified during this study are listed in the MBDB under the official names Catalina 004, 034, 045–050, 075, 092, 107, 108, 146, 162, 163, 167, 188, 201, 226, 229, 245, 246, 338, 339, 341–343, 399, 409, 410, 423, 424, 426–443, 445–450, 452–460, 462–483, 485–494, 496–498, 500–531, 534–568, 570–573, 575–669, 671–698, 700, 703–731, 734–744, 746–770, 772–793, 797–799, 801–821, 823–934, 948, and 954–958. In the following, except for the mass distribution that takes into account all the recovered 1599 meteorites, only the collection of meteorites >20 g is discussed. Macroscopically, the recovered meteorite samples display a wide range of shapes and preservation states, ranging from rounded or smooth-edged specimens to irregular, shapeless fragments, with some exhibiting a flattened morphology (Figure 2d). Most samples are characterized by a brownish color, and fewer than 10% retained a preserved fusion crust. The meteorites were only slightly buried, and several are covered with a white caliche deposit in their buried part. Many samples consist of several fragments. For meteorites above 20 g, the average number of fragments is 2.9, usually found over a few m^2. While chemical weathering is low in the Atacama Desert, meteorites experience fragmentation driven by the formation of iron oxyhydroxides and oxides, and thermoclasty favored by a strong daily temperature cycle inducing high-temperature gradients in the rocks (McKay et al., 2009). Subsequent abrasion by wind and sand processes lead to the gradual disappearance of meteorites. These observations are described in detail in Pinto et al. (2024).

Classification

Meteorite classification was based on petrography, magnetic properties, and mineral composition. Microscopic petrographic examinations performed with a Leica DM polarizing microscope or a Keyence VHX-7000 digital microscope were conducted on polished sections to examine the mineralogy and texture. Mineral elemental composition was determined by electron probe microanalyses performed at the CAMPARIS facility in Sorbonne Université, Paris, using a Cameca SX Five electron beam (~1 µm in diameter), an accelerating voltage of 15 kV, and a beam current of 10 nA.

19455100, 0, Downloaded from https://onlinelibrary.wiley.com/doi/10.1111/maps.14307 by Cnu Marseille Aix-Hmr/Aix-Marseille Universite Direction Du Scd, Wiley Online Library on [13/01/2025]. See the Terms and Conditions (https://onlinelibrary.wiley.com/terms-and-conditions) on Wiley Online Library for rules of use; OA articles are governed by the applicable Creative Commons License

The measurement of magnetic susceptibility is a robust, rapid, and nondestructive meteorite classification method, especially for ordinary chondrites (Folco et al., 2006; Rochette et al., 2003). Magnetic susceptibility was measured on whole meteorites at CEREGE using a KLY2 susceptibility meter from Agico equipped with a large coil (65 cm^3). Samples that did not fit in the coil were measured using an SM30 contact probe from ZH Instruments following the calibration of Gattacceca et al. (2004). The smallest samples (<2 g) were measured with an MFK instrument from Agico or an SM150 instrument from ZH instruments.

Pairing

Meteoroids often undergo fragmentation during their atmospheric entry, resulting in the fall of multiple stones. Consequently, multiple fragments from the same meteorite are often found scattered within a geographical area called strewn field. Moreover, individual stones may fragment on the Earth's surface due to alteration processes. In dense collection areas, pairing these fragments is challenging and time-consuming regarding data acquisition. However, pairing assessment remains extremely important in any study involving a large meteorite collection, as it can reduce statistical bias and prevent duplicate laboratory analyses (Scott, 1984). Pairing is crucial mostly for equilibrated ordinary chondrites, which are the most abundant types of meteorites.

In our case, of 457 meteorites >20 g, 440 are ordinary chondrites, leading to a staggering 96,580 different possible pairs, making it unrealistic to check each pair of meteorites individually. For these reasons, we tackle the pairing problem using a probability approach with a model similar to that developed by Benoit et al. (2000) and Hutzler et al. (2016). This model can be used for a quick pairing assessment of a large number of meteorites. We modified the model to suit our collection and search area. The mathematical model is coded in Python and available online on GitHub (https://github.com/csadaka2/ordinary_chondrites_pairing).

Among the main criteria used in the literature for ordinary chondrites pairing (Benoit et al., 2000; Schlüter et al., 2002), our pairing code incorporates the petrographic type (Van Schmus & Wood, 1967), the weathering grade (Wlotzka, 1993), the fayalite content of olivine, the ferrosilite content of low-Ca pyroxene, the magnetic susceptibility, and the distance between stones. We consider that two meteorites from different groups cannot be paired, so we separated H, L, and LL chondrites. We also assume that unequilibrated ordinary chondrites of type 3 cannot be paired with equilibrated chondrites.

The pairing code was used only for ordinary chondrites, since in our collection, other groups are rare enough for their pairing to be assessed by checking all possible pairs based on the above-mentioned criteria and petrographic observations. The number of type 3 ordinary chondrites is low enough that whenever pairing was suggested by the pairing code, we checked the possible pairs individually using additional criteria: percentage mean deviation of the fayalite content of olivine, average chondrule size, and other petrographic features (presence of shock veins, melt pockets, polycrystalline troilite, texture of inter-chondrule matrix).

The pairing code calculates a factor P that reflects the likelihood of two meteorites being paired, using the following equation:

$$P = (\Pi_i {p_i}^{w_i})^{\mathbf{1}/\Sigma w_i}$$

Here, p_i is the probability of pairing for two meteorites for the given criterion i, and w_i is the weight assigned for each criterion i. Given that some criteria are more robust than others, a different weight was assigned to each (Table 1). Magnetic susceptibility, petrographic type, fayalite content of olivine, and ferrosilite content of low-Ca pyroxene were given a weight of 2, while distance and weathering grade were given a weight of 1. Missing criteria were assigned a weight of zero for mathematical homogeneity. P is not a probability stricto sensu; hence, we use the term factor for mathematical correctness. To invalidate the pairing between two meteorites, it only takes one single criterion being invalid. For this, the weighted geometric mean, where each value is raised to the power of its assigned weight, is a suitable approach for combining probabilities from different criteria when each criterion has a different level of importance. If any of the criteria suggests a very low probability (close to zero), it will significantly impact the overall pairing factor P, potentially invalidating the pairing. Additionally, each criterion was assigned a probability function. For the weathering grade, petrographic type, and inter-meteorite distance, we applied a discrete function. Magnetic susceptibility, fayalite content, and ferrosilite content probability functions follow a Gaussian distribution, with their standard deviations as listed in Table 1. Therefore, for these properties, the factor p_i can be computed as the probability that two measurements of a given property for two meteorites (x_A and x_B) are from the Gaussian distribution with a standard deviation $\boldsymbol{\sigma}$ and a mean value of $(x_A + x_B)/2$:

$$p = e - \left(\frac{x_A - x_B}{2\sigma}\right)^2$$

Ordinary chondrite groups have specific ranges of magnetic susceptibility (Rochette et al., 2003, 2012). We chose the parameter σ of the magnetic susceptibility in the pairing code based on the intra-meteorite standard

19455100, 0, Downloaded from https://onlinelibrary.wiley.com/doi/10.1111/maps.14307 by Cnu Marseille Ap-Hm/Aix-Marseille Universite Direction Du Scd, Wiley Online Library on [13/01/2025]. See the Terms and Conditions (https://onlinelibrary.wiley.com/terms-and-conditions) on Wiley Online Library for rules of use; OA articles are governed by the applicable Creative Commons License

TABLE 1. Characteristics of the parameters used in the pairing model for the Catalina systematic collection.

Criterion	Distribution	Parameters	Weight
Magnetic susceptibility	Gaussian	0.10	2
Fayalite content	Gaussian	0.63	2
Ferrosilite content	Gaussian	0.61	2
Weathering grade	Discrete	$p = 1$ if $\Delta = 0$ $p = 0.75$ if $\Delta = 1$ $p = 0.5$ if $\Delta = 2$ $p = 0.1$ if $\Delta > 2$	1
Petrographic type	Discrete	$p = 1$ if $\Delta = 0$ or 0.5 $p = 0.75$ if $\Delta = 1$ $p = 0$ if $\Delta > 1$	2
Distance (m)	Discrete	$p = 1$ if $d < 200$ $p = 0.9$ if $200 < d < 300$ $p = 0.8$ if $300 < d < 400$ $p = 0.7$ if $400 < d < 500$ $p = 0.6$ if $500 < d < 700$ $p = 0.5$ if $700 < d < 900$ $p = 0.4$ if $900 < d < 1000$ $p = 0.3$ if $1000 < d < 1500$ $p = 0.2$ if $1500 < d < 2000$ $p = 0.1$ if $2000 < d < 3000$ $p = 0.05$ if $d > 3000$	1

deviation of magnetic susceptibility measured in OC falls and finds (Table S1). We use a conservative SD of 0.10 for all ordinary chondrite groups.

To have an estimate of the standard deviations for the fayalite content of olivine and the ferrosilite content of low-Ca pyroxene within a given equilibrated ordinary chondrite, we used data from several paired meteorites from strewn fields: the Los Vientos 014 L6 strewn field from the Atacama Desert, the Kumtag L5 strewn field from China (Zeng et al., 2018), and the Jiddat al Harasis 073 L6 strewn field (Gnos et al., 2009). We calculated mean values of the intra-strewn field standard deviation of 0.63 for the fayalite content of olivine and 0.61 for the ferrosilite content of low-Ca pyroxene (Table S2). We use only data from types 5 and 6 ordinary chondrites that represent over 99% of equilibrated ordinary chondrites in the CSC. Standard deviations for the silicate composition of type 4 ordinary chondrites may be higher, especially for low-Ca pyroxene, but are not relevant for this study.

The pairing code returns a symmetrical matrix displaying the pairing factors. These estimates remain qualitative as pairing can never be confirmed with absolute certainty in very dense collection areas, even by checking individual pairs under a microscope. Additional criteria could be used for a more accurate diagnostic of this pairing code: shock stage, presence or absence of specific petrographic features (polycrystallinity of troilite, presence of shock veins, presence of melt pockets, etc.).

STATISTICS OF THE CSC

Spatial Distribution

A total of 1599 meteorites, amounting to a total of 52.5 kg, were recovered over 6.80 km^2. The spatial distribution of the CSC meteorites is shown in Figure 3. Meteorites are found throughout the searched area with no obvious preferential concentration areas or size sorting. The average distance between a meteorite and its closest neighbor is 27 m (Figure 4) and 61 m when considering only meteorites >20 g. These values reflect the extremely high density of meteorites in this area. A small number of meteorites (39) were found immediately outside of our systematic search area by other meteorite hunters (Figure 3). The resulting apparent meteorite density, calculated for the area in Figure 3 that we did not investigate ourselves, is 2.0 meteorites per km^2, two orders of magnitude lower than the density in the area that we searched in a systematic way (235 meteorites per km^2), illustrating the efficiency of our collection method. Moreover, the average mass of these 39 meteorites is 50 g, higher than the average mass of 33 g in the CSC (see below), evidencing the incomplete recovery biased toward larger meteorites.

The distribution of magnetic susceptibility (Figure 3), which roughly reflects the distribution of ordinary chondrite groups (Rochette et al., 2003), shows a concentration of meteorites with low susceptibility

19455100, 0, Downloaded from https://onlinelibrary.wiley.com/doi/10.1111/maps.14307 by Cnu Marseille Ap-Hm/Aix-Marseille Universite Direction Du Scd, Wiley Online Library on [13/01/2025]. See the Terms and Conditions (https://onlinelibrary.wiley.com/terms-and-conditions) on Wiley Online Library for rules of use; OA articles are governed by the applicable Creative Commons License

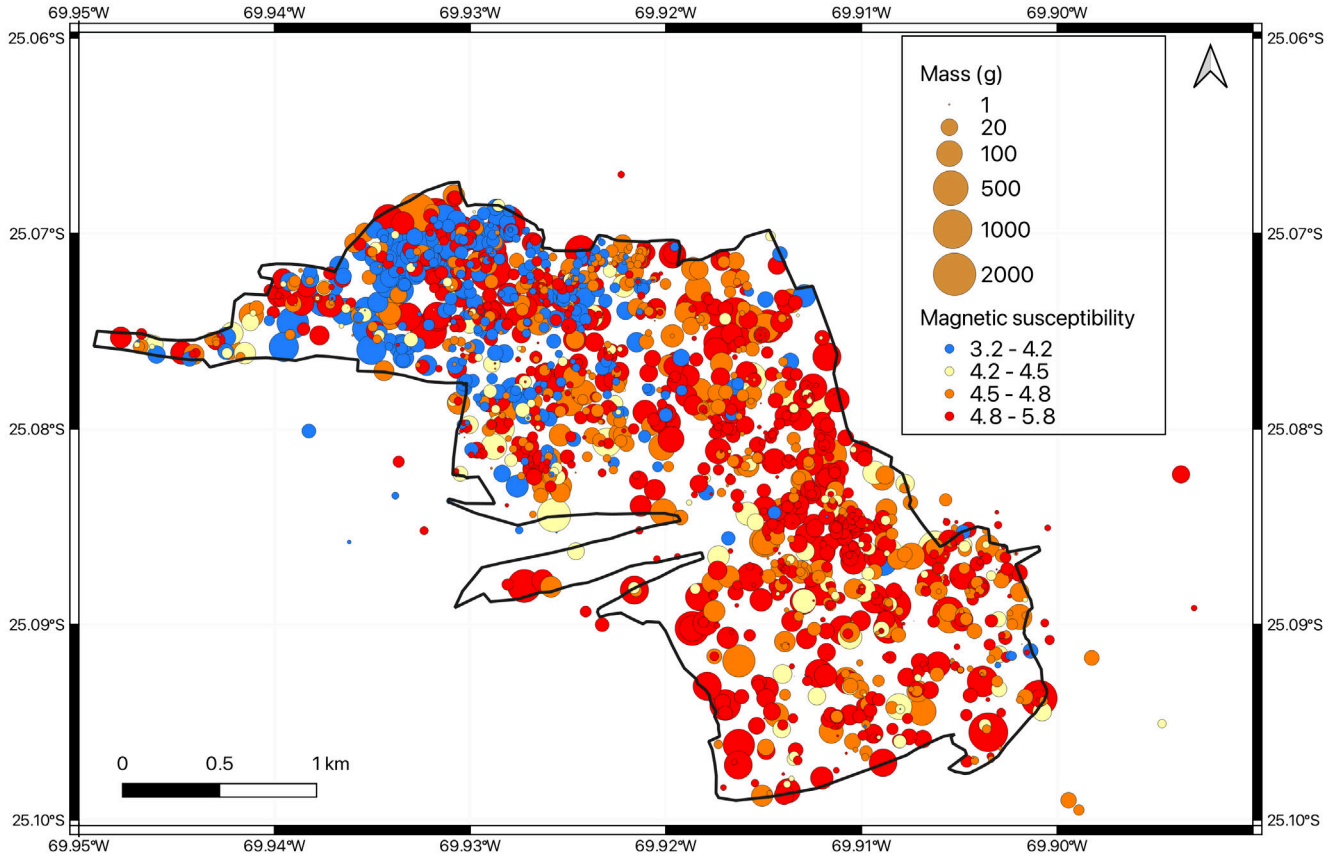

FIGURE 3. Map of the investigated area with the position of the meteorites ($n = 1599$). Meteorites are represented with different sizes reflecting their mass and different colors depending on their magnetic susceptibility values ($\log\chi$ in 10^{-9} m^3 kg^{-1}).

($\log\chi$ <4.2) in the northwestern part of the searched area. This is indicative of a cluster of paired LL chondrites in that area. All 457 meteorites >20 g have been classified and their spatial distribution is shown in Figure 5.

A concentration of LL5 meteorites is visible in the northwestern part of the area, confirming the existence of an LL5 strewn field in that area. This strewn field contains 262 LL5 samples (including 70 above 20 g), for a total mass of 5.703 kg with no obvious mass-dependent spatial distribution. No significant concentration mechanisms are present that could alter the distribution of meteorites. The gentle slopes (2° on average) prevent meteorite movements, and the small-scale heterogeneity in slope direction across the study area ensures that any movement would result only in localized and minor redistribution. In this study, we solely focused on meteorites weighing more than 20 g, which are not susceptible to wind-driven movement on flat, gravel-covered surfaces.

Pairing Detection Using Other Methods

We also evaluated pairing using a cluster analysis algorithm, originally developed for the identification of crater clusters on planetary surfaces (Automatic Secondary Crater Identification algorithm—ASCI, Lagain et al., 2021), inspired by a protein cluster detection algorithm (Andronov et al., 2016). This tool compares the spatial distribution of the recovered meteorite population in the searched area with a set of randomly distributed meteorite population with a similar number of meteorites over the same area. It then identifies meteorites in clusters with a criteria distance based on their closest neighbors, that is, meteorites are flagged if their presence is unlikely the result of a random stochastic process (meteoritic fall) but rather from a fragmentation process (atmospheric or on the ground). Thus, they are considered paired from a statistical point of view.

This algorithm was applied to the three groups of ordinary chondrites >20 g described here. Among the 81 LL chondrites, 114 L chondrites, and 245 H chondrites, 48 (59%), 38 (33%), and 59 (24%), respectively, were found to be clustered (Figure 6). The LL chondrite cluster in the NW part of our study area is well identified by the algorithm. Three main other H chondrite clusters and two main L chondrite clusters are also identified and could originate from individual meteorite fall events.

19455100, 0, Downloaded from https://onlinelibrary.wiley.com/doi/10.1111/maps.14307 by Cnu Marseille Ap-Hm/Aix-Marseille Universite Direction Du Scd, Wiley Online Library on [13/01/2025]. See the Terms and Conditions (https://onlinelibrary.wiley.com/terms-and-conditions) on Wiley Online Library for rules of use; OA articles are governed by the applicable Creative Commons License

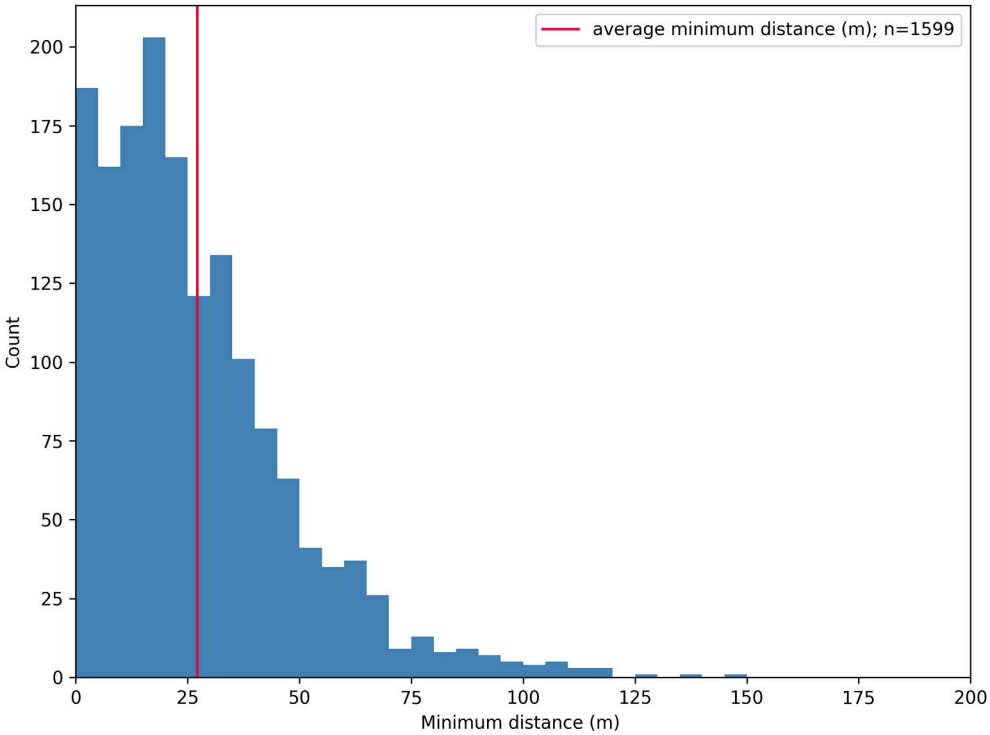

FIGURE 4. Histogram of the distribution of distances to the nearest neighbor of each meteorite ($n = 1599$, 10 m bins). The vertical line indicates the mean of 27 m.

Assuming that each cluster represents a single meteorite fall, we obtain 34 LL chondrites, 78 L chondrites, and 189 H chondrites.

Independently, the distance between each meteorite and its closest neighbor was computed within each group (LL, L, and H). A simulation of the same meteorite population randomly distributed across the searched area was conducted and iterated 10,000 times. The average distribution and standard deviation over the 10,000 simulations were computed and compared to the observed distribution (Figure 7). This method highlights the high degree of clustering for LL meteorites: The observed distribution is skewed toward small distances, with 35% of meteorites falling beyond 1σ of the simulated random distribution. H and L chondrites also show clustering but to a lesser extent, with 16% and 5% of meteorites beyond 1σ of the simulated random distribution, respectively.

Mass Distribution

Meteorite masses range from 0.31 to 2.183 kg, with 93% weighing less than 100 g and 71% under 20 g, a median mass of 8.9 g, and an average mass of 33 g. The total recovered mass is 52.5 kg. Only one meteorite >2 kg was found, making the CSC depleted in high masses compared to other collections (Table 2). The large proportion of smaller stones highlights the efficiency of a slow-paced systematic collection that yields smaller specimens compared to searches by car. Moreover, the investigated area has a flat topography and a light-colored surface, enabling the recovery of small meteorites. The cumulative mass distribution of the CSC, shown on a log-number versus log-mass plot, is linear above 135 g with a slope of −1.47 over the 135 g to 1 kg range (Figure 8). Below 135 g, the distribution flattens gradually, likely evidencing the lower efficiency for the recovery of small meteorites. In fact, below a given threshold mass, a flattening can also be observed in the mass distributions of meteorite falls, meteorites from Antarctica and Oman, and from the extensively studied neighboring El Médano systematic collection (Figure 8). It is noteworthy that this threshold mass is variable across the collections: 135 g for CSC and El Médano systematic collection, 1 kg for Oman meteorites, 5 kg for Antarctica meteorites, and 50 kg for meteorite falls. We propose that this threshold mass serves as a proxy for the overall preservation and recovery efficiency of meteorites in a given collection.

Weathering Grade

The most common weathering grade of meteorites in the CSC is W2 (51%) followed by W1 (37%). We also note the low amount of W3 (10%) and scarcity of W4

19455100, 0, Downloaded from https://onlinelibrary.wiley.com/doi/10.1111/maps.14307 by Cnu Marseille Ap-Hm/Aix-Marseille Universite Direction Du Scd, Wiley Online Library on [13/01/2025]. See the Terms and Conditions (https://onlinelibrary.wiley.com/terms-and-conditions) on Wiley Online Library for rules of use; OA articles are governed by the applicable Creative Commons License

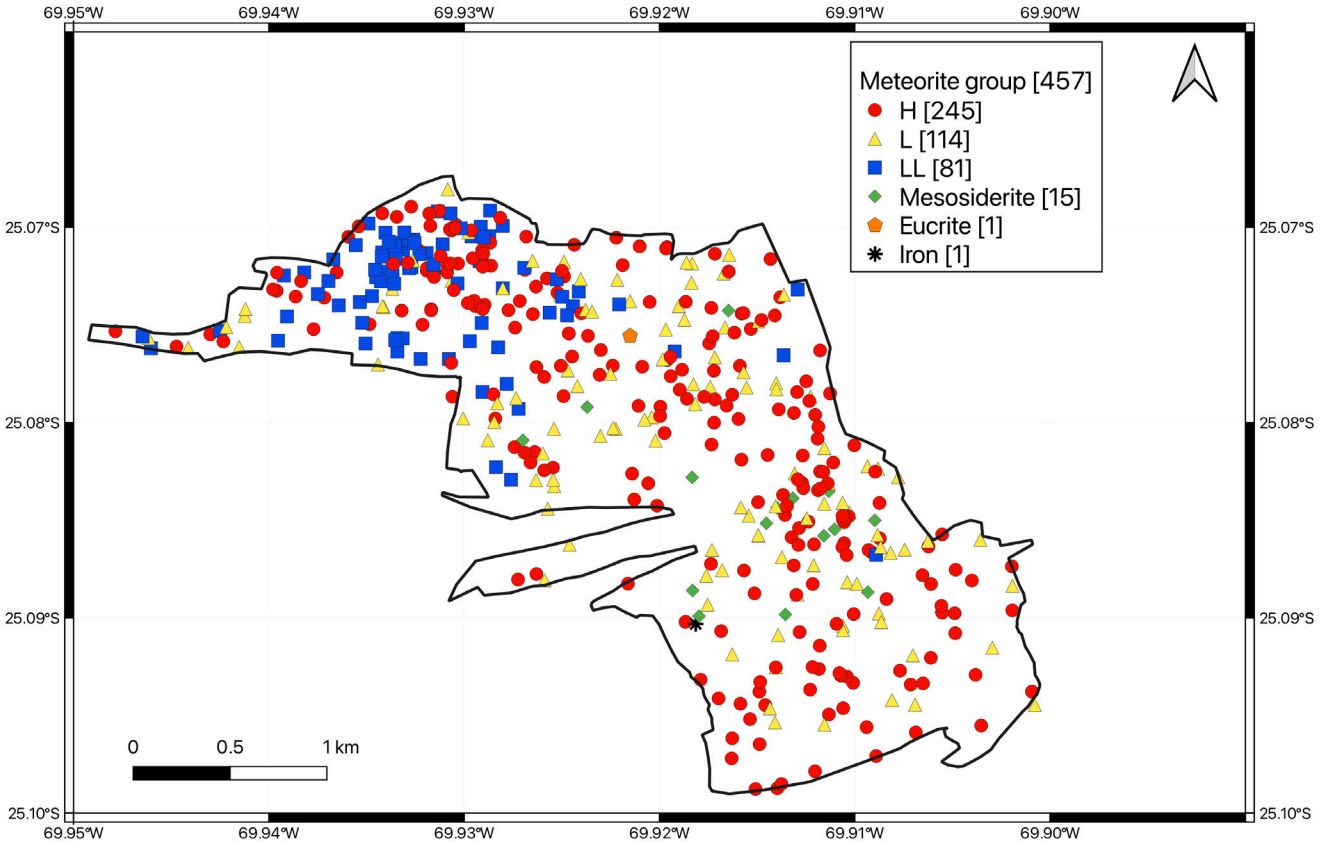

FIGURE 5. Map of the classified meteorites >20 g. The number of meteorites in each group is shown in square brackets.

and above. Since our collection and classification were done systematically, we eliminate the potential bias by hunters or meteorite classifiers for fresh meteorites. We compared the weathering grade distributions in the CSC, the Omani collection, and the Sahara meteorite collection (Figure 9). Despite the non-systematic collection of these samples, their classification was systematic, reducing the bias from the non-declaration of highly altered ordinary chondrites. The meteorites in the CSC are less weathered on average than in other hot deserts. Therefore, this confirms that, despite older surface ages, meteorites from the central depression of the Atacama Desert are better preserved than in hot deserts thanks to the prevailing hyper-aridity (Pinto et al., 2024). The near absence of meteorites with a weathering grade above W3 suggests that rather than chemical processes, physical processes such as fragmentation and abrasion by wind, sand, and dust, are the primary drivers of meteorite removal from the surface of the studied area.

Group and Type Abundances

The CSC is composed of 96.3% of ordinary chondrites, with 53.6% H, 25.0% L, and 17.7% LL before pairing (Table 3). Compared to falls, Antarctic meteorites, and other collections in which meteorites have been systematically declared, the CSC is characterized by an overabundance of H and LL chondrites (Table 4). Non-OC meteorites account for 3.7% of the CSC, including 15 mesosiderites, one eucrite, and one iron meteorite (for meteorites >20 g, before pairing). Similar to the other reference collections (modern falls, Antarctic, Oman), the most abundant types in the CSC are H5 and L6 chondrites, with 149 and 92 samples >20 g, respectively, accounting for 60.8% of H chondrites, and 80.7% of L chondrites, before pairing.

Pairing of equilibrated ordinary chondrites was estimated using the pairing model described above. Figure 10 displays the distribution obtained for the pairing factor P among LL, L, and H chondrites of the CSC. We calculated the mean pairing likelihood factor P for each group (Table 3). The number of meteorites after pairing was estimated by simply multiplying the total number of meteorites in a given group by the corresponding mean value of P. The obtained numbers of 22 LL chondrites, 61 L chondrites, and 156 H chondrites are comparable to the results given by the clustering algorithm (34 LL chondrites, 78 L chondrites, and 189 H chondrites).

19455100, 0, Downloaded from https://onlinelibrary.wiley.com/doi/10.1111/maps.14307 by Cnu Marseille Ap-Hm/Aix-Marseille Universite Direction Du Scd, Wiley Online Library on [13/01/2025]. See the Terms and Conditions (https://onlinelibrary.wiley.com/terms-and-conditions) on Wiley Online Library for rules of use; OA articles are governed by the applicable Creative Commons License

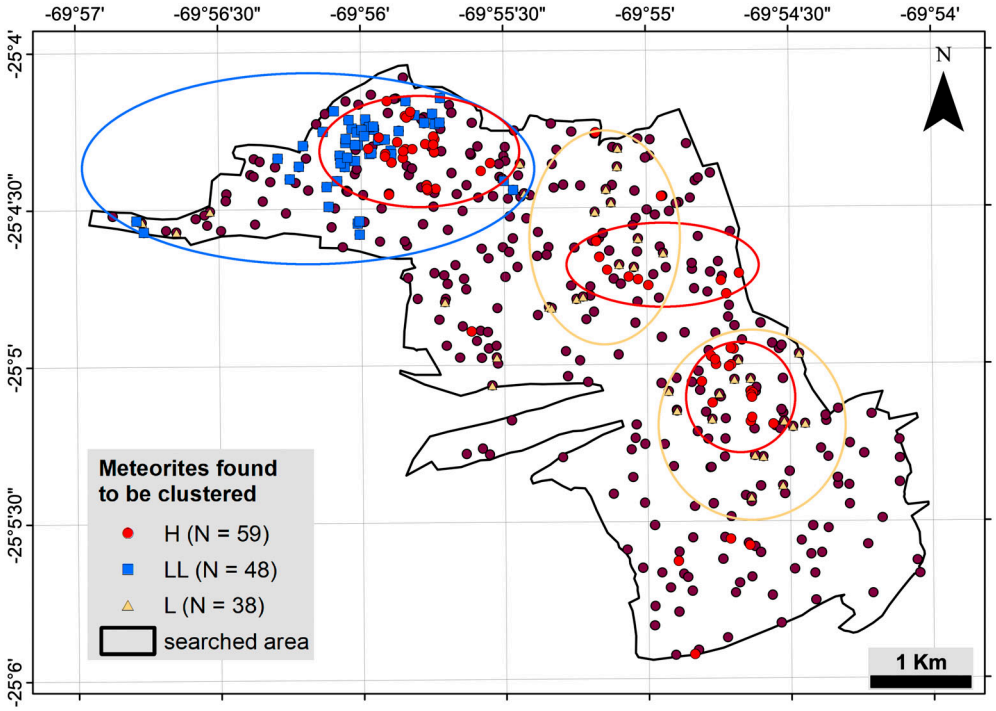

FIGURE 6. Clusters of ordinary chondrites. All meteorites >20 g are shown here, and those recognized as being too close to each other by ASCI are shown in color. Ellipses highlight potential meteorite strewn fields.

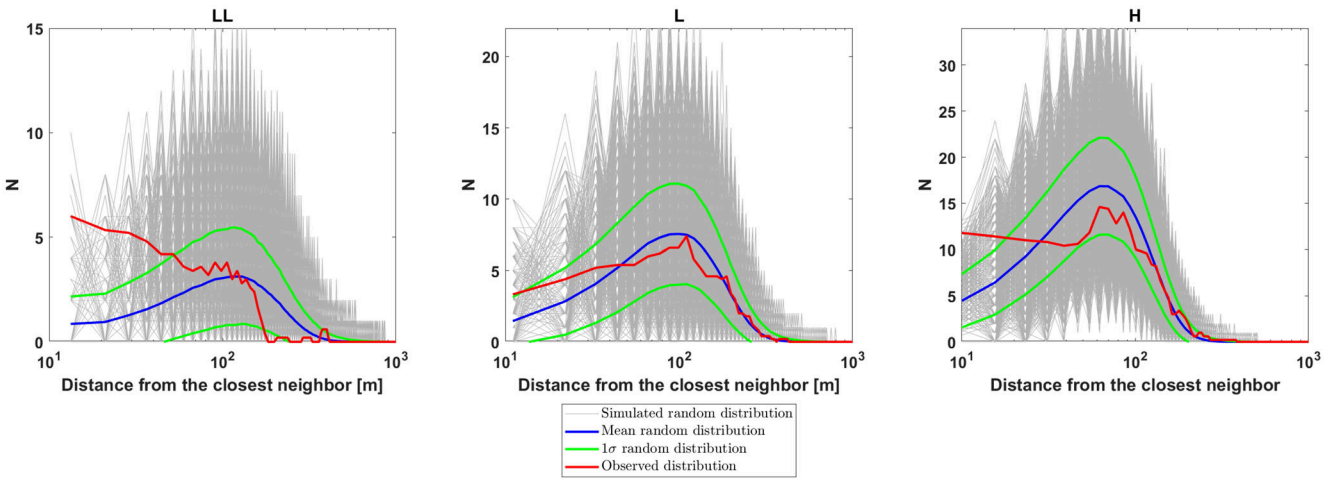

FIGURE 7. Distribution of the observed distance between each meteorite and its closest neighbor within each group (LL, L, and H). Also shown is the simulated random distribution of the same meteorite population across the searched area, iterated 10,000 times. The average distribution and standard deviation over the 10,000 simulations are displayed.

The small number of unequilibrated ordinary chondrites in the CSC (six L3 chondrites and four H3 chondrites) allowed pairing assessment pair by pair, resulting in the tentative pairing of Catalina 815 and Catalina 817 (L3) and Catalina 818 and Catalina 819 (H3). Fifteen mesosiderites >20 g were found in the CSC. Since mesosiderites represent only 0.56% of modern falls (MBDB), pairing is very likely and was assessed pair by pair using petrographic criteria. Catalina 611 (mesosiderite-A3) differs from other mesosiderites in the CSC by a different texture with exsolution lamellae in pyroxene, different pyroxene composition (Fs39Wo3), and higher magnetic susceptibility (logχ=5.70), suggesting that it represents a different meteorite fall. Catalina 399 (mesosiderites-B2) also differs in texture and composition from the other mesosiderites in the CSC and is not likely

19455100, 0, Downloaded from https://onlinelibrary.wiley.com/doi/10.1111/maps.14307 by Cnu Marseille Ap-Hm/Aix-Marseille Universite Direction Du Scd, Wiley Online Library on [13/01/2025]. See the Terms and Conditions (https://onlinelibrary.wiley.com/terms-and-conditions) on Wiley Online Library for rules of use; OA articles are governed by the applicable Creative Commons License

TABLE 2. Ordinary chondrites mass distribution (g) from the CSC, Antarctica, Omani finds, and modern falls.

	CSC OCs	Antarctic OC finds[a]	Omani OC finds[a]	OC falls[a]
Mode	20.0	5.2	62.0	2000
Median	8.75	11.1	185	2580
Mean	31.8	117	1375	22,513
Standard deviation	95.9	2170	12,790	144,331
Minimum	0.31	0.06	0.1	0.1
Maximum	2183	407,000	550,000	4,000,000
Number of meteorites	1577	42,166	4148	966

[a]Data extracted from the Meteoritical Bulletin Database in December 2024.

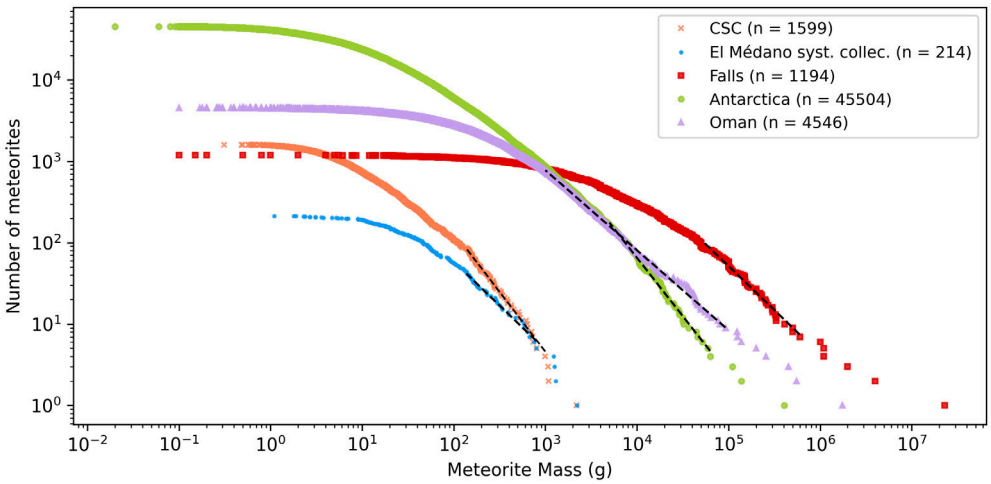

FIGURE 8. Mass distribution of the CSC meteorites (orange crosses, $n = 1599$) on a log–log scale. The linear fit for the mass range from 135 g to 1 kg (dashed line; slope = −1.47; $R^2 = 0.998$) is displayed. Also included are the mass distributions of meteorite falls (red squares), as well as meteorites from Antarctica (green spheres) and Oman (purple triangles) (data from MBDB), and meteorites from the El Médano systematic collection (blue dots) (Hutzler et al., 2016). Dashed lines represent the linear fits for each collection over a specific mass range: Antarctica: mass range, 5–100 kg; slope = −1.43; $R^2 = 0.995$, falls: mass range, 50–900 kg; slope = −1.08; $R^2 = 0.983$, Oman: mass range, 1–100 kg; slope = −0.984; $R^2 = 0.998$, and El Médano: mass range, 135 g to 1 kg; slope = −1.08; $R^2 = 0.987$.

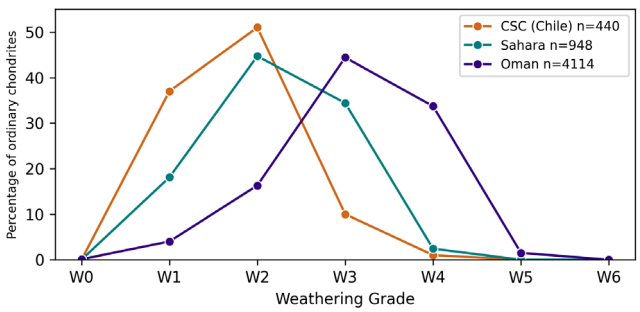

FIGURE 9. Distribution of weathering grade of ordinary chondrites from the CSC (this study), Omani finds, and Sahara finds (Meteoritical Bulletin Database as of December 2024).

paired with them. For the remaining mesosiderites, the following potential pairing groups can be suggested: Catalina 108 and Catalina 581; Catalina 004, Catalina 581, Catalina 589, Catalina 590, Catalina 591, Catalina 610, Catalina 612, Catalina 820, and Catalina 821. Further measurements such as bulk chemistry, terrestrial age, and cosmic ray exposure age can be of use to confirm the pairing of these mesosiderites. The H/L ratio is 2.15 before pairing and 2.56 after pairing, both of which are significantly higher than the H/L ratio of modern falls (0.88), Antarctic meteorites (1.04), and Omani meteorites (1.35). It is also higher than the H/L ratio of 1.22 for meteorites from other extensively searched Chilean DCAs (Calama, Sierra Gorda, and Chug Chug). It is, however, remarkably similar to the 2.13 H/L ratio of the neighboring El Médano collection (Table 4). Although Kouvatsis and Hofmann (2020) suggested that the H/L ratio is mass dependent and decreases with increasing masses, this observation is not relevant for the CSC. Indeed, in their study, the H/L ratios are constant over the mass range 10 g–1 kg, a range that includes 99% of the meteorites

19455100, 0, Downloaded from https://onlinelibrary.wiley.com/doi/10.1111/maps.14307 by Cnu Marseille Aix-Hmi/Aix-Marseille Universite Direction Du Scd, Wiley Online Library on [13/01/2025]. See the Terms and Conditions (https://onlinelibrary.wiley.com/terms-and-conditions) on Wiley Online Library for rules of use; OA articles are governed by the applicable Creative Commons License

TABLE 3. Relative abundances by groups and types for meteorites >20 g from the CSC.

Classification	Number	Abundance (%)	Mean P[a]	Number after pairing	Abundance after pairing (%)
H	245	53.6	0.369	156	63.2
H3	4	1.63		3	1.92
H4	2	0.81		2	1.28
H5	149	60.8		94	60.3
H6	73	29.8		46	29.5
H5-6	15	6.12		9	5.77
H3-5	1	0.41		1	0.64
H3-6	1	0.41		1	0.64
L	114	25.0	0.480	61	24.7
L3	6	5.26		5	8.20
L4	1	0.88		1	1.64
L5	14	12.3		7	11.5
L6	92	80.7		47	77.1
L5-6	1	0.88		1	1.64
LL	81	17.7	0.732	22	8.91
LL3	0	0.00		0	0.00
LL4	0	0.00		0	0.00
LL5	73	90.1		19	86.4
LL6	7	8.64		2	9.1
LL5-6	1	1.23		1	4.6
Mesosiderite	15	3.28		6	2.43
Iron	1	0.22		1	0.40
HED	1	0.22		1	0.40
Total number	457			247	
H/L ratio	2.15			2.56	

Note: For the petrologic type, abundance is within the group.
[a]Mean P was calculated separately for H, L, and LL chondrites.

TABLE 4. Relative abundances of meteorite groups and types in the CSC before and after pairing, El Médano (Chile), Calama area (Chile), Oman, Antarctica, and falls.

Abundance (%)							
Type	CSC		El Médano[a]	Calama[b]	Oman[b]	Antarctic[b]	Falls[b]
H	53.6	63.2	62.9	52.4	49.9	40.7	32.1
H5	60.8	60.3	46.3	63.1	39.9	40.8	49.3
H6	29.8	29.5	21.6	16.8	22.9	30.0	24.1
L	25.0	24.7	29.6	42.8	37.1	39.1	36.7
L5	12.3	11.5	6.3	32.0	26.1	39.5	22.5
L6	80.7	77.1	74.6	60.7	56.0	49.4	65.0
LL	17.7	8.91	4.70	2.42	4.53	12.8	8.90
HED	0.22	0.40	0.00	0.31	1.54	1.85	5.59
CC	0.00	0.00	1.90	1.16	1.30	2.98	4.31
Iron	0.22	0.40	0.00	0.18	0.02	0.45	3.91
H/L	2.15	2.56	2.13	1.22	1.35	1.04	0.88
N total	457	247	213	1117	4545	45,509	1252

Note: For the petrologic type, abundance is within the group.
[a]Hutzler et al. (2016).
[b]Data from the MBDB (as of December 2024). Calama meteorites encompass all meteorites from the Calama, Sierra Gorda, and Chug Chug DCA.

classified in the CSC. Moreover, although a detailed discussion is beyond the scope of our study, an updated data set extracted from the MBDB as of December 2024 does not show any dependence of the H/L ratio with mass over the 20 g–10 kg range, neither for falls nor for meteorites from Chile, Libya, and Oman. The

19455100, 0, Downloaded from https://onlinelibrary.wiley.com/doi/10.1111/maps.14307 by Cnu Marseille Ap-Hm/Aix-Marseille Universite Direction Du Scd, Wiley Online Library on [13/01/2025]. See the Terms and Conditions (https://onlinelibrary.wiley.com/terms-and-conditions) on Wiley Online Library for rules of use; OA articles are governed by the applicable Creative Commons License

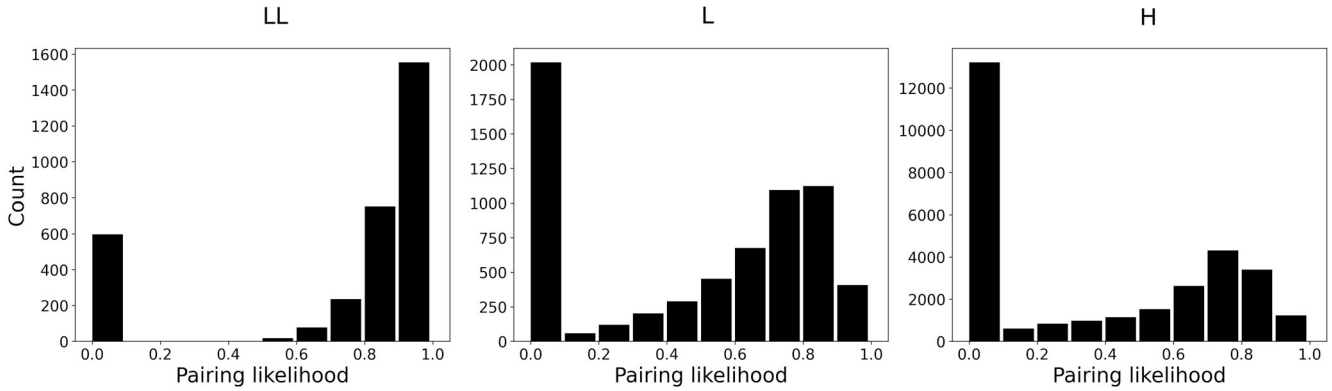

FIGURE 10. Distribution of the pairing likelihood factor P for LL, L, and H chondrites in the CSC zone for meteorites >20 g, estimated using the pairing code.

overabundance of LL chondrites compared to all other collections (Table 4) is due to the large number of LL5, and persists after pairing, suggesting that our pairing estimate for these meteorites is slightly too conservative. The deficit of HED achondrites in the CSC compared to Oman, Antarctic, and falls collections (Table 4) can be explained by the difficulty in identifying these metal-poor meteorites on the ground when their fusion crust has been abraded because of the presence of numerous terrestrial igneous rocks at the surface. A similar deficit was observed in the El Médano collection (Hutzler et al., 2016). The absence of carbonaceous chondrites in the CSC can be attributed to their fragility and friability, which make them more susceptible to abrasion by wind and sand, the primary driver of meteorite disappearance in the Atacama Desert. This vulnerability reduces their life expectancy at the surface compared to other meteorites, resulting in their lower abundance in old meteorite collections. Finally, the relative scarcity of iron meteorites in the CSC, compared to other world collections could be attributed to their high specific gravity, which causes them to sink and eventually be buried beneath the surface over time (see, e.g., figure 1h in Pinto et al., 2024). Alternatively, it is possible that they were recovered by native peoples in prehistoric and protohistoric times, a practice already documented in other regions of the world (Sparavigna, 2024).

Meteorite Density

The meteorite recovery density is 235 meteorites per km^2 (7.73 kg of meteorites per km^2). The recovery density is higher than in any other hot desert, including the neighboring El Médano DCA which yielded 142 meteorites per km^2 and a mass density of 16.38 kg per km^2 (Hutzler et al., 2016). The mass distribution of the CSC (Figure 8) shows that the population of meteorites <20 g is biased by incomplete recovery. Therefore, we only consider the 457 meteorites >20 g in the following discussion. The recovery density of meteorites >20 g is 67 per km^2. This is lower than in the El Médano DCA which has 100 meteorites >20 g per km^2.

For an accurate estimation of the true meteorite density on the ground, some corrections must be made to account for various recovery biases. The first one involves metal-poor achondrites (mostly HEDs), which are more difficult to spot in the field (see above), iron meteorites, and carbonaceous chondrites. Only one eucrite, one iron meteorite, and no CCs were found among the 457 meteorites >20 g, making up only 0.44% of the CSC, whereas modern falls include 13.82% of HED achondrites, iron meteorites, and carbonaceous chondrites (Table 4). We applied a +13.38% correction factor to take into account this deficit. The second bias involves meteorites missed during systematic research. For each meteorite, we noted the distance between the walking line and the meteorite. Ideally, the meteorites should be found with identical abundances at all distances from the walking lines that are separated by 8 m. However, we note a deficit of meteorites with increasing distance from the line, especially between 2.5 and 4 m from the walking line. In detail, 85% of the meteorites >20 g were found within 2.5 m of the walking line, and only 15% were found in the 2.5–4 m distance interval. If we assume that all meteorites >20 g within 2.5 m of the walking line were recovered, the deficit in the 2.5–4 m interval can be taken into account by applying a +36.0% correction factor to the total number of recovered meteorites >20 g. The third bias is due to the variable efficiency of individual meteorite searchers. A correction was applied for searchers whose number of recovered meteorites was 2σ below the average number. Based on yearly recovery statistics, a correction factor of +26% is calculated to take this effect into account. Overall, we estimated that 94.3% of the meteorites >20 g

19455100, 0, Downloaded from https://onlinelibrary.wiley.com/doi/10.1111/maps.14307 by Cnu Marseille Ap-Hm/Aix-Marseille Universite Direction Du Scd, Wiley Online Library on [13/01/2025]. See the Terms and Conditions (https://onlinelibrary.wiley.com/terms-and-conditions) on Wiley Online Library for rules of use; OA articles are governed by the applicable Creative Commons License

were not recovered during fieldwork despite careful search. The corrected meteorite density on the ground is 131 meteorites >20 g per km^2. After pairing, this density goes down to 71 meteorites >20 g per km^2.

The obtained densities, whatever the mass range and the pairing hypotheses considered, are much higher than in any other hot desert: 0.1 meteorites per km^2 after pairing in Dar al Gani, Libya, 1 meteorite per km^2 in the DCAs of the Sahara (Aboulahris et al., 2019; Schlüter et al., 2002), 2.8 meteorites per km^2 in Saudi Arabia by systematic foot search, 1.1 meteorites per km^2 in Oman through systematic car search, and 7.3 meteorites per km^2 through systematic foot search (Hofmann et al., 2018; Hofmann & Gnos, 2024). However, in specific blowout areas of the Saudi Arabian desert, a density of 150 meteorites per km^2 was found (based on only 21 meteorites found over an area of 0.14 km^2; Hofmann & Gnos, 2024). The meteorite density in the CSC is matched only by the El Médano area that has estimated densities of 181 meteorites >20 g per km^2 before pairing and of 123 meteorites >20 g per km^2 after pairing, with both densities corrected for the same recovery biases considered for the CSC.

CONCLUSION

Through systematic on-foot collection, we recovered a total of 1599 meteorites over a continuous zone of 6.80 km^2 in the Catalina DCA. The meteorite recovery density of 235 meteorites per km^2 (67 meteorites per km^2 for stones >20 g) is the highest ever recorded in hot deserts, even surpassing the neighboring El Médano DCA collection. This confirms that the central depression of the Atacama Desert is by far the densest meteorite collection area in hot deserts.

We classified the 457 meteorites above 20 g. After correcting the recovery density for various recovery biases, we estimated a true meteorite density on the ground of 131 meteorites per km^2 for meteorites >20 g before pairing. We used different approaches to assess the pairing of ordinary chondrites; either involving a clustering algorithm, the distance to the nearest neighbor, or a probabilistic approach utilizing a mathematical model. These methods gave comparable results in terms of number of meteorites after pairing. Using the probabilistic approach, we assessed an average pairing likelihood, yielding a meteorite density on the ground of 71 fall events per km^2 after pairing. In the absence of meteorite concentration mechanisms, we interpret this high density as an indication of an old meteorite population, likely several hundreds of kyr by comparison with the El Médano DCA where an ~700 ka average terrestrial age has been measured (Drouard et al., 2019). This long meteorite accumulation duration is linked to the long-term hyper-aridity and associated surface stability over time scales of several Myr. Despite this long accumulation period, meteorites from the CSC are less weathered on average than in other hot deserts. An old age for the CSC meteorites would also explain the absence of carbonaceous chondrites that are more prone to erosion than other meteorites.

The H/L ratio in the CSC is higher than in meteorites from other hot deserts, Antarctica, and falls, but similar to the El Médano collection. This is an indication that the composition of the meteorite flux may have varied over the last Myr. Future work involving measurement of the terrestrial ages of the Catalina meteorite collection will help constrain these possible variations.

Acknowledgments—We would like to thank all the people, in addition to the authors, who contributed to the meteorite collection in the CSC area throughout the search campaigns in 2017, 2019, 2022, 2023, and 2024, namely, Jolantha Eschrig, Luigi Folco, Anna Musolino, Chloé Brillatz, Camille Cartier, Marine Ciocco, Foteini Vervelidou, Gabriel Pinto, Kevin Soto, Louna Perez, Anthony Lagain, Lisa Krämer Ruggiu, Katie Joy, Pierre-Marie Zanetta, Lionel Vacher, Audrey Bouvier Nicolas Carcamo, Hamed Pourkhorsandi, Maud Boyet, Pierre Beck, Alexis Drouard, Yves Marrocchi, Maria-Eugenia Varela, Laura Flores, Alexandra Roussopoulos, and Julien Magre. We are grateful to the Meteoritical Society for the Research Grant awarded in 2023 to the first author.

Data availability statement—The data that support the findings of this study are available in Meteoritical Bulletin Database at https://www.lpi.usra.edu/meteor/metbull.php. Name of meteorites are listed in the manuscript.The pairing code used in this paper is available online on GitHub at https://github.com/csadaka2/ordinary_chondrites_pairing.

Editorial Handling—Righter, Kevin

REFERENCES

Aboulahris, M., Chennaoui Aoudjehane, H., Rochette, P., Gattacceca, J., Jull, T., Laridhi Ouazaa, N., Folco, L., and Buhl, S. 2019. Characteristics of the Sahara as a Meteorite Recovery Surface. *Meteoritics & Planetary Science* 54: 2908–28. https://doi.org/10.1111/maps.13398.

Al-Kathiri, A., Hofmann, B. A., Jull, A. J. T., and Gnos, E. 2005. Weathering of Meteorites from Oman: Correlation of Chemical and Mineralogical Weathering Proxies With14C Terrestrial Ages and the Influence of Soil Chemistry. *Meteoritics & Planetary Science* 40: 1215–39. https://doi.org/10.1111/j.1945-5100.2005.tb00185.x.

Andronov, L., Orlov, I., Lutz, Y., Jean-Luc Vonesch, J.-L., and Klaholz, B. P. 2016. ClusterViSu, a Method for Clustering of Protein Complexes by Voronoi Tessellation in Super-Resolution Microscopy. *Scientific Reports* 6 (24084): 2045–2322. https://doi.org/10.1038/srep24084.

19455100, 0, Downloaded from https://onlinelibrary.wiley.com/doi/10.1111/maps.14307 by Cnu Marseille Ap-Hm/Aix-Marseille Universite Direction Du Scd, Wiley Online Library on [13/01/2025]. See the Terms and Conditions (https://onlinelibrary.wiley.com/terms-and-conditions) on Wiley Online Library for rules of use; OA articles are governed by the applicable Creative Commons License

Belhai, D. 2023. Spatial Distribution and Classification of Algerian Meteorites: Qualitative and Quantitative Inventory. *Journal of African Earth Sciences* 207: 105058. https://doi.org/10.1016/j.jafrearsci.2023.105058.

Benedix, G. K., Keil, K., and Murakami, J. Y. 1999. Classification of Ten New Nullarbor Region Meteorites. *Meteoritics & Planetary Science* 34: 813–15. https://doi.org/10.1111/j.1945-5100.1999.tb01395.x.

Benoit, P. H., Sears, D. W. G., Akridge, J. M. C., Bland, P. A., Berry, F. J., and Pillinger, C. T. 2000. The Non-Trivial Problem of Meteorite Pairing. *Meteoritics & Planetary Science* 35: 393–417. https://doi.org/10.1111/j.1945-5100.2000.tb01785.x.

Carretier, S., Tolorza, V., Regard, V., Aguilar, G., Bermúdez, M. A., Martinod, J., Guyot, J.-L., Hérail, G., and Riquelme, R. A. 2018. Review of Erosion Dynamics along the Major N-S Climatic Gradient in Chile and Perspectives. *Geomorphology* 300(January): 45–68. https://doi.org/10.1016/j.geomorph.2017.10.016.

Clarke, J. D. A. 2006. Antiquity of Aridity in the Chilean Atacama Desert. *Geomorphology* 73: 101–114. https://doi.org/10.1016/j.geomorph.2005.06.008.

Devillepoix, H. A. R., Sansom, E. K., Shober, P., Anderson, S. L., Towner, M. C., Lagain, A., Cupák, M., et al. 2022. Trajectory, Recovery, and Orbital History of the Madura Cave Meteorite. *Meteoritics & Planetary Science* 57: 1328–38. https://doi.org/10.1111/maps.13820.

Drouard, A. J., Gattacceca, A., Hutzler, P., Rochette, R., Braucher, D., Bourlès, M., Gounelle, M., et al. 2019. The Meteorite Flux of the Past 2 m.y. Recorded in the Atacama Desert. *Geology* 47: 673–76. https://doi.org/10.1130/g45831.1.

Dunai, T. J., González López, G. A., and Juez-Larré, J. 2005. Oligocene–Miocene Age of Aridity in the Atacama Desert Revealed by Exposure Dating of Erosion-Sensitive Landforms. *Geology* 33: 321. https://doi.org/10.1130/g21184.1.

Espinoza, G. F., Matthews, S. J., Cornejo, P. P., and Venegas, B. C. 2011. Carta Catalina-Región de Antofagasta. Serie Geologìa Bàsica. Subdirección Nacional De Geología.

Folco, L., Rochette, P., Gattacceca, J., and Perchiazzi, N. 2006. In Situ Identification, Pairing, and Classification of Meteorites from Antarctica through Magnetic Susceptibility Measurements. *Meteoritics & Planetary Science* 41: 343–353. https://doi.org/10.1111/j.1945-5100.2006.tb00467.x.

Gattacceca, J., Eisenlohr, P., and Rochette, P. 2004. Calibration of Situ Magnetic Susceptibility Measurements. *Geophysical Journal International* 158: 42–49. https://doi.org/10.1111/j.1365-246x.2004.02297.x.

Gattacceca, J., Valenzuela, M., Uehara, M., Jull, T., Giscard, M. D., Rochette, P., Braucher, R., et al. 2011. The Densest Meteorite Collection Area in Hot Deserts: The San Juan Meteorite Field (Atacama Desert, Chile). *Meteoritics & Planetary Science* 46: 1276–87. https://doi.org/10.1111/j.1945-5100.2011.01229.x.

Gnos, E., Lorenzetti, S., Eugster, O., Jull, T., Hofmann, B. A., Al-Kathiri, A., and Eggimann, M. 2009. The Jiddat al Harasis 073 Strewn Field, Sultanate of Oman. *Meteoritics & Planetary Science* 44: 375–387. https://doi.org/10.1111/j.1945-5100.2009.tb00739.x.

Hofmann, B. A., and Gnos, E. 2024. *The Meteoritic Record of Arabia*. Geological Society London Special Publications 550 (1). Geological Society of London: SP550-2024-8. https://doi.org/10.1144/sp550-2024-8.

Hofmann, B. A., Gnos, E., Jull, T., Szidat, S., Majoub, A., Al Wagdani, K., Habibullah, S. N., et al. 2018. Meteorite Reconnaissance in Saudi Arabia. *Meteoritics & Planetary Science* 53: 2372–94. https://doi.org/10.1111/maps.13132.

Houston, J., and Hartley, A. J. 2003. The Central Andean West-Slope Rainshadow and its Potential Contribution to the Origin of Hyper-Aridity in the Atacama Desert. *International Journal of Climatology* 23: 1453–64. https://doi.org/10.1002/joc.938.

Hutzler, A., Gattacceca, J., Rochette, P., Braucher, R., Carro, B., Christensen, E., Cournede, C., et al. 2016. Description of a Very Dense Meteorite Collection Area in Western Atacama: Insight into the Long-Term Composition of the Meteorite Flux to Earth. *Meteoritics & Planetary Science* 51: 468–482. https://doi.org/10.1111/maps.12607.

Kouvatsis, I., and Hofmann, B. A. 2020. A Statistical Analysis of the H/L Ratio of Ordinary Chondrite Finds and Falls: A Comparison of Oman Finds with Other Populations. *Meteoritics & Planetary Science* 55: 67–76. https://doi.org/10.1111/maps.13410.

Lagain, A., Servis, K., Benedix, G., Norman, C., Anderson, S., and Bland, P. A. 2021. Model Age Derivation of Large Martian Impact Craters, Using Automatic Crater Counting Methods. *Earth and Space Science*,8: ae2020EA001598. https://doi.org/10.1029/2020ea001598.

McKay, C. P., Molaro, J. L., and Marinova, M. M. 2009. High-Frequency Rock Temperature Data from Hyper-Arid Desert Environments in the Atacama and the Antarctic Dry Valleys and Implications for Rock Weathering. *Geomorphology* 110: 182–87. https://doi.org/10.1016/j.geomorph.2009.04.005.

Pfeiffer, M., Morgan, A. M., Heimsath, A. M., Jordan, T. E., Howard, A. D., and Amundson, R. 2021. Century Scale Rainfall in the Absolute Atacama Desert: Landscape Response and Implications for Past and Future Rainfall. *Quaternary Science Reviews* 254: 106797. https://doi.org/10.1016/j.quascirev.2021.

Pinto, G. A., Tavernier, A., Gattacceca, J., Corgne, A., Valenzuela, M., Luais, B., Flores, L., Olivares, F., and Marrocchi, Y. 2024. Dense Collection Areas and Terrestrial Alteration of Meteorites in the Atacama Desert. *Meteoritics & Planetary Science* 59: 351–367. https://doi.org/10.1111/maps.14125.

Pourkhorsandi, H., Gattacceca, J., Rochette, P., D'Orazio, M., Kamali, H., Avillez, R., Letichevsky, S., et al. 2019. Meteorites from the Lut Desert (Iran). *Meteoritics & Planetary Science* 54: 1737–63. https://doi.org/10.1111/maps.13311.

Rochette, P., Gattacceca, J., and Lewandowski, M. 2012. Magnetic Classification of Meteorites and Application to the Soøtmany Fall. *Meteoritics & Planetary Science* 2: 67–71. https://doi.org/10.5277/met120108.

Rochette, P., Sagnotti, L., Bourot-Denise, M., Consolmagno, G., Folco, L., Gattacceca, J., Osete, M. L., and Pesonen, L. 2003. Magnetic Classification of Stony Meteorites: 1. Ordinary Chondrites. *Meteoritics & Planetary Science* 38: 251–268. https://doi.org/10.1111/j.1945-5100.2003.tb00263.x.

Schlüter, J., Schultz, L., Thiedig, F., Al-Mahdi, B. O., and Abu Aghreb, A. E. 2002. The Dar al Gani Meteorite Field (Libyan Sahara): Geological Setting, Pairing of Meteorites, and Recovery Density. *Meteoritics & Planetary Science* 37: 1079–93. https://doi.org/10.1111/j.1945-5100.2002.tb00879.x.

19455100, 0, Downloaded from https://onlinelibrary.wiley.com/doi/10.1111/maps.14307 by Cha Marseille Ap-Hm/Aix-Marseille Universite Direction Du Scd, Wiley Online Library on [13/01/2025]. See the Terms and Conditions (https://onlinelibrary.wiley.com/terms-and-conditions) on Wiley Online Library for rules of use; OA articles are governed by the applicable Creative Commons License

Scott, E. R. D. 1984. Pairing of Meteorites Found in Victoria Land, Antarctica. *Memoirs of National Institute of Polar Research* 35: 102–125.

Sparavigna, A. C. 2024. Meteoric Iron in Ancient Egyptian and Chinese Cultures, from Pyramids to Circumpolar Stars. *SSRN Electronic Journal*. https://doi.org/10.2139/ssrn.4113311.

Tapia, J., González, R., Townley, B., Oliveros, V., Álvarez, F., Aguilar, G., Menzies, A., and Calderón, M. 2018. Geology and Geochemistry of the Atacama Desert. *Antonie Van Leeuwenhoek* 111: 1273–91. https://doi.org/10.1007/s10482-018-1024-x.

Van Ginneken, M., Wozniakiewicz, P. J., Brownlee, D. E., Debaille, V., Corte, V. D., Delauche, L., Duprat, J., et al. 2024. Micrometeorite Collections: A Review and their Current Status. *Philosophical Transactions of the Royal Society a Mathematical Physical and Engineering Sciences* 382: 20230195. https://doi.org/10.1098/rsta.2023.0195.

Van Schmus, W. R., and Wood, J. A. 1967. A Chemical-Petrologic Classification for the Chondritic Meteorites. *Geochimica et Cosmochimica Acta* 31. Elsevier BV: 747–765. https://doi.org/10.1016/s0016-7037(67)80030-9.

Wlotzka, F. 1993. A Weathering Scale for the Ordinary Chondrites (Abstract). *Meteoritics* 28: 460.

Zekollari, H., Goderis, S., Debaille, V., Van Ginneken, M., Gattacceca, J., Jull, T., Lenaerts, J. T. M., Yamaguchi, A., Huybrechts, P., and Claeys, P. 2019. Unravelling the High-Altitude Nansen Blue Ice Field Meteorite Trap (East Antarctica) and Implications for Regional Palaeo-Conditions. *Geochimica et Cosmochimica Acta* 248: 289–310. https://doi.org/10.1016/j.gca.2018.12.035.

Zeng, X., Li, S., Leya, I., Wang, S., Smith, T., Li, Y., and Wang, P. 2018. The Kumtag 016 L5 Strewn Field, Xinjiang Province, China. *Meteoritics & Planetary Science* 53: 1113–30. https://doi.org/10.1111/maps.13073.

Zolensky, M., Bland, P., Brown, P., and Halliday, I. 2006. Flux of Extraterrestrial Materials. In *Meteorites and the Early Solar System II*, edited by D. S. Lauretta & H. Y. McSween Jr., 853–896. University of Arizona Press.

Zolensky, M. E., Wells, G. L., and Rendell, H. M. 1990. The Accumulation Rate of Meteorite Falls at the Earth's Surface: The View from Roosevelt County, New Mexico. *Meteoritics* 25: 11–17. https://doi.org/10.1111/j.1945-5100.1990.tb00965.x.

Zurfluh, F. J., Hofmann, B. A., Gnos, E., Eggenberger, U., and Jull, A. J. T. 2016. Weathering of Ordinary Chondrites from Oman: Correlation of Weathering Parameters With14C Terrestrial Ages and a Refined Weathering Scale. *Meteoritics & Planetary Science* 51: 1685–1700. https://doi.org/10.1111/maps.12690.

SUPPORTING INFORMATION

Additional supporting information may be found in the online version of this article.

Table S1. Intra-meteorite variability of magnetic susceptibility.

Table S2. Intra-strewnfield variability of silicate composition in equilibrated ordinary chondrites.

19455100, 0, Downloaded from https://onlinelibrary.wiley.com/doi/10.1111/maps.14307 by Cnu Marseille Ap-Hm/Aix-Marseille Universite Direction Du Scd, Wiley Online Library on [13/01/2025]. See the Terms and Conditions (https://onlinelibrary.wiley.com/terms-and-conditions) on Wiley Online Library for rules of use; OA articles are governed by the applicable Creative Commons License

2.4. Conclusion

This study confirms that the Atacama Desert hosts exceptionally high meteorite densities, making it a unique environment for meteorite preservation and recovery. The Catalina Dense Collection Area (DCA) shows a meteorite density only matched by the neighboring El Médano DCA, both exceeding values reported from other hot deserts by orders of magnitude.

The discrepancy observed in the H/L ratios of falls, Atacama, Antarctic, and other hot desert collections could reflect temporal variations in the composition of the meteorite flux, since these collections have different average terrestrial ages.

A follow-up study to this work is the measurement of terrestrial ages of meteorites from the CSC and other DCAs of the Atacama, which, combined with corrected density estimates, will help to reconstruct the long-term meteorite flux to Earth (Chapter 3 and 4).

Chapter three

Terrestrial ages of Atacama meteorites: insight into the past meteorite flux to Earth over the last 2 Myr



Curiosity is not a sin…But we should exercise caution with our curiosity… yes, indeed.
— Albus Dumbledore

Chapter summary

3. ***Chapter 3***

100

3.1. Introduction 100

3.1.1. Flux of extraterrestrial material to Earth 100

3.1.2. Terrestrial ages 102

3.1.3. Accelerator Mass Spectrometry 103

3.1.4. Chlorine-36 104

3.2. Article summary 106

3.3. Article 106

3.4. Conclusion 206

3. Chapter 3

3.1. Introduction

3.1.1. Flux of extraterrestrial material to Earth

Earth is not an isolated body in space but is constantly hit by extraterrestrial material originating from asteroids, comets, and planets. Sizes span across a wide range, from micrometer-sized dust particles, through centimeter–meter scale meteoroids, and to, thankfully rare, kilometer-sized impactors. The mass flux is dominated by smallest particles with fluxes decreasing steeply with increasing size (Taylor et al. 1998; Love and Brownlee 1993; Zolensky et al. 2006) .

In Chapter 1, we saw that the transfer of extraterrestrial material to Earth is governed by a combination of collisional, dynamical, and orbital processes that depend on particle size (Bottke 2000; Bottke et al. 2015; Morbidelli and Vokrouhlický 2003). In brief, micrometer to centimeter-sized particles, such as Interplanetary Dust Particles (IDPs) and micrometeorites, are influenced by the Poynting-Robertson drag, which causes them to spiral slowly towards the Sun and intersect Earth's orbit. Centimeter- to meter-sized meteoroids are affected by thermal forces, mainly the Yarkovsky effect (Farinella et al. 1998) and the Yarkovsky-O'Keefe-Radzievskii-Paddack (YORP) effect (Rubincam 2000), which slowly drifts meteoroids into strong resonances, mainly the ν6 secular resonance (at ~2.1 AU), mean-motion resonances (3:1, 5:2, 7:3, 2:1), that define Kirkwood gaps and inject them straight into Earth-crossing trajectories. Moreover, gravitational interactions with planets, particularly Jupiter, can also modify their orbits. For kilometer-scale bodies, gravitational interactions with planets are the main factor affecting their orbits, while thermal effects are relatively negligible, so such impacts on Earth are relatively rare (Bottke et al. 2006; Vokrouhlický et al. 2015).

In the following, I present the estimated fluxes at different particle sizes and the methods used for their determination.

3.1.1.1. Large impactors

Upon atmospheric entry, objects larger than a few tens of meters create impact craters at the surface of the Earth with little or no preservation of the original extraterrestrial material. Impact structures constitute, therefore, a valuable record for assessing the past flux of large impactors (Farinella et al. 1998). However, there are currently only 205 confirmed impact structures on Earth (Lagain et al. 2022). This number is many orders of magnitude lower than the number of craters on the surfaces of the Moon or Mars. This is due to erosion (in the case of continental craters), sedimentation (in the case of oceanic craters), and tectonic activity, with all these processes blurring Earth records older than a few hundred million years. Nonetheless, impact-induced features, such as tektites (Glass 2002), shocked minerals (French 1999), and platinum group elemental anomalies, like the iridium spike at the K-Pg boundary (Alvarez et al. 1980),

help estimate impact rates over time. Independently, the Moon's cratering record offers a longer-term perspective on impact events. In fact, the lunar surface, lacking atmospheric and tectonic activity, preserves a much more complete record of impacts within the shared Earth-Moon environment (Joy et al. 2016; Lagain et al. 2021; 2022; Mazrouei et al. 2019).

3.1.1.2. Interplanetary dust particles and micrometeorites

Dust particles smaller than ~5 mm, originating from collision of asteroids or ejection from active comets (Farley et al. 2012) and entering the atmosphere, can either undergo complete ablation upon atmospheric entry, survive as an unmelted micrometeorite (if the melting temperature is not reached), or reach the surface as a cosmic spherule (partially or completely melted), depending on the mass, velocity and radiant of the particle. They may be preserved at the surface or in the geological record and thus provide invaluable data for assessing present and past flux patterns. Such particles can be collected in the form of Interplanetary Dust Particles (IDPs) in the stratosphere or on rooftops, while larger ones are collected as micrometeorites or cosmic spherules in polar ice in Antarctica and deep-sea sediments (see references hereafter).

Many geochemical techniques combined with spacecraft data and models can be used to constrain both pre-ablation (top-of-the-atmosphere) and post-ablation (at the surface) extraterrestrial dust flux to Earth.

For the current flux, Love and Brownlee (1993) estimated a mass flux using hypervelocity impact craters on the space-facing end of the Long Duration Exposure Facility (LDEF) satellite. They found a peak contribution of particles ~200 μm and an accretion rate of 40 000 ± 20 000 tons per year.

Using the South Pole water well (SPWW) micrometeorite collection in Antarctica, Taylor et al. (1998) estimated a present-day global accretion rate of ~1600 ± 300 tons per year of melted micrometeorites (cosmic spherules) in the 50-700 μm range, and showed that ~90% of the mass of sub-millimeter particles are lost during entry.

More recently, Carrillo-Sánchez et al. (2020) studied the accretion rate of cosmic dust by combing an ablation model with a zodiacal cloud model and estimated a pre-atmospheric flux of ~10 000 ± 3 000 tons per year across all sizes, with 30% of particles ablated by heating and deceleration. They also show that particles larger than 87.5 μm are more likely to ablate, while smaller particles tend to survive as micrometeorites.

Based on the micrometeorite collection in the vicinity of the CONCORDIA Station at Dome C in Antarctica, Rojas et al. (2021) determined a global flux of 1600 ± 500 ton per year of micrometeorites in the size range 12-700 μm at Earth's surface and infer a pre-ablation total of 15 000 tons per year. In fact, the atmosphere filters out most of the incoming dust, where the majority of particles are destroyed during atmospheric entry and arrive at the surface as nanoparticles ("meteorite smoke").

Independently, Fénisse et al. (2025) estimated a global ET mass flux of particles < 100 μm of 3500 ± 500 tons per year through measurements of ^{3}He in cosmic dust extracted from clean snow from the Concordia station (Dome C, Antarctica).

Past fluxes can be determined using fossil micrometeorites preserved in sedimentary rocks (Voldman et al. 2013; Genge et al. 2020) or using Os concentrations and $^{187}Os/^{186}Os$ isotopic

ratios in deep-sea and continental deposits, which yielded a total flux range of 49 000–56 000 tons per year (Esser and Turekian 1988).

3.1.1.3. Meteorites

Meteorites are centimeter- to meter-scale objects that survive atmospheric entry and reach the Earth's surface. Estimating the meteorite flux provides better insight into the delivery mechanisms of meteoroids from the Main Asteroid Belt to Earth and assesses potential hazards.

Ground-based cameras, Doppler weather radars, meteor radars, satellites, and meteorite recovery assisted by radar and camera data yield a comprehensive estimate of the current meteorite flux (e.g., Bland et al., 2012; Devillepoix et al., 2018; Colas et al., 2020; Jones et al., 2005). Using observations of fireballs with the Canadian Meteorite Observation and Recovery Project (MORP), Halliday et al. (1989) estimated a total mass of ~53.8 tons per year of meteorites in the 10 g to 1 t mass range. The present-day meteorite flux, as represented by observed falls, is dominated by ordinary chondrites, which account for ~78% of meteorites in the MBDB.

The long-term meteorite paleoflux is assessed through fossil meteorites and extraterrestrial spinel grains embedded in sedimentary layers, from the Late Cambrian to the Early Paleocene (e.g., Farley et al., 2006; Schmitz et al., 2001; 2017; Terfelt and Schmitz (2021).

On intermediate timescales, the past meteorite flux is inferred through accumulation sites in cold and hot deserts, usually through a combination of pairing-corrected density estimations with terrestrial ages measurements (Evatt et al. 2020; Zolensky et al. 2006; Drouard et al. 2019).

In this chapter, I present an article, submitted to *Meteoritics & Planetary Science* in August 2025, on the meteorite flux to Earth over the past 2 Myr, based on systematic meteorite collections from the Atacama Desert and measurements of meteorite terrestrial ages. The following subsections introduce the terrestrial age notion, the analytical methods used, and details on the cosmogenic nuclide ^{36}Cl.

3.1.2. Terrestrial ages

The terrestrial age, or residence time, of a meteorite is the time elapsed since its fall on Earth. Determining the terrestrial ages of a set of meteorites is essential to studying the past meteorite flux. These ages are most commonly obtained through measurements of cosmogenic radionuclides.

The concentration of ^{14}C or a combination of ^{14}C, ^{10}Be and noble gases (Tauseef et al., 2024; 2025) are used for falls younger than ~50 ka. For older ages, cosmogenic nuclides with longer half-lives are employed, including ^{10}Be, ^{26}Al, ^{36}Cl, ^{41}Ca, ^{53}Mn (Nishiizumi, 1987; Welten et al., 2024). In our study, we use the cosmogenic nuclide ^{36}Cl (see Methods in Article for more details).

3.1.3. Accelerator Mass Spectrometry

Accelerator Mass Spectrometry (AMS) is a highly sensitive analytical technique used in isotopic geochemistry. It allows the measurement of isotopic ratios of cosmogenic nuclides, down to extremely low abundances of ~10^{-15} (Synal 2013).

A major challenge arises from isobaric interferences, where isotopes of different elements have the same mass number but exist at significantly higher natural abundances (e.g., ^{10}B with ^{10}Be, ^{36}S with ^{36}Cl, or ^{26}Mg with ^{26}Al). Conventional mass spectrometry separation techniques (i.e., separation of ions according to their mass-to-charge ratio in magnetic and electrostatic fields), cannot fully manage isobaric interferences. AMS overcomes this by combining traditional magnetic and electrostatic separation with particle accelerator techniques. Ions are accelerated and stripped to high-energy positive charge states, thus eliminating molecular interferences. Subsequent separation of isobars is achieved by differential energy loss in absorbers and ionization detectors, which depend on nuclear charge.



Figure 3.1. Accelerator Mass Spectrometer at the ASTER facility in CEREGE (Aix-en-Provence, France). Credit: ASTER, LN2C laboratory.

Sample preparation follows a similar procedure across nuclides. In brief, a carrier of the element is added, followed by chemical purification and concentration of the target nuclide. The final product is a solid target pressed into a target holder. Negative ions are produced by cesium sputtering, which allows the efficient ionization of the sample and suppresses interferences from elements that cannot form stable negative ions (e.g., ^{36}S in ^{36}Cl). The extracted negative ions are accelerated, stripped of electrons in a foil stripper, and re-accelerated as positive ions, which are then analyzed.

At CEREGE, AMS includes a dedicated 5 MV tandem accelerator named ASTER (Accélérateur pour les Sciences de la Terre, Environnement, Risques) (Figure 3.1). ASTER conducts routine measurements of the isotopic ratios $^{10}Be/^{9}Be$, $^{26}Al/^{27}Al$, and $^{36}Cl/^{35}Cl$ (Arnold et al. 2010).

For ^{10}Be and ^{36}Cl, suppression of isobaric interferences is achieved by using nuclear charge-dependent energy loss in an absorber foil, followed by energy selection using a 35° electrostatic deflector and a 30° vertical magnet (Arnold et al. 2010) . Final separation is performed in a high-resolution, four-anode gas ionization chamber (ΔE1, ΔE2, ΔE3, E-final), where the ΔE−E technique distinguishes ions based on their specific energy loss. Routine analysis of standards and blanks ensures measurement accuracy and reproducibility. For ^{10}Be, the used standard is the NIST SRM 4325, while for ^{36}Cl, the ICN chemical standard is employed as reference.

Given its unique sensitivity and ability to suppress isobars, AMS is the only feasible method for quantifying cosmogenic radionuclides (^{10}Be, ^{26}Al, ^{36}Cl, ^{14}C) in meteorites, making it essential for the determination of exposure histories and terrestrial ages.

3.1.4. Chlorine-36

Cosmogenic ^{36}Cl (half-life of 301.3 ka; Nica et al. 2012) is ideal for terrestrial ages in the 0.05–2 Ma range. For accurate terrestrial age determination, cosmogenic nuclide concentrations must have reached saturation during the transfer of the meteoroid in interplanetary space. This requires an exposure time in space (i.e., cosmic-ray exposure age) greater than approximately five times the radionuclide's half-life in space before entering the terrestrial atmosphere, corresponding to ~97% of the saturation. Indeed, around 97% of ordinary chondrites have CRE ages >1.5 Ma (> $5\times T_{half}$) (Eugster 2003; Graf and Marti 1995), ensuring ^{36}Cl saturation in most samples.

The main pathways for the production of the radionuclide ^{36}Cl are:

- Spallation: high-energy nuclear reactions from target elements heavier than Cl, i.e., mostly Ca, Fe, and Ni
- Muon capture: Muons are highly unstable particles produced in the high atmosphere (thus irrelevant in space) and have higher masses than electrons. ^{36}Cl is produced when a ^{39}K or ^{40}Ca nucleus captures a muon.
- Thermal and epithermal neutron capture (a low-energy reaction) on ^{35}Cl: contributions from neutron capture depend on the size and chemical composition of the studied meteorite and on the Cl content of the analyzed sample, which makes the interpretation of ^{36}Cl data in bulk meteorite samples challenging.

By analyzing the metal fraction (composed of > 99% of Fe and Ni) exclusively, contributions from thermal neutrons are avoided, making the interpretation of ^{36}Cl data much more straightforward because production is only via spallation from Fe and Ni.

Because the atmosphere and the magnetosphere act as a shield, filtering most cosmic rays, the terrestrial production of cosmogenic nuclides is negligible, lower by a factor $<10^{-4}$ than the production in space (see Discussion in article). Therefore, once the meteorite reaches the

Earth's surface, the cosmogenic radionuclide concentrations evolve only through radioactive decay.

In my thesis, I measured ^{36}Cl in the metal phase of meteorite samples using AMS at the ASTER facility. The target samples were prepared as silver chlorine (AgCl) precipitates (~10 mg), pressed into cathodes, and introduced into the accelerator (Figure 3.1). The potential effect of HCl treatment before Cl extraction was tested by Hutzler (2015), who concluded that diluted HCl (0.2 M) does not affect the Cl isotopic composition and is thus suitable for metal purification. The full protocol is detailed in the methods of the paper and in Appendices as well.

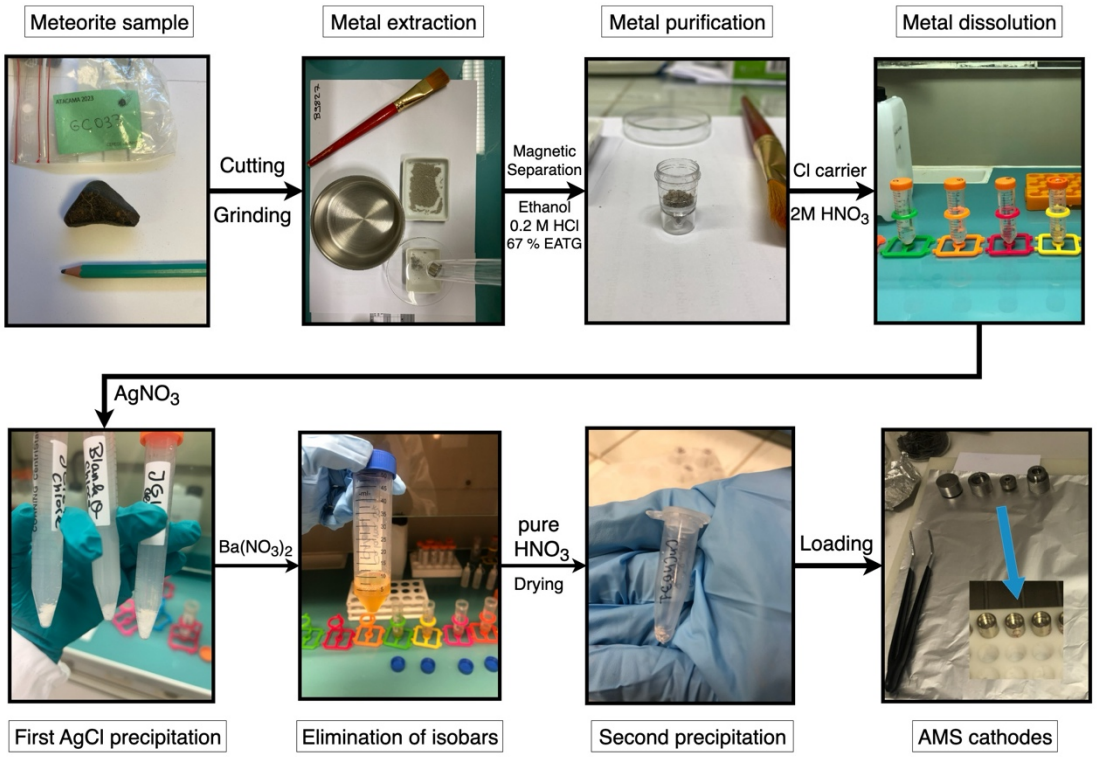

Figure 3.2. Chemical protocol for metal extraction, purification, and AgCl precipitation for ^{36}Cl measurements in the metal phase of meteorites.

For ^{36}Cl specifically, AgCl targets encapsulated in cathodes are sputtered with cesium ions (Cs^+) in the ion source. The collision ionizes Cs^+ into Cs^{2+} and breaks the bonds between AgCl, thus forming Cl^- and Ag^+ ions. The negative ions Cl^- are accelerated into the 5 MV tandem accelerator, stripped of electrons in a thin foil, and re-accelerated as positive ions. Chlorine isotopes are then separated as a function of their mass-to-charge ratios. ^{36}S interferences are subsequently eliminated through absorber foils and filters before final measurement in a multi-anode gas ionization chamber.

The ^{36}Cl-based terrestrial ages are presented in the following article, where we combine density estimates of the Catalina Systematic Collection (Chapter 2) with terrestrial ages to investigate the meteorite flux over the past 2 Myr in terms of intensity and composition.

3.2. Article summary

The Atacama Desert in northern Chile, with its extreme aridity and long-term climatic stability, is one of the most favorable environments on Earth for the preservation of meteorites. In fact, this desert holds the densest and oldest meteorite collections among hot deserts. In this study, we determine the terrestrial ages of 51 ordinary chondrites from the Catalina Systematic Collection (CSC), assembled in a 6.80 km^2 zone of the Catalina Dense Collection Area in the Central Depression of the Atacama. The aim of this study is to reconstruct the past long-term flux of meteorites to Earth over the past 2 Myr.

Terrestrial ages were derived from the concentration of the cosmogenic nuclide ^{36}Cl in the metal fraction of the meteorites. For a subset of the oldest samples, cosmic-ray exposure (CRE) ages were measured using the noble gas ^{21}Ne to assess ^{36}Cl saturation in space. We also discuss potential shielding effects on terrestrial ages.

We show that the CSC meteorite collection is the oldest on Earth with an average terrestrial age approaching 1 Ma (median 750 ka) and some values exceeding 2 Ma. This confirms the exceptional stability of the Atacama Desert surfaces.

By combining terrestrial ages with meteorite density estimates corrected for pairing, we calculated a meteorite flux of 69 ± 8 meteorites >20 g per km^2 per Myr over the past 2 Myr. This value is in broad agreement with flux estimates derived from observed falls, Antarctic collections, and other hot desert collections over shorter timescales (10–100 ka). These results suggest that the intensity of the bulk meteorite flux has remained roughly stable over the last 2 Myr.

Besides the bulk flux, we also investigated the composition of the meteorite flux over the past 2 Myr, by normalizing the abundance of H chondrites to the total number of ordinary chondrites (the most abundant in world collections). We evidence some temporal variations in the composition of the flux with a statistically significant peak of H chondrites between 1200 and 400 ka, followed by a marked decline to present-day values.

This compositional variation is not captured by current dynamical models of meteoroid delivery from the asteroid belt, which mainly consider large asteroid families. We attribute this variability to transient contributions from collisions of relatively small asteroid(s) in a favorable position, i.e., near a resonance. Such collisions would form minor asteroid families that are too small to be detected by current asteroid surveys.

3.3. Article

Sadaka, C., Gattacceca, J., Dumas, F., Braucher, R., ASTER Team, Leya, I., Tauseef, M., Blard, P.-H., Bekaert, D., Füri, E., Zimmermann, L., Lagain, A., Devillepoix, H.A.R. and Gounelle, M. (2026), Terrestrial ages of meteorites from the Atacama Desert (Chile) and insights into the past meteorite flux to Earth. Meteorit Planet Sci. https://doi.org/10.1111/maps.70125

Check for updates

The Meteoritical Society

Meteoritics & Planetary Science 1–20 (2026)
doi: 10.1111/maps.70125

Terrestrial ages of meteorites from the Atacama Desert (Chile) and insights into the past meteorite flux to Earth

Carine SADAKA[1]*, Jérôme GATTACCECA[1], Florian DUMAS[1,2,3], Régis BRAUCHER[1], ASTER Team[1], Ingo LEYA[4], Mohammad TAUSEEF[4], Pierre-Henri BLARD[5], David BEKAERT[5], Evelyn FÜRI[5], Laurent ZIMMERMANN[5], Anthony LAGAIN[1,6,7], Hadrien A. R. DEVILLEPOIX[7], and Matthieu GOUNELLE[8]

[1]Aix-Marseille Université, CNRS, IRD, INRAE, CEREGE, Aix-en-Provence, France
[2]Laboratoire G-Time, Université Libre de Bruxelles, Brussels, Belgium
[3]AMGC, Vrije Universiteit Brussel, Brussel, Belgium
[4]Space Sciences and Planetology, University of Bern, Bern, Switzerland
[5]Centre de Recherches Pétrographiques et Géochimiques, CNRS, Université de Lorraine, Nancy, France
[6]Institut ORIGINES, Aix-Marseille Univ, Marseille, France
[7]Space Science and Technology Centre, School of Earth and Planetary Sciences, Curtin University, Perth, Western Australia, Australia
[8]Muséum National d'Histoire Naturelle, Institut de minéralogie, de physique des matériaux et de cosmochimie—UMR7590, Paris, France

***Correspondence**
Carine Sadaka, CNRS, IRD, INRAE, CEREGE, Aix-Marseille Univ, Aix-en-Provence, France.
Email: sadaka@cerege.fr

(Received 05 August 2025; revision accepted 23 February 2026)

Abstract–The Atacama Desert in Chile is characterized by its high meteorite density and old meteorite terrestrial ages. In this work, we present new terrestrial ages derived from measurements of the concentration of cosmogenic ^{36}Cl in the metal fraction of 51 ordinary chondrites collected over a 6.8 km^2 area located in the Catalina Dense Collection Area (Atacama Desert). Cosmic-ray exposure ages were also measured on a subset of the oldest meteorites to confirm that all but one had reached ^{36}Cl saturation before atmospheric entry. These meteorites have exceptionally old terrestrial ages, with an average of 937 ka (median 701 ka), making this collection the oldest known meteorite collection among hot deserts. This confirms that the Atacama Desert can preserve meteorites for long periods due to the prevailing stable hyper-arid climatic conditions. By combining terrestrial ages with pairing-corrected meteorite density estimates, we estimate the long-term meteorite flux to Earth over the past 2 Myr to be 74 ± 9 meteorites >20 g per km^2 per Myr. This is consistent with estimates of (i) the modern flux, (ii) the integrated flux over the last ~100 kyr determined from Antarctic meteorites, and (iii) the average flux during the last ~50 kyr inferred from other hot desert collections. This suggests that the bulk meteorite flux to Earth has remained roughly stable over the past 2 Myr. We also investigate the compositional evolution of the flux by normalizing the H chondrite abundance to the total abundance of ordinary chondrites. Our results show a higher H chondrite abundance between 1200 and 400 ka, followed by a decline to present-day values. This temporal variation is not captured by the current dynamical models for meteoroid transfer to Earth, suggesting that short-term changes in the meteorite flux may be influenced by additional processes operating at a scale not considered by these models.

© 2026 The Author(s). *Meteoritics & Planetary Science* published by Wiley Periodicals LLC on behalf of The Meteoritical Society.
This is an open access article under the terms of the Creative Commons Attribution-NonCommercial License, which permits use, distribution and reproduction in any medium, provided the original work is properly cited and is not used for commercial purposes.

INTRODUCTION

Earth experiences an influx of extraterrestrial material spanning a broad size range, from dust particles to centimeter- to meter-scale meteoroids, and to larger, potentially hazardous asteroids. Overall, smaller particles are far more abundant than larger objects, with fluxes (by number of objects) decreasing sharply with increasing size (Bland, 2001; Huss, 1990; Rojas et al., 2021; Zolensky et al., 2006).

The transfer of extraterrestrial material to Earth is governed by a complex combination of collisional, dynamical, and orbital mechanisms influenced by particle size, composition, source region, and orbital configuration (Bottke et al., 2015; Morbidelli & Vokrouhlický, 2003; Rubin, 2018). At the smallest scale, up to a few micrometers, Interplanetary Dust Particles (IDPs) and micrometeorites are influenced by the Poynting–Robertson drag (Wyatt & Whipple, 1950). In contrast, centimeter- to meter-sized meteoroids are mostly affected by thermal forces, including the Yarkovsky and the Yarkovsky-O'Keefe-Radzievskii-Paddack (YORP) effect (Farinella et al., 1998; Rubincam, 2000). These nongravitational thermal forces can cause meteoroids to drift into resonance zones, notably the $\nu 6$ Secular Resonance, the 5:2 Resonance, and the 3:1 Mean-Motion Resonance, which can destabilize orbits and inject meteoroids into Earth-crossing trajectories (Gladman et al., 1997). Moreover, close encounters with planets, particularly Jupiter, can also modify meteoroid orbits and increase the likelihood of crossing Earth's orbit (Bottke et al., 2002). Finally, larger bodies (with diameters $\gtrsim$10–30 km) are primarily influenced by gravitational interactions and resonances, while thermal effects are negligible, making their transfer to Earth relatively rare (Carruba et al., 2003; Minton & Malhotra, 2010).

Meteorites (centimeter to meter-sized objects) have long been a central focus of planetary science, as they provide a tangible record of the early solar system history, offering insights into its formation, evolution, and the physical and chemical processes that shaped it and ultimately led to planetary formation. Except for lunar and Martian meteorites, all meteorites found on Earth originate from the main asteroid belt. Recent studies combining spectroscopy and dynamical modeling have linked meteorite groups to young asteroid families within the belt, formed by collisional break-ups of parent bodies (Brož, Vernazza, Marsset, Binzel, et al., 2024; Brož, Vernazza, Marsset, DeMeo, et al., 2024; Marsset et al., 2024). Quantifying the meteorite flux is thus essential for a better understanding of the delivery mechanisms of meteoroids to Earth and recent collisional events that replenish Earth's impactor reservoirs. In this study, we focus on centimeter- to meter-scale meteoroids that survive atmospheric entry and reach Earth's surface as meteorites.

The present meteorite flux is inferred from meteorite recovery that can be assisted by radar and camera data. Ground-based camera networks use automated fisheye cameras to track meteors, estimate orbits, and predict potential fall locations (Bland et al., 2012; Colas et al., 2020; Devillepoix et al., 2018). Doppler weather radars can also help estimate strewn field locations of meteorite falls by directly imaging the falling meteorites during their dark flight (Fries & Fries, 2010). Meteor radars, such as the Canadian Meteor Orbit Radar (CMOR), can detect ionization trails from meteoroids, giving nearly continuous coverage regardless of weather or daylight conditions (Jones et al., 2005). Satellites, such as the Geostationary Operational Environmental Satellite (GOES), also contribute to the detection of meteoroids entering the atmosphere. In addition, the future LUMIO (Lunar Meteoroid Impacts Observer) CubeSat mission will observe impact flashes on the lunar farside to investigate the spatial and temporal characteristics of meteoroids impacting the lunar surface (Cervone et al., 2022). Together, these techniques yield a comprehensive record of the present-day infall rate of meteoroids and meteorites.

Using observations of fireballs from the Canadian Meteorite Observation and Recovery Project (MORP), Halliday et al. (1989) estimated a global meteorite mass flux of ~3900 kg per year for meteorites in the 10 g–1 kg mass range (i.e., ranging from 2 to 8 cm in diameter). The mass distribution of meteorites larger than 10 g, after accounting for pairing (i.e., when two or more recovered meteorites actually belong to the same fall), follows a power-law relationship with a slope of −0.83, indicating a steep drop-off in the occurrence frequency of larger bodies (Huss, 1990). In terms of composition, the present-day flux is largely dominated by ordinary chondrites, which account for 78% of documented meteorite falls over the last ~200 years (Meteoritical Bulletin Database, MBDB, https://www.lpi.usra.edu/meteor/, as of July 2025).

Estimating the meteorite flux over longer time scales is more challenging due to the relatively rapid degradation of meteorites at Earth's surface through erosion, weathering, and burial. The paleoflux of meteorites has been investigated using fossil meteorites, ^{3}He, and extraterrestrial spinel grains embedded in sedimentary layers, dating back from the Late Cambrian to the Early Paleocene (Farley et al., 2006; Schmitz et al., 2001, 2017). For instance, based on extraterrestrial chrome-spinel grains preserved in marine sediments, Terfelt and Schmitz (2021) reported a significant increase in the meteorite flux (up to 2 to 3 orders of magnitude) following the L chondrite parent-body break-up at

19455100, 0, Downloaded from https://onlinelibrary.wiley.com/doi/10.1111/maps.70125 by Carine Sadaka - Cochrane France , Wiley Online Library on [09/03/2026]. See the Terms and Conditions (https://onlinelibrary.wiley.com/terms-and-conditions) on Wiley Online Library for rules of use; OA articles are governed by the applicable Creative Commons License

19455100, 0, Downloaded from https://onlinelibrary.wiley.com/doi/10.1111/maps.70125 by Carine Sadaka - Cochrane France , Wiley Online Library on [09/03/2026]. See the Terms and Conditions (https://onlinelibrary.wiley.com/terms-and-conditions) on Wiley Online Library for rules of use; OA articles are governed by the applicable Creative Commons License

~470 Ma. ^{3}He flux reconstructions also documented several increases in the extraterrestrial flux, notably at ~34 and ~8 Ma (Farley et al., 2006; McGee & Mukhopadhyay, 2013).

On shorter time scales, meteorite accumulation sites act as natural archives, preserving an integrated meteorite flux at Earth's surface over tens of thousands to a few million years. This integration period can be constrained by determining the terrestrial age of recovered meteorites, which is defined as the time a meteorite has spent on Earth's surface since its fall. It is typically determined by measuring the concentration of cosmogenic radionuclides in the meteorite. For falls younger than ~50 ka, dating can be performed using the ^{14}C concentration, or, ideally, a combination of ^{14}C, ^{10}Be, and noble gases (Tauseef et al., 2024; Tauseef, Leya, Gattacceca, et al., 2025; Tauseef, Leya, & Hofmann, 2025). For older ages, cosmogenic nuclides with longer half-lives (such as ^{10}Be, ^{26}Al, ^{36}Cl, ^{41}Ca, ^{53}Mn) can be used (Nishiizumi, 1987; Welten et al., 2008, 2024). For example, FRO 01149, the oldest meteorite found on Earth to date, has a terrestrial age of ~3 Ma (Welten et al., 2008). Throughout this paper, we use Ma/ka to denote absolute ages and Myr/kyr to refer to time intervals or durations, following widespread convention.

Specific environmental conditions are necessary for the long-term preservation of meteorites at Earth's surface. Deserts provide such favorable conditions due to arid conditions and low erosion rates. Minimal vegetation and relatively flat surfaces also facilitate meteorite recovery, which is often achieved through systematic field searches. Notably, meteorites retrieved from hot and cold deserts account for approximately 95% of officially recognized meteorites (MBDB, as of July 2025).

The cold desert of Antarctica hosts the largest collection of recovered meteorites (~60%) with an average terrestrial age of around 100 ka (Drouard et al., 2019; Jull et al., 2006). However, reconstructing the past flux in this region is challenging due to ice flow dynamics and difficulties in pairing corrections (Corti et al., 2003; Zekollari et al., 2019). In contrast, hot deserts act as passive collection surfaces for infalling meteorites, making them more suitable to study the long-term meteorite flux. However, because climatic and geomorphological conditions differ among deserts, meteorite survival, and hence terrestrial age distributions vary significantly among different hot deserts.

The Atacama Desert is characterized by an extreme aridity and long-term climatic stability, which have led to the accumulation of the densest (Gattacceca et al., 2011; Hutzler et al., 2016; Pinto et al., 2024; Sadaka et al., 2025) and oldest (Drouard et al., 2019) meteorite collections worldwide. Consequently, the Atacama Desert offers the opportunity to study the meteorite flux over longer time scales than in any other desert, including Antarctica, with terrestrial ages up to ~1 Myr (e.g., Nishiizumi et al., 1989).

Based on the study of the El Médano Systematic Collection (EMSC) by Hutzler et al. (2016), assembled in the El Médano and Caleta el Cobre Dense Collection Areas (DCAs), Drouard et al. (2019) suggested a higher meteorite flux over the 0–2 Myr interval compared to more recent periods. Their study also reported possible variations in the composition of the meteorite flux, with a significant increase in the relative abundance of H chondrites compared to L chondrites between 500 ka and 1 Ma. Key questions arise as to whether the old terrestrial ages recorded in the EMSC represent a local anomaly or a broader regional feature, and whether the meteorite flux properties, including intensity and composition, determined from the EMSC are representative of global features.

To evaluate the spatial extent and robustness of the patterns observed in the EMSC, this study focuses on a distinct and independent area within the Atacama Desert, the Catalina DCA, located ~60 km away from the EMSC, and characterized by an exceptional meteorite density (Sadaka et al., 2025). Using the cosmogenic nuclide ^{36}Cl and additional constraints from cosmogenic ^{21}Ne, we determined the terrestrial ages of 51 meteorites from the Catalina Systematic Collection (CSC) (Sadaka et al., 2025). We combined the terrestrial age distribution with the meteorite density to estimate the meteorite flux over the last 2 Myr. In addition, we explore the temporal variations in the flux composition by analyzing the evolution of the relative abundances of H, L, and LL chondrites over the same period. This time window (0–2 Myr) is long enough to overlap with the time scales of the dynamic transfer of meteoroids from the asteroid belt to Earth, as evidenced by modeling (Brož, Vernazza, Marsset, Binzel, et al., 2024; Brož, Vernazza, Marsset, DeMeo, et al., 2024; Farinella et al., 1998) and constraints from meteorite cosmic-ray exposure ages (i.e., the time the meteorite spent in space before entering Earth's atmosphere) (Eugster, 2003; Graf & Marti, 1995).

GEOLOGY AND CLIMATE OF THE STUDIED AREA

The Atacama Desert lies in Northern Chile, between the Pacific Ocean and the Andes, comprising four main geological units: the Coastal Range, the Central Depression, the pre-Andean Range, and the Western Cordillera, with the Altiplano forming the high-elevation plateau immediately to the east. It is the driest and oldest nonpolar desert on Earth, with some areas receiving <5 mm of precipitation annually (Pfeiffer et al., 2021). The long-standing arid to hyper-arid climate of this desert is

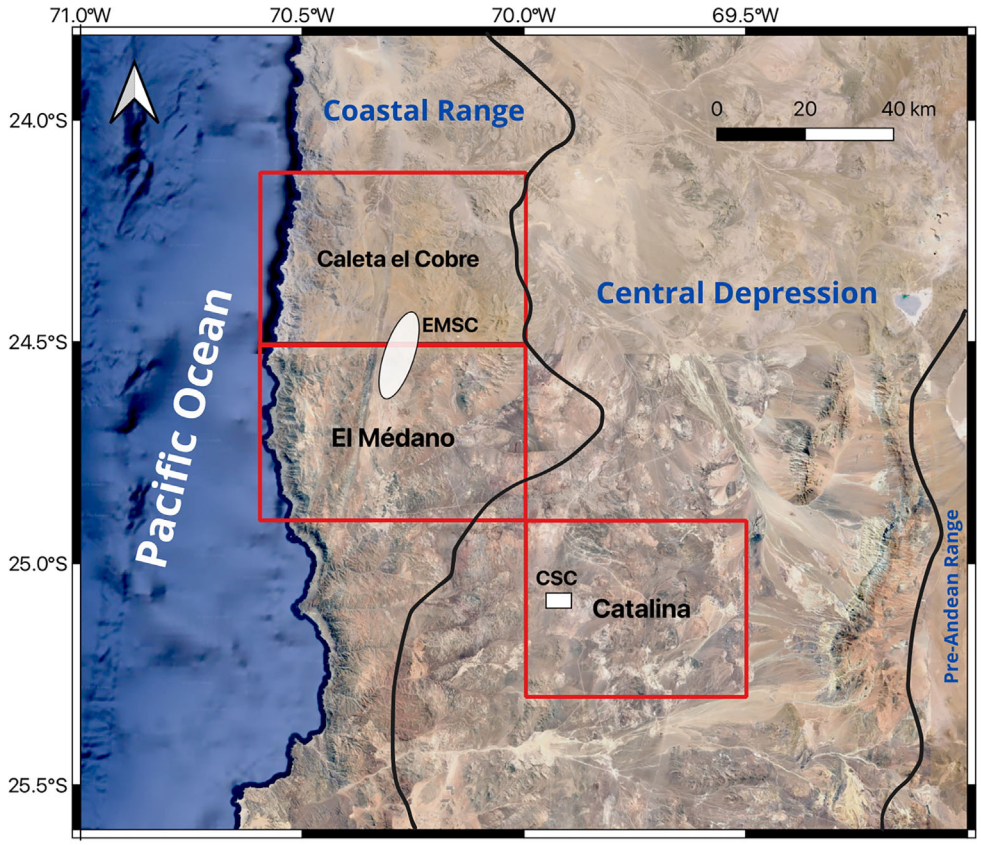

FIGURE 1. Map of the Atacama Desert showing the three Dense Collection Areas (DCAs) of interest in this study, outlined in red, within the major morphotectonic units (Coastal Range, Central Depression, and Pre-Andean Range). The white ellipse represents the area in which the El Médano Systematic Collection (EMSC) was studied by Hutzler et al. (2016), and the white rectangle marks the Catalina Systematic Collection (CSC) investigated by Sadaka et al. (2025). The background image is from Google Earth.

thought to have been established between 3 and 25 Ma (Clarke, 2006; Dunai et al., 2005). The Catalina DCA lies in the Central Depression (Figure 1), which includes some of most productive areas in terms of meteorite recovery in the Atacama Desert (Pinto et al., 2024). It is characterized by a hyper-arid climate with a mean annual air temperature of ∼16°C and annual precipitation of ∼15 mm year^{-1}, recorded between 2001 and 2021 (Pinto et al., 2024). Further details on the geology and climate of the CSC are provided in Sadaka et al. (2025), while information on the El Médano Systematic Collection is given in Hutzler et al. (2016). Table 1 provides a comparative overview of the two regions.

METHODS

Meteorite Flux Estimation

In this study, we follow the approach of Zolensky et al. (1990), Huss et al. (1990), and Drouard et al. (2019) to estimate the meteorite flux using recovered meteorite collections. This method is based on the estimate of the meteorite density on the ground and measurements of terrestrial ages of a randomly selected subset of unpaired meteorites. Several parameters must be constrained to estimate the meteorite flux:

1. The meteorite density in the studied area, corrected for recovery biases and pairing.
2. The terrestrial age distribution of the meteorite population.
3. The rate at which meteorites are removed from the surface, derived from the terrestrial age spectrum, assumes physical processes and chemical weathering as the main factors in meteorite removal. This assumes that the processes responsible for meteorite removal have remained relatively constant over the time scale covered by the terrestrial age distribution.

In the Atacama Desert, most specimens remain where they originally fell in the collection zone without significant lateral transport, due to gentle slopes (∼2°) and low precipitation rates. Also, the collection area is a

19455100, 0, Downloaded from https://onlinelibrary.wiley.com/doi/10.1111/maps.70125 by Carine Sadaka - Cochrane France , Wiley Online Library on [09/03/2026]. See the Terms and Conditions (https://onlinelibrary.wiley.com/terms-and-conditions) on Wiley Online Library for rules of use; OA articles are governed by the applicable Creative Commons License

TABLE 1. Climate, meteorite density, and terrestrial age statistics of the Catalina (CSC) and El Médano (EMSC) collections.

Collection	Catalina	El Médano
Climate[a]		
Geological unit	Central depression	Coastal range
Climatic regime	Hyper-arid	Hyper-arid
Average cumulative precipitation (mm year^{-1})	15	14
Average annual air temperature (°C)	16	15
Meteorite inventory[c]		
N total	1599	213
Total surface (km^2)	6.8	1.5
Density (meteorites per km^2)	235	251
Density >20 g	67	181
Corrected density[b] >20 g	71	123
Slope of mass distribution (1 g^{-1} kg)	−0.71	−0.59
Terrestrial ages		
Mean ± SD	937 ± 809	716 ± 617[d]
Range (min–max)	39–2939	13–2600
Median	701	535
Half-life (ka)	662	514
Flux (meteorites >20 g per km^2 per Myr)	74 ± 9	166 ± 13

[a]Over the period 2001–2021 (data from Pinto et al., 2024).
[b]Corrected for recovery biases and pairing.
[c]Sadaka et al. (2025) for the CSC; Hutzler et al. (2016) for the EMSC.
[d]Ages recalculated from Drouard et al. (2019). See text for details.

deflation zone, implying minimal burial of meteorites. Over time, the oldest meteorites disintegrate due to physical fragmentation and erosion caused by abrasion from wind-blown sand and dust. These processes gradually reduce their size and integrity, eventually leading to their disappearance.

The variation of the meteorite density at the surface, $dN(t)/dt$, follows this equation:

$$dN(t)/dt = \alpha - \gamma\, N(t) \quad (1)$$

where α represents the incoming meteorite flux (number per unit time and area), and γ is the decay rate, corresponding to the fraction of the meteorite population lost per unit time (Zolensky et al., 1990). The half-life of the meteorites in the collection, hereafter referred to as the meteorite surface residence half-life, is the time required for half of the meteorite population to be lost and is related to the decay rate by $T_{1/2} = \ln(2)/\gamma$.

Solving Equation (1) yields:

$$N(t) = \frac{\alpha}{\gamma}(1 - e^{-\gamma t}) + N_0 e^{-\gamma t} \quad (2)$$

with N_0 as the initial meteorite surface density at $t = 0$. Assuming a constant flux α, and regardless of the initial value of N_0, the number of meteorites increases with time, until a steady-state equilibrium is reached between meteorite accumulation and removal after a few half-lives. At this point, the density of meteorites reaches a saturation value $N_{sat} = \alpha/\gamma$. Therefore, if both the surface meteorite density at saturation N_{sat} and the decay rate γ are known, the meteorite flux α can be estimated with $\alpha = g \times N_{sat}$.

This approach, however, relies on two key assumptions:

1. A steady state has been reached between meteorite accumulation and removal over the studied period (typically after a few half-lives).
2. The intensity of the meteorite flux has remained relatively constant over the accumulation period.

Sample Selection for Age Determination

We first performed an initial random selection among CSC ordinary chondrites weighing more than 20 g ($n = 440$). We then assessed potential pairings based on petrographic, geochemical, magnetic properties, as well as the distance between the meteorite find locations. If a high probability of pairing was identified, a new sample was drawn in an iterative process.

In this way, we selected 51 meteorites from the CSC. Samples are from the CEREGE meteorite collection or were provided by the Museo del Meteorito in San Pedro de Atacama. The selected samples include 35 H chondrites (20 H5, 12 H6, 3 H5-6), 13 L chondrites (12 L6, one L5), and 3 LL5 chondrites. Most samples show low degrees of weathering (51% W1, 39% W2, 10% W3). The geographic distribution of the selected samples within the CSC is shown in Figure 2.

Terrestrial Age Estimation Using Cosmogenic ^{36}Cl

Cosmogenic ^{36}Cl Production and Relevance

In this study, we use the cosmogenic radionuclide ^{36}Cl because its half-life of 301.3 kyr (Nica et al., 2012) allows measuring meteorite terrestrial ages ranging from ~60 ka to ~3 Ma, which is suitable in view of the terrestrial ages measured in Atacama meteorites (Drouard et al., 2019; Gattacceca et al., 2011). An accurate ^{36}Cl-based terrestrial age determination requires a CRE age longer than approximately five times the radionuclide's half-life, by which point ~97% of the saturation level has been reached. Around 97% of ordinary chondrites have CRE ages >1.5 Ma (Eugster, 2003; Graf & Marti, 1995), indicating that ^{36}Cl saturation has been reached for most ordinary chondrites (Figure S2).

19455100, 0, Downloaded from https://onlinelibrary.wiley.com/doi/10.1111/maps.70125 by Carine Sadaka - Cochrane France , Wiley Online Library on [09/03/2026]. See the Terms and Conditions (https://onlinelibrary.wiley.com/terms-and-conditions) on Wiley Online Library for rules of use; OA articles are governed by the applicable Creative Commons License

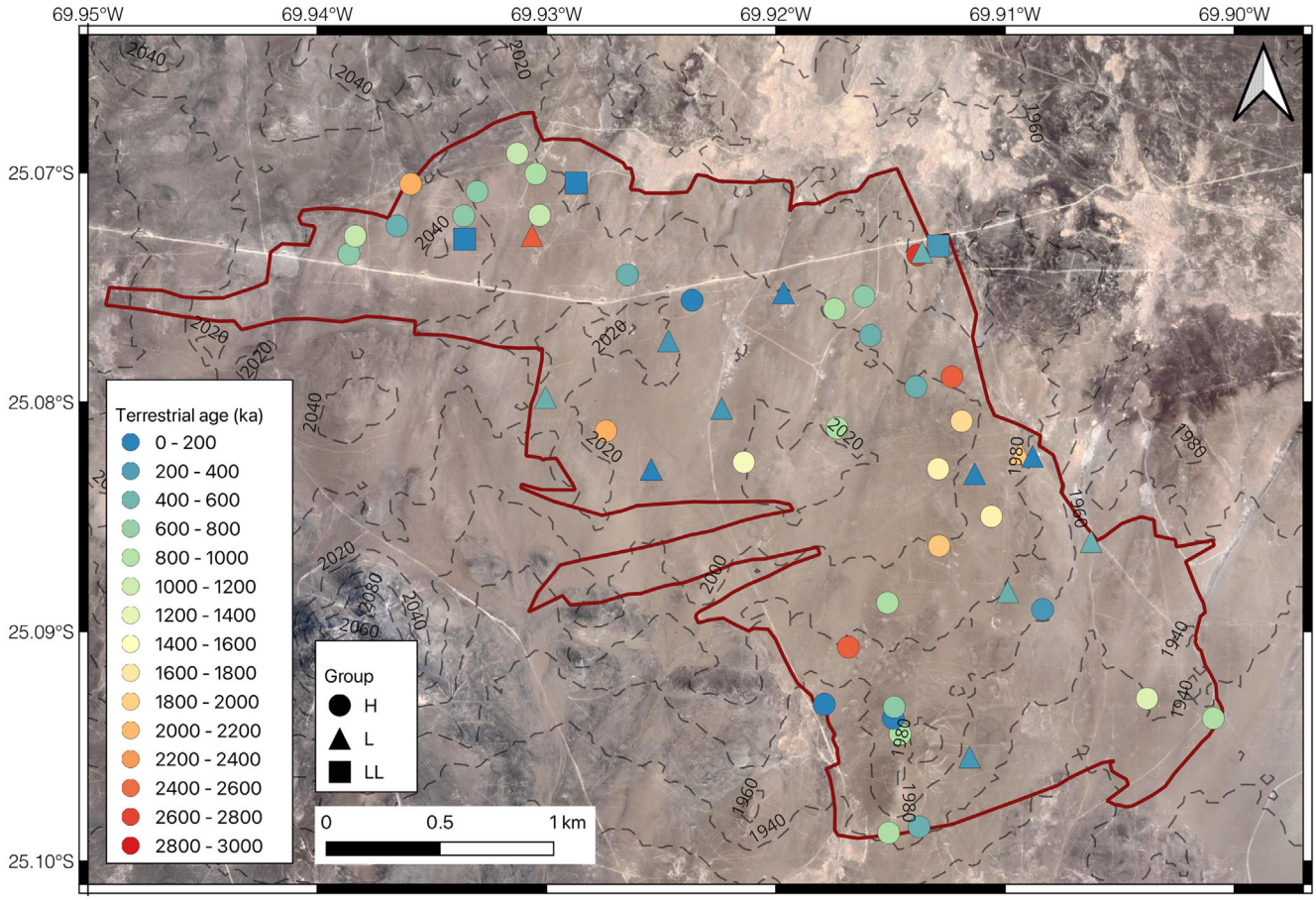

FIGURE 2. Map showing the recovery locations of the meteorites selected for ^{36}Cl dating in the Catalina Systematic Collection ($n = 51$), with symbol shape indicating the ordinary chondrite group and color representing the terrestrial age. The background image is from Google Earth.

Cosmogenic ^{36}Cl is produced through spallation (high-energy nuclear reactions) on target elements heavier than Cl, that is, predominantly Ca, Fe, and Ni, as well as through muon capture (a process irrelevant in space), and thermal neutron capture (low-energy reactions) on ^{35}Cl. Contributions from neutron capture depend on the size and chemical composition of the studied meteorite and on the Cl content of the analyzed sample, making the interpretation of ^{36}Cl data in bulk meteorite samples challenging. By focusing on the metal fraction (Fe and Ni), contributions from thermal neutron capture are avoided, simplifying the interpretation of ^{36}Cl data as solely reflecting production via spallation from Fe and Ni.

With $N_{36\mathrm{Cl}}(t)$ the number of ^{36}Cl atoms at time t, P_{space} the production activity in space, and $\lambda_{(36\mathrm{Cl})}$ the ^{36}Cl radioactive decay constant defined as the fraction of the nuclei that decay per unit time, $N_{36\mathrm{Cl}}$ during the irradiation phase of the meteorite is given by:

$$N_{36\mathrm{Cl}(t)} = \frac{P_{\mathrm{space}}}{\lambda(36\mathrm{Cl})}\left(1-e^{-\lambda(36\mathrm{Cl})t}\right) \quad (3)$$

After an irradiation time of a few half-lives, an equilibrium state is reached between production and decay, and the number of ^{36}Cl atoms reaches the saturation value $N_{(36\mathrm{Cl})\mathrm{sat}} = \frac{P_{\mathrm{space}}}{\lambda(36\mathrm{Cl})}$.

After the meteorite falls on Earth, ^{36}Cl continues to be produced at a rate P_{Earth}, and the number of ^{36}Cl atoms as a function of terrestrial residence time t is governed by:

$$N_{36\mathrm{Cl}(t)} = \frac{P_{\mathrm{space}}-P_{\mathrm{Earth}}}{\lambda(36\mathrm{Cl})}e^{-\lambda(36\mathrm{Cl})t} + \frac{P_{\mathrm{Earth}}}{\lambda(36\mathrm{Cl})} \quad (4)$$

To estimate the terrestrial production of ^{36}Cl in meteorites, we use the model of Schimmelpfennig et al. (2009). We accounted for the effects of elevation

19455100, 0, Downloaded from https://onlinelibrary.wiley.com/doi/10.1111/maps.70125 by Carine Sadaka - Cochrane France , Wiley Online Library on [09/03/2026]. See the Terms and Conditions (https://onlinelibrary.wiley.com/terms-and-conditions) on Wiley Online Library for rules of use; OA articles are governed by the applicable Creative Commons License

and latitude on production rates using the scaling approach of Stone (2000). For the cosmogenic production of ^{36}Cl from Fe, we used a reference value of 1.28 ± 0.11 atoms per g of Fe per year at sea level and high latitude, reported by Moore and Granger (2019). This estimate indicates that ^{36}Cl production on Earth is negligible compared to production in space (see "Terrestrial Ages of the CSC and the EMSC" section), and therefore, by measuring the present-day ^{36}Cl concentration in meteorites, the terrestrial age can be calculated as:

$$T_{\text{terr}} = \frac{1}{\lambda(36\text{Cl})} \ln\left(\frac{P_{\text{sat}}}{P_{\text{meas}}}\right) \quad (5)$$

where P_{meas} represents the measured activity of ^{36}Cl ($P_{\text{meas}} = \lambda N_{\text{meas}}$), and N_{meas} is the number of ^{36}Cl atoms in the sample determined by Accelerator Mass Spectrometry (AMS).

Since we use only the metallic fraction to study ^{36}Cl terrestrial ages, the equilibrium activity depends solely on the abundances of Fe and Ni in the analyzed metallic fraction. These Fe/Ni ratios have been measured (see "Sample Preparation for ^{36}Cl Measurements" section) and introduced in the production rate model of Leya and Masarik (2009) to estimate P_{sat}. As a reference, measurements of the activity of ^{36}Cl (in units of disintegrations per minute per kilogram or dpm kg^{-1}) in the metal phase of falls give a mean of 23.2 ± 1.4 ($n = 18$) dpm kg^{-1} for H chondrites and 22.7 ± 1.0 ($n = 10$) dpm kg^{-1} for L chondrites (Dalcher et al., 2013; Graf et al., 2001).

Sample Preparation for ^{36}Cl Measurements

The procedures for ^{36}Cl extraction and measurement follow the protocols outlined in Vogt and Herpers (1988), Merchel and Herpers (1999), and Drouard et al. (2019). The protocol first involves metal extraction and purification to isolate 50–100 mg of pure metal. Briefly, the meteorite fragment is ground using an agate mortar, and metal is extracted from all fractions <400 μm using a hand magnet. This extract is then rinsed in an ultrasonic ethanol bath for 10 min to detach silicates, which are recovered for subsequent analyses. After drying and a second magnetic separation, metal grains undergo cleaning in a sequence of ultrasonic baths at room temperature, each lasting 30 min: a 0.2 M hydrochloric acid (HCl) solution to remove troilite, followed by a 67% ethanolamine thioglycolate (EATG) solution to eliminate iron oxides and oxyhydroxides (terrestrial weathering products). The potential effect of HCl treatment before Cl extraction was tested by Hutzler (2015), who concluded that diluted HCl (0.2 M) does not affect the Cl isotopic composition and is thus suitable for metal purification.

A Cl carrier solution containing 6 mg Cl per g (^{36}Cl/^{35}Cl $= 7.2\ 10^{-16} \pm 6.1\ 10^{-17}$) is added to the purified metal, which is then dissolved in 10 mL of 2 M nitric acid (HNO_3) at 70–80°C in an ultrasonic bath for at least 48 h. To isolate chlorine, silver chloride (AgCl) is precipitated by adding silver nitrate ($AgNO_3$) to the solution. To obtain high quality ^{36}Cl data, the removal of isobaric interferences, specifically ^{36}S (Jiang et al., 2004), and some carbonate species is necessary. To this end, barium sulfate ($BaSO_4$) and barium carbonate ($BaCO_3$) are coprecipitated in a basic medium using a saturated solution of barium nitrate ($Ba(NO_3)_2$). AgCl is reprecipitated from the leachate with 1 mL of pure HNO_3. The final precipitates (average mass 8 ± 2 mg) are rinsed three times with Milli-Q water, dried, and loaded into cathodes for measurement at the French National Accelerator Mass Spectrometry facility (ASTER) in CEREGE, Aix-en-Provence.

AMS Measurements and Production Rate Calculations

The ^{36}Cl and Cl concentrations were measured by isotope dilution by AMS and were both normalized to a ^{36}Cl standard (SM-CL12) with a given ^{36}Cl/^{35}Cl-value of $(1.428 \pm 0.02) \times 10^{-12}$ (Merchel et al., 2011). The decay constant of $2.303 \pm 0.016 \times 10^{-6}$ year^{-1} used corresponds to a ^{36}Cl half-life ($T_{36\text{Cl}}$) of 301.3 ± 1.5 kyr. Analytical uncertainties include counting statistics, machine stability, and blank correction. The ^{36}Cl/^{35}Cl given by AMS measurements have average uncertainties of approximately 5%–6%.

After metal dissolution and prior to the first precipitation step, a 300 μL aliquot of the supernatant liquid is sampled, and Fe and Ni concentrations are measured on this aliquot using Inductively Coupled Plasma Optical Emission Spectrometry (ICP-OES) at CEREGE. Using the model of Leya and Masarik (2009), which estimates the ^{36}Cl production based on the chemical composition (here, the Ni and Fe content), the pre-atmospheric radius, and the depth, we calculated the depth-integrated ^{36}Cl production rate, assuming a meteoroid radius of 10 cm and a depth range of 1 to 10 cm.

One factor that can influence ^{36}Cl production is shielding, which refers to the attenuation of cosmic-ray flux with increasing depth inside a meteoroid, leading to lower ^{36}Cl production rates (Leya & Masarik, 2009). To assess the impact of shielding on ^{36}Cl-based terrestrial ages, we calculated terrestrial ages using depth-integrated ^{36}Cl saturation activity for different radii, omitting the top 1 cm (usually lost due to ablation during atmospheric entry). For the Catalina meteorites, assuming pre-atmospheric radii of 50 cm versus 10 cm results in terrestrial ages younger by

19455100, 0, Downloaded from https://onlinelibrary.wiley.com/doi/10.1111/maps.70125 by Carine Sadaka - Cochrane France , Wiley Online Library on [09/03/2026]. See the Terms and Conditions (https://onlinelibrary.wiley.com/terms-and-conditions) on Wiley Online Library for rules of use; OA articles are governed by the applicable Creative Commons License

80 ± 2 ka on average. This would correspond to a small effect for a meteorite population with an average terrestrial age of 937 ka. Therefore, possible shielding-related uncertainties are unlikely to significantly bias the overall age distributions discussed in this study.

Shielding indicators based on cosmogenic Ne are not available or robust for all studied samples and thus cannot be used to exclude the possibility that some samples originate from a large meteoroid (>50 cm in radius). However, such meteoroids with $R > 50$ cm are rare (<~1% of occurrences) in the present-day ordinary chondrite flux. Therefore, a reference pre-atmospheric radius of 10 cm (a condition fulfilled by about 85% of present day meteorite falls considering their total mass and an ablation rate of 80% [Halliday et al., 1989]) represents a reasonable assumption for modeling ^{36}Cl production and computing terrestrial ages, while acknowledging that the presence in our data set of a very limited number of meteorites originating from larger meteorites cannot be fully excluded.

Reliability of ^{36}Cl Terrestrial Ages: Insights From Cosmogenic Neon

CRE ages are constrained using the abundance and the isotopic composition of cosmogenic nuclides. Here, we derive CRE ages using the $(^{22}Ne/^{21}Ne)_{cos}$–$^{21}Ne_{cos}$ method, the most widely used method for stony meteorites (Leya & Masarik, 2009). Thirty-nine meteorites were selected from the CSC and the EMSC, based on their ^{36}Cl terrestrial age >1 Ma, to test whether these old ages could be an artifact caused by CRE ages shorter than ~1.5 Ma (5 half-lives of ^{36}Cl). Eight meteorites were measured at the University of Bern (Space Research and Planetary Sciences), Switzerland, and 31 samples were measured at the Centre de Recherches Pétrographiques et Géochimiques (CRPG) in Nancy, France. Full details of the analytical procedures, neon data, and CRE age calculations are provided in the Supporting Information.

RESULTS

Terrestrial Ages of the CSC and the EMSC

The terrestrial production rate of ^{36}Cl in the metal phase of meteorites from the CSC and EMSC is typically on the order of 10^{-3} dpm kg^{-1}, which is ~10^{-4} times lower than the mean measured activity of all samples from the Atacama Desert (7.6 dpm kg^{-1}; range 0.03–21.9 dpm kg^{-1}, $n = 104$, data from this study and Drouard et al., 2019). Terrestrial production is therefore negligible compared to production in space. Resulting ^{36}Cl-based terrestrial ages and sample details are provided in Table 2. For three samples, replicate measurements were performed, all of which gave similar ages within uncertainties.

Importantly, the Ne data allowed us to verify that the concentration of ^{36}Cl in the meteorite samples had reached saturation at the time of fall. Indeed, out of the 39 measured meteorites, only one sample showed a CRE age <1.5 Ma (Figure S2; Table S1), indicating that 97% of the studied meteorites reached saturation of ^{36}Cl concentration in space, in agreement with literature data from Graf and Marti (1994, 1995) and Marti and Graf (1992) (Figure S2).

The only meteorite with a CRE age shorter than 1.5 Myr is Catalina 478. Because this meteorite did not reach ^{36}Cl saturation during its exposure in space, its terrestrial age was corrected for incomplete saturation using:

$$T_{corr} = T_{sat} + \frac{1}{\lambda_{36}} \ln\left(1 - e^{-\lambda_{36} T_{CRE}}\right)$$

where T_{corr} is the corrected terrestrial age, T_{sat} is the terrestrial age calculated assuming saturation in space, λ_{36} is the decay constant of ^{36}Cl, and T_{CRE} is the CRE age. Uncertainties were calculated using 1σ error propagation. The terrestrial age decreases from 884 ± 63 ka (saturation assumption) to 395 ± 218 ka after correction. Given the large uncertainty on the corrected terrestrial age of Catalina 478, this age was not considered in the following discussion.

In the CSC, meteorite terrestrial ages range from 39 to 2939 ka (Table 2; Figures 2 and 3), with an average of 937 ± 809 ka (median 701 ka; $n = 50$). For homogeneity, we also recalculated the terrestrial ages of the EMSC (Drouard et al., 2019) with the same approach as for the CSC, that is, by using the weight averaged saturated activity for a meteoroid with a radius of 10 cm, starting at a depth of 1 cm from the surface, using the model of Leya and Masarik (2009). The recalculated terrestrial ages of the EMSC range from 13 to 2600 ka, with an average of 716 ± 617 ka (median 535 ka; $n = 54$). These values do not differ significantly from those reported by Drouard et al. (2019), for which the average age is 708 ± 617 ka. Results are given in Table S2 and displayed in Figure 3.

DISCUSSION

Terrestrial Ages

In the combined data set of 104 ordinary chondrites from the CSC and EMSC, terrestrial ages range from <60 to 2939 ka, with an average of 823 ka (median 619 ka; standard deviation 721 ka). These old terrestrial ages are readily explained by the long-standing hyper-aridity and

19455100, 0, Downloaded from https://onlinelibrary.wiley.com/doi/10.1111/maps.70125 by Carine Sadaka - Cochrane France , Wiley Online Library on [09/03/2026]. See the Terms and Conditions (https://onlinelibrary.wiley.com/terms-and-conditions) on Wiley Online Library for rules of use; OA articles are governed by the applicable Creative Commons License

TABLE 2. Meteorite characteristics and ^{36}Cl-based terrestrial ages of the metal fraction from the Catalina Systematic Collection (CSC) meteorites.

Official name	Meteorite mass (g)	Group	Petrographic type	Weathering grade	Ni/(Fe/Ni) %	Dissolved metal mass (mg)	Computed ^{36}Cl activity at saturation (dpm kg^{-1})	Calculated activity from measured ^{36}Cl (dpm kg^{-1})	Terrestrial age (ka)	Uncertainty (ka)
Catalina 049	117	LL	5	3	23.4	60	22.57	14.56	190	67
Catalina 146	159	H	5	1	8.0	66	23.73	16.95	146	67
Catalina 229	248	H	5	1	7.4	117	23.81	1.31	1261	68
Catalina 440	25	L	6	2	8.9	115	23.66	6.40	568	67
Catalina 445	58	L	6	1	12.6	98	23.35	21.33	39	67
Catalina 447	58	LL	5	2	19.3	84	22.88	11.78	288	68
Catalina 467	30	H	5	1	7.2	132	23.81	18.50	110	67
Catalina 474 (1)	46	H	5	3	9.0	77	23.66	3.61	817	68
Catalina 474 (2)	46	H	5	3	9.1	70	23.66	3.95	777	68
Catalina 475	67	L	6	2	12.7	115	23.35	5.89	598	67
Catalina 476	47	H	5	1	7.6	90	23.73	0.32	1867	71
Catalina 477 (1)	268	H	5	1	7.6	143	23.73	0.06	2621	76
Catalina 477 (2)	268	H	5	1	7.0	205	23.81	0.05	2691	75
Catalina 478 (1)	22	H	5	1	22.6	62	22.57	2.95	883[a]	68
Catalina 478 (2)	22	H	5	1	9.4	30	23.66	3.09	885[a]	70
Catalina 479	65	L	6	2	12.9	45	23.35	0.21	2055	73
Catalina 480	425	H	5	1	8.3	110	23.73	2.27	1019	68
Catalina 481	635	H	5	2	7.2	129	23.81	2.83	925	69
Catalina 483	21	LL	5	2	13.5	72	23.35	21.14	43	67
Catalina 494	39	H	6	2	7.7	53	23.73	0.03	2939	94
Catalina 503	29	H	6	1	6.8	143	23.81	16.51	159	67
Catalina 517	79	H	5	1	8.9	120	23.66	6.12	587	67
Catalina 524	48	H	6	3	6.0	172	23.64	0.04	2751	76
Catalina 535	27	H	5	1	7.5	100	23.73	0.80	1470	69
Catalina 538	92	H	5	1	7.4	114	23.81	3.87	789	67
Catalina 541	21	H	5	1	6.9	51	23.81	8.36	454	68
Catalina 542	75	L	6	2	9.4	65	23.66	9.26	407	68
Catalina 544	46	L	6	2	7.6	28	23.73	14.36	218	69
Catalina 548	99	H	6	1	7.8	115	23.73	3.74	802	68
Catalina 551	32	H	6	2	6.7	37	23.81	2.25	1024	70
Catalina 555	31	H	5	2	8.0	95	23.73	0.11	2350	74
Catalina 556	78	L	6	2	10.1	62	23.58	15.44	184	67
Catalina 562	22	L	6	2	8.5	108	23.73	15.38	188	67
Catalina 563	27	L	6	2	12.4	91	23.42	15.70	174	67
Catalina 572	532	H	5	1	5.4	99	23.96	13.53	248	67
Catalina 588	43	H	6	3	6.8	52	23.81	9.07	419	68
Catalina 600	194	H	5	1	7.1	46	23.81	6.09	592	68
Catalina 617	46	H	6	2	6.5	79	23.89	7.33	513	68
Catalina 637	56	H	5	1	7.0	39	23.81	4.79	696	69
Catalina 652	46	H	6	1	8.1	156	23.73	2.20	1033	68

19455100, 0, Downloaded from https://onlinelibrary.wiley.com/doi/10.1111/maps.70125 by Caine Sadaka - Cochrane France , Wiley Online Library on [09/03/2026]. See the Terms and Conditions (https://onlinelibrary.wiley.com/terms-and-conditions) on Wiley Online Library for rules of use; OA articles are governed by the applicable Creative Commons License

TABLE 2. *Continued*. Meteorite characteristics and ^{36}Cl-based terrestrial ages of the metal fraction from the Catalina Systematic Collection (CSC) meteorites.

Official name	Meteorite mass (g)	Group	Petrographic type	Weathering grade	Ni/(Fe/Ni) %	Dissolved metal mass (mg)	Computed ^{36}Cl activity at saturation (dpm kg^{-1})	Calculated activity from measured ^{36}Cl (dpm kg^{-1})	Terrestrial age (ka)	Uncertainty (ka)
Catalina 660	26	L	6	2	12.4	63	23.42	0.05	2653	83
Catalina 662	75	H	5–6	1	7.5	83	23.73	3.46	836	68
Catalina 664	20	H	5	1	7.6	99	23.73	0.11	2339	76
Catalina 667	20	H	5	1	7.2	132	23.81	5.46	640	68
Catalina 673	388	L	6	2	10.1	91	23.58	6.78	541	68
Catalina 677	174	H	5–6	2	7.6	54	23.73	4.66	707	68
Catalina 682	706	H	5–6	1	7.3	62	23.81	2.67	950	69
Catalina 684	59	H	6	1	7.9	156	23.73	2.96	904	68
Catalina 689	28	H	5	2	8.4	8	23.73	0.23	2010	108
Catalina 692	66	H	6	3	6.3	116	23.89	4.70	706	68
Catalina 707	52	H	6	1	6.8	41	23.81	0.41	1760	72
Catalina 739	92	H	6	1	7.6	133	23.73	0.42	1756	70
Catalina 740	76	L	6	2	8.9	29	23.66	12.14	290	69
Catalina 754	52	L	5	1	8.8	36	23.66	13.04	258	68

Note: Samples marked (1) and (2) correspond to replicate measurements; their average was used for figures and statistics.
[a]Uncorrected age.

19455100, 0, Downloaded from https://onlinelibrary.wiley.com/doi/10.1111/maps.70125 by Carine Sadaka - Cochrane France , Wiley Online Library on [09/03/2026]. See the Terms and Conditions (https://onlinelibrary.wiley.com/terms-and-conditions) on Wiley Online Library for rules of use; OA articles are governed by the applicable Creative Commons License

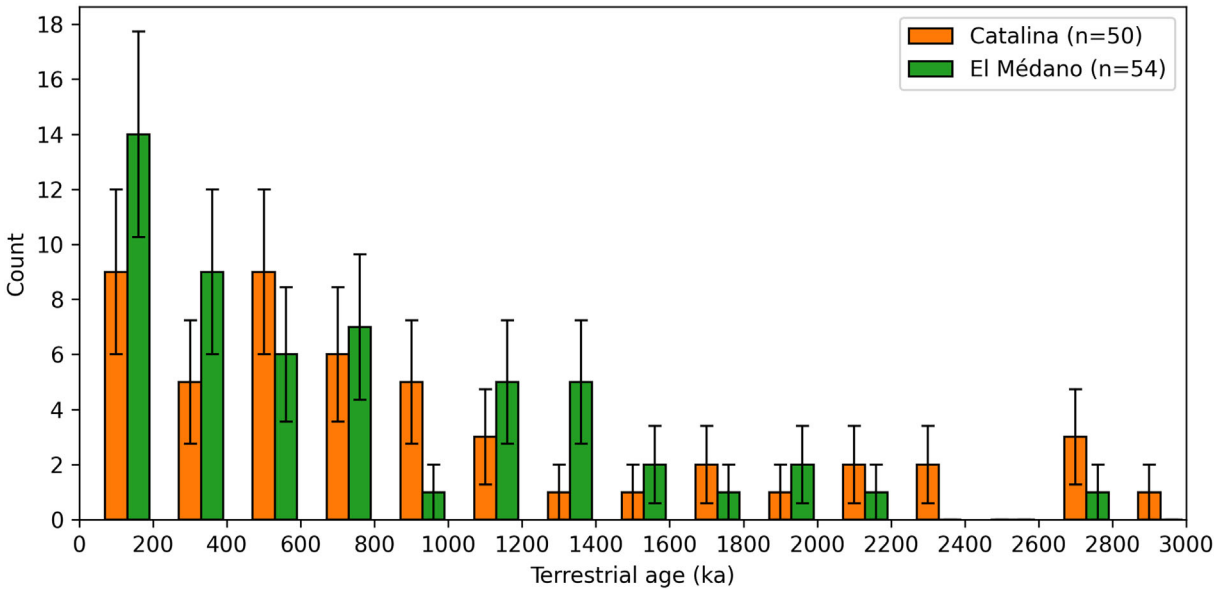

FIGURE 3. Histogram of ^{36}Cl-based terrestrial age distributions for meteorites from the Catalina Systematic Collection (CSC; $n = 50$; orange) and the El Médano Systematic Collection (EMSC; $n = 54$; green) meteorites, based on recalculated ages. Bin width is 200 ka. The error bars are calculated as Poisson uncertainties for each bin.

geomorphological stability of the Atacama Desert (see "Geology and Climate of the Studied Area" section). The CSC samples exhibit slightly older terrestrial ages, with an average of 937 ka, compared to a recalculated average age of 716 ka for the EMSC (Table 1, Figure 3).

In other hot deserts, meteorites from the Sahara exhibit terrestrial ages ranging from 0 to 35 ka (Jull et al., 2006; Tauseef, Leya, & Hofmann, 2025), and those from Western Australia have typical ages in the range 0 to >49 ka, with a mean age of approximately 20 ka (Jull et al., 2006, 2010). In Roosevelt County (New Mexico, USA), meteorite terrestrial ages span from 7 to over 44 ka (Jull et al., 2006). Those recovered from Oman and Saudi Arabia display ages between 10 and 35 ka (mean 20 ± 12 ka; Hofmann & Gnos, 2024; Tauseef, Leya, Gattacceca, et al., 2025), while specimens from the Lut Desert in Iran have ages ranging from 10 to 30 ka (Pourkhorsandi et al., 2019). Notably, meteorites from the Atacama Desert yield the oldest terrestrial ages among hot deserts, averaging ~820 ka for the combined CSC and EMSC data set, and maximum ages approaching 3 Ma. This highlights the exceptional potential of the Atacama Desert for meteorite preservation and its suitability for studying the meteorite flux over the last 2 Myr.

Despite the rare occurrence of older meteorites from other hot deserts, such as DaG 343 at ~150 ka (Welten et al., 2004) and two Oman achondrites at 500–600 ka (Nishiizumi et al., 2002; Nishiizumi & Caffee, 2001), and the possibility that a few additional old meteorites may have been overlooked because of the upper limit of the ^{14}C method (~50 ka), the terrestrial age distribution in other hot deserts remains much younger than the one observed in the Atacama Desert. This is also reflected in a much lower meteorite density in these deserts.

Meteorite Flux Intensity

To infer the rate at which meteorites are removed from the Atacama Desert surface, we use the decreasing cumulative distribution of the terrestrial ages (Zolensky et al., 1990). Figure 4 shows the decreasing cumulative terrestrial age distributions of the CSC and EMSC, along with corresponding exponential fits. The low root mean squared error (RMSE) values of 0.030 for the CSC and 0.026 for the EMSC indicate good agreement between the age data and the exponential decay model. This decay pattern is consistent with a broadly constant influx of meteorites combined with removal due to chemical and physical alteration (Equation 1). Notably, neither region shows evidence of a major surface resetting event, which would result in a sharp cutoff in the cumulative age distribution. This agrees with the typical surface ages >3 Ma of the Atacama Desert (Dunai et al., 2005; Hutzler et al., 2016).

For the CSC, the terrestrial age distribution allows us to infer a meteorite half-life of 662 ka, corresponding to a destruction rate g of 1.05 Myr^{-1} (Figure 4, Table 1). This half-life is at least five times shorter than the typical surface age, indicating that the assumption of a steady state between meteorite accumulation and removal is satisfied. Using the corrected density N_{sat} of 71 falls

19455100, 0, Downloaded from https://onlinelibrary.wiley.com/doi/10.1111/maps.70125 by Carine Sadaka - Cochrane France , Wiley Online Library on [09/03/2026]. See the Terms and Conditions (https://onlinelibrary.wiley.com/terms-and-conditions) on Wiley Online Library for rules of use; OA articles are governed by the applicable Creative Commons License

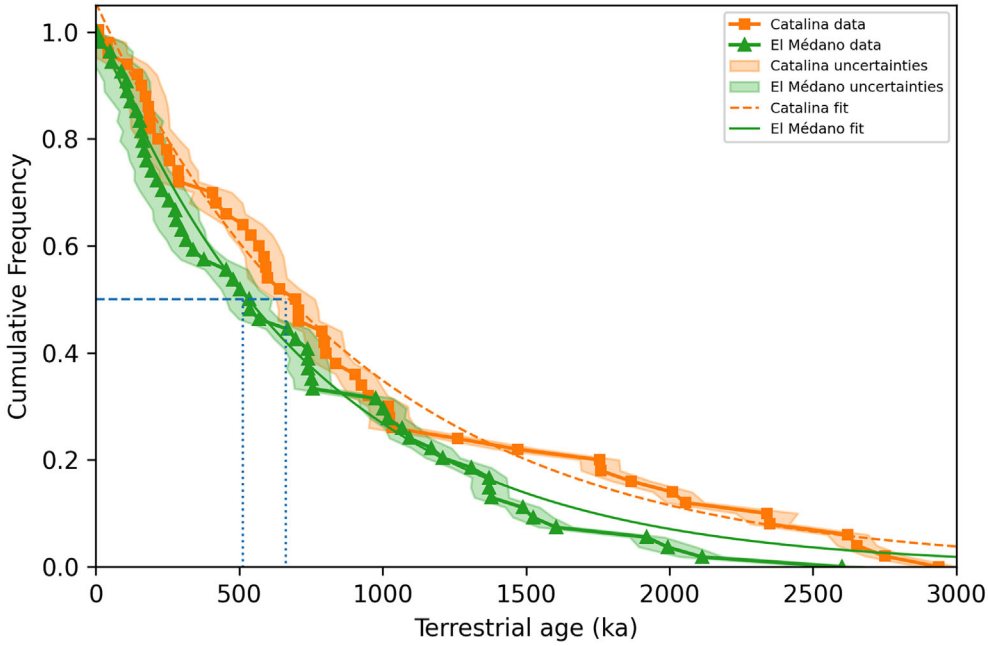

FIGURE 4. Decreasing cumulative distribution of terrestrial ages for meteorites from the Catalina Systematic Collection (CSC, orange) and the El Médano Systematic Collection (EMSC, green) with shaded areas representing age uncertainties. Dashed and solid lines correspond to best-fit exponential decay for CSC and EMSC, respectively. The root mean squared error (RMSE) of the fits is CSC = 0.030 and EMSC = 0.026. Vertical and horizontal dashed lines mark the 50% decay threshold used to estimate the meteorite half-life ($T_{1/2}$) for meteorite removal.

(meteorites >20 g per km^2) after pairing (Sadaka et al., 2025), we derive a flux of $\alpha = g \times N_{sat} = 74 \pm 9$ meteorites >20 g per km^2 per Myr over the last 2 Myr.

For the EMSC, the recalculated terrestrial ages yield a half-life of 514 ka and a corresponding destruction rate of 1.38 Myr^{-1} (Figure 4, Table 1). Considering a density of 123 falls (meteorites >20 g per km^2; Hutzler et al., 2016), we estimate a flux of 166 ± 13 meteorites >20 g per km^2 per Myr over the last 2 Myr.

Several studies have estimated the meteorite flux across a wide range of masses, time periods, and geographic regions, using various approaches including camera network observations, glaciological modeling, and meteorite accumulation site analyses. For homogeneity, we recalculated all flux estimates to meteorites with masses >20 g (Table 3). This was done by converting each reported flux to a common mass threshold using the slope of the corresponding mass distribution, assuming a power-law relationship: flux ($>M$ g) = reported flux × M^b; where b is the slope of the mass distribution (Zolensky et al., 2006).

For comparison, using other hot desert accumulation sites, Bland et al. (1996) studied the meteorite flux over the last 50 kyr in various regions worldwide and reported accumulation rates of 79 meteorites >20 g per km^2 per Myr in Roosevelt County (southwestern USA), 24 in the Nullarbor Region (Australia), and 60 in the Sahara (northern Africa), with uncertainties estimated to be a factor of 2 to 3. Using a different approach, Evatt et al. (2020) combined glaciological modeling with Antarctic meteorite recovery data and estimated a meteorite flux of 41 [28–59] >20 g per km^2 per Myr over the last ~100 kyr. For the present-day flux, Halliday et al. (1989) used fireball observations from the Canadian MORP camera network covering 11 years from 1974 to 1985, and estimated a meteorite flux of 59 meteorites >20 g per km^2 per Myr, with an uncertainty of a factor of 2. All these values are summarized in Table 3 and Figure S3.

We did not apply latitudinal corrections to flux estimates since existing models (Evatt et al., 2020; Robertson et al., 2021, 2023) show significant discrepancies. These models are based on larger near-Earth objects (NEOs) and may not be applicable to smaller meteoroid populations. Additionally, whether a latitudinal variation exists for the flux of small objects from the main belt remains uncertain, and such corrections would be negligible for hot desert sites, which are located at latitudes where models tend to converge (Evatt et al., 2020; Robertson et al., 2021, 2023).

Overall, the CSC flux aligns well with other estimates, suggesting a relatively stable bulk meteorite flux over the past 2 Myr. The two notable exceptions are the extreme values of 24 and 166 meteorites >20 g per

19455100, 0, Downloaded from https://onlinelibrary.wiley.com/doi/10.1111/maps.70125 by Carine Sadaka - Cochrane France , Wiley Online Library on [09/03/2026]. See the Terms and Conditions (https://onlinelibrary.wiley.com/terms-and-conditions) on Wiley Online Library for rules of use; OA articles are governed by the applicable Creative Commons License

TABLE 3. Meteorite recovery statistics, mass distribution, and local flux estimate across different studies (Flux unit: meteorites per km^2 per Myr).

Location	Covered area (km^2)	N of meteorites used	Slope of mass distribution (1–1000 g)	Covered time scale	Size range	Local flux in size range	Local flux >20 g	References
Canada	1.26×10^6	56	−0.49	Present-day	>1 g	83	59	Halliday et al. (1989)
Antarctica	3022[a]	13,178[a]	−0.51[b]	Last 100 kyr	>50 g	26 [18–37]	41 [28–59]	Evatt et al. (2020), Jull et al. (2006)
Roosevelt County, USA	10.8	39[c]	−0.54	Last 50 kyr	>10 g	116	79	Bland et al. (1996)
Nullarbor Region, Australia	51.4	226[c]	−0.58	Last 50 kyr	>10 g	36	24	Bland et al. (1996), Jull et al. (2006), Jull et al. (2010)
Sahara Desert	>3000	316[c]	−0.67	Last 50 kyr	>10 g	95	60	Bland et al. (1996), Jull et al. (2006)
El Médano, Chile	1.5	213[c]	−0.59[b]	Last 2 Myr	>10 g	222 ± 15	166 ± 13	Hutzler et al. (2016), Drouard et al. (2019)
Catalina, Chile	6.8	1599	−0.71	Last 2 Myr	>20 g	74 ± 9	74 ± 9	Sadaka et al. (2025), This study

Note: Uncertainties for CSC and EMSC are given as $\sqrt{(n)}$. Values from Bland et al. (1996) have uncertainties of a factor of 2–3 and the value of Halliday et al. (1989) a factor of 2.
[a]Results as sum from 13 systematically searched areas (Evatt et al., 2020).
[b]Using MBDB data as of July 2025.
[c]After pairing.

km^2 per Myr, reported for the Nullarbor Region and the EMSC, respectively (Table 3). The elevated flux observed in the EMSC may result from the sampling strategy, as the systematic meteorite collection was conducted over 25 small separate areas totaling only 1.5 km^2 (Hutzler et al., 2016). These 25 individual areas are small (~0.06 km^2) compared to the typical size of a meteorite fall strewn field (~km^2), leading to an overestimation of the meteorite density (see Benoit et al. (2000) for a discussion on this statistical effect). In contrast, the anomalously low flux reported for the Nullarbor Region may reflect the limited terrestrial ages data set available at the time of the Bland et al. (1996) study and the lack of systematic meteorite collection in this desert. To refine this estimate, we used the terrestrial ages of Nullarbor meteorites reported by Jull et al. (2010) to recalculate this flux, which yielded a value of ~47 meteorites >20 g per km^2 per Myr, bringing the Nullarbor flux estimate more in line with the broader range observed in other deserts.

Meteorite Flux Composition

Since ordinary chondrites (H, L, and LL chondrites) are the most abundant meteorite groups, accounting for ~84% of meteorites in the global collections (MBDB, July 2025), they represent a robust proxy to monitor possible changes in the composition of the meteorite flux to Earth over time. Kouvatsis and Hofmann (2019) suggested a mass dependence of the H/L ratio based on meteorites from Oman, Chile, Libya, and observed falls listed in the MBDB as of June 2018. However, when we consider an updated data set that includes meteorites documented in the MBDB as of July 2025, we obtain significantly different results showing no obvious dependence of the H/L ratio on the meteorite mass (Figure S4). In addition, Kouvatsis and Hofmann (2019) reported constant H/L ratios across the 10 g–1 kg mass range, which includes 99% of the meteorites classified in the CSC and 87% in the EMSC. Consequently, a mass-dependent bias cannot account for the variations observed in these collections. A Kolmogorov–Smirnov test performed on the mass distributions of H and L chondrites of the CSC (Figure S5) yields a p-value of 0.137, further indicating no statistically significant difference between the two populations. Therefore, variations in the H/L ratio observed across different collections should be interpreted in terms of variations in the composition of the meteorite flux rather than differences in the mass distributions of recovered meteorites.

To evaluate whether temporal changes in the composition of the meteorite flux have occurred, we examine the relative abundance of H chondrites over time. The total flux is approximated by the sum of H, L, and LL chondrites. Rather than using the H/L ratio, we apply the normalized ratio H/(H+L+LL), which is bounded between

19455100, 0, Downloaded from https://onlinelibrary.wiley.com/doi/10.1111/maps.70125 by Carine Sadaka - Cochrane France , Wiley Online Library on [09/03/2026]. See the Terms and Conditions (https://onlinelibrary.wiley.com/terms-and-conditions) on Wiley Online Library for rules of use; OA articles are governed by the applicable Creative Commons License

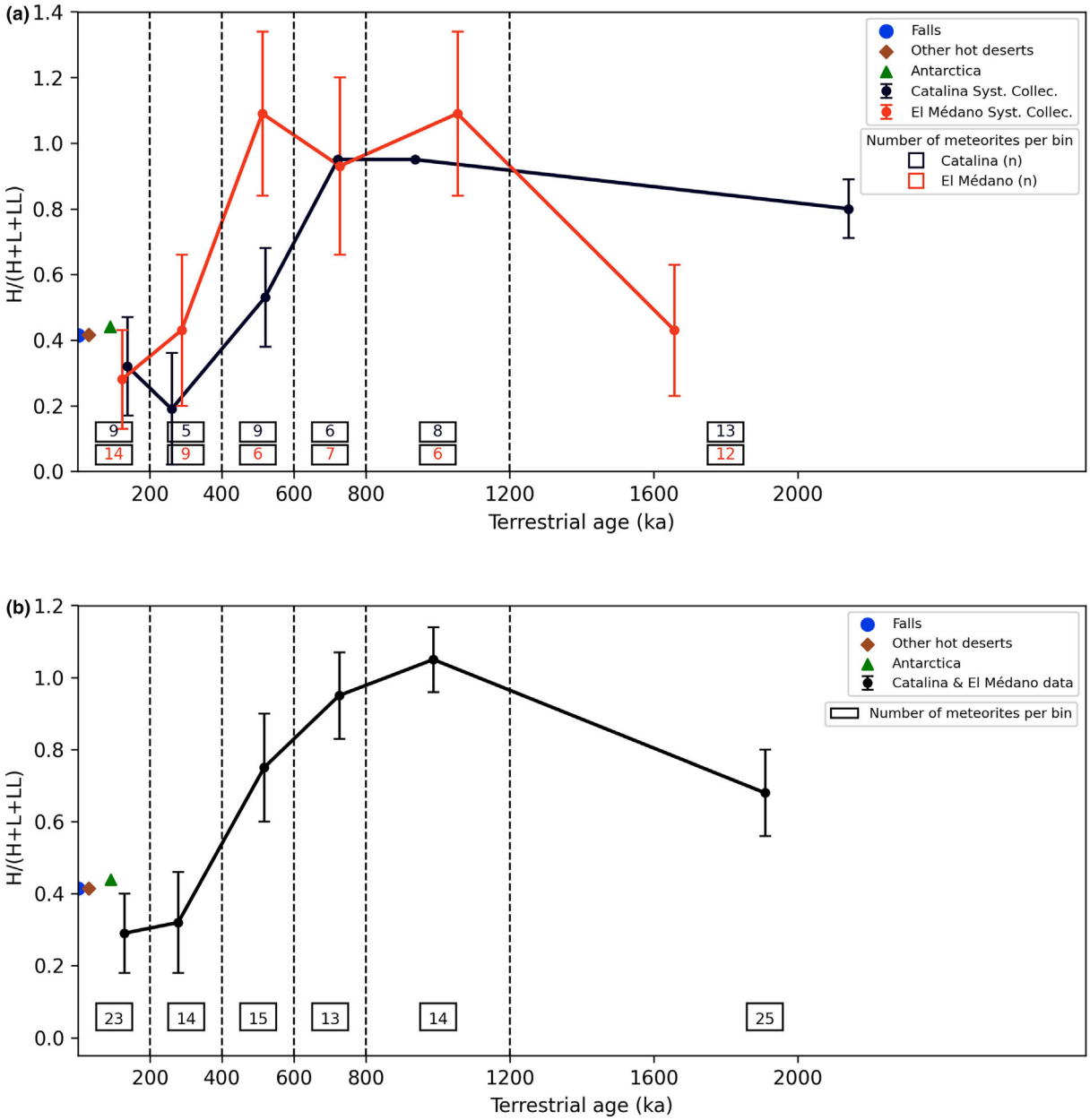

FIGURE 5. Relative abundance of H chondrites (with respect to H+L+LL chondrites) as a function of the terrestrial age. Data points are plotted at the average age of each bin. Vertical dashed lines show the limits of the age bins used. Numbers in boxes represent the number of samples in each bin. The blue dot shows the current ratio estimated from the meteorite fall population, the brown diamond is computed for the hot desert collections, and the green triangle corresponds to the Antarctic meteorite collection (all three using MBDB data as of July 2025; uncertainties shown or too small). See the text for more details. (a) Includes terrestrial ages of CSC and EMSC plotted separately. The value exceeding 1 in the 400–600 and 800–1200 ka bins for the EMSC is a statistical artifact of the correction applied to match the ratio of the whole EMSC collection (see text). (b) Includes combined terrestrial ages of the CSC and EMSC (total number = 104).

0 and 1, ensuring more consistent comparisons. To account for the potential bias introduced by our random sampling within each collection, values were corrected by a scaling factor so that the overall H/(H+L+LL) ratio of our random selection matches the H/(H+L+LL) ratio estimated for the entire collection after pairing correction (CSC factor = 0.65/0.68 = 0.95 and EMSC factor = 0.60/0.46 = 1.30).

Figure 5a shows the H/(H+L+LL) ratio as a function of terrestrial age, plotted separately for EMSC and CSC.

19455100, 0, Downloaded from https://onlinelibrary.wiley.com/doi/10.1111/maps.70125 by Carine Sadaka - Cochrane France , Wiley Online Library on [09/03/2026]. See the Terms and Conditions (https://onlinelibrary.wiley.com/terms-and-conditions) on Wiley Online Library for rules of use; OA articles are governed by the applicable Creative Commons License

Data points represent the mean age of each bin, and uncertainties were calculated assuming a Poisson distribution. Note that the abovementioned correction applied for the overall H/(H+L+LL) ratio of the meteorite population may result in corrected values exceeding 1 in a few bins for the EMSC, as is the case for the 400–600 and 800–1200 ka intervals.

For comparison, we include the current H chondrite relative abundance estimated from the meteorite fall population covering the past ~200 years. We also report the ratios derived from hot desert meteorite finds with an average terrestrial age of ~12 ka (including meteorites from Northwest Africa [NWA], the Sahara, and Oman meteorites), as well as from Antarctic finds with an average terrestrial age of ~100 ka. All three data points were calculated using MBDB data as of July 2025, and average ages were taken from Drouard et al. (2019).

Except for the 400–600 ka bin, the H chondrite abundances of the CSC and EMSC are comparable (Figure 5a), indicating that the pattern observed by Drouard et al. (2019) in the EMSC does not reflect a local anomaly confined to a single collection, but rather a global trend. For this reason, we combined the two data sets in Figure 5b. This reveals that the fraction of H chondrites among Atacama meteorites amounts to ~30% for falls that occurred <400 kyr ago, which is slightly lower but still consistent with the ~40% abundance for recent falls, Antarctic meteorites, and hot deserts. However, the H chondrite abundance is significantly higher between 400 and 1200 ka, averaging 92% over that period. Beyond 1200 ka, the H chondrite fraction declines to 68% (Figure 5b).

Knowing that H, L, and LL chondrites exhibit different mineralogical compositions, they do not necessarily weather at the same rate. The main mineralogical difference is the metal abundance: 18.2 wt %, 8.45 wt%, and 2.94 wt% on average in H, L, and LL chondrites, respectively (Gattacceca et al., 2014). Oxidation of metal and troilite induces internal stress and volume expansion, leading to fracture development and fragmentation (Al-Kathiri et al., 2005; Bland et al., 1998). Consequently, owing to their higher metal content, H chondrites may be more susceptible to weathering than L and LL chondrites. Therefore, preferential removal of H chondrites due to weathering would decrease the H/(H+L+LL) ratio over time, whereas the opposite is observed in the data (Figure 5).

Meteorite weathering in the hyper-arid Atacama Desert may differ from that observed in other hot deserts. The only hypothesis that could favor the preservation of H versus L chondrites is that the higher metal content of the former would enhance their mechanical strength and resistance to wind abrasion and sandblasting. However, this hypothesis is refuted by a number of observations. Differences in weathering between ordinary chondrite groups primarily pertain to chemical alteration rather than physical breakdown (Bland et al., 1998; Velbel, 2012). Moreover, the mechanical behavior of ordinary chondrites is primarily controlled by microporosity and the density and orientation of shock-induced microcracks rather than by bulk metal content (Flynn et al., 2018). Because shock stages overlap among H, L, and LL chondrites, no systematic difference in resistance to wind abrasion is expected between these groups. In addition, the similar mass distributions of H and L chondrites in the CSC (Figure S5) suggest that there is no significant preferential fragmentation of H chondrites with respect to L or LL chondrites.

Although differences between ordinary chondrite groups are primarily chemical, chemical weathering is limited under the hyper-arid conditions in the Atacama, where physical weathering dominates. In contrast to other hot desert collections, no clear correlation is observed between terrestrial age and weathering grade for the Atacama meteorites (Figure S6). Meteorites with terrestrial ages spanning from a few hundred ka to over 1–2 Ma exhibit similar weathering grades, notably including some well-preserved meteorites (W1) that have old ages (>1 Ma). This suggests that weathering in the Atacama is not primarily controlled by the residence time on Earth, but rather by other petrographic properties. For instance, initial meteorite porosity, itself controlled by shock stage in equilibrated ordinary chondrites, was identified as the key factor controlling the weathering rate of meteorites from the San Juan DCA (Gattacceca et al., 2011). This is consistent with the suggestion of Sadaka et al. (2025) that physical weathering processes dominate over chemical alteration under hyper-arid Atacama conditions, while chemical weathering is the main driver in other hot deserts (Al-Kathiri et al., 2005; Bland et al., 1998). Taken together, these observations suggest that if they existed, preservation biases would rather favor the preservation of L and LL chondrites versus H chondrites. Therefore, such biases, if they are significant, cannot account for the long-term evolution of the H/(H+L+LL) ratio, which therefore reflects genuine variations in meteorite flux composition.

To further assess the potential influence of unresolved pairing on the increase of the H/(H+L+LL) ratio between 600 and 1200 ka, we performed an additional pairing reassessment for the 15 H chondrites in this time interval using the pairing model described in Sadaka et al. (2025). This approach integrates olivine and orthopyroxene compositions (Fa and Fs), magnetic susceptibility, petrographic type, distance between meteorites, terrestrial age, and CRE age. Out of the 15 H chondrites considered, only two show a high likelihood of being paired (Catalina 682 and Catalina 684) (Figure S7).

19455100, 0, Downloaded from https://onlinelibrary.wiley.com/doi/10.1111/maps.70125 by Carine Sadaka - Cochrane France , Wiley Online Library on [09/03/2026]. See the Terms and Conditions (https://onlinelibrary.wiley.com/terms-and-conditions) on Wiley Online Library for rules of use; OA articles are governed by the applicable Creative Commons License

Pairing of these two meteorites would not significantly modify the H/(H+L+LL) ratio or the overall interpretation, indicating that unresolved pairing is unlikely to significantly affect the observed signal.

In principle, an increase in the H/(H+L+LL) ratio may result either from an increase in the flux of H chondrites or from a reduction in the flux of L chondrites. While both scenarios would have the same effect on the ratio, there is no obvious mechanism capable of producing a transient decrease in the flux of a specific meteorite group. In contrast, transient increases in the flux of a given group are well explained by collisional events in the asteroid belt. We therefore interpret the higher H/(H+L+LL) values observed between ~600 and 1200 ka as reflecting a temporary increase in the H chondrite flux. It is noteworthy that this increase in the relative H flux is not resolvable in terms of bulk meteorite flux. In fact, the terrestrial age data set is not large enough to enable a robust computation of the bulk meteorite flux over sub-Myr time scales.

Finally, Figure 5 suggests that a change in the H chondrite abundance beyond 2 Ma cannot be excluded. However, the limited number of meteorites with terrestrial ages >2 Ma does not allow us to draw a robust conclusion. Assessing whether the change began earlier than 2 Ma would require a larger sample size.

According to recent dynamical studies (Brož, Vernazza, Marsset, Binzel, et al., 2024; Brož, Vernazza, Marsset, DeMeo, et al., 2024; Marsset et al., 2024), the H/(H+L+LL) ratio remained nearly constant over the last 3 Myr, which appears at odds with our conclusions based on data analysis. However, as new asteroids are being discovered, our knowledge of asteroid families in the belt is constantly being reassessed (Nesvorný et al., 2024). The current census is far from complete, especially for small families. Small asteroid families can become transient meteorite sources on relatively short time scales (~10^5 years), similar to the time scale for resonance-driven delivery to near-Earth space (e.g., Morbidelli & Gladman, 1998; Shober et al., 2025). Hence, it is not surprising that the origin of the observed relative flux variation in the Atacama data set cannot be explained solely by current collisional models, which mainly account for the dynamical evolution of the sizable S-type and C-type families believed to substantially contribute to the meteoroid flux in the inner solar system.

One plausible explanation is that minor recent collisions in near-Earth space, for example, between relatively small asteroids (<5–10 km) originating from Karin and $Koronis_2$ (H-chondrite sources) families (Brož, Vernazza, Marsset, DeMeo, et al., 2024) could cause a substantial change in the influx of objects colliding with Earth. It is conceivable that such small, recent families can skew the impact flux on time scales of a couple of hundred thousand years, but remain undetected by the present-day asteroidal surveys, which are complete only for objects larger than ~1 km in diameter. With the Rubin Observatory expected to discover 4 million asteroids in its first year of operation (Kurlander, 2025), identifying these smaller families should become feasible in the near future.

CONCLUSION

We investigated the terrestrial ages of meteorites from the Atacama Desert based on measurements of the cosmogenic nuclide ^{36}Cl in the metal phase of 51 ordinary chondrites from the Catalina Systematic Collection (CSC). The terrestrial ages are exceptionally old, with an average of 937 ka, making the CSC the oldest known meteorite collection on Earth.

To estimate the long-term meteorite flux to Earth, we combined terrestrial ages with pairing-corrected meteorite density estimates. This yields a meteorite flux of 74 ± 9 meteorites >20 g per km^2 per Myr over the last 2 Myr. This value is consistent with previous estimates from falls, Antarctica, and the hot deserts of Roosevelt County, Nullarbor Region, and the Sahara Desert, indicating that the long-term bulk meteorite flux has remained broadly constant for the past 2 Myr. However, our results reveal a change in the composition of the meteorite flux over this period, with an increase in the relative H chondrite abundance with respect to L and LL chondrites between 1200 and 400 ka, followed by a marked decline to current values in the last 400 kyr. This recent decrease cannot be explained by long-term dynamical models based on observation and modeling of large asteroid families. This suggests that short-term variations in the meteorite flux to Earth may be driven by additional processes such as transient contributions from a smaller, recently formed asteroid family in near-Earth space, which is not captured by the present-day asteroidal surveys.

In light of this study, future work will focus on measuring additional cosmic-ray exposure ages of Atacama meteorites and combining them with their terrestrial ages to provide a direct constraint on the ejection ages of the meteorites from their parent asteroids. This approach will help to better constrain the collisional events that may have driven the observed variations in the relative abundances of H and L chondrites over the last 2 Myr.

Acknowledgments—This work was partly supported by the CLASTS project (grant ANR-22-CE49-0013) of the French Agence Nationale de la Recherche, and the French Programme Nationale de Planétologie (INSU/

19455100, 0, Downloaded from https://onlinelibrary.wiley.com/doi/10.1111/maps.70125 by Carine Sadaka - Cochrane France , Wiley Online Library on [09/03/2026]. See the Terms and Conditions (https://onlinelibrary.wiley.com/terms-and-conditions) on Wiley Online Library for rules of use; OA articles are governed by the applicable Creative Commons License

CNES). We thank the Meteoritical Society for the Research Grant awarded in 2023 to the first author. Open access publication funding provided by COUPERIN CY26.

Conflict of Interest Statement—None of the authors have a conflict of interest to disclose.

Data Availability Statement—The data that support the findings of this study are openly provided in the manuscript and tables.

Editorial Handling—Dr. Michael Zolensky

REFERENCES

Al-Kathiri, A., Hofmann, B. A., Jull, A. J. T., and Gnos, E. 2005. Weathering of Meteorites from Oman: Correlation of Chemical and Mineralogical Weathering Proxies with ^{14}C Terrestrial Ages and the Influence of Soil Chemistry. *Meteoritics & Planetary Science* 40: 1215–39. https://doi.org/10.1111/j.1945-5100.2005.tb00185.x.

Benoit, P. H., Sears, D. W. G., Akridge, J. M. C., Bland, P. A., Berry, F. J., and Pillinger, C. T. 2000. The Non-Trivial Problem of Meteorite Pairing. *Meteoritics & Planetary Science* 35: 393–417. https://doi.org/10.1111/j.1945-5100.2000.tb01785.x.

Bland, P. A. 2001. Quantification of Meteorite Infall Rates from Accumulations in Deserts, and Meteorite Accumulations on Mars. In *Accretion of Extraterrestrial Matter throughout Earth's History*, edited by B. Schmitz, and B. Peucker-Ehrenbrink, 267–303. Berlin: Springer.

Bland, P. A., Sexton, A. S., Jull, A. J. T., Bevan, A. W. R., Berry, F. J., Thornley, D. M., Astin, T. R., Britt, D. T., and Pillinger, C. T. 1998. Climate and Rock Weathering: A Study of Terrestrial Age Dated Ordinary Chondritic Meteorites from Hot Desert Regions. *Geochimica et Cosmochimica Acta* 62: 3169–84. https://doi.org/10.1016/s0016-7037(98)00199-9.

Bland, P. A., Smith, T., Jull, T., Berry, F. J., Bevan, R., Cloudt, S., and Pillinger, C. T. 1996. The Flux of Meteorites to the Earth over the Last 50 000 Years. *Monthly Notices of the Royal Astronomical Society* 283: 551–565. https://doi.org/10.1093/mnras/283.2.551.

Bland, P. A., Spurný, P., Bevan, R., Howard, K. T., Towner, M. C., Benedix, G., Greenwood, R. C., et al. 2012. The Australian Desert Fireball Network: A New Era for Planetary Science. *Australian Journal of Earth Sciences* 59: 177–187. https://doi.org/10.1080/08120099.2011.595428.

Bottke, W. F., Brož, M., O'Brien, D. P., Campo Bagatin, A., Morbidelli, A., and Marchi, S. 2015. The Collisional Evolution of the Main Asteroid Belt. In *Asteroids IV*, 701–724. Tucson, AZ: Univ. of Arizona. https://doi.org/10.2458/azu_uapress_9780816532131-ch036.

Bottke, W. F., Morbidelli, A., Jedicke, R., Petit, J.-M., Levison, H. F., Michel, P., and Metcalfe, T. S. 2002. Debiased Orbital and Absolute Magnitude Distribution of the Near-Earth Objects. *Icarus* 156: 399–433. https://doi.org/10.1006/icar.2001.6788.

Brož, M., Vernazza, P., Marsset, M., Binzel, R. P., DeMeo, F., Birlan, M., Colas, F., et al. 2024. Source Regions of Carbonaceous Meteorites and Near-Earth Objects. *Astronomy and Astrophysics* 689: A183. https://doi.org/10.1051/0004-6361/202450532.

Brož, M., Vernazza, P., Marsset, M., DeMeo, F. E., Binzel, R. P., Vokrouhlický, D., and Nesvorný, D. 2024. Young Asteroid Families as the Primary Source of Meteorites. *Nature* 634: 566–571. https://doi.org/10.1038/s41586-024-08006-7.

Carruba, V., Burns, J. A., Bottke, W., and Nesvorný, D. 2003. Orbital Evolution of the Gefion and Adeona Asteroid Families: Close Encounters with Massive Asteroids and the Yarkovsky Effect. *Icarus* 162: 308–327. https://doi.org/10.1016/s0019-1035(02)00062-3.

Cervone, A., Topputo, F., Speretta, S., Menicucci, A., Turan, E., Di Lizia, P., Massari, M., et al. 2022. LUMIO: A CubeSat for Observing and Characterizing Micro-Meteoroid Impacts on the Lunar Far Side. *Acta Astronautica* 195: 309–317. https://doi.org/10.1016/j.actaastro.2022.03.032.

Clarke, J. D. A. 2006. Antiquity of Aridity in the Chilean Atacama Desert. *Geomorphology* 73: 101–114. https://doi.org/10.1016/j.geomorph.2005.06.008.

Colas, F., Zanda, B., Bouley, S., Jeanne, S., Malgoyre, A., Birlan, M., Blanpain, C., et al. 2020. FRIPON: A Worldwide Network to Track Incoming Meteoroids. *Astronomy & Astrophysics* 644: A53. https://doi.org/10.1051/0004-6361/202038649.

Corti, G., Zeoli, A., and Bonini, M. 2003. Ice-Flow Dynamics and Meteorite Collection in Antarctica. *Earth and Planetary Science Letters* 215: 371–78. https://doi.org/10.1016/S0012-821X(03)00440-0.

Dalcher, N., Caffee, M. W., Nishiizumi, K., Welten, K. C., Vogel, N., Wieler, R., and Leya, I. 2013. Calibration of Cosmogenic Noble Gas Production in Ordinary Chondrites Based on ^{36}Cl-^{36}Ar Ages. Part 1: Refined Produced Rates for Cosmogenic ^{21}Ne and ^{38}Ar. *Meteoritics & Planetary Science* 48: 1841–62. https://doi.org/10.1111/maps.12203.

Devillepoix, H. A. R., Bland, P. A., Sansom, E. K., Towner, M. C., Cupák, M., Howie, R. M., Hartig, B. A. D., Jansen-Sturgeon, T., and Cox, M. A. 2018. Observation of Metre-Scale Impactors by the Desert Fireball Network. *Monthly Notices of the Royal Astronomical Society (Print)* 483: 5166–78. https://doi.org/10.1093/mnras/sty3442.

Drouard, A., Gattacceca, J., Hutzler, A., Rochette, P., Braucher, R., Bourlès, D., Gounelle, M., et al. 2019. The Meteorite Flux of the Past 2 M.y. Recorded in the Atacama Desert. *Geology* 47: 673–76. https://doi.org/10.1130/g45831.1.

Dunai, T. J., González López, G. A., and Juez-Larré, J. 2005. Oligocene–Miocene Age of Aridity in the Atacama Desert Revealed by Exposure Dating of Erosion-Sensitive Landforms. *Geology* 33: 321. https://doi.org/10.1130/g21184.1.

Eugster, O. 2003. Cosmic-Ray Exposure Ages of Meteorites and Lunar Rocks and their Significance. *Geochemistry* 63: 3–30. https://doi.org/10.1078/0009-2819-00021.

Evatt, G. W., Smedley, A. R. D., Joy, K. H., Hunter, L., Tey, W. H., Abrahams, I. D., and Gerrish, L. 2020. The Spatial Flux of Earth's Meteorite Falls Found Via Antarctic Data. *Geology* 48: 683–87. https://doi.org/10.1130/G46733.1.

Farinella, P., Vokrouhlický, D., and Hartmann, W. K. 1998. Meteorite Delivery via Yarkovsky Orbital Drift. *Icarus* 132: 378–387. https://doi.org/10.1006/icar.1997.5872.

Farley, K. A., Vokrouhlický, D., Bottke, W. F., and Nesvorný, D. 2006. A Late Miocene Dust Shower from

19455100, 0, Downloaded from https://onlinelibrary.wiley.com/doi/10.1111/maps.70125 by Carine Sadaka - Cochrane France , Wiley Online Library on [09/03/2026]. See the Terms and Conditions (https://onlinelibrary.wiley.com/terms-and-conditions) on Wiley Online Library for rules of use; OA articles are governed by the applicable Creative Commons License

the Break-Up of an Asteroid in the Main Belt. *Nature* 439: 295–97. https://doi.org/10.1038/nature04391.

Flynn, G. J., Consolmagno, G. J., Brown, P., and Macke, R. J. 2018. Physical Properties of the Stone Meteorites: Implications for the Properties of their Parent Bodies. *Geochemistry* 78: 269–298. https://doi.org/10.1016/j.chemer.2017.04.002.

Fries, M., and Fries, J. 2010. Doppler Weather Radar as a Meteorite Recovery Tool. *Meteoritics & Planetary Science* 45: 1476–87. https://doi.org/10.1111/j.1945-5100.2010.01115.x.

Gattacceca, J., Suavet, C., Rochette, P., Weiss, B. P., Winklhofer, M., Uehara, M., and Friedrich, J. M. 2014. Metal Phases in Ordinary Chondrites: Magnetic Hysteresis Properties and Implications for Thermal History. *Meteoritics & Planetary Science* 49: 652–676. https://doi.org/10.1111/maps.12268.

Gattacceca, J., Valenzuela, M., Uehara, M., Jull, T., Giscard, M. D., Rochette, P., Braucher, R., et al. 2011. The Densest Meteorite Collection Area in Hot Deserts: The San Juan Meteorite Field (Atacama Desert, Chile). *Meteoritics & Planetary Science* 46: 1276–87. https://doi.org/10.1111/j.1945-5100.2011.01229.x.

Gladman, B. J., Migliorini, F., Morbidelli, A., Zappalà, V., Michel, P., Cellino, A., Froeschlé, C., Levison, H. F., Bailey, M., and Duncan, M. 1997. Dynamical Lifetimes of Objects Injected into Asteroid Belt Resonances. *Science* 277: 197–201. https://doi.org/10.1126/science.277.5323.197.

Graf, T., Caffee, M. W., Marti, K., Nishiizumi, K., and Ponganis, K. V. 2001. Dating Collisional Events: ^{36}Cl–^{36}Ar Exposure Ages of H-Chondritic Metals. *Icarus* 150: 181–88. https://doi.org/10.1006/icar.2000.6560.

Graf, T., and Marti, K. 1994. Collisional Records in LL-Chondrites. *Meteoritics* 29: 643–48. https://doi.org/10.1111/j.1945-5100.1994.tb00777.x.

Graf, T., and Marti, K. 1995. Collisional History of H Chondrites. *Journal of Geophysical Research* 100(E10): 21247–63. https://doi.org/10.1029/95je01903.

Halliday, I., Blackwell, A. T., and Griffin, A. A. 1989. The Flux of Meteorites on the Earth's Surface. *Meteoritics* 24: 173–78. https://doi.org/10.1111/j.1945-5100.1989.tb00959.x.

Hofmann, B. A., and Gnos, E. 2024. The Meteoritic Record of Arabia. *Geological Society of London, Special Publication* 550: SP550-2024-8. https://doi.org/10.1144/sp550-2024-8.

Huss, G. R. 1990. Meteorite Infall as a Function of Mass: Implications for the Accumulation of Meteorites on Antarctic Ice. *Meteoritics* 25(1): 41–56. https://doi.org/10.1111/j.1945-5100.1990.tb00969.x.

Hutzler, A. 2015. *The Flux of Meteorites on Earth: Contribution of Measuring the Concentration of Multiple Cosmogenic Nuclides, and Collections in Arid Areas*. Aix-en-Provence: Aix-Marseille Université. https://theses.fr/2015AIXM4302.

Hutzler, A., Gattacceca, J., Rochette, P., Braucher, R., Carro, B., Christensen, E., Cournede, C., et al. 2016. Description of a Very Dense Meteorite Collection Area in Western Atacama: Insight into the Long-Term Composition of the Meteorite Flux to Earth. *Meteoritics & Planetary Science* 51: 468–482. https://doi.org/10.1111/maps.12607.

Jiang, S., Lin, Y., and Zhang, H. 2004. Improvement of the Sample Preparation Method for AMS Measurement of ^{36}Cl in Natural Environment. *Nuclear Instruments and Methods in Physics Research Section B Beam Interactions with Materials and Atoms* 223-224: 318–322. https://doi.org/10.1016/j.nimb.2004.04.063.

Jones, J., Brown, P., Ellis, K. J., Webster, A. R., Campbell-Brown, M., Krzemenski, Z., and Weryk, R. J. 2005. The Canadian Meteor Orbit Radar: System Overview and Preliminary Results. *Planetary and Space Science* 53: 413–421. https://doi.org/10.1016/j.pss.2004.11.002.

Jull, A. J. T., Binzel, R. P., Walker, R. M., and Cameron, A. G. W. 2006. Terrestrial Ages of Meteorites. In *Meteorites and the Early Solar System II*, edited by D. S. Lauretta, and H. Y. McSween, 889–906. Tucson, AZ: University of Arizona Press.

Jull, A. J. T., McHargue, L. R., Bland, P. A., Greenwood, R. C., Bevan, A. W. R., Kim, K. J., LaMotta, S. E., and Johnson, J. A. 2010. Terrestrial Ages of Meteorites from the Nullarbor Region, Australia, Based on ^{14}C and ^{14}C-^{10}Be Measurements. *Meteoritics & Planetary Science* 45: 1271–83. https://doi.org/10.1111/j.1945-5100.2010.01289.x.

Kouvatsis, I., and Hofmann, B. A. 2019. A Statistical Analysis of the H/L Ratio of Ordinary Chondrite Finds and Falls: A Comparison of Oman Finds with Other Populations. *Meteoritics & Planetary Science* 55: 67–76. https://doi.org/10.1111/maps.13410.

Kurlander, J. A. 2025. Predictions of the LSST Solar System Yield: Near-Earth Objects, Main Belt Asteroids, Jupiter Trojans, and Trans-Neptunian Objects. *The Astronomical Journal* 170: 99. https://doi.org/10.5194/epsc-dps2025-418.

Leya, I., and Masarik, J. 2009. Cosmogenic Nuclides in Stony Meteorites Revisited. *Meteoritics & Planetary Science* 44: 1061–86. https://doi.org/10.1111/j.1945-5100.2009.tb00788.x.

Marsset, M., Vernazza, P., Brož, M., Thomas, C. A., DeMeo, F. E., Burt, B., Binzel, R. P., et al. 2024. The Massalia Asteroid Family as the Origin of Ordinary L Chondrites. *Nature* 634: 561–65. https://doi.org/10.1038/s41586-024-08007-6.

Marti, K., and Graf, T. 1992. Cosmic-Ray Exposure History of Ordinary Chondrites. *Annual Review of Earth and Planetary Sciences* 20: 221–243. https://doi.org/10.1146/annurev.ea.20.050192.001253.

McGee, D., and Mukhopadhyay, S. 2013. Extraterrestrial He in Sediments: From Recorder of Asteroid Collisions to Timekeeper of Global Environmental Changes. In *The Noble Gases as Geochemical Tracers. Advances in Isotope Geochemistry*. Berlin: Springer.

Merchel, S., Bremser, W., Alfimov, V., Arnold, M., Aumaître, G., Benedetti, L., Bourlès, D. L., et al. 2011. Ultra-Trace Analysis of 36Cl by Accelerator Mass Spectrometry: An Interlaboratory Study. *Analytical and Bioanalytical Chemistry* 400: 3125–32. https://doi.org/10.1007/s00216-011-4979-2.

Merchel, S., and Herpers, U. 1999. An Update on Radiochemical Separation Techniques for the Determination of Long-Lived Radionuclides Via Accelerator Mass Spectrometry. *Radiochimica Acta* 84: 215–220. https://doi.org/10.1524/ract.1999.84.4.215.

Minton, D. A., and Malhotra, R. 2010. Dynamical Erosion of the Asteroid Belt and Implications for Large Impacts in the Inner Solar System. *Icarus* 207: 744–757. https://doi.org/10.1016/j.icarus.2009.12.008.

Moore, A. K., and Granger, D. E. 2019. Calibration of the Production Rate of Cosmogenic ^{36}Cl from Fe. *Quaternary Geochronology* 51: 87–98. https://doi.org/10.1016/j.quageo.2019.02.002.

19455100, 0, Downloaded from https://onlinelibrary.wiley.com/doi/10.1111/maps.70125 by Carine Sadaka - Cochrane France , Wiley Online Library on [09/03/2026]. See the Terms and Conditions (https://onlinelibrary.wiley.com/terms-and-conditions) on Wiley Online Library for rules of use; OA articles are governed by the applicable Creative Commons License

Morbidelli, A., and Gladman, B. 1998. Orbital and Temporal Distributions of Meteorites Originating in the Asteroid Belt. *Meteoritics & Planetary Science* 33: 999–1016. https://doi.org/10.1111/j.1945-5100.1998.tb01707.x.

Morbidelli, A., and Vokrouhlický, D. 2003. The Yarkovsky-Driven Origin of Near-Earth Asteroids. *Icarus* 163: 120–134. https://doi.org/10.1016/s0019-1035(03)00047-2.

Nesvorný, D., Roig, F., Vokrouhlický, D., and Brož, M. 2024. Catalog of Proper Orbits for 1.25 Million Main-Belt Asteroids and Discovery of 136 New Collisional Families. *The Astrophysical Journal Supplement Series* 274: 25. https://doi.org/10.3847/1538-4365/ad675c.

Nica, N., Cameron, J., and Singh, B. 2012. Nuclear Data Sheets for a = 36. *Nuclear Data Sheets* 113: 1–155. https://doi.org/10.1016/j.nds.2012.01.001.

Nishiizumi, K. 1987. ^{53}Mn, ^{26}Al, ^{10}Be and ^{36}Cl in Meteorites: Data Compilation. *International Journal of Radiation Applications and Instrumentation. Part D. Nuclear Tracks and Radiation Measurements* 13: 209–273. https://doi.org/10.1016/1359-0189(87)90038-0.

Nishiizumi, K., and Caffee, M. W. 2001. Exposure Histories of Lunar Meteorites Dhofar 025, 026, and Northwest Africa 482. *Meteoritics & Planetary Science* 36: A482. Abstract presented at the 64th Annual Meeting of the Meteoritical Society.

Nishiizumi, K., Elmore, D., and Kubik, P. W. 1989. Update on Terrestrial Ages of Antarctic Meteorites. *Earth and Planetary Science Letters* 93: 299–313. https://doi.org/10.1016/0012-821x(89)90029-0.

Nishiizumi, K., Okazaki, R., Park, J., Nagao, K., Masarik, J., and Finkel, R. C. 2002. Exposure and Terrestrial Histories of Dhofar 019 Martian Meteorite. *33rd Lunar and Planetary Science Conference*, abstract #1366.

Pfeiffer, M., Morgan, A. M., Heimsath, A. M., Jordan, T. E., Howard, A. D., and Amundson, R. 2021. Century Scale Rainfall in the Absolute Atacama Desert: Landscape Response and Implications for Past and Future Rainfall. *Quaternary Science Reviews* 254: 106797. https://doi.org/10.1016/j.quascirev.2021.106797.

Pinto, G. A., Tavernier, A., Gattacceca, J., Corgne, A., Valenzuela, M., Luais, B., Flores, L., Olivares, F., and Marrocchi, Y. 2024. Dense Collection Areas and Terrestrial Alteration of Meteorites in the Atacama Desert. *Meteoritics & Planetary Science* 59: 351–367. https://doi.org/10.1111/maps.14125.

Pourkhorsandi, H., Gattacceca, J., Rochette, P., D'Orazio, M., Kamali, H., Avillez, R., Letichevsky, S., et al. 2019. Meteorites from the Lut Desert (Iran). *Meteoritics & Planetary Science* 54: 1737–63. https://doi.org/10.1111/maps.13311.

Robertson, D., Ozerov, A., Wheeler, L., Pokorný, P., Granvik, M., and Rumpf, C. 2023. Erratum: 'Latitude Variation of Flux and Impact Angle of Asteroid Collisions with Earth and the Moon' (2021, PSJ, 2, 88). *The Planetary Science Journal* 4: 19. https://doi.org/10.3847/PSJ/aca1a7.

Robertson, D., Pokorný, P., Granvik, M., Wheeler, L., and Rumpf, C. 2021. Latitude Variation of Flux and Impact Angle of Asteroid Collisions with Earth and the Moon. *The Planetary Science Journal* 2: 88. https://doi.org/10.3847/psj/abefda.

Rojas, J., Duprat, J., Engrand, C., Dartois, E., Delauche, L., Godard, M., Gounelle, M., Carrillo-Sánchez, J. D., Pokorný, P., and Plane, J. M. C. 2021. The Micrometeorite Flux at Dome c (Antarctica), Monitoring the Accretion of Extraterrestrial Dust on Earth. *Earth and Planetary Science Letters* 560(April): 116794. https://doi.org/10.1016/j.epsl.2021.116794.

Rubin, A. E. 2018. Mechanisms Accounting for Variations in the Proportions of Carbonaceous and Ordinary Chondrites in Different Mass Ranges. *Meteoritics & Planetary Science* 53: 2181–92. https://doi.org/10.1111/maps.13117.

Rubincam, D. P. 2000. Radiative Spin-Up and Spin-Down of Small Asteroids. *Icarus* 148: 2–11. https://doi.org/10.1006/icar.2000.6485.

Sadaka, C., Gattacceca, J., Gounelle, M., Roskosz, M., Lagain, A., Tartese, R., Bonal, L., Maurel, C., Martinez, R., and Valenzuela, M. 2025. Systematic Meteorite Collection in the Catalina Dense Collection Area (Chile): Description and Statistics. *Meteoritics & Planetary Science* 60: 308–323. https://doi.org/10.1111/maps.14307.

Schimmelpfennig, I., Benedetti, L., Finkel, R., Pik, R., Blard, P.-H., Bourlès, D., Burnard, P., and Williams, A. 2009. Sources of in-Situ ^{36}Cl in Basaltic Rocks. Implications for Calibration of Production Rates. *Quaternary Geochronology* 4: 441–461. https://doi.org/10.1016/j.quageo.2009.06.003.

Schmitz, B., Heck, P. R., Alvarez, W., Kita, N. T., Rout, S. S., Cronholm, A., Defouilloy, C., Martin, E., Smit, J., and Terfelt, F. 2017. Meteorite Flux to Earth in the Early Cretaceous as Reconstructed from Sediment-Dispersed Extraterrestrial Spinels. *Geology* 45: 807–810. https://doi.org/10.1130/g39297.1.

Schmitz, B., Tassinari, M., and Peucker-Ehrenbrink, B. 2001. A Rain of Ordinary Chondritic Meteorites in the Early Ordovician. *Earth and Planetary Science Letters* 194: 1–15. https://doi.org/10.1016/s0012-821x(01)00559-3.

Shober, P. M., Devillepoix, H. A. R., Vaubaillon, J., Anghel, S., Deam, S. E., Sansom, E. K., Colas, F., Zanda, B., Vernazza, P., and Bland, P. 2025. Perihelion History and Atmospheric Survival as Primary Drivers of the Earth's Meteorite Record. *Nature Astronomy* 9. https://doi.org/10.1038/s41550-025-02526-6.

Stone, J. O. 2000. Air Pressure and Cosmogenic Isotope Production. *Journal of Geophysical Research: Solid Earth* 105: 23753–59. https://doi.org/10.1029/2000jb900181.

Tauseef, M., Leya, I., Gattacceca, J., Hofmann, B., Szidat, S., and Braucher, R. 2024. ^{14} C and ^{14}C-^{10}Be Terrestrial Age Dating System for Meteorites—New Data for Four Recently Fallen Meteorites. *Meteoritics & Planetary Science* 59: 1219–35. https://doi.org/10.1111/maps.14144.

Tauseef, M., Leya, I., Gattacceca, J., Szidat, S., Braucher, R., Kruttasch, P. M., and Zappatini, A. 2025. Evaluating ^{14}C and ^{14}C/^{10}Be Terrestrial Age Dating Systems for Meteorites Using Experimental Data and Model Calculations. *Meteoritics & Planetary Science* 60: 1263–83. https://doi.org/10.1111/maps.14355.

Tauseef, M., Leya, I., and Hofmann, B. 2025. Cosmic Ray Exposure Ages and Pre-Atmospheric Shielding of Omani Meteorites: Implications for ^{14}C and ^{14}C/^{10}Be Terrestrial Ages of Meteorites from Hot and Cold Deserts. *Meteoritics & Planetary Science* 60: 2184–96. https://doi.org/10.1111/maps.70029.

Terfelt, F., and Schmitz, B. 2021. Asteroid Break-Ups and Meteorite Delivery to Earth the Past 500 Million Years. *Proceedings of the National Academy of Sciences of the United States of America* 118: e2020977118. https://doi.org/10.1073/pnas.2020977118.

19455100, 0, Downloaded from https://onlinelibrary.wiley.com/doi/10.1111/maps.70125 by Carine Sadaka - Cochrane France , Wiley Online Library on [09/03/2026]. See the Terms and Conditions (https://onlinelibrary.wiley.com/terms-and-conditions) on Wiley Online Library for rules of use; OA articles are governed by the applicable Creative Commons License

Velbel, M. A. 2012. Terrestrial Weathering of Ordinary Chondrites in Nature and Continuing during Laboratory Storage and Processing: Review and Implications for Hayabusa Sample Integrity. *Meteoritics & Planetary Science* 49: 154–171. https://doi.org/10.1111/j.1945-5100.2012.01405.x.

Vogt, S., and Herpers, U. U. 1988. Radiochemical Separation Techniques for the Determination of Long-Lived Radionuclides in Meteorites by Means of Accelerator-Mass-Spectrometry. *Fresenius' Zeitschrift für Analytische Chemie* 331: 186–88. https://doi.org/10.1007/bf01105164.

Welten, K. C., Caffee, M. W., Kress, M. E., Giscard, M. D., Jull, T., Harvey, R. P., and Schutt, J. 2024. Cosmogenic Radionuclides in Meteorites from the Otway Massif Blue Ice Area, Antarctica: An Unusual, Well-Preserved H5 Chondrite Strewn Field. *Meteoritics & Planetary Science* 59: 3056–71. https://doi.org/10.1111/maps.14264.

Welten, K. C., Folco, L., Nishiizumi, K., Caffee, M. W., Grimberg, A., Meier, M. M. M., and Kober, F. 2008. Meteoritic and Bedrock Constraints on the Glacial History of Frontier Mountain in Northern Victoria Land, Antarctica. *Earth and Planetary Science Letters* 270: 308–315. https://doi.org/10.1016/j.epsl.2008.03.052.

Welten, K. C., Nishiizumi, K., Finkel, R. C., Hillegonds, D. J., Jull, T., Franke, L., and Schultz, L. 2004. Exposure History and Terrestrial Ages of Ordinary Chondrites from the Dar al Gani Region, Libya. *Meteoritics & Planetary Science* 39: 481–498. https://doi.org/10.1111/j.1945-5100.2004.tb00106.x.

Wyatt, S. P., and Whipple, F. L. 1950. The Poynting-Robertson Effect on Meteor Orbits. *The Astrophysical Journal* 111: 134. https://doi.org/10.1086/145244.

Zekollari, H., Goderis, S., Debaille, V., Van Ginneken, M., Gattacceca, J., Jull, A. J. T., Lenaerts, J. T. M., Yamaguchi, A., Huybrechts, P., and Claeys, P. 2019. Unravelling the High-Altitude Nansen Blue Ice Field Meteorite Trap (East Antarctica) and Implications for Regional Palaeo-Conditions. *Geochimica et Cosmochimica Acta* 248: 289–310. https://doi.org/10.1016/j.gca.2018.12.035.

Zolensky, M., Bland, P., Brown, P., and Halliday, I. 2006. Flux of Extraterrestrial Materials. In *Meteorites and the Early Solar System II*, edited by H. Y. Mcsween. Tucson, AZ: University of Arizona Press.

Zolensky, M. E., Wells, G. L., and Rendell, H. M. 1990. The Accumulation Rate of Meteorite Falls at the Earth's Surface: The View from Roosevelt County, New Mexico. *Meteoritics* 25: 11–17. https://doi.org/10.1111/j.1945-5100.1990.tb00965.x.

SUPPORTING INFORMATION

Additional supporting information may be found in the online version of this article.

Figure S1. $^{20}Ne/^{22}Ne$ as a function of $^{21}Ne/^{22}Ne$ for 46 measurements (including replicas) of 39 ordinary chondrites from the Catalina Systematic Collection and the El Médano Systematic Collection. Also shown is the atmospheric component with $^{20}Ne/^{22}Ne = 9.80$ and $^{21}Ne/^{22}Ne = 0.02904$ (Ozima & Podosek, 2002) and fractionated Solar Wind (fSW) with $^{20}Ne/^{22}Ne = 11.16$ and $^{21}Ne/^{22}Ne = 0.03$ (Grimberg et al., 2006). All data can be found in Table S1.

Figure S2. Distribution of the cosmic-ray exposure (CRE) ages of ordinary chondrites compiled from Graf and Marti (1994, 1995) and Marti and Graf (1992), together with CRE ages of the Atacama meteorites determined in this study ($n = 39$). The minimum CRE age of 1.5 Ma (five half-lives of ^{36}Cl), required to attain ^{36}Cl into saturation, is represented by the dashed red line.

Figure S3. Comparative overview of the meteorite flux values (meteorites >20 g per km^2 per Myr) reported in different studies.

Figure S4. H/L ratios as a function of mass in log scale for observed falls and hot deserts meteorites from Chile and Libya. Each data point represents the H/L ratio in each mass interval, with lower mass limit as x-axis data. Error bars calculated as the standard deviation of the Poisson distribution. Data from MBDB as of July 2025. Slopes for falls, Chile, and Libya are −0.043 ($R^2 = 0.440$); −0.056 ($R^2 = 0.247$); 0.072 ($R^2 = 0.352$), respectively.

Figure S5. Mass distribution of H chondrites ($n = 271$) and L chondrites ($n = 131$) from the Catalina Systematic Collection (Sadaka et al., 2025) on a log-log scale. Kolmogorov-Smirnov test on the two distributions: p-value = 0.137.

Figure S6. Terrestrial age as a function of the weathering grade of Catalina and El Médano meteorites ($n = 104$).

Figure S7. Distribution of the pairing likelihood factor P for the 15 H chondrites in the 600–1200 ka terrestrial age interval using the pairing model described in Sadaka et al. (2025).

Table S1. Neon isotopic ratios and cosmic-ray exposure (CRE) ages of the Catalina and El Médano meteorites measured in this study ($n = 39$). Samples marked (1) and (2) correspond to replicate measurements; their average was used for figures and statistics.

Table S2. Sample details and recalculated terrestrial ages of meteorites from the El Médano Systematic collection (EMSC), based on data originally reported by Drouard et al. (2019).

19455100, 0, Downloaded from https://onlinelibrary.wiley.com/doi/10.1111/maps.70125 by Carine Sadaka - Cochrane France , Wiley Online Library on [09/03/2026]. See the Terms and Conditions (https://onlinelibrary.wiley.com/terms-and-conditions) on Wiley Online Library for rules of use; OA articles are governed by the applicable Creative Commons License

Terrestrial ages of meteorites from the Atacama Desert (Chile) and insights into the past meteorite flux to Earth

Carine SADAKA[1*], Jérôme GATTACCECA[1], Florian DUMAS[1,2,3], Régis BRAUCHER[1], ASTER Team[1], Ingo LEYA[4], Mohammad TAUSEEF[4], Pierre-Henri BLARD[5], David BEKAERT[5], Evelyn FÜRI[5], Laurent ZIMMERMANN[5], Anthony LAGAIN[1,6,7], Hadrien A. R. DEVILLEPOIX[7], Matthieu GOUNELLE[8]

SUPPLEMENTARY MATERIAL

S1. Methods: Analytical procedure for neon measurements

S1.1. ^{21}Ne production rate

For cosmic-ray exposure (CRE) age calculations, we use the $(^{22}Ne/^{21}Ne)_{cos}$ –$^{21}Ne_{cos}$ method for stony meteorites (Leya and Masarik, 2009). The cosmogenic $(^{22}Ne/^{21}Ne)_{cos}$ and $^{21}Ne_{cos}$ values were derived using a two-component deconvolution, assuming a cosmogenic endmember with $(^{22}Ne/^{21}Ne)_{cos}$ = 0.82 (Dalcher et al., 2013). Atmospheric neon ($^{20}Ne/^{22}Ne$ = 9.80 and $^{21}Ne/^{22}Ne$ = 0.02904; Ozima and Podosek, 2002) was used as the trapped endmember for most samples. For samples plotting outside the air-cosmogenic mixing field (Figure S1) a fractionated solar wind composition ($^{20}Ne/^{22}Ne$ = 11.16 and $^{21}Ne/^{22}Ne$ = 0.03; Grimberg et al., 2006) was adopted. Only the appropriate endmember was used for each sample, resulting in a single corrected cosmogenic neon value (Table S1). We use these corrected $(^{22}Ne/^{21}Ne)_{cos}$ ratios to calculate the ^{21}Ne production rates, $P(^{21}Ne_{cos})$ (10^{-8} cm^3 STP g^{-1} Ma^{-1}) based on the empirical relationship established by Dalcher et al. (2013):

$$P(^{21}Ne_{cos}) = F / [49.2 - 99.3 \times (^{22}Ne_{cos}/^{21}Ne_{cos}) + 51.8 \times (^{22}Ne_{cos}/^{21}Ne_{cos})^2]$$

Here, *F* is a scaling factor that corrects for the differences in bulk chemical composition by accounting for variations in target element abundances (e.g., Mg, Al, Si, Fe) that influence spallation reactions. For bulk samples, *F* = 0.93, 1.00, and 1.03, for H, L, and LL chondrites,

757 respectively (Dalcher et al., 2013). Since this correlation is calibrated for bulk ordinary
758 chondrite samples, we adjusted the *F* value to either the cleaned bulk fraction or the separated
759 silicate fraction.
760
761 S1.2. Sample preparation and production rate corrections
762 At the University of Bern, neon analyses were performed on ~20 mg fragments of the bulk
763 fraction of meteorite samples. Each fragment was cleaned in two successive ultrasonic baths in
764 acid at room temperature, each lasting one hour: first leaching in 1M HCl to remove troilite and
765 residual metal, followed by a 67% ethanolamine thioglycolate (EATG) solution to remove iron
766 oxides and hydroxides. For these samples, we evaluated the opaque mineral fraction that had
767 been transformed into oxides and hydroxides (and therefore dissolved during EATG treatment)
768 by comparing the meteorite's saturation magnetization M_S (from Kuzina et al., 2025) with that
769 of fresh H chondrite falls ($M_{S,falls}$ = 40.46 A.m^2/kg, from Gattacceca et al., 2014). The factor *F*
770 was then computed for each meteorite as:

771 $$F = \left(F_{bulk} \times \frac{M_s}{M_{s\,falls}}\right) + \left(1 - \frac{M_s}{M_{s\,falls}}\right) \times F_{silicate}$$

772
773 At the Centre de Recherches Pétrographiques et Géochimiques (CRPG), neon was
774 extracted from the silicate fraction. After crushing, magnetic separation, and sieving to isolate
775 non-magnetic grains between 400-800 µm, the silicate grains were cleaned in an ultrasonic bath
776 in 1M HCl at 60°C for 24h to remove troilite and residual metal. This was followed by an
777 ultrasonic bath in a 67% EATG solution at room temperature for 24h to remove iron oxides and
778 hydroxides.
779 For these samples, the production rate of ^{21}Ne was corrected with a factor of 1.40 for H
780 chondrites, 1.29 for L chondrites, and 1.25 for LL-chondrites (Leya and Masarik, 2009).
781

S1.3. Neon measurements at the University of Bern

Measurements of the Ne abundance and isotopic composition were conducted following the protocol for stony meteorites described in Leya et al. (2013) and Tauseef et al. (2024; 2025). In summary, ~20 mg of silicates were wrapped in aluminum foil and loaded into the noble gas extraction and cleaning line. The samples were preheated in vacuum at ~80°C for 48 hours to remove absorbed atmospheric gases. The samples were degassed in a molybdenum crucible held at 1750°C for 20 minutes. Blanks were measured before and after sample extractions. Typical blanks (in 10^{-12} cm^3 STP) are ~0.86, 0.096, and 0.26 for ^{20}Ne, ^{21}Ne, and ^{22}Ne, respectively. On average, blanks for ^{20}Ne, ^{21}Ne, and ^{22}Ne contributed ~6%, 1%, and 2% to the measured sample gas amounts, respectively. Data were corrected for interferences and instrument nonlinearities. Calibration with known amounts of standard gases with atmospheric isotope composition were performed regularly. Released gases were cleaned using SAES ® getters operating at various temperatures between 180 and 450°C. The He-Ne fraction was isolated from the Ar fraction using activated charcoals held at the temperature of liquid nitrogen. The Ne fraction was measured in a static sector field mass spectrometer built in-house at the University of Bern. The gas was further cleaned, and the background was further reduced from the remaining impurities using an additional Ti getter (to reduce H_2) and an activated charcoal held at the temperature of liquid nitrogen to minimize hydrocarbons and Ar. Gas concentrations were calculated by peak height comparison between samples and standards. The associated uncertainties for the noble gas data include statistical uncertainties from the measurements, uncertainties related to blank corrections, and to the corrections for mass fractionation. Moreover, a systematic uncertainty of 4% for gas concentrations and 2% for isotope ratios were added (see Leya et al., 2013 for further details).

S1.4. Neon measurements at CRPG, Nancy

807 At CRPG's noble gas facility, meteorite fragments weighing between 1.05 and 2.2 mg
808 (average 1.48 ± 0.29; n = 31) were loaded into a clean, ZnSe-windowed laser cell connected to
809 the purification line of either a Noblesse–HR or a Helix MC Plus noble gas mass spectrometer.
810 In both cases, the laser chamber was evacuated to ~10^{-9} bar and heated to ~100 °C overnight to
811 desorb atmospheric gases. Procedural blanks were measured prior to sample analysis to verify
812 the absence of leaks or degassing from the samples. Gases were then extracted by heating the
813 samples under vacuum with a power-modulated CO_2 infrared laser (λ = 10.6 μm; Humbert et
814 al., 2000; Gamblin et al., 2024). Following each extraction, the formation of a molten silicate
815 spherule confirmed that the melting point had been reached and that ≥99% of the gas was
816 released (Humbert et al., 2000).
817
818 S1.4. 1. Noblesse–HR noble gas mass spectrometer
819 For Ne analyses on the Noblesse–HR 3F4M noble gas mass spectrometer (Nu
820 Instruments), extracted gases were purified using a hot (600 ºC) Ti sponge getter and two SAES
821 ® Ti-Al getters held at room temperature. Argon was separated from Ne by adsorption onto a
822 charcoal finger held at –196 °C using liquid nitrogen. Neon abundances and isotopic ratios were
823 determined in multi-collection mode, with a trap current of 150 μA, using source settings
824 optimized to maximize sensitivity, minimize instrumental mass fractionation, and achieve high
825 mass resolution and mass resolving power (Zimmermann et al., 2025). The three Ne isotopes
826 were measured simultaneously on three ion counters ($^{22}Ne^+$ on IC0, $^{21}Ne^+$ on IC2, $^{20}Ne^+$ on
827 IC3) for 25 cycles. Throughout the analytical sequence, a charcoal finger held at –196 °C and
828 two GP-50 SAES getters, connected to the source and detector blocks, minimized contributions
829 from doubly charged $^{40}Ar^{2+}$ and $^{44}CO_2^{2+}$ to the $^{20}Ne^+$ and $^{22}Ne^+$ signals, respectively. The $^{40}Ar^{2+}$
830 signal was monitored during each cycle; however, because the $^{40}Ar^{2+}$ peak is partially resolved
831 from that of $^{20}Ne^+$, no correction was applied to the ^{20}Ne signal. The $^{44}CO_2^+$ signal was also

monitored during each cycle by peak-jumping, and the $^{22}Ne^{+}$ signal was corrected for potential $^{44}CO_2^{++}$ interference based on the instrument's $^{44}CO_2^{2+}/^{44}CO_2^{+}$ ionization ratio. However, the contribution of $^{44}CO_2^{++}$ to the $^{22}Ne^{+}$ signal was negligible. The $^{21}Ne^{+}$ signal was measured at the peak center, and no hydride ($^{20}NeH^{+}$) correction was applied due to the low hydrogen background maintained by the getters. Neon abundances and isotope ratios were calculated based on the mass spectrometer sensitivity and instrumental mass fractionation, estimated using air aliquots analyzed before and during the measurement period. On average, blanks for ^{20}Ne, ^{21}Ne, and ^{22}Ne contributed ~3.8%, 0.01%, and 0.5% to the measured sample gas amounts, respectively.

S1.4.2. Helix MC Plus noble gas mass spectrometer

For Ne analyses on the Helix MC Plus noble gas mass spectrometer (Thermo Fisher Scientific), daily blanks and standards were run before and during each analytical session for blank correction and mass discrimination monitoring. Typical blanks (in 10^{-12} cm^3 STP) were ~ 4.8, 0.015, and 0.56 for ^{20}Ne, ^{21}Ne, and ^{22}Ne, respectively. On average, blanks for ^{20}Ne, ^{21}Ne, and ^{22}Ne contributed ~5.9%, 0.04%, and 1.2% to the measured sample gas amounts, respectively.

Extracted gases were first exposed to a charcoal trap cooled to liquid nitrogen temperature to concentrate heavy noble gases (notably argon). The remaining gas fraction was then passed over two sets of titanium-sponge getters (hot: 650 °C; cold: room temperature), each for 10 minutes. Near the ion source of the mass spectrometer, a charcoal finger at 77 K and a Zr-Al getter at room temperature were used to reduce interferences from doubly charged ^{40}Ar and CO_2 on the ^{20}Ne and ^{22}Ne signals, respectively. Neon isotopes were measured using compact

discrete dynode (CDD) detectors in multicollection mode. Manual peak centering was performed at the start of each analysis, which consisted of 60 cycles. The Helix MC Plus's high mass resolution (m/Δm ≈ 1800) allowed clear separation of the ^{20}Ne signal from $^{40}Ar^{++}$ (Honda et al., 2015). The contribution of CO_2^{++} to the ^{22}Ne signal was corrected by measuring CO_2^{+} abundance and applying the instrument's CO_2^{++}/CO_2^{+} ratio. The CO_2^{++} contribution to ^{22}Ne was consistently <1%. The acceleration voltage was 9.9 kV, filament trap current was 200 µA, and filament trap voltage was 50.0 V. Daily standards were analyzed for instrument mass discrimination correction, to assess analytical reproducibility, and to compute the sensitivity of the instrument used for subsequent computation of neon abundances. Additional information about error propagation and isotope concentration determination are provided in Bekaert et al. (2017).

S2. Terrestrial age calculation and uncertainty propagation

Terrestrial ages were calculated following Drouard (2019), assuming that terrestrial production of ^{36}Cl at the surface is negligible (see main text). The terrestrial age is given by:

$$T_{terr} = \frac{1}{\lambda_{36_{Cl}}} ln\left(\frac{P_{sat}}{P_{meas}}\right)$$

With $\lambda_{36_{Cl}} = \frac{ln(2)}{T_{36_{Cl}}}$

S2.1. Constants

Parameter	Value	Reference
^{36}Cl half-life T_{36Cl}	301 000 years	(Nica et al., 2012)
Avogadro's number: N_A	6.02214076×10^{23} mol^{-1}	

Molar mass of Cl spike M_{Cl}	35.976 g mol^{-1}	
C_{spike}	6.0 mg Cl/g	ASTER, CEREGE

S2.2. Measured variables

- mass of the dissolved metal in g (m_{metal})
- mass of spike solution in g (m_{spike})
- measured isotopic ratio R = ($^{36}Cl/^{35}Cl$)
  - saturated activity P_{sat} calculated using the model of Leya and Masarik (2009) in disintegration per minute / kg (dpm/kg)

S2.3. Adopted analytical and constant uncertainties

- $\sigma_{P_{sat}}$= 15%. Uncertainties on P_{sat} are mainly from model uncertainties and are estimated on the order of 10–15% (Leya and Masarik, 2009; Ammon et al., 2009). We adopt a conservative relative uncertainty of 15%. The uncertainty on the Ni/(Fe+Ni) ratio was estimated by standard error propagation assuming a relative Inductively Coupled Plasma Optical Emission Spectrometry (ICP-OES) uncertainty of 5% on both Fe and Ni concentrations. This results in an absolute uncertainty of ~0.003–0.005 on Ni/(Fe+Ni) for typical ordinary chondrite metal compositions. Uncertainties on Ni/(Fe+Ni) derived from ICP measurements are small compared to the uncertainty on the modeled ^{36}Cl production rates and were therefore not propagated separately in the terrestrial age uncertainty.
- $\sigma_{m_{metal}}$ = 0.001 g (balance precision)
- $\sigma_{m_{spike}}$ = 0.0001 g (balance/pipette precision)
- σ_{Cspike} = 0.01 mg g^{-1} (absolute uncertainty on Cl concentration in spike)

- $\sigma_{T_{36Cl}}$ = 1500 years (uncertainty on ^{36}Cl half-life; Nica et al., 2012)

S2.4. Calculation of measured activity

The number of stable chlorine atoms added by the spike is calculated as:

$$N_{spike} = \frac{m_{spike}\, C_{spike}\, N_A}{1000 \times M_{Cl}}$$

The number of ^{36}Cl atoms measured in the metal by AMS is given by:

$$N_{Cl} = N_{spike} \times R$$

The measured ^{36}Cl activity of the metal fraction (in dpm/kg) is calculated as:

$$P_{meas} = \frac{N_{Cl}\, ln(2) \times 1000}{(365 \times 24 \times 60)\, T_{36Cl}\, m_{metal}}$$

Combining the expressions above, the terrestrial age can be written as:

$$T_{terr} = \frac{T_{36Cl}}{ln(2)} ln\left(\frac{P_{sat}\,(365 \times 24 \times 60)\, T_{36}\, M_{Cl}\, m_{metal}}{ln(2)\, m_{spike}\, C_{spike} N_A\, R}\right)$$

S2.5. Uncertainty propagation

The 1σ uncertainty on the terrestrial age is propagated in quadrature as:

$$\sigma^2_{Tterr} = \left(\frac{\sigma P_{sat}}{P_{sat}}\right)^2 + \left(\frac{\sigma R}{R}\right)^2 + \left(\frac{\sigma m_{metal}}{m_{metal}}\right)^2 + \left(\frac{\sigma m_{spike}}{m_{spike}}\right)^2 + \left(\frac{\sigma C_{spike}}{C_{spike}}\right)^2 + \left(\frac{1}{ln(2)} + \frac{T_{terr}}{T_{36}}\right)^2 \sigma^2_{T36}$$

FIGURES

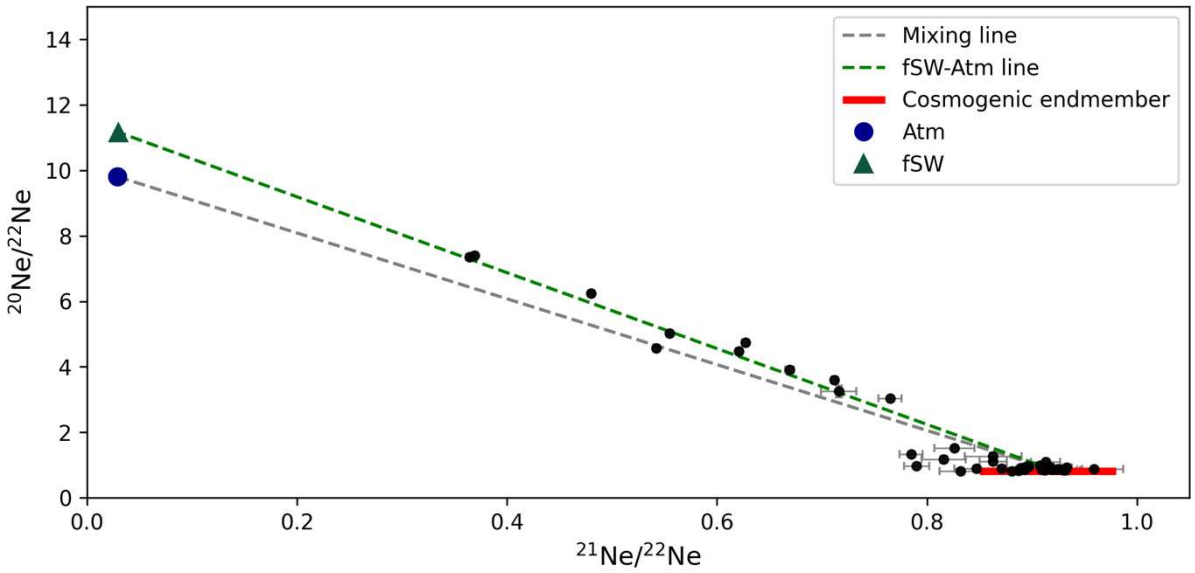

Figure S1. $^{20}Ne/^{22}Ne$ as a function of $^{21}Ne/^{22}Ne$ for 46 measurements (including replicas) of 39 ordinary chondrites from the Catalina Systematic Collection and the El Médano Systematic Collection. Also shown is the atmospheric component with $^{20}Ne/^{22}Ne = 9.80$ and $^{21}Ne/^{22}Ne = 0.02904$ (Ozima and Podosek, 2002) and fractionated Solar Wind (fSW) with $^{20}Ne/^{22}Ne = 11.16$ and $^{21}Ne/^{22}Ne = 0.03$ (Grimberg et al., 2006). All data can be found in Table S1.

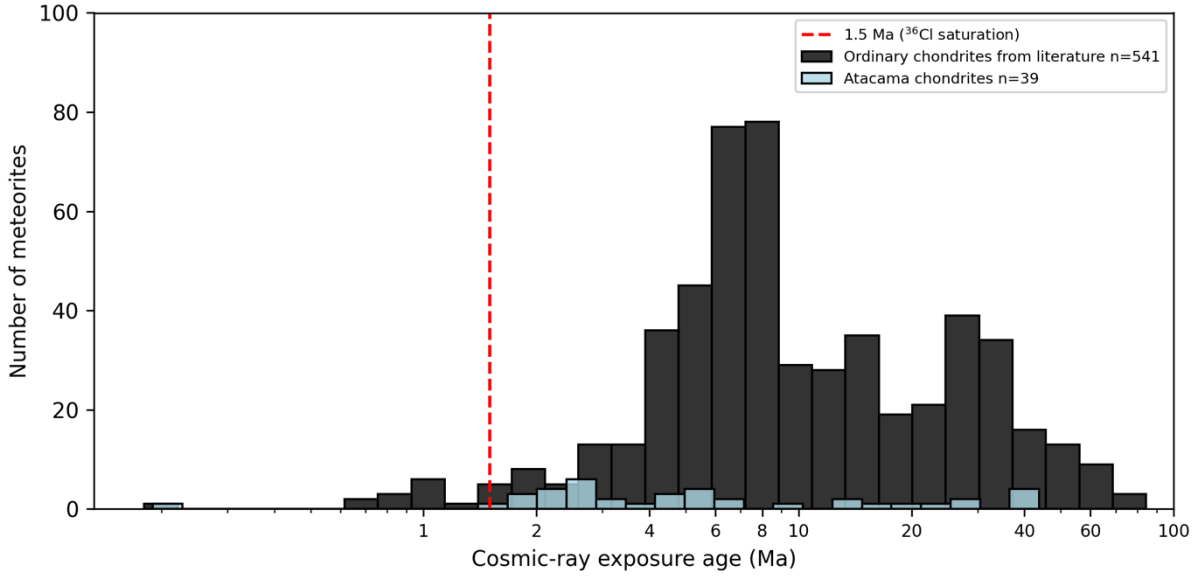

926 Figure S2. Distribution of the cosmic-ray exposure (CRE) ages of ordinary chondrites
927 compiled from Graf and Marti (1994; 1995) and Marti and Graf (1992), together with CRE ages
928 of the Atacama meteorites determined in this study (n=39). The minimum CRE age of 1.5 Ma
929 (five half-lives of ^{36}Cl), required to attain ^{36}Cl into saturation, is represented by the dashed red
930 line.
931

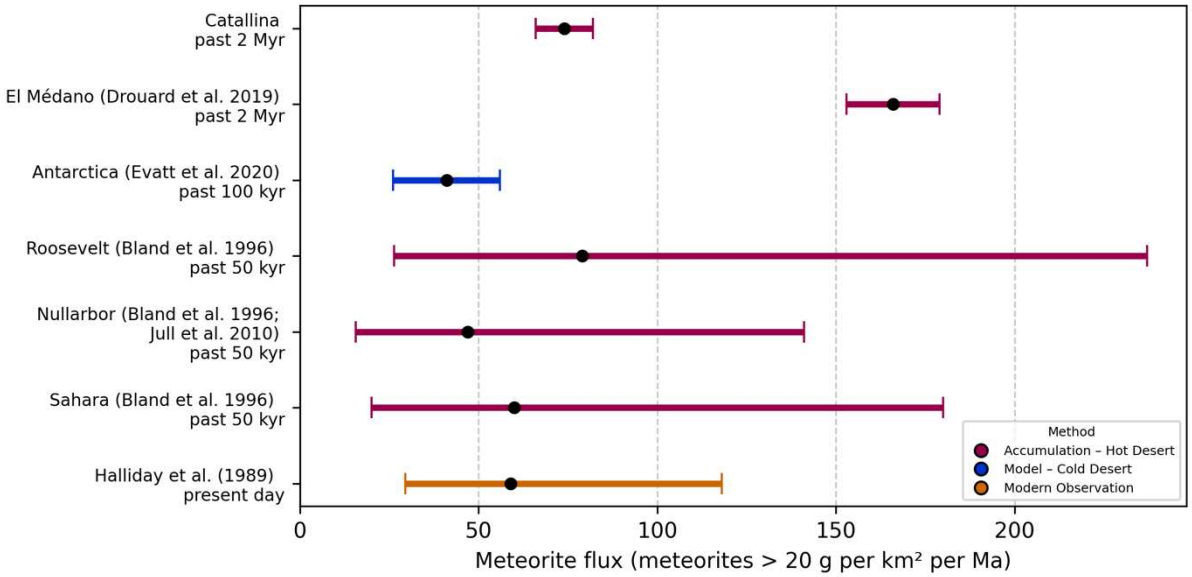

932

933 Figure S3. Comparative overview of the meteorite flux values (meteorites >20 g per km^2 per
934 Myr) reported in different studies.
935

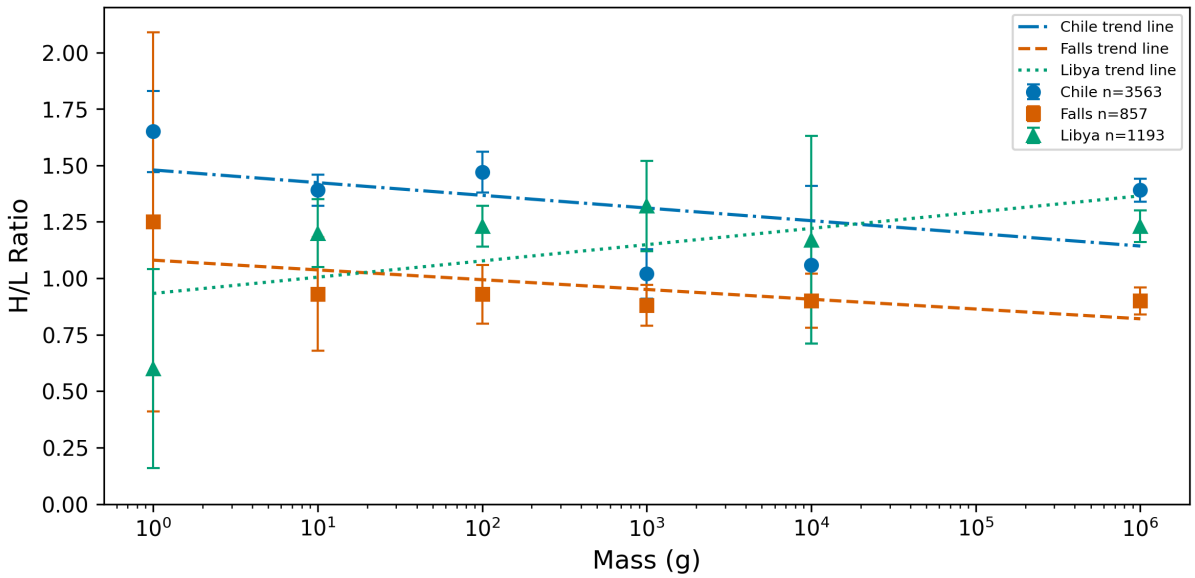

Figure S4. H/L ratios as a function of mass in log scale for observed falls and hot deserts meteorites from Chile and Libya. Each data point represents the H/L ratio in each mass interval, with lower mass limit as x-axis data. Error bars calculated as the standard deviation of the Poisson distribution. Data from MBDB as of July 2025. Slopes for falls, Chile, and Libya are -0.043 (R^2 = 0.440); -0.056 (R^2 = 0.247); 0.072 (R^2 = 0.352), respectively.

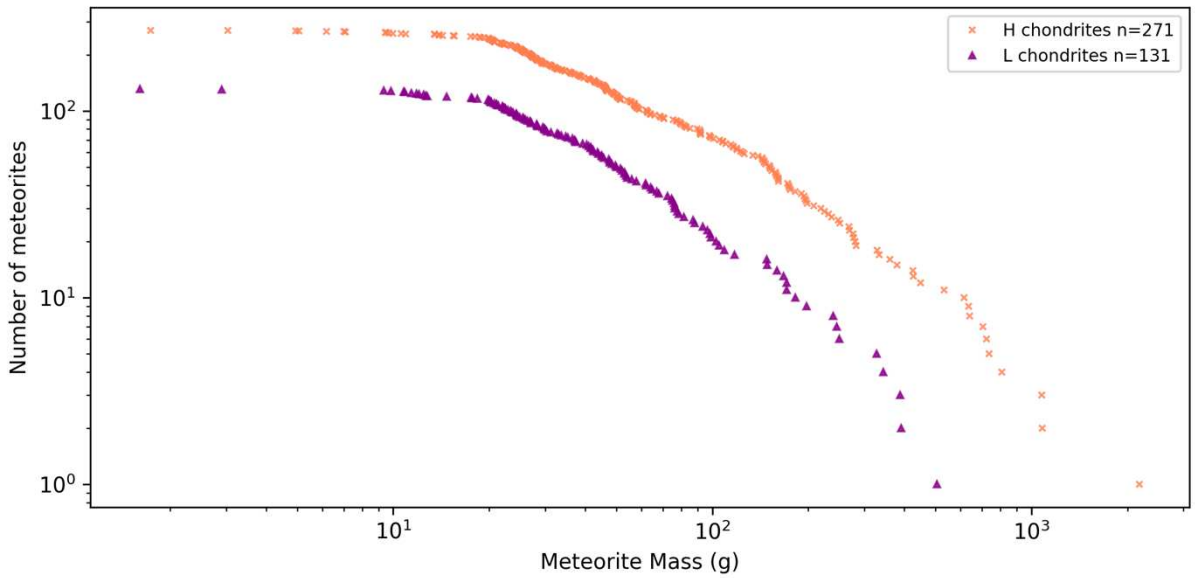

Figure S5. Mass distribution of H chondrites (n = 271) and L chondrites (n = 131) from the Catalina Systematic Collection (Sadaka et al., 2025) on a log-log scale. Kolmogorov-Smirnov test on the two distributions: p-value = 0.137.

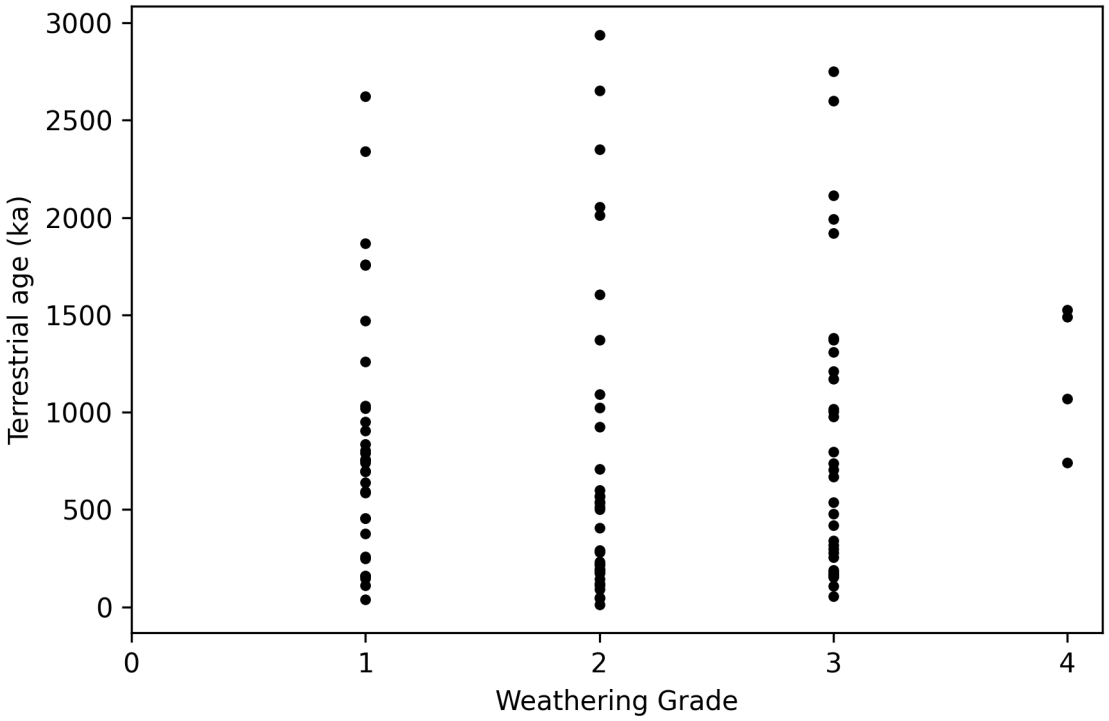

Figure S6. Terrestrial age as a function of the weathering grade of Catalina and El Médano meteorites (n = 104).

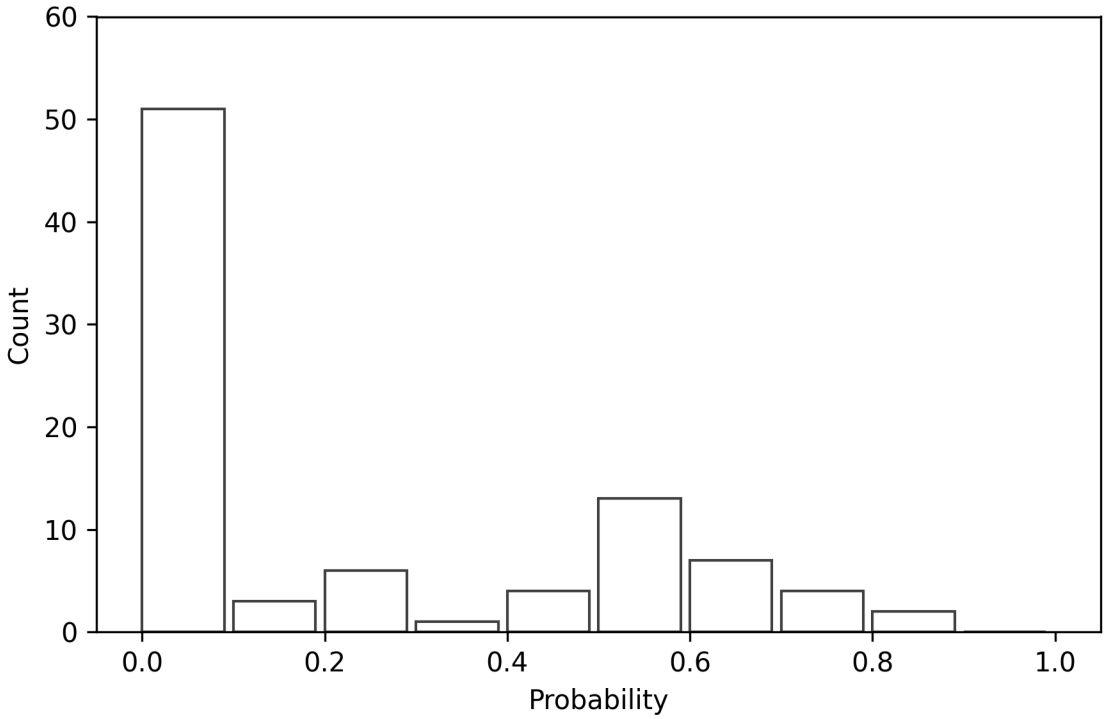

Figure S7. Distribution of the pairing likelihood factor *P* for the 15 H chondrites in the 600–1200 ka terrestrial age interval using the pairing model described in Sadaka et al. (2025).

956

957 TABLES

958 Table S1. Neon isotopic ratios and cosmic-ray exposure (CRE) ages of the Catalina and El Médano meteorites measured in this study (n = 39).

959 Samples marked (1) and (2) correspond to replicate measurements; their average was used for figures and statistics.

Sample	Classification	Lab	F	$^{20}Ne/^{22}Ne$	unc ertainty	$^{21}Ne/^{22}Ne$	unc ertainty	$^{22}Ne/^{21}Ne_{(cos)}$	unc ertainty	$^{21}Ne_{(cos)}$ (10^{-8} cm^3 STP g^{-1})	unc ertainty	P(^{21}Ne) (10^{-8} cm^3 STP g^{-1} Ma^{-1})	unc ertainty	CRE age (Ma)	unc ertainty
Cat 229	H5	Bern	1.05	0.885	0.058	0.842	0.019	1.173	0.037	1.48	0.19	0.26	0.04	5.6	1.0
Cat 474	H5	CR PG	1.40	0.928	0.093	0.933	0.005	1.061	0.005	1.35	0.18	0.65	0.09	2.1	0.4
Cat 476	H5	Bern	0.98	0.828	0.066	0.881	0.019	1.125	0.035	1.69	0.17	0.32	0.03	5.3	0.8

Sample	Classification	Lab	F	$^{20}Ne/^{22}Ne$	unc ertainty	$^{21}Ne/^{22}Ne$	unc ertainty	$^{22}Ne/^{21}Ne_{(cos)}$	unc ertainty	$^{21}Ne_{(cos)}$ (10^{-8} cm^3 STP g^{-1})	unc ertainty	P(^{21}Ne) (10^{-8} cm^3 STP g^{-1} Ma^{-1})	unc ertainty	CRE age (Ma)	unc ertainty
Cat 477	H5	Bern	1.03	0.860	0.076	0.919	0.021	1.076	0.027	1.48	0.18	0.44	0.05	3.3	0.6
Cat 478 (1)	H5	CR PG	1.40	3.650	0.244	0.625	0.027	1.201	0.231	0.05	0.02	0.30	0.13	0.16	0.1
Cat 478 (2)	H5	CR PG	1.40	4.115	0.285	0.591	0.033	1.201	0.295	0.04	0.02	0.30	0.15	0.15	0.1
Cat 479	L6	Bern	1.26	1.043	0.029	0.901	0.011	1.079	0.029	3.53	0.19	0.53	0.03	6.6	0.5
Cat 480	H5	Bern	1.06	0.859	0.072	0.952	0.025	1.038	0.036	1.09	0.12	0.55	0.07	2.0†	0.3

Sample	Classification	Lab	F	$^{20}Ne/^{22}Ne$	unc ertainty	$^{21}Ne/^{22}Ne$	unc ertainty	$^{22}Ne/^{21}Ne_{(cos)}$	unc ertainty	$^{21}Ne_{(cos)}$ (10^{-8} cm^3 STP g^{-1})	unc ertainty	P(^{21}Ne) (10^{-8} cm^3 STP g^{-1} Ma^{-1})	unc ertainty	CRE age (Ma)	unc ertainty
Cat 481	H5	CR PG	1.40	0.85 3	0.14 1	0.93 1	0.01 5	1.07 1	0.01 8	1.39	0.33	0.62	0.14	2.3	0.7
Cat 494	H6	CR PG	1.40	0.89 9	0.09 3	0.87 1	0.00 4	1.14 0	0.00 6	1.04	0.15	0.42	0.06	2.5	0.5
Cat 517	H5	CR PG	1.40	4.57 2	0.09 2	0.54 2	0.00 3	1.23 8	0.05 0	1.17	0.03	0.25	0.01	4.7	0.3
Cat 524	H6	Bern	1.16	0.85 4	0.03 0	0.90 3	0.01 8	1.09 6	0.03 2	4.42	0.25	0.45	0.03	9.9	0.8
Cat 535	H5	Bern	1.12	1.49 8	0.04 7	0.82 1	0.01 7	1.13 6	0.04 2	1.76	0.18	0.34	0.04	5.1	0.7

Sample	Classification	Lab	F	$^{20}Ne/^{22}Ne$	unc ertainty	$^{21}Ne/^{22}Ne$	unc ertainty	$^{22}Ne/^{21}Ne_{(cos)}$	unc ertainty	$^{21}Ne_{(cos)}$ (10^{-8} cm^3 STP g^{-1})	unc ertainty	P(^{21}Ne) (10^{-8} cm^3 STP g^{-1} Ma^{-1})	unc ertainty	CRE age (Ma)	unc ertainty
Cat 538 (1)	H5	CR PG	1.40	0.96 1	0.09 2	0.89 5	0.00 4	1.10 3	0.00 8	1.37	0.15	0.52	0.06	2.6	0.4
Cat 538 (2)	H5	CR PG	1.40	0.96 1	0.09 4	0.89 7	0.00 4	1.10 1	0.00 8	1.45	0.20	0.53	0.07	2.8	0.5
Cat 548	H6	CR PG	1.40	7.35 2	0.09 3	0.36 4	0.00 2	1.16 9	0.03 7	1.64	0.02	0.36	0.01	4.6	0.2
Cat 551	H6	CR PG	1.40	0.86 4	0.09 1	0.88 8	0.00 3	1.12 2	0.00 4	17.7 4	1.87	0.47	0.05	38.0	5.7
Cat 555	H5	Bern	1.17	1.25 6	0.10 6	0.85 7	0.02 5	1.11 3	0.04 1	0.64	0.04	0.41	0.03	1.6	0.2

Sample	Classification	Lab	F	$^{20}Ne/^{22}Ne$	uncertainty	$^{21}Ne/^{22}Ne$	uncertainty	$^{22}Ne/^{21}Ne_{(cos)}$	uncertainty	$^{21}Ne_{(cos)}$ (10^{-8} cm^3 STP g^{-1})	uncertainty	P(^{21}Ne) (10^{-8} cm^3 STP g^{-1} Ma^{-1})	uncertainty	CRE age (Ma)	uncertainty
Cat 600	H5	CR PG	1.40	4.738	0.092	0.627	0.003	1.042	0.039	1.66	0.04	0.71	0.03	2.3†	0.1
Cat 637	H5	CR PG	1.40	0.862	0.093	0.919	0.004	1.084	0.005	1.47	0.20	0.58	0.08	2.5	0.5
Cat 660	L6	CR PG	1.29	0.933	0.042	0.826	0.004	1.199	0.007	4.05	0.26	0.28	0.02	14.5	1.3
Cat 662	H5-6	CR PG	1.40	3.606	0.092	0.712	0.003	1.060	0.049	1.61	0.05	0.65	0.04	2.5	0.2
Cat 664 (1)	H5	CR PG	1.40	5.024	0.094	0.552	0.002	1.130	0.040	2.65	0.05	0.43	0.02	6.1	0.3

Sample	Classification	Lab	F	$^{20}Ne/^{22}Ne$	unc ertainty	$^{21}Ne/^{22}Ne$	unc ertainty	$^{22}Ne/^{21}Ne_{(cos)}$	unc ertainty	$^{21}Ne_{(cos)}$ (10^{-8} cm^3 STP g^{-1})	unc ertainty	P(^{21}Ne) (10^{-8} cm^3 STP g^{-1} Ma^{-1})	unc ertainty	CRE age (Ma)	unc ertainty
Cat 664 (2)	H5	CR PG	1.40	7.40 4	0.09 3	0.36 9	0.00 2	1.13 7	0.03 8	2.64	0.04	0.43	0.02	6.1	0.2
Cat 677	H5-6	CR PG	1.40	0.86 4	0.09 1	0.89 3	0.00 3	1.11 6	0.00 4	18.9 4	2.00	0.48	0.05	39.2	5.8
Cat 682 (1)	H5-6	CR PG	1.40	6.23 5	0.09 2	0.48 0	0.00 2	1.08 8	0.03 5	1.41	0.02	0.57	0.02	2.5	0.1
Cat 682 (2)	H5-6	CR PG	1.40	3.91 1	0.09 3	0.66 9	0.00 4	1.08 7	0.05 8	0.84	0.03	0.57	0.04	1.5	0.1
Cat 684	H6	CR PG	1.40	4.46 9	0.09 2	0.62 1	0.00 3	1.09 2	0.04 2	1.17	0.03	0.55	0.03	2.1	0.1

Sample	Classification	Lab	F	$^{20}Ne/^{22}Ne$	unc ertainty	$^{21}Ne/^{22}Ne$	unc ertainty	$^{22}Ne/^{21}Ne_{(cos)}$	unc ertainty	$^{21}Ne_{(cos)}$ (10^{-8} cm^3 STP g^{-1})	unc ertainty	P(^{21}Ne) (10^{-8} cm^3 STP g^{-1} Ma^{-1})	unc ertainty	CRE age (Ma)	unc ertainty
Cat 707	H6	CR PG	1.40	0.81 8	0.09 1	0.88 1	0.00 3	1.13 6	0.00 4	18.9 3	2.11	0.43	0.05	43.8	6.9
Cat 739	H6	CR PG	1.40	0.87 0	0.09 1	0.92 4	0.00 3	1.07 8	0.00 3	17.8 3	1.87	0.60	0.06	29.9	4.4
ElM 020	L6	CR PG	1.40	0.86 5	0.00 5	0.91 8	0.01 3	1.08 5	0.01 5	12.4 6	2.48	0.57	0.11	21.7	6.1
ElM 025	H6	CR PG	1.40	0.86 7	0.00 5	0.93 0	0.01 3	1.07 0	0.01 5	16.4 5	4.28	0.62	0.16	26.5	9.8
ElM 027	H5	CR PG	1.40	0.99 3	0.00 6	0.90 8	0.01 3	1.08 4	0.01 6	1.83	0.03	0.58	0.01	3.2	0.1

Sample	Classification	Lab	F	$^{20}Ne/^{22}Ne$	unc ertainty	$^{21}Ne/^{22}Ne$	unc ertainty	$^{22}Ne/^{21}Ne_{(cos)}$	unc ertainty	$^{21}Ne_{(cos)}$ (10^{-8} cm^3 STP g^{-1})	unc ertainty	P(^{21}Ne) (10^{-8} cm^3 STP g^{-1} Ma^{-1})	unc ertainty	CRE age (Ma)	unc ertainty
ElM049	H4	CR PG	1.40	0.967	0.008	0.792	0.012	1.250	0.019	1.14	0.02	0.23	0.01	4.9	0.2
ElM097	L5-6	CR PG	1.29	0.867	0.007	0.922	0.010	1.081	0.011	8.34	0.12	0.54	0.01	15.4	0.4
ElM099	H5	CR PG	1.40	1.110	0.010	0.863	0.013	1.129	0.017	1.22	0.03	0.45	0.01	2.7	0.1
ElM111	H5	CR PG	1.40	0.842	0.005	0.912	0.013	1.094	0.015	9.86	0.16	0.55	0.01	18.0	0.5
ElM115 (1)	H5	CR PG	1.40	0.916	0.006	0.886	0.013	1.115	0.016	2.37	0.10	0.49	0.02	4.9	0.3

Sample	Classification	Lab	F	$^{20}Ne/^{22}Ne$	unc ertainty	$^{21}Ne/^{22}Ne$	unc ertainty	$^{22}Ne/^{21}Ne_{(cos)}$	unc ertainty	$^{21}Ne_{(cos)}$ (10^{-8} cm^3 STP g^{-1})	unc ertainty	P(^{21}Ne) (10^{-8} cm^3 STP g^{-1} Ma^{-1})	unc ertainty	CRE age (Ma)	unc ertainty
ElM 115 (2)	H5	CR PG	1.40	0.820	0.050	0.832	0.022	1.202	0.029	2.32	0.47	0.30	0.06	7.8	2.2
ElM 115 (3)	H5	CR PG	1.40	1.170	0.100	0.816	0.021	1.181	0.031	1.49	0.27	0.32	0.06	4.6	1.2
ElM 199 (1)	H6	CR PG	1.40	3.029	0.018	0.765	0.011	1.045	0.058	3.33	0.18	0.70	0.06	4.7†	0.5
ElM 199 (2)	H6	CR PG	1.40	3.250	0.180	0.710	0.016	1.089	0.154	1.37	0.15	0.56	0.10	2.4	0.5
ElM 236	H5	CR PG	1.40	0.942	0.012	0.910	0.014	1.079	0.017	1.17	0.03	0.59	0.02	2.0	0.1

Sample	Classification	Lab	F	$^{20}Ne/^{22}Ne$	unc	$^{21}Ne/^{22}Ne$	unc	$^{22}Ne/^{21}Ne_{(cos)}$	unc	$^{21}Ne_{(cos)}$ (10^{-8} cm^3 STP g^{-1})	unc	P(^{21}Ne) (10^{-8} cm^3 STP g^{-1} Ma^{-1})	unc	CRE age (Ma)	unc
ElM245	H5-6	CR PG	1.40	1.100	0.008	0.913	0.014	1.068	0.016	1.58	0.05	0.63	0.02	2.5	0.1
ElM261	H3	CR PG	1.40	1.332	0.007	0.785	0.011	1.215	0.035	10.50	1.74	0.28	0.05	38.0	9.0
CeC006	L6	CR PG	1.29	0.841	0.005	0.856	0.012	1.166	0.017	4.61	0.35	0.34	0.03	13.7	1.5

† The cosmogenic $(^{22}Ne/^{21}Ne)_{cos}$ ratios are below 1.06, which is commonly considered a lower limit for purely cosmogenic neon. For these samples, the derived production rates should therefore be regarded as upper limits, and the corresponding CRE ages as lower limits.

962 Table S2. Sample details and recalculated terrestrial ages of meteorites from the El Médano Systematic collection (EMSC), based on data
963 originally reported by Drouard et al. (2019).

Name	Group	Petrographic Type	Weathering Grade	Ni/Fe+Ni (%)	Computed ^{36}Cl activity at saturation (dpm/kg)	Calculated activity from measured ^{36}Cl (dpm/kg)	Terrestrial age (ka)	Uncertainty (ka)
El Médano 004	H	4	1	6.6	23.81	10.0	377	80
El Médano 017	L	6	3	6.5	23.89	12.0	299	80
El Médano 020	L	6	3	14.1	23.27	0.18	2113	70
El Médano 023	L	6	3	12.7	23.35	15.5	178	80
El Médano 025	H	6	3	7.1	23.81	2.37	1002	80

Name	Group	Petrographic Type	Weathering Grade	Ni/Fe+Ni (%)	Computed ^{36}Cl activity at saturation (dpm/kg)	Calculated activity from measured ^{36}Cl (dpm/kg)	Terrestrial age (ka)	Uncertainty (ka)
El Médano 026	L	6	3	10.1	23.58	11.4	316	80
El Médano 027	H	5	3	18.5	22.88	2.42	976	65
El Médano 029	L	5	1	14.9	23.19	16.1	159	60
El Médano 037	L	6	3	9.1	23.66	16.0	170	80
El Médano 042	L	6	3	18.9	22.88	1.12	1310	65
El Médano 049	H	4	3	7.3	23.81	0.286	1921	80

Name	Group	Petrographic Type	Weathering Grade	Ni/Fe+Ni (%)	Computed ^{36}Cl activity at saturation (dpm/kg)	Calculated activity from measured ^{36}Cl (dpm/kg)	Terrestrial age (ka)	Uncertainty (ka)
El Médano 055	H	6	2	15.2	23.19	6.25	569	60
El Médano 070	L	6	3	10.8	23.50	12.4	278	60
El Médano 071	H	5	2	11.5	23.50	12.3	281	60
El Médano 075	L	4	3	10.9	23.50	0.980	1380	80
El Médano 078	L	6	3	12.5	23.59	13.1	255	80
El Médano 079	H	5	2	7.0	23.81	6.96	534	80

Name	Group	Petrographic Type	Weathering Grade	Ni/Fe+Ni (%)	Computed ^{36}Cl activity at saturation (dpm/kg)	Calculated activity from measured ^{36}Cl (dpm/kg)	Terrestrial age (ka)	Uncertainty (ka)
El Médano 086	H	4	1	8.8	23.66	8.30	455	80
El Médano 089	L	6	4	10.6	23.50	4.28	740	80
El Médano 092	H	6	3	7.1	23.81	2.29	1017	80
El Médano 095	LL	6	3	40.0	21.26	9.75	339	70
El Médano 097	L	5-6	4	14.1	23.27	0.756	1488	75
El Médano 098	L	6	4	10.5	23.50	2.01	1068	80

Name	Group	Petrographic Type	Weathering Grade	Ni/Fe+Ni (%)	Computed ^{36}Cl activity at saturation (dpm/kg)	Calculated activity from measured ^{36}Cl (dpm/kg)	Terrestrial age (ka)	Uncertainty (ka)
El Médano 099	H	5	3	11.0	23.50	0.239	1993	75
El Médano 103	LL	6	2	32.3	21.88	17.8	90	70
El Médano 104	LL	5	3	30.3	22.03	17.2	108	65
El Médano 111	H	5	4	7.8	23.73	0.711	1524	80
El Médano 113	L	6	3	20.0	22.81	4.17	738	70
El Médano 115	H	5	1	25.0	22.42	3.92	757	70

Name	Group	Petrographic Type	Weathering Grade	Ni/Fe+Ni (%)	Computed ^{36}Cl activity at saturation (dpm/kg)	Calculated activity from measured ^{36}Cl (dpm/kg)	Terrestrial age (ka)	Uncertainty (ka)
El Médano 118	H	5	3	6.0	23.89	7.94	478	75
El Médano 126	H	5	3	7.7	23.73	5.10	668	75
El Médano 128	L	6	2	12.5	23.59	17.0	142	80
El Médano 129	L	6	2	21.3	22.73	20.3	49	65
El Médano 135	L	6	3	11.1	23.50	1.00	1371	75
El Médano 170	L	4	2	20.8	22.73	13.9	214	65

Name	Group	Petrographic Type	Weathering Grade	Ni/Fe+Ni (%)	Computed ^{36}Cl activity at saturation (dpm/kg)	Calculated activity from measured ^{36}Cl (dpm/kg)	Terrestrial age (ka)	Uncertainty (ka)
El Médano 172	H	5	2	14.9	23.19	14.8	195	65
El Médano 173	L	6	2	18.9	22.88	17.3	121	60
El Médano 191	H	5	2	13.5	23.27	1.88	1093	80
El Médano 199	H	6	1	15.4	23.19	4.66	697	60
El Médano 231	H	4	2	11.6	23.42	18.2	110	60
El Médano 236	H	5	1	22.7	22.57	3.99	753	70

Name	Group	Petrographic Type	Weathering Grade	Ni/Fe+Ni (%)	Computed ^{36}Cl activity at saturation (dpm/kg)	Calculated activity from measured ^{36}Cl (dpm/kg)	Terrestrial age (ka)	Uncertainty (ka)
El Médano 245	H	5-6	2	11.1	23.50	0.585	1604	70
El Médano 253	L	6	2	23.3	22.57	21.9	13	60
El Médano 257	L	3	2	19.2	22.88	0.971	1372	70
El Médano 261	H	3	2	9.0	23.66	7.44	502	60
El Médano 263	L	6	3	20.4	22.81	20.1	55	65
El Médano 276	L	6	3	12.8	23.35	16.0	164	60

Name	Group	Petrographic Type	Weathering Grade	Ni/Fe+Ni (%)	Computed ^{36}Cl activity at saturation (dpm/kg)	Calculated activity from measured ^{36}Cl (dpm/kg)	Terrestrial age (ka)	Uncertainty (ka)
El Médano 278	H	5	2	12.8	23.35	13.7	232	60
El Médano 286	L	6	3	13.3	23.35	1.44	1210	70
El Médano 304	H	5	1	8.8	23.66	4.31	740	60
El Médano 309	H	5	3	8.9	23.66	16.6	154	60
Caleta el Cobre 06	L	6	3	7.4	23.81	0.060	2600	100
Caleta el Cobre 15	L	6	3	9.1	23.66	6.89	536	75

Name	Group	Petrographic Type	Weathering Grade	Ni/Fe+Ni (%)	Computed ^{36}Cl activity at saturation (dpm/kg)	Calculated activity from measured ^{36}Cl (dpm/kg)	Terrestrial age (ka)	Uncertainty (ka)
Caleta el Cobre 20	H	5	3	7.1	23.81	1.61	1170	80

964

965 REFERENCES

966 Ammon, K., J. Masarik, and I. Leya. 2009. “New Model Calculations for the Production
967 Rates of Cosmogenic Nuclides in Iron Meteorites.” *Meteoritics & Planetary Science*
968 44: 485–503. https://doi.org/10.1111/j.1945-5100.2009.tb00746.x.
969 Bekaert, D., G. Avice, B. Marty, B. L. Henderson, and M. S. Gudipati. 2017. “Stepwise
970 Heating of Lunar Anorthosites 60025, 60215, 65315 Possibly Reveals an Indigenous
971 Noble Gas Component on the Moon.” *Geochimica et Cosmochimica Acta* 218
972 (December): 114–31. https://doi.org/10.1016/j.gca.2017.08.041.
973 Dalcher, N., M. W. Caffee, K. Nishiizumi, K. C. Welten, N. Vogel, R. Wieler, and I. Leya.
974 2013. “Calibration of Cosmogenic Noble Gas Production in Ordinary Chondrites
975 Based on ^{36}Cl-^{36}Ar Ages. Part 1: Refined Produced Rates for Cosmogenic ^{21}Ne and
976 ^{38}Ar.” *Meteoritics and Planetary Science* 48 (10): 1841–62.
977 https://doi.org/10.1111/maps.12203.
978 Drouard, Alexis. 2019. *Évolution des corps-parents des chondrites ordinaires : du sol à*
979 *l’espace*. PhD diss., Aix-Marseille Université.
980 Drouard, A., J. Gattacceca, A. Hutzler, P. Rochette, R. Braucher, D. Bourlès, M. Gounelle, et
981 al. 2019. “The Meteorite Flux of the Past 2 M.y. Recorded in the Atacama Desert.”
982 *Geology* 47 (7): 673–76. https://doi.org/10.1130/g45831.1.
983 Gamblin, J., E. Füri, B. Marty, L. Zimmermann, and D.V. Bekaert. 2024. “Dissecting the
984 Complex Ne-Ar-N Signature of Asteroid Ryugu by Step-Heating Analysis.”
985 *Geochemical Perspectives Letters* 31 (August): 44–48.
986 https://doi.org/10.7185/geochemlet.2431.
987 Gattacceca, J., C. Suavet, P. Rochette, B. P. Weiss, M. Winklhofer, M. Uehara, and J. M.
988 Friedrich. 2014. “Metal Phases in Ordinary Chondrites: Magnetic Hysteresis

Properties and Implications for Thermal History." *Meteoritics and Planetary Science* 49 (4): 652–76. https://doi.org/10.1111/maps.12268.

Graf, T., and K. Marti. 1994. "Collisional Records in LL-Chondrites." *Meteoritics* 29 (5): 643–48. https://doi.org/10.1111/j.1945-5100.1994.tb00777.x.

Graf, T., and K. Marti. 1995. "Collisional History of H Chondrites." *Journal of Geophysical Research* 100 (E10): 21247. https://doi.org/10.1029/95je01903.

Grimberg, A. , H. Baur, P. Bochsler, BühlerF. , D. S. Burnett, C. C. Hays, V. S. Heber, A. J. G. Jurewicz, and R. Wieler. 2006. "Solar Wind Neon from Genesis: Implications for the Lunar Noble Gas Record." *Science* 314 (5802): 1133–35. https://doi.org/10.1126/science.1133568.

Honda, M., X. Zhang, D. Phillips, D. Hamilton, M. Deerberg, and J. B. Schwieters. 2015. "Redetermination of the 21Ne Relative Abundance of the Atmosphere, Using a High Resolution, Multi-Collector Noble Gas Mass Spectrometer (HELIX-MC Plus)." *International Journal of Mass Spectrometry* 387 (August): 1–7. https://doi.org/10.1016/j.ijms.2015.05.012.

Humbert, F., G. Libourel, C. France-Lanord, L. Zimmermann, and B. Marty. 2000. "CO_2-Laser Extraction-Static Mass Spectrometry Analysis of Ultra-Low Concentrations of Nitrogen in Silicates." *Geostandards Newsletter* 24 (2): 255–60. https://doi.org/10.1111/j.1751-908x.2000.tb00777.x.

Hutzler, A. 2015. "The Flux of Meteorites on Earth: Contribution of Measuring the Concentration of Multiple Cosmogenic Nuclides, and Collections in Arid Areas." Aix-Marseille Université. https://theses.fr/2015AIXM4302.

Kouvatsis, I., and B. A. Hofmann. 2019. "A Statistical Analysis of the H/L Ratio of Ordinary Chondrite Finds and Falls: A Comparison of Oman Finds with Other Populations." *Meteoritics & Planetary Science* 55 (1): 67–76. https://doi.org/10.1111/maps.13410.

1014 Kuzina, D., J. Gattacceca, H. Gouilloux, H. Mertens, R. Lacube, F. Demory, and C. Lorenz.
1015 2025. “The Effect of Terrestrial Weathering on the Magnetic Properties of Meteorites
1016 from the Atacama Desert.” *Učënye Zapiski Kazanskogo Universiteta. Seriâ*
1017 *Estestvennye Nauki/Učënye Zapiski Kazanskogo Universiteta. Seriâ Estestvennye*
1018 *Nauki/Učenye Zapiski Kazanskogo Gosudarstvennogo Universiteta. Seriâ*
1019 *Estestvennye Nauki* 167 (2): 353–66. https://doi.org/10.26907/2542-064x.2025.2.353-
1020 366.
1021 Leya, I., K. Ammon, M. Cosarinsky, N. Dalcher, E. Gnos, B. Hofmann, and L. Huber. 2013.
1022 “Light Noble Gases in 12 Meteorites from the Omani Desert, Australia, Mauritania,
1023 Canada, and Sweden.” *Meteoritics & Planetary Science* 48 (8): 1401–14.
1024 https://doi.org/10.1111/maps.12142.
1025 Leya, I., and J. Masarik. 2009. “Cosmogenic Nuclides in Stony Meteorites Revisited.”
1026 *Meteoritics & Planetary Science* 44 (7): 1061–86. https://doi.org/10.1111/j.1945-
1027 5100.2009.tb00788.x.
1028 Marti, K., and T. Graf. 1992. “Cosmic-Ray Exposure History of Ordinary Chondrites.”
1029 *Annual Review of Earth and Planetary Sciences* 20 (1): 221–43.
1030 https://doi.org/10.1146/annurev.ea.20.050192.001253.
1031 Nica, N., J. Cameron, and B. Singh. 2012. “Nuclear Data Sheets for a = 36.” *Nuclear Data*
1032 *Sheets* 113 (1): 1–155. https://doi.org/10.1016/j.nds.2012.01.001.
1033 Ozima, M., and F. A. F. A. Podosek. 2002. “Noble Gas Geochemistry.” *Cambridge, UK:*
1034 *Cambridge University Press.*, 616–17. https://doi.org/10.1017/s0016756803258349.
1035 Pinto, G. A., A. Tavernier, J. Gattacceca, A. Corgne, M. Valenzuela, B. Luais, L. Flores, F.
1036 Olivares, and Y. Marrocchi. 2024. “Dense Collection Areas and Terrestrial Alteration
1037 of Meteorites in the Atacama Desert.” *Meteoritics & Planetary Science* 59 (2): 351–
1038 67. https://doi.org/10.1111/maps.14125.

1039 Sadaka, C., J. Gattacceca, M. Gounelle, M. Roskosz, A. Lagain, R. Tartese, L. Bonal, C.
1040 Maurel, R. Martinez, and M. Valenzuela. 2025. “Systematic Meteorite Collection in
1041 the Catalina Dense Collection Area (Chile): Description and Statistics.” *Meteoritics &*
1042 *Planetary Science*, no. 60 (January): 308–23. https://doi.org/10.1111/maps.14307.
1043 Tauseef, M., I. Leya, J. Gattacceca, B. Hofmann, S. Szidat, and R. Braucher. 2024. “^{14}C and
1044 ^{14}C-^{10}Be Terrestrial Age Dating System for Meteorites—New Data for Four Recently
1045 Fallen Meteorites.” *Meteoritics & Planetary Science* 59 (6): 1219–35.
1046 https://doi.org/10.1111/maps.14144.
1047 Tauseef, M., Leya, I., Hofmann, B. 2025. “Cosmic ray exposure ages and pre-atmospheric
1048 shielding of Omani meteorites: Implications for ^{14}C and ^{14}C/^{10}Be terrestrial ages of
1049 meteorites from hot and cold deserts.” *Meteoritics & Planetary Science* 60 (9): 2184–
1050 96. https://doi.org/10.1111/maps.70029.
1051 Zimmermann, L., E. Füri, J. Boulliung, and J. M. Saxton. 2025. “Performance of the 3F4M
1052 Noblesse–HR Noble Gas Mass Spectrometer for Multicollection Ne-Ar-N_2 Analyses.”
1053 *Geochemistry, Geophysics, Geosystems* 26 (7). https://doi.org/10.1029/2025gc012247.
1054
1055

Chapter 3

REFERENCES

Al-Kathiri, A., B. A. Hofmann, A. J. T. Jull, and E. Gnos. 2005. "Weathering of Meteorites from Oman: Correlation of Chemical and Mineralogical Weathering Proxies With14C Terrestrial Ages and the Influence of Soil Chemistry." *Meteoritics & Planetary Science* 40 (8): 1215–39. https://doi.org/10.1111/j.1945-5100.2005.tb00185.x.

Benoit, P H, D. W. G. Sears, J.M.C. Akridge, P. A. Bland, F.J. Berry, and C.T. Pillinger. 2000. "The Non-Trivial Problem of Meteorite Pairing." *Meteoritics & Planetary Science* 35 (2): 393–417. https://doi.org/10.1111/j.1945-5100.2000.tb01785.x.

Bland, P. A. 2001. "Quantification of Meteorite Infall Rates from Accumulations in Deserts, and Meteorite Accumulations on Mars." In *Accretion of Extraterrestrial Matter throughout Earth's History*, edited by B. Schmitz and B. Peucker-Ehrenbrink, 267–303. Springer.

Bland, P. A., T. Smith, T. Jull, F. J. Berry, R. Bevan, S. Cloudt, and C. T. Pillinger. 1996. "The Flux of Meteorites to the Earth over the Last 50 000 Years." *Monthly Notices of the Royal Astronomical Society* 283 (2): 551–65. https://doi.org/10.1093/mnras/283.2.551.

Bland, P. A., P. Spurný, R. Bevan, K. T. Howard, M. C. Towner, G. Benedix, R. C. Greenwood, et al. 2012. "The Australian Desert Fireball Network: A New Era for Planetary Science." *Australian Journal of Earth Sciences* 59 (2): 177–87. https://doi.org/10.1080/08120099.2011.595428.

Bland, P.A., A.S. Sexton, A.J.T. Jull, A.W.R. Bevan, F.J. Berry, D.M. Thornley, T.R. Astin, D.T. Britt, and C.T. Pillinger. 1998. "Climate and Rock Weathering: A Study of Terrestrial Age Dated Ordinary Chondritic Meteorites from Hot Desert Regions." *Geochimica et Cosmochimica Acta* 62 (18): 3169–84. https://doi.org/10.1016/s0016-7037(98)00199-9.

Bottke, W. F., M. Brož, D. P. O'Brien, A. Campo Bagatin, A. Morbidelli, and S. Marchi. 2015. "The Collisional Evolution of the Main Asteroid Belt." In *Asteroids IV*, 701–24. Univ. of Arizona, Tucson. 10.2458/azu_uapress_9780816532131-ch036.

Bottke, W. F., A. Morbidelli, R. Jedicke, J.-M. Petit, H.F. Levison, P. Michel, and T. S. Metcalfe. 2002. "Debiased Orbital and Absolute Magnitude Distribution of the Near-Earth Objects." *Icarus* 156 (2): 399–433. https://doi.org/10.1006/icar.2001.6788.

Brož, M., P. Vernazza, M. Marsset, R. P. Binzel, F. DeMeo, M. Birlan, F Colas, et al. 2024. "Source Regions of Carbonaceous Meteorites and Near-Earth Objects." *Astronomy and Astrophysics* 689 (July). https://doi.org/10.1051/0004-6361/202450532.

Brož, M., P. Vernazza, M. Marsset, F. E. DeMeo, R. P. Binzel, D. Vokrouhlický, and D. Nesvorný. 2024. "Young Asteroid Families as the Primary Source of Meteorites." *Nature* 634 (8034): 566–71. https://doi.org/10.1038/s41586-024-08006-7.

Carruba, V, J.A. Burns, W. Bottke, and D. Nesvorný. 2003. "Orbital Evolution of the Gefion and Adeona Asteroid Families: Close Encounters with Massive Asteroids and the Yarkovsky Effect." *Icarus* 162 (2): 308–27. https://doi.org/10.1016/s0019-1035(02)00062-3.

Cervone, A., F. Topputo, S. Speretta, A. Menicucci, E. Turan, P. Di Lizia, M. Massari, et al. 2022. "LUMIO: A CubeSat for Observing and Characterizing Micro-Meteoroid Impacts on the Lunar Far Side." *Acta Astronautica* 195 (June): 309–17. https://doi.org/10.1016/j.actaastro.2022.03.032.

Clarke, J.D.A. 2006. "Antiquity of Aridity in the Chilean Atacama Desert." *Geomorphology* 73 (1-2): 101–14. https://doi.org/10.1016/j.geomorph.2005.06.008.

Colas, F., B. Zanda, S. Bouley, S. Jeanne, A. Malgoyre, M. Birlan, C. Blanpain, et al. 2020. "FRIPON: A Worldwide Network to Track Incoming Meteoroids." *Astronomy & Astrophysics* 644 (December): A53. https://doi.org/10.1051/0004-6361/202038649.

Corti, G., A. Zeoli, and M. Bonini. 2003. “Ice-Flow Dynamics and Meteorite Collection in Antarctica.” *Earth and Planetary Science Letters* 215 (3-4): 371–78. https://doi.org/10.1016/S0012-821X(03)00440-0.

Dalcher, N., M. W. Caffee, K. Nishiizumi, K. C. Welten, N. Vogel, R. Wieler, and I. Leya. 2013. “Calibration of Cosmogenic Noble Gas Production in Ordinary Chondrites Based on ^{36}Cl-^{36}Ar Ages. Part 1: Refined Produced Rates for Cosmogenic ^{21}Ne and ^{38}Ar.” *Meteoritics and Planetary Science* 48 (10): 1841–62. https://doi.org/10.1111/maps.12203.

Devillepoix, H. A. R. , P. A. Bland, E. K. Sansom, M. C. Towner, M. Cupák, R. M. Howie, B. A. D. Hartig, T. Jansen-Sturgeon, and M. A. Cox. 2018. “Observation of Metre-Scale Impactors by the Desert Fireball Network.” *Monthly Notices of the Royal Astronomical Society (Print)* 483 (4): 5166–78. https://doi.org/10.1093/mnras/sty3442.

Drouard, A., J. Gattacceca, A. Hutzler, P. Rochette, R. Braucher, D. Bourlès, M. Gounelle, et al. 2019. “The Meteorite Flux of the Past 2 M.y. Recorded in the Atacama Desert.” *Geology* 47 (7): 673–76. https://doi.org/10.1130/g45831.1.

Dunai, T. J., G. A. González López, and J. Juez-Larré. 2005. “Oligocene–Miocene Age of Aridity in the Atacama Desert Revealed by Exposure Dating of Erosion-Sensitive Landforms.” *Geology* 33 (4): 321. https://doi.org/10.1130/g21184.1.

Eugster, O. 2003. “Cosmic-Ray Exposure Ages of Meteorites and Lunar Rocks and Their Significance.” *Geochemistry* 63 (1): 3–30. https://doi.org/10.1078/0009-2819-00021.

Evatt, G.W., A.R.D. Smedley, K.H. Joy, L. Hunter, W.H. Tey, I.D. Abrahams, and L. Gerrish. 2020. “The Spatial Flux of Earth’s Meteorite Falls Found via Antarctic Data.” *Geology* 48 (7): 683–87. https://doi.org/10.1130/G46733.1.

Farinella, P., D. Vokrouhlický, and W. K. Hartmann. 1998. “Meteorite Delivery via Yarkovsky Orbital Drift.” *Icarus* 132 (2): 378–87. https://doi.org/10.1006/icar.1997.5872.

Farley, K.A., D. Vokrouhlický, W. F. Bottke, and D. Nesvorný. 2006. "A Late Miocene Dust Shower from the Break-up of an Asteroid in the Main Belt." *Nature* 439 (7074): 295–97. https://doi.org/10.1038/nature04391.

Flynn, G. J., G. J. Consolmagno, P. Brown, and R. J. Macke. 2018. "Physical Properties of the Stone Meteorites: Implications for the Properties of Their Parent Bodies." *Geochemistry* 78 (3): 269–98. https://doi.org/10.1016/j.chemer.2017.04.002.

Fries, M., and J. Fries. 2010. "Doppler Weather Radar as a Meteorite Recovery Tool." *Meteoritics & Planetary Science* 45 (9): 1476–87. https://doi.org/10.1111/j.1945-5100.2010.01115.x.

Gattacceca, J., C. Suavet, P. Rochette, B. P. Weiss, M. Winklhofer, M. Uehara, and J. M. Friedrich. 2014. "Metal Phases in Ordinary Chondrites: Magnetic Hysteresis Properties and Implications for Thermal History." *Meteoritics and Planetary Science* 49 (4): 652–76. https://doi.org/10.1111/maps.12268.

Gattacceca, J., M. Valenzuela, M. Uehara, T. Jull, M. D. Giscard, P. Rochette, R. Braucher, et al. 2011. "The Densest Meteorite Collection Area in Hot Deserts: The San Juan Meteorite Field (Atacama Desert, Chile)." *Meteoritics & Planetary Science* 46 (9): 1276–87. https://doi.org/10.1111/j.1945-5100.2011.01229.x.

Gladman, B. J., F. Migliorini, A. Morbidelli, V. Zappalà, P. Michel, A. Cellino, C. Froeschlé, H. F. Levison, M. Bailey, and M. Duncan. 1997. "Dynamical Lifetimes of Objects Injected into Asteroid Belt Resonances." *Science* 277 (5323): 197–201. https://doi.org/10.1126/science.277.5323.197.

Graf, T., M.W. Caffee, K. Marti, K. Nishiizumi, and K.V. Ponganis. 2001. "Dating Collisional Events: 36Cl–36Ar Exposure Ages of H-Chondritic Metals." *Icarus* 150 (1): 181–88. https://doi.org/10.1006/icar.2000.6560.

Graf, T., and K. Marti. 1994. "Collisional Records in LL-Chondrites." *Meteoritics* 29 (5): 643–48. https://doi.org/10.1111/j.1945-5100.1994.tb00777.x.

Graf, T., and K. Marti. 1995. “Collisional History of H Chondrites.” *Journal of Geophysical Research* 100 (E10): 21247. https://doi.org/10.1029/95je01903.

Halliday, I., A. T. Blackwell, and A. A. Griffin. 1989. “The Flux of Meteorites on the Earth’s Surface.” *Meteoritics* 24 (3): 173–78. https://doi.org/10.1111/j.1945-5100.1989.tb00959.x.

Hofmann, Beda A, and Edwin Gnos. 2024. “The Meteoritic Record of Arabia.” *Geological Society London Special Publications* 550 (1): SP550-20248. https://doi.org/10.1144/sp550-2024-8.

Huss, G. R. 1990. “Meteorite Infall as a Function of Mass: Implications for the Accumulation of Meteorites on Antarctic Ice.” *Meteoritics* 25 (1): 41–56. https://doi.org/10.1111/j.1945-5100.1990.tb00969.x.

Hutzler, A. 2015. “The Flux of Meteorites on Earth: Contribution of Measuring the Concentration of Multiple Cosmogenic Nuclides, and Collections in Arid Areas.” Aix-Marseille Université. https://theses.fr/2015AIXM4302.

Hutzler, A., J. Gattacceca, P. Rochette, R. Braucher, B. Carro, E. Christensen, C. Cournede, et al. 2016. “Description of a Very Dense Meteorite Collection Area in Western Atacama: Insight into the Long-Term Composition of the Meteorite Flux to Earth.” *Meteoritics & Planetary Science* 51 (3): 468–82. https://doi.org/10.1111/maps.12607.

Jenniskens, P., and H. A. R. Devillepoix. 2025. “Review of Asteroid, Meteor, and Meteorite-Type Links.” *Meteoritics & Planetary Science* 60 (4): 928–73. https://doi.org/10.1111/maps.14321.

Jiang, S., Y. Lin, and H. Zhang. 2004. “Improvement of the Sample Preparation Method for AMS Measurement of 36Cl in Natural Environment.” *Nuclear Instruments and Methods in Physics Research Section B Beam Interactions with Materials and Atoms* 223-224 (May): 318–22. https://doi.org/10.1016/j.nimb.2004.04.063.

Jones, J., P. Brown, K.J. Ellis, A.R. Webster, M. Campbell-Brown, Z. Krzemenski, and R.J. Weryk. 2005. “The Canadian Meteor Orbit Radar: System Overview and Preliminary Results.” *Planetary and Space Science* 53 (4): 413–21. https://doi.org/10.1016/j.pss.2004.11.002.

Jull, A. J. T., R. P. Binzel, R. M. Walker, and A. G. W. Cameron. 2006. “Terrestrial Ages of Meteorites.” In *Meteorites and the Early Solar System II,* edited by D. S. Lauretta and H. Y. McSween, 889–906. University of Arizona Press.

Jull, A. J. T., L. R. McHargue, P. A. Bland, R. C. Greenwood, A. W. R. Bevan, K. J. Kim, S. E. LaMotta, and J. A. Johnson. 2010. “Terrestrial Ages of Meteorites from the Nullarbor Region, Australia, Based on 14C and 14C-10Be Measurements.” *Meteoritics & Planetary Science* 45 (8): 1271–83. https://doi.org/10.1111/j.1945-5100.2010.01289.x.

Kouvatsis, I., and B. A. Hofmann. 2019. “A Statistical Analysis of the H/L Ratio of Ordinary Chondrite Finds and Falls: A Comparison of Oman Finds with Other Populations.” *Meteoritics & Planetary Science* 55 (1): 67–76. https://doi.org/10.1111/maps.13410.

Kurlander, J. A. 2025. “Predictions of the LSST Solar System Yield: Near-Earth Objects, Main Belt Asteroids, Jupiter Trojans, and Trans-Neptunian Objects.” Edited by P.H. Bernardinelli. *The Astronomical Journal*.

Leya, I., and J. Masarik. 2009. “Cosmogenic Nuclides in Stony Meteorites Revisited.” *Meteoritics & Planetary Science* 44 (7): 1061–86. https://doi.org/10.1111/j.1945-5100.2009.tb00788.x.

Marsset, M., P. Vernazza, M. Brož, C. A. Thomas, F. E. DeMeo, B. Burt, R. P. Binzel, et al. 2024. “The Massalia Asteroid Family as the Origin of Ordinary L Chondrites.” *Nature* 634 (8034): 561–65. https://doi.org/10.1038/s41586-024-08007-6.

Marti, K., and T. Graf. 1992. “Cosmic-Ray Exposure History of Ordinary Chondrites.” *Annual Review of Earth and Planetary Sciences* 20 (1): 221–43. https://doi.org/10.1146/annurev.ea.20.050192.001253.

McGee, D., and S. Mukhopadhyay. 2013. “Extraterrestrial He in Sediments: From Recorder of Asteroid Collisions to Timekeeper of Global Environmental Changes.” In *The Noble Gases as Geochemical Tracers.* Advances in Isotope Geochemistry. : Springer, Berlin, Heidelberg.

Merchel, S., and U. Herpers. 1999. “An Update on Radiochemical Separation Techniques for the Determination of Long-Lived Radionuclides via Accelerator Mass Spectrometry.” *Radiochimica Acta* 84 (4): 215–20. https://doi.org/10.1524/ract.1999.84.4.215.

Minton, D. A., and R. Malhotra. 2010. “Dynamical Erosion of the Asteroid Belt and Implications for Large Impacts in the Inner Solar System.” *Icarus* 207 (2): 744–57. https://doi.org/10.1016/j.icarus.2009.12.008.

Moore, A. K., and D. E. Granger. 2019. “Calibration of the Production Rate of Cosmogenic 36Cl from Fe.” *Quaternary Geochronology* 51 (April): 87–98. https://doi.org/10.1016/j.quageo.2019.02.002.

Morbidelli, A., and B. Gladman. 1998. “Orbital and Temporal Distributions of Meteorites Originating in the Asteroid Belt.” *Meteoritics & Planetary Science* 33 (5): 999–1016. https://doi.org/10.1111/j.1945-5100.1998.tb01707.x.

Morbidelli, A., and D. Vokrouhlický. 2003. “The Yarkovsky-Driven Origin of Near-Earth Asteroids.” *Icarus* 163 (1): 120–34. https://doi.org/10.1016/s0019-1035(03)00047-2.

Nesvorný, D., F. Roig, D. Vokrouhlický, and M. Brož. 2024. “Catalog of Proper Orbits for 1.25 Million Main-Belt Asteroids and Discovery of 136 New Collisional Families.” *The Astrophysical Journal Supplement Series* 274 (2): 25–25. https://doi.org/10.3847/1538-4365/ad675c.

Nica, N., J. Cameron, and B. Singh. 2012. “Nuclear Data Sheets for a = 36.” *Nuclear Data Sheets* 113 (1): 1–155. https://doi.org/10.1016/j.nds.2012.01.001.

Nishiizumi, K. 1987. “53Mn, 26Al, 10Be and 36Cl in Meteorites: Data Compilation.” *International Journal of Radiation Applications and Instrumentation. Part D. Nuclear*

Tracks and Radiation Measurements 13 (4): 209–73. https://doi.org/10.1016/1359-0189(87)90038-0.

Nishiizumi, K., D. Elmore, and P. W. Kubik. 1989. "Update on Terrestrial Ages of Antarctic Meteorites." *Earth and Planetary Science Letters* 93 (3-4): 299–313. https://doi.org/10.1016/0012-821x(89)90029-0.

Nishiizumi, K., and M. W. Caffee. 2001. "Exposure Histories of Lunar Meteorites Dhofar 025, 026, and Northwest Africa 482." *Meteoritics & Planetary Science* **36** (Suppl.): A482. Abstract presented at the 64th Annual Meeting of the Meteoritical Society.

Nishiizumi, K., R. Okazaki, J. Park, K. Nagao, J. Masarik, and R. C. Finkel. 2002. "Exposure and Terrestrial Histories of Dhofar 019 Martian Meteorite." *Lunar and Planetary Science Conference* **33**: Abstract 1366.

Pfeiffer, M., A. M. Morgan, A. M. Heimsath, T. E. Jordan, A. D. Howard, and R. Amundson. 2021. "Century Scale Rainfall in the Absolute Atacama Desert: Landscape Response and Implications for Past and Future Rainfall." *Quaternary Science Reviews* 254 (8): 106797–97. https://doi.org/10.1016/j.quascirev.2021.106797.

Pinto, G. A., A. Tavernier, J. Gattacceca, A. Corgne, M. Valenzuela, B. Luais, L. Flores, F. Olivares, and Y. Marrocchi. 2024. "Dense Collection Areas and Terrestrial Alteration of Meteorites in the Atacama Desert." *Meteoritics & Planetary Science* 59 (2): 351–67. https://doi.org/10.1111/maps.14125.

Pourkhorsandi, H., J. Gattacceca, P. Rochette, M. D'Orazio, H. Kamali, R. Avillez, S. Letichevsky, et al. 2019. "Meteorites from the Lut Desert (Iran)." *Meteoritics & Planetary Science* 54 (8): 1737–63. https://doi.org/10.1111/maps.13311.

Robertson, D., A. Ozerov, L. Wheeler, P. Pokorný, M. Granvik, and C. Rumpf. 2023. " Erratum: 'Latitude Variation of Flux and Impact Angle of Asteroid Collisions with Earth and the Moon' (2021, PSJ, 2, 88)." *The Planetary Science Journal* 4 (1): 19. https://doi.org/10.3847/PSJ/aca1a7.

Robertson, D., P. Pokorný, M. Granvik, L. Wheeler, and C. Rumpf. 2021. “Latitude Variation of Flux and Impact Angle of Asteroid Collisions with Earth and the Moon .” *The Planetary Science Journal* 2 (3): 88. https://doi.org/10.3847/psj/abefda.

Rojas, J., J. Duprat, C. Engrand, E. Dartois, L. Delauche, M. Godard, M. Gounelle, J.D. Carrillo-Sánchez, P. Pokorný, and J.M.C. Plane. 2021. “The Micrometeorite Flux at Dome c (Antarctica), Monitoring the Accretion of Extraterrestrial Dust on Earth.” *Earth and Planetary Science Letters* 560 (April): 116794. https://doi.org/10.1016/j.epsl.2021.116794.

Rubin, A. E. 2018. “Mechanisms Accounting for Variations in the Proportions of Carbonaceous and Ordinary Chondrites in Different Mass Ranges.” *Meteoritics & Planetary Science* 53 (10): 2181–92. https://doi.org/10.1111/maps.13117.

Rubincam, D. P. 2000. “Radiative Spin-up and Spin-down of Small Asteroids.” *Icarus* 148 (1): 2–11. https://doi.org/10.1006/icar.2000.6485.

Sadaka, C., J. Gattacceca, M. Gounelle, M. Roskosz, A. Lagain, R. Tartese, L. Bonal, C. Maurel, R. Martinez, and M. Valenzuela. 2025. “Systematic Meteorite Collection in the Catalina Dense Collection Area (Chile): Description and Statistics.” *Meteoritics & Planetary Science*, no. 60 (January): 308–23. https://doi.org/10.1111/maps.14307.

Schimmelpfennig, I., L. Benedetti, R. Finkel, R. Pik, P.-H. Blard, D. Bourlès, P. Burnard, and A. Williams. 2009. “Sources of In-Situ 36Cl in Basaltic Rocks. Implications for Calibration of Production Rates.” *Quaternary Geochronology* 4 (6): 441–61. https://doi.org/10.1016/j.quageo.2009.06.003.

Schmitz, B., P. R. Heck, W. Alvarez, N. T. Kita, S. S. Rout, A. Cronholm, C. Defouilloy, E. Martin, J. Smit, and F. Terfelt. 2017. “Meteorite Flux to Earth in the Early Cretaceous as Reconstructed from Sediment-Dispersed Extraterrestrial Spinels.” *Geology* 45 (9): 807–10. https://doi.org/10.1130/g39297.1.

Schmitz, B., M. Tassinari, and B. Peucker-Ehrenbrink. 2001. “A Rain of Ordinary Chondritic Meteorites in the Early Ordovician.” *Earth and Planetary Science Letters* 194 (1-2): 1–15. https://doi.org/10.1016/s0012-821x(01)00559-3.

Shober, P. M., H. A. R. Devillepoix, J. Vaubaillon, S. Anghel, S. E. Deam, E. K. Sansom, F. Colas, B. Zanda, P. Vernazza, and P. Bland. 2025. “Perihelion History and Atmospheric Survival as Primary Drivers of the Earth’s Meteorite Record.” *Nature Astronomy* 9 (6). https://doi.org/10.1038/s41550-025-02526-6.

Stone, J.O. 2000. “Air Pressure and Cosmogenic Isotope Production.” *Journal of Geophysical Research: Solid Earth* 105 (B10): 23753–59. https://doi.org/10.1029/2000jb900181.

Tauseef, M., I. Leya, J. Gattacceca, B. Hofmann, S. Szidat, and R. Braucher. 2024. “^{14}C and ^{14}C-^{10}Be Terrestrial Age Dating System for Meteorites—New Data for Four Recently Fallen Meteorites.” *Meteoritics & Planetary Science* 59 (6): 1219–35. https://doi.org/10.1111/maps.14144.

Tauseef, M., I. Leya, J. Gattacceca, S. Szidat, R. Braucher, P. M. Kruttasch, and A. Zappatini. 2025a. “Evaluating ^{14}C and ^{14}C/^{10}Be Terrestrial Age Dating Systems for Meteorites Using Experimental Data and Model Calculations.” *Meteoritics & Planetary Science* 60 (5): 1263–83. https://doi.org/10.1111/maps.14355.

Tauseef, M., Leya, I., Hofmann, B. 2025b. “Cosmic ray exposure ages and pre-atmospheric shielding of Omani meteorites: Implications for ^{14}C and ^{14}C/^{10}Be terrestrial ages of meteorites from hot and cold deserts.” *Meteoritics & Planetary Science* 60 (9): 2184–96. https://doi.org/10.1111/maps.70029.

Terfelt, F., and B. Schmitz. 2021. “Asteroid Break-Ups and Meteorite Delivery to Earth the Past 500 Million Years.” *Proceedings of the National Academy of Sciences* 118 (24). https://doi.org/10.1073/pnas.2020977118.

Velbel, M.A. 2012. “Terrestrial Weathering of Ordinary Chondrites in Nature and Continuing during Laboratory Storage and Processing: Review and Implications for Hayabusa

Sample Integrity." *Meteoritics & Planetary Science* 49 (2): 154–71. https://doi.org/10.1111/j.1945-5100.2012.01405.x.

Vogt, S, and U. U. Herpers. 1988. "Radiochemical Separation Techniques for the Determination of Long-Lived Radionuclides in Meteorites by Means of Accelerator-Mass-Spectrometry." *Fresenius' Zeitschrift Für Analytische Chemie* 331 (2): 186–88. https://doi.org/10.1007/bf01105164.

Welten, K. C., M. W. Caffee, M. E. Kress, M. D. Giscard, T. Jull, R. P. Harvey, and J. Schutt. 2024. "Cosmogenic Radionuclides in Meteorites from the Otway Massif Blue Ice Area, Antarctica: An Unusual, Well-Preserved H5 Chondrite Strewn Field." *Meteoritics and Planetary Science*, no. 59 (September): 3056–71. https://doi.org/10.1111/maps.14264.

Welten, K. C., K. Nishiizumi, R. C. Finkel, D. J. Hillegonds, T. Jull, L. Franke, and L. Schultz. 2004. "Exposure History and Terrestrial Ages of Ordinary Chondrites from the Dar al Gani Region, Libya." *Meteoritics & Planetary Science* 39 (3): 481–98. https://doi.org/10.1111/j.1945-5100.2004.tb00106.x.

Welten, K.C., L Folco, K. Nishiizumi, M.W Caffee, A Grimberg, M.M.M Meier, and F Kober. 2008. "Meteoritic and Bedrock Constraints on the Glacial History of Frontier Mountain in Northern Victoria Land, Antarctica." *Earth and Planetary Science Letters* 270 (3-4): 308–15. https://doi.org/10.1016/j.epsl.2008.03.052.

Wyatt, S. P., and F. L. Whipple. 1950. "The Poynting-Robertson Effect on Meteor Orbits." *The Astrophysical Journal* 111 (January): 134. https://doi.org/10.1086/145244.

Zekollari, H., S. Goderis, V. Debaille, M. Van Ginneken, J. Gattacceca, A. J. T. Jull, J. T. M. Lenaerts, A. Yamaguchi, P. Huybrechts, and P. Claeys. 2019. "Unravelling the High-Altitude Nansen Blue Ice Field Meteorite Trap (East Antarctica) and Implications for Regional Palaeo-Conditions." *Geochimica et Cosmochimica Acta* 248 (248): 289–310. https://doi.org/10.1016/j.gca.2018.12.035.

Zolensky, M. E., G. L. Wells, and H. M. Rendell. 1990. “The Accumulation Rate of Meteorite Falls at the Earth’s Surface: The View from Roosevelt County, New Mexico.” *Meteoritics* 25 (1): 11–17. https://doi.org/10.1111/j.1945-5100.1990.tb00965.x.

Zolensky, M., P. Bland, P. Brown, and I. Halliday. 2006. “Flux of Extraterrestrial Materials.” In *Meteorites and the Early Solar System II*, edited by H. Y. Mcsween. Tucson, Ariz.: University Of Arizona Press ; Houston, Ariz.

3.4. Conclusion

This study proves that Atacama meteorite collections provide a unique record of the long-term meteorite flux to Earth, owing to the unparalleled preservation conditions of the Atacama Desert. These timescales overlap with those of meteoroid delivery to Earth, which allows us to bridge the gap between dynamic modelling of meteorite delivery and meteorite ground truth. The results confirm the stability of the bulk flux over the past 2 Myr, while also revealing compositional variations that point to distinct processes affecting meteoroid delivery to Earth on shorter timescales, not considered in current dynamical models.

The follow-up study will focus on cosmic-ray exposure ages of Atacama meteorites and combining them with their terrestrial ages to provide a direct constraint on the ejection ages of the meteorites from their parent asteroids (Chapter 5). This approach will improve our understanding of the collisional events that are potentially responsible for the observed variations in the relative abundance of H chondrites over the last 2 Myr, and the mechanisms governing meteorite delivery to Earth.

1

Chapter four

Calama area meteorite collection: density, classification, and terrestrial ages



We are limited, not by our abilities, but by our vision.

2 – ***Gibran Khalil Gibran***

3

Summary

4.1. Introduction **209**

4.2. Article **209**

4.3. Conclusion **246**

4. Chapter 4

4.1. Introduction

The studied Dense Collection Areas (DCAs) in the Atacama Desert mentioned in previous chapters (i.e., Catalina, El Médano, Caleta el Cobre, and San Juan) are adjacent and located in the southern part of the Atacama Desert. In earlier chapters, I presented the Catalina Systematic Collection (CSC), with details on recovery density, classification, pairing, and terrestrial ages. These datasets were used to estimate the long-term meteorite flux to Earth in one of the most stable desert environments on Earth.

In this chapter, I focus on the Calama area, which is located around 300 km further north and includes the Calama, Sierra Gorda, and Chug Chug DCAs. With more than 1200 meteorites in the Meteoritical Bulletin Database (as of September 2025), the Calama area is one of the major meteorite recovery zones in the Atacama Desert. Its distinct geomorphological features, including proximity to the pre-Andean range, slightly higher humidity, and more active surface processes, allow us to investigate the effect of local environmental factors on meteorite preservation and terrestrial ages.

By comparing both systematic and non-systematic recoveries, along with ^{36}Cl-based terrestrial ages of 49 ordinary chondrites, this chapter aims to evaluate whether the trends observed in the southern DCAs extend across the entire Atacama Desert under different climatic and geomorphological conditions.

4.2. Article

Article in preparation for submission in *Meteoritics & Planetary Science*.

Sadaka, C., J. Gattacceca, F. Dumas, et al. 2025. In Prep. “Description of the Calama Area Meteorite Collection (Atacama Desert, Chile)”.

33

Description and terrestrial ages of the Calama Area Meteorite Collection (Atacama Desert, Chile)

Carine SADAKA[1*], Jérôme GATTACCECA[1], Florian DUMAS[1,2,3], Régis BRAUCHER[1], ASTER Team[1], Matthieu GOUNELLE[4], Dilyara KUZINA[5], Cyril LORENZ[6], Alexandre CORGNE[7]

[1]Aix-Marseille Univ, CNRS, IRD, INRAE, CEREGE, Aix-en-Provence, France

[2] Laboratoire G-Time, Université Libre de Bruxelles, Brussels, Belgium

[3] AMGC, Vrije Universiteit Brussel, Brussels, Belgium

[4]Institut de minéralogie, de physique des matériaux et de cosmochimie—UMR7590, Muséum National d'Histoire Naturelle, Paris, France

[5]Institute of Geology and Petroleum Technologies, Kazan Federal University, Kazan, Russia

[6]Vernadsky Institute of geochemistry and analytical chemistry, Moscow, 119991, Russia

[7]Instituto de Ciencias de la Tierra, Universidad Austral de Chile, Valdivia, Chile

*Corresponding author: sadaka@cerege.fr

Abstract

We present a comprehensive study of a meteorite collection from the Atacama Desert (Chile), the driest and most climatically stable desert in the world. This collection includes meteorites from three adjacent Dense Collection Areas (DCAs): Calama, Sierra Gorda, and Chug Chug DCAs in the northern part of the Atacama Desert, hereafter referred to as the

"Calama area". Within this region (~550 km^2), we conducted a systematic search over a 2.5 km^2 zone in the Calama DCA and compared it to the non-systematic density in the Calama area. We also present the ^{36}Cl-based terrestrial ages of 49 ordinary chondrites selected from the Calama area. The systematic search yielded a meteorite recovery density of 37 meteorites per km^2 (15 meteorites per km^2 for meteorites > 20 g), and the collection exhibits a median terrestrial age of 235 ka. Notably, compared to the El Médano and Catalina DCAs, the Calama area is characterized by a lower meteorite density and younger meteorite terrestrial ages, most likely reflecting the region's more humid climate and more dynamic geomorphology due to its proximity to the pre-Andean range. Nevertheless, the Calama area still exhibits higher densities and older terrestrial ages than in any other hot desert in the world, confirming that the long-term preservation of meteorites in observed across the entire Atacama Desert.

1. INTRODUCTION

Meteorites are key materials to study the formation and evolution of the Solar System. As fragments of asteroids, or more rarely, the Moon or Mars, they hold a unique record of early planetary processes and the composition of the Solar System.

The number of meteorites in world collections has been rapidly growing for the past decade through recovery from cold and hot deserts. Over the last ten years, the number of meteorites in the Meteoritical Bulletin database (MBDB; https://www.lpi.usra.edu/meteor/metbull.cfm) has jumped from ~50 000 to ~78 000. In 2024 only, 3646 meteorites have been approved in the MBDB, with >90% coming from cold and hot deserts (Gattacceca et al., 2025a).

Hot deserts are particularly suitable for meteorite recovery, with ~35% of officially recognized meteorites coming from these areas (MBDB, as of September 2025). Hot deserts, such as the the Nullarbor Region in Australia (Jull et al., 2010; Benedix et al., 1999), the Northwest African deserts (Aboulahris et al., 2019; Belhai, 2023; Schlüter et al., 2002), the

Arabian Peninsula (Hofmann et al., 2018; Hofmann and Gnos, 2024; Pourkhorsandi et al., 2019), Roosevelt County in southwestern USA (Zolensky et al., 1990), and the Atacama Desert in Chile (Gattacceca et al., 2011; Hutzler et al., 2016; Sadaka et al., 2025), have been for decades, and still are thoroughly searched for meteorite recovery. They have provided a wealth of scientifically invaluable meteorites such as, for the recent years alone, NWA 7034, a Martian meteorite containing 4.4 Ga zircons (Cartwright et al., 2014), Oued Chebeika 002 CI1 that shows no sign of terrestrial weathering (Gattacceca et al., 2025b), Erg Chech 002, a 4565 Myr old andesite (Barrat et al., 2021), as well as about 1000 kg of lunar meteorites and 300 kg of Martian meteorites.

Among hot deserts, the Atacama Desert, stands out for its hyperaridity and long-term climatic stability (e.g., Dunai et al., 2005). A total of 3990 meteorites from the Atacama Desert are listed in the MBDB as of September 2025. Several studies have shown that the Atacama is home to the densest (Gattacceca et al., 2011; Hutzler et al., 2016; Sadaka et al., 2025) and oldest (Drouard et al., 2019; Sadaka et al., 2026) meteorite collections in the world. These studies have focused on the driest Dense Collection Areas (DCAs) of the Atacama Desert's Central Depression (Figure 1): the San Juan DCA (Gattacceca et al., 2011), the El Médano and Caleta el Cobre DCAs (Hutzler et al., 2016; Drouard et al., 2019), and the Catalina DCA (Sadaka et al., 2025a;b).

The scope of this study is to investigate a meteorite collection from a different area of the Atacama Desert. This area, which combines the Calama, Chug Chug and Sierra Gorda DCAs, will be referred to collectively as the "Calama area" hereafter. This zone is one of the major meteorite recovery areas in the Atacama Desert with 1281 meteorites in the MBDB as of September 2025). The Calama area is located ~300 km north from the above-mentioned

collections (i.e., El Médano, Caleta el Cobre, San Juan, and Catalina) and is characterized by distinct geomorphological and climatic settings (Pinto et al., 2024). These environmental conditions offer valuable potential for assessing the spatial variability of meteorite accumulation and preservation across the Atacama Desert.

We present here the statistical properties of the Calama Area Collection (CAC). They include the outcomes of a systematic meteorite collection that we performed over a 2.5 km^2 surface in the Calama area, as well as the terrestrial ages measured in 49 meteorites from the CAC. We then compared these observations with the other well-documented meteorite collections from the Atacama Desert.

2. CLIMATE & GEOLOGY OF THE CALAMA AREA

2.1. Climate

The Atacama Desert is located in Northern Chile, bordered by the coast of the Pacific Ocean to the west and the Andes to the east. It includes four main geological units: Coastal Range, Central Depression, pre-Andean Range, and Western Cordillera, while the Altiplano forms a high-elevation plateau to the east. This desert is one of the most arid regions on Earth as it is characterized by a long-standing arid to hyperarid climate, estimated to have been established between 3 and 25 Ma ago (Clarke, 2006; Dunai et al., 2005, Jungers et al., 2013).

The “Calama area” encompasses meteorites from three adjacent DCAs: Chug Chug, Sierra Gorda, and Calama DCAs (Figure 1). The Calama, Sierra Gorda, and Chug Chug DCAs are characterized by an arid climate with an average annual air temperature range of ~13–16°C and an average annual cumulative precipitation of ~ 18–30 mm/year, recorded between 2001 and 2021 (Pinto et al., 2024). While still arid, this area experiences slightly higher annual

precipitation compared to the hyperarid conditions of the Catalina, El Médano, Caleta el Cobre and San Juan DCAs (Table 1).

2.2. Geomorphology

The investigated region is part of the Calama Basin, a northern prolongation of the Preandean Depression, bordered by the Domeyko Cordillera to the west and the Western Cordillera to the east. It is filled with Neogene to Quaternary sediments, with important tectono-volcanic and climatic control (Tomlinson et al., 2018). The main geological units are: (1) the Opache Formation (Miocene–Pliocene, ~7–3 Ma) which includes lacustrine limestones, travertines, and sandstones, often fossiliferous; (2) the **Chiquinaputo/Chiquicamata Formation** (10–3 Ma) composed of conglomerates, sandstones, and siltstones with diatomite and carbonate interbeds; (3) Plio-Quaternary **piedmont and alluvial deposits** with extensive alluvial fans and gravel plains forming the pampas (gravel or sand plains formed by coalescing fans); and (4) **Holocene fluvial deposits composed of** gravels and silts along the Río Loa and San Salvador valleys, representing active sedimentation zones. The **Domeyko Cordillera** hosts **Eocene–Oligocene porphyry intrusions and volcanic rocks** (Chuquicamata district), which supply abundant detritus to the basin through erosion and episodic alluvial fan deposition.

The landscape is dominated by broad and flat **alluvial pampas,** dissected by the Río Loa, the longest perennial river of the Atacama Desert, and its main affluent, the Río Salado (Figure 2). These rivers have carved **incised valleys** into the basin fill, but most meteorites are located on stable **interfluves** and **pampas** away from active channels.

Meteorites are spread across the three DCAs of the **CAC region** at altitudes between 1600 and 2800 m a.s.l., extending from the western side to the eastern side on a gentle slope (<1°) **(Figure 2)**. In the **Calama DCA**, meteorites are located on Late Pleistocene–Holocene fluvial

terraces along the Río Loa and Río Salado, on adjacent alluvial and piedmont surfaces, and locally on Miocene lacustrine–fluvial units (Opache Formation). In the **Chug Chug and Sierra Gorda DCA**, the meteorites are mostly located on an isolated plain between the Río Loa and Río San Salvador, mainly on the Opache Formation (Tomlinson et al., 2018; Duhart et al., 2018; Ladino et al., 2001).

In the systematically searched zone of the **Calama DCA (CASC, Figure 3)** only the **Opache Formation** is exposed (Tomlinson et al., 2018). The surface is flat (slope <1°), light beige in color, and consists of gravels scattered with abundant centimeter-sized pebbles of diverse sedimentary lithologies, including palustrine limestones, shales, sandstones, and calcareous conglomerates (Figure 4).

For comparison, the **Catalina DCA** lies further south (Figure 1) in the Central Depression at ~2000 m a.s.l. and is characterized by continuous flat plains of Cretaceous and Jurassic volcanic formations (see Sadaka et al., 2025a for more details). The San Juan DCA, also located in the Central Depression, lies on Tertiary–Quaternary colluvium and alluvium. The surface is flat, with slopes of ~1.5°. On the **coastal side**, the **El Médano and Caleta el Cobre DCAs** are situated at 1950–2400 m a.s.l. on relatively flat surfaces with slopes <3° interspersed between irregular relief. They are composed mainly of Jurassic–Cretaceous intrusive igneous rocks (granodiorites, diorites, gabbros) overlain by Mio-Pliocene alluvium and colluvium (Hutzler et al., 2016). Despite these geological differences, the meteorite-rich areas in all these DCAs are deflation surfaces characterized by a thin gravel layer underlain by gypsum- and anhydrite-rich caliche, as well as the presence of desert pavement and ventifacts. This deflation setting, combined with hyperaridity, are key factors for exceptional meteorite preservation and accumulation.

178 ## 3. METHODS

179 ### 3.1.Surface Ages

180 To estimate the age of the surface, we measured the concentration of cosmogenic ^{36}Cl (half-
181 life 301.3 ka; Nica et al., 2012) produced in situ in two carbonate rocks (#497 and #498) in the
182 Calama DCA collected at the surface using Accelerator Mass Spectrometry (AMS) (Figure 5).
183 Samples were processed at CEREGE. For the carbonate rocks, ^{36}Cl was measured following
184 standard procedures adapted from Schimmelpfennig et al. (2009, 2011) and Baroni et al. (2025).
185 Each carbonate rock was crushed and sieved to isolate the 250-1000 µm grain size fraction. The
186 finer fraction (<250 µm) was retained for bulk chemical analysis. Dry rock densities were
187 determined using the Archimedes principle on representative clasts and were found to be 2.53
188 g/cm³ for #497 and 2.45 g/cm³ for #498. Approximately 100 g of sieved grains per sample were
189 used for chemical preparation, and a procedural blank was processed in parallel to monitor for
190 contamination. Atmospheric Cl was removed by washing the samples sequentially with Milli-
191 Q water and 2 M HNO_3, which dissolved roughly 10% of the sample mass. The remaining
192 material was dried and weighed (target fraction), and a calibrated in-house ^{35}Cl-enriched carrier
193 solution ($^{35}Cl/^{37}Cl$ = 294; ~6 mg Cl) was added. The samples were then fully dissolved in 2 M
194 HNO_3 and filtered to remove insoluble residues. Aliquots (1 ml) of the filtered solutions were
195 collected to measure Ca and K concentrations using ICP-AES at CEREGE. Chloride was
196 precipitated as AgCl by the addition of $AgNO_3$. The precipitate was redissolved in NH_4OH, and
197 $Ba(NO_3)_2$ was added to remove sulfur (including the ^{36}Cl isobar ^{36}S) as $BaSO_4$. Following
198 filtration, AgCl was reprecipitated by acidification with HNO_3, then collected, dried, and
199 prepared for AMS measurements of $^{36}Cl/^{35}Cl$ and $^{35}Cl/^{37}Cl$ ratios at the French National
200 Accelerator Mass Spectrometry facility (ASTER) in CEREGE, Aix-en-Provence.
201
202 ### 3.2. Meteorite collection

Meteorites were collected applying a systematic collection method similar to the ones previously undertaken for the El Médano DCA (El Médano systematic collection or EMSC, Hutzler et al., 2016) and the Catalina DCA (Catalina systematic collection or CSC, Sadaka et al., 2025a). We performed systematic collections in three small zones within the Calama DCA for a total of 2.5 km^2 (Figure 3). This collection was assembled for 4 days, representing a total of 39 (wo)man-days of systematic search on foot, organized by CEREGE in collaboration with MNHN (Museum national d'Histoire naturelle de Paris, France), and the Universidad Austral (Valdivia, Chile). Samples were then classified at CEREGE.

In the Calama area, meteorites were collected by private hunters during random walks and classified at the Vernadsky Institute.

3.3. Meteorite classification

At Vernadsky Institute, classification of meteorites was performed using optical microscopy (Leica DMRX microscope equipped with Leica DFC 320 digital camera) for petrographic description of the sections, scanning electron microscopy (Tescan Mira 3) for mineralogical investigation, energy-dispersive X-ray microanalysis coupled with scanning electron microscope Tescan Mira 3 (Ultim MAX 100 EDS detector and Aztec Automate 6.0 software, Oxford Instruments), and wave-dispersive X-ray microanalysis (electron microprobe analyser Cameca SX 100) for chemical composition analysis of the minerals. The chemical composition of minerals was determined under the followed conditions: SEM-based EDS at 20 kV accelerating voltage, beam current ~0.9 nA, spot size 1 µm, using INCA C321 set of standards (Oxford Instruments Microanalysis); WDS - 15 kV accelerating voltage, 20 nA beam current, spot size 1.5 1 µm, peak counting times of 20 seconds, ZAF matrix correction, using

natural and synthetic minerals (Smithsonian Microbeam Standards, Smitsonian Institution, Washington D.C., USA).

In CEREGE, meteorite classification was based on petrographic observations, magnetic measurements, and mineral compositional analysis. Mineralogy and textures were examined on polished sections under either a Keyence VHX-7000 digital microscope or a Leica DM polarizing microscope. The chemical composition of minerals was determined by electron probe microanalyses using a Cameca SX Five at the CAMPARIS facility (Sorbonne Université, Paris), operating at 15 kV accelerating voltage, 10 nA beam current, and a 1 μm in diameter electron. Magnetic susceptibility was measured on whole samples at CEREGE using a KLY2 susceptibility meter (Agico, 65 cm^3 coil), or a SM30 contact probe from ZH Instruments, following the calibration of Gattacceca et al. (2004), for samples too large to fit in the KLY2 coil. Samples smaller than ~2 g were measured using either an Agico MFK or a ZH Instruments SM150.

3.4. Terrestrial age measurements

3.4.1. Sample selection

In the Calama area collection, we first performed an initial random draw among meteorites weighing more than 20 g. We then assessed potential pairings based on petrographic, geochemical, and magnetic properties, as well as the distance between the meteorites. If a high probability of pairing was identified, a new sample was drawn in an iterative process. We selected a total of 49 meteorites from the Calama area. Meteorite samples from the Calama area were provided by the Vernadsky Institute (Moscow, Russia). The dataset dataset consists of 32 H chondrites (25 H5, 5 H6, and 2 H4), 15 L chondrites (9 L5 and 6 L6), and 2 LL chondrites

(one LL5 and one LL6). The geographical distribution of selected samples is displayed in Figure 5.

3.4.2. ^{36}Cl measurements

Terrestrial ages of the selected meteorites were estimated by measuring the concentration of the cosmogenic nuclide ^{36}Cl in the metallic fraction. In brief, the procedure involves extracting and purifying 50–100 mg of metal by grinding, sieving, and magnetic separation, followed by sequential ultrasonic cleaning (ethanol, 0.2M HCl, 67% EATG). A Cl carrier was added, and the metal was dissolved in 2M HNO_3 at 70–80 °C for ≥48 h. Chlorine was isolated by precipitating AgCl with $AgNO_3$, removing isobaric interferences through $BaSO_4$ and $BaCO_3$ co-precipitation, and finally reprecipitating AgCl. The resulting AgCl precipitates were rinsed, dried, and loaded into Accelerator Mass Spectrometer cathodes. A full description of the analytical procedure is provided in Sadaka et al. (2025b).

^{36}Cl measurements were performed at the ASTER facility in CEREGE. Both ^{36}Cl and Cl concentrations were determined by isotope dilution and normalized to the SM-CL12 standard (^{36}Cl/^{35}Cl-value of (1.428 ± 0.02) × 10^{-12}; Merchel et al., 2011). A decay constant of 2.303 ± 0.016 ×10^{-6} yr^{-1} was used, corresponding to a ^{36}Cl half-life (T_{36Cl}) of 301.3 ± 1.5 kyr. Analytical uncertainties include counting statistics, machine stability and blank correction, yielding average ^{36}Cl/^{35}Cl uncertainties of approximately 5–6%.

The terrestrial production rate (expressed in disintegration per minute per kilogram) of ^{36}Cl in the metal phase of meteorites located at the collection site in the Calama area is approximately 10^{-3} dpm/kg, which is ~10^{-4} times lower than the mean activity of samples measured in this study of 10.2 dpm/kg (range 0.15–18.83 dpm/kg, n = 49). Thus, the terrestrial

production is negligible to production in space. Knowing the remaining ^{36}Cl concentration in the meteorite, the terrestrial age (T_{terr}) can be calculated with the following equation:

$$T_{terr} = \frac{1}{\lambda(36Cl)} ln(\frac{P_{sat}}{P_{meas}})$$

Where λ_{36Cl} is the decay constant defined as the fraction of the nuclei that decay per unit time (λ_{36Cl}= ln(2)/ $T_{1/2}$), P_{sat} is the saturated production rate in space, P_{meas} is the measured activity of ^{36}Cl ($P_{meas} = \lambda N_{meas}$), and N_{meas} is the number of ^{36}Cl atoms in the sample, measured using AMS (see Supplementary Material in Sadaka et al., 2025b).

After metal dissolution and prior to the first precipitation step, a 300 µL aliquot of the supernatant liquid is sampled, and Fe and Ni concentrations are measured on this aliquot using Inductively Coupled Plasma Optical Emission Spectrometry (ICP-OES) at CEREGE. Using the model of Leya and Masarik (2009), which estimates the ^{36}Cl production based on the chemical composition (here, the Ni and Fe content), the pre-atmospheric radius, and the depth, we calculated the depth-integrated ^{36}Cl production rate P_{sat}, assuming a meteoroid radius of 10 cm and a depth range of 1 to 10 cm (see Sadaka et al. 2025b).

4. RESULTS AND DISCUSSION

4.1.Calama Area Systematic Collection (CASC)

The CASC was assembled over a total surface of 2.5 km^2, where we recovered 73 meteorites through systematic collection. An additional 20 meteorites were found by other meteorite searchers within the same area, raising the total to 93 meteorites (Figure 3). Meteorite masses range from 1.30 to 713 g, with a mean mass of 42.2 g (s.d. 94.5 g), and a median mass of 13.7

295 g. The resulting meteorite recovery density is 37 meteorites per km^2. The density of meteorites
296 with mass >20 g (n=38) is 15 meteorites per km^2 (Table 2).
297
298 The meteorite "productive zone" of the Calama area, broadly defined as the light-colored
299 area with a favorable geomorphologic setting, represents about 550 km^2 (Figure 2). A total of
300 1206 meteorites have been recovered in this area (Figure 2), giving a density of 2.2 meteorites
301 per km^2, much lower than the density in the area that we searched in a systematic way (37
302 meteorites per km^2). This illustrates the efficiency of our systematic collection method.
303 Considering a density of 37 meteorites per km^2, the productive zone may still host about 20000
304 meteorites. The average and median masses for these 1206 meteorites are 290 g and 48.2 g,
305 higher than the average and median masses of 42.2 g and 13.7 g in the CASC, evidencing the
306 incomplete recovery biased toward larger meteorites. An even larger difference was observed
307 between the systematic and non-systematic collections in the Catalina DCA (Sadaka et al.,
308 2025a), with a 118 times higher meteorite recovery density in the area investigated
309 systematically.
310
311 The mass distribution of the different collections considered here (CAC, CASC, CSC,
312 EMSC) is plotted in Figure 6. Compared to the systematic collections (CASC, CSC, and
313 EMSC), the CAC (non-systematic) is characterized by a flatter slope (-0.80), which reflects a
314 higher abundance of larger meteorites. The differences in slopes reflect different recovery
315 methodology and efficiency, and potentially climatic and geomorphological conditions. The
316 climatic factor is especially important in the Calama area with wetter conditions in which
317 smaller meteorites are less likely to survive at the surface than in the CSC, for example.
318

In the CASC, we classified all meteorites weighing more than 5 g and a selection of 10 meteorites < 5 g, for a total of 59 meteorites. Except for Calama 058 (CR2) and Calama 800 (EL4b-an), all classified meteorites are ordinary chondrites, belonging to H5, H6, L5, and L6 groups, with one H5-6 breccia, one LL3, one LL5, and two LL7 (Table 3).

We compare the weathering grade of the CASC with that of the three systematically collected collections from different DCAs in the Atacama Desert. Among meteorites >5 g, the most abundant weathering grade is W2 (37%), followed by W3 (35%) (Figure 7). The CASC exhibits a weathering grade distribution similar to that of the EMSC and SJSC. These three collections have a weathering grade distribution shifted to higher values than the CSC, which has only ~11% samples with a weathering grade above W2 (Figure 7).

Pairing was assessed using the model described in Sadaka et al. (2025a). After pairing, the density decreases to 9 meteorites >20 g per km^2. Similarly to the approach followed in Sadaka et al. (2025a), we applied further corrections to estimate the true meteorite density on the ground, accounting for several recovery biases: the poor recovery efficiency of metal-poor achondrites (mainly HEDs), the scarcity of iron meteorites due to previous collection, and the underrepresentation of the friable carbonaceous chondrites that are eroded more easily than other meteorites. We also considered the estimated fraction of meteorites missed during systematic research, and the variable efficiency of individual searchers (see Sadaka et al., 2025a for more details). Correcting for these biases, we estimate that the real meteorite density on the ground after pairing is 18 meteorites $_{>20\ g}$ per km^2.

These results provide additional evidence that the Atacama Desert holds the highest meteorite density among hot deserts, as densities in other regions do not exceed 10 meteorites per km^2. For comparison, reported densities in the DCAs of the Sahara average ~1 meteorite

per km^2 (Aboulahris et al., 2019; Schlüter et al., 2002), ~2.8 meteorites per km^2 in Saudi Arabia by systematic foot search, ~1.1 meteorites per km^2 in Oman through systematic car search, and 7.3 meteorites per km^2 through systematic foot search (Hofmann et al., 2018; Hofmann & Gnos, 2024).

4.2.Terrestrial ages

In this section, it is important to note that the age spectrum applies to the entire Calama area (CAC). The 49 terrestrial ages measured in the CAC range from 75 to 2183 ka, with an average age of 491 ka (standard deviation 559 ka) and a median age of 235 ka (Table 4; Figures 5 and 8). We do not observe any correlation between the ages and the position of the meteorites in the Calama area (Figure 5), suggesting that the age spectrum is indeed characteristic of the whole area. The old terrestrial ages reflect a long-standing aridity and geomorphological and climatic stability of the Calama area.

Among the three Atacama collections where terrestrial ages have been measured (CSC, EMSC, and CAC), the CSC exhibits the oldest ages, with a median age of 706 ka (Table 2, Figure 9). The EMSC, under comparable climatic conditions, but closer to the coast than the CSC, follows with a median age of 526 ka. In contrast, the CAC displays both a lower median age (243 ka) and lower meteorite densities than the other two collections (Table 2). We attribute this difference to the different geographic and climatic settings of the Calama area, with a proximity to the pre-Andean range and overall higher humidity and precipitation (22 mm per year) compared to the CSC area (15 mm per year) and EMSC area (14 mm per year) over the period 2001–2021 (Pinto et al., 2024). This higher humidity enhances meteorite weathering and accelerates their disappearance.

The exposure ages measured for surface carbonate rocks in the Calama DCA (up to 1.35 Ma) confirm that the surface is stable but younger than the El Medano and Caleta el Cobre surfaces where exposure ages up to > 6 Ma have been measured (Hutzler et al., 2016).

Nevertheless, terrestrial ages in the CAC (average 491 ka) are much older than those reported in any other hot desert. Meteorite collections from Oman and Saudi Arabia show ages between 10 and 25 ka (mean 20 ± 12 ka; Hofmann and Gnos, 2024), while meteorites from the Lut Desert in Iran display ages ranging from 10 to 30 ka (Pourkhorsandi et al., 2019). In the Nullarbor Region, Australia meteorites are characterized by an average terrestrial age of 19± 13 ka (Jull et al., 2006; 2010), while the Sahara collections exhibit terrestrial ages ranging from 0 to 35 ka, and those from Roosevelt County (New Mexico, USA) vary between 7 and >44 ka (Jull et al., 2006).

CONCLUSIONS

We investigated a meteorite collection from the Calama area (550 km^2), located ~300 km north of previously well-described Atacama Desert meteorite collections. The Calama collection exhibits a median terrestrial age of 235 ka for this collection. A systematic search over a 2.5 km^2 zone in the Calama area yielded a meteorite recovery density of 37 meteorites per km^2 (15 meteorites per km^2 for meteorites > 20 g). Based on these findings, we estimate that the favorable surface for meteorite recovery of ~550 km^2 in the Calama area may host about 20000 meteorites.

Compared to the El Médano and Catalina dense collection areas, the Calama area is characterized by a lower meteorite density and younger meteorite terrestrial ages, likely linked to the slightly more humid long-term climatic setting of the Calama region and its proximity to the pre-Andean range, which leads to more active geomorphologic processes.

Despite these differences, both the meteorite density and meteorite terrestrial ages in the Calama area remain much higher than those observed in any other hot desert, confirming that the Atacama is a unique environment favorable for the long-term preservation of meteorites and that the trends observed are not localized to a specific zone in the Atacama but spread across the entire desert.

ACKNOWLEDGEMENTS

We are grateful to all the individuals, in addition to the listed authors, who contributed to the meteorite collection in the Calama systematic collection area throughout the search campaigns in 2022, 2023, and 2024, namely, Lydie Bonal, Chloé Brillatz, Camille Cartier, Marine Ciocco, Jolantha Eschrig, Luigi Folco, Anthony Lagain, Clara Maurel, Anna Musolino, Julien Magre, Rodrigo Martinez, Louna Perez, Gabriel Pinto, Matthieu Roskosz, Alexandra Roussopoulos, Romain Tartese, Lionel Vacher, Millarca Valenzuela, Foteini Vervelidou, Pierre-Marie Zanetta. We thank Timur Kryachko and his partner meteorite hunters who collected most of the meteorites found in the general Calama area, provided the samples for classification at the Verdnasky Institute, and provided additional material for dating at CEREGE. The study was supported by the Russian Science Foundation (project no. 24-27-00388, https://rscf.ru/project/24-27-00388/).

Calama Area Meteorite Collection (Atacama Desert, Chile)

Figure caption

Figure 1. Map of the three main morphotectonic units of the Atacama Desert, showing the seven DCAs of interest in this study. The background image is Google Earth Image. Boundaries for geological units are from Pinto et al. (2024).

Figure 2. Map showing all the meteorites in the Meteoritical Bulletin Database (as of September 2025) from the Calama, Sierra Gorda, and Chug Chug Dense Collection Areas (DCAs) in the "productive zone" of the Calama area, outlined in black dashed lines. Google Earth Image.

Figure 3. Map of the systematically searched areas in the Chug Chug DCA with the position of the meteorites (n=93). The size of meteorite symbols is related to meteorite mass. Google Earth Image.

Figure 4. (a) Typical surface of the systematic collection zone in the Calama DCA (b) Calama 787 (LL7) in situ. (c) Systematic search campaign in the Calama Area Systematic Collection (CASC) in November 2023.

Figure 5. Map showing the position of the meteorites selected for ^{36}Cl dating in the Calama area (n=49), along with the two carbonate rocks collected for surface age determination. The position of the CASC is also shown. Google Earth Image.

Figure 6. Mass distribution (log-log scale) of meteorites from the Calama Area Collection (CAC, light pink spheres), Calama Area Systematic Collection (CASC, dark blue triangles), Catalina Systematic Collection (CSC, light orange crosses), and El Médano Systematic Collection (EMSC, dark green dots). Best linear fits in the 100 g–1 kg mass range are shown, along with slopes reported for each collection: CAC $R^2 = 0.9921$; CASC $R^2 = 0.9537$; CSC $R^2 = 0.9919$; EMSC $R^2 = 0.9906$.

Figure 7. Distribution of weathering grade of ordinary chondrites from the four systematic collections in the Atacama Desert in Catalina (CSC), San Juan (SJSC), El Médano/Caleta el Cobre (EMSC), and Calama (CASC, this work).

Figure 8. Distribution of the terrestrial ages measured in CAC (n = 49). Red dashed line represents median age.

Figure 9. Normalized cumulative distributions of terrestrial ages of Atacama meteorites from the Calama Area Collection (CAC, dark blue), Catalina Systematic Collection (CSC, light

orange), El Médano Systematic Collection (EMSC, dark green), with median ages reported for each collection.

FIGURES

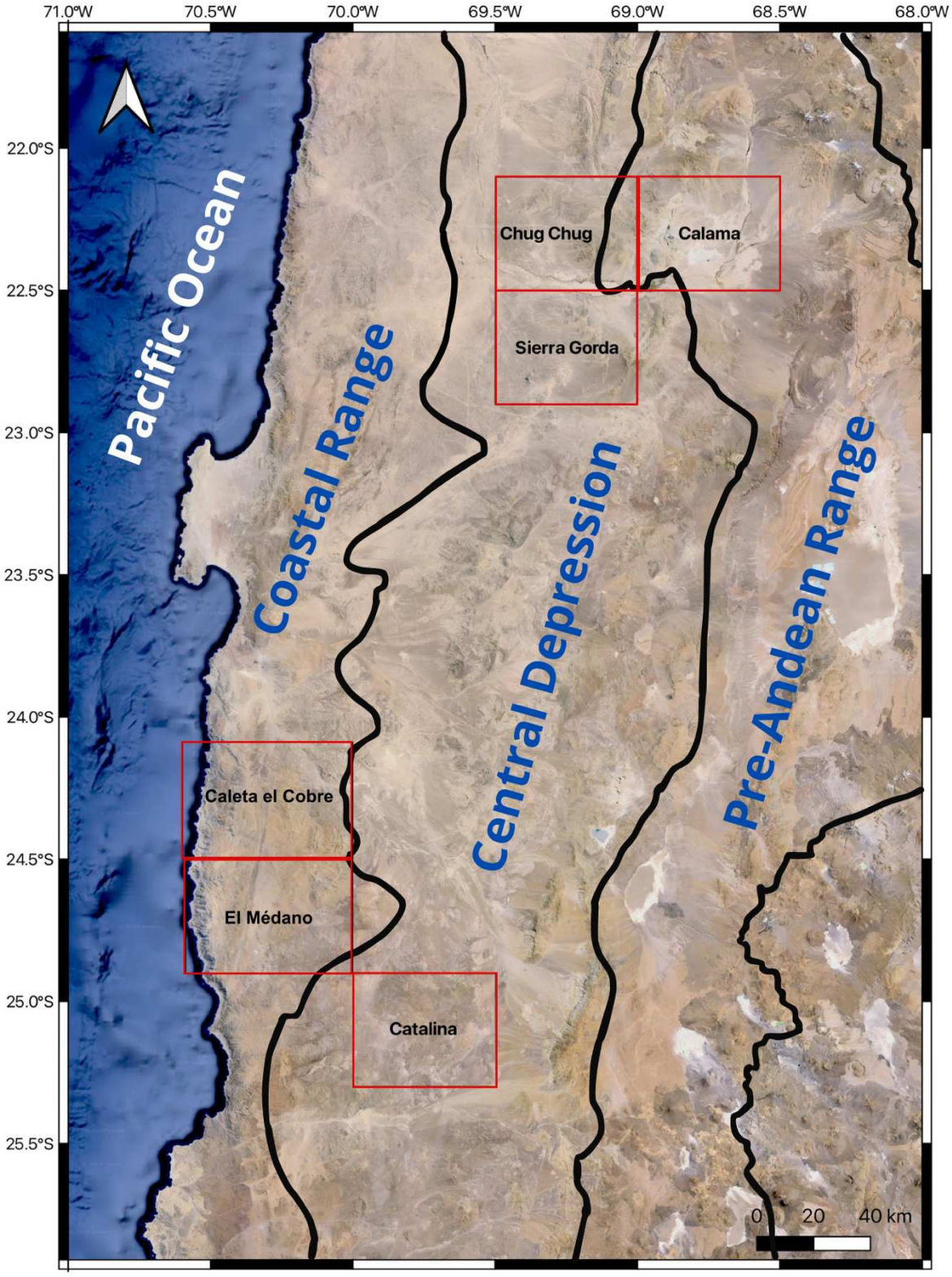
71.0°W
70.5°W
70.0°W
69.5°W
69.0°W
68.5°W
68.0°W
22.0°S
22.5°S
23.0°S
23.5°S
24.0°S
24.5°S
25.0°S
25.5°S
Pacific Ocean
Coastal Range
Central Depression
Pre-Andean Range
Chug Chug
Calama
Sierra Gorda
Caleta el Cobre
El Médano
Catalina
0
20
40 km

Fig. 1

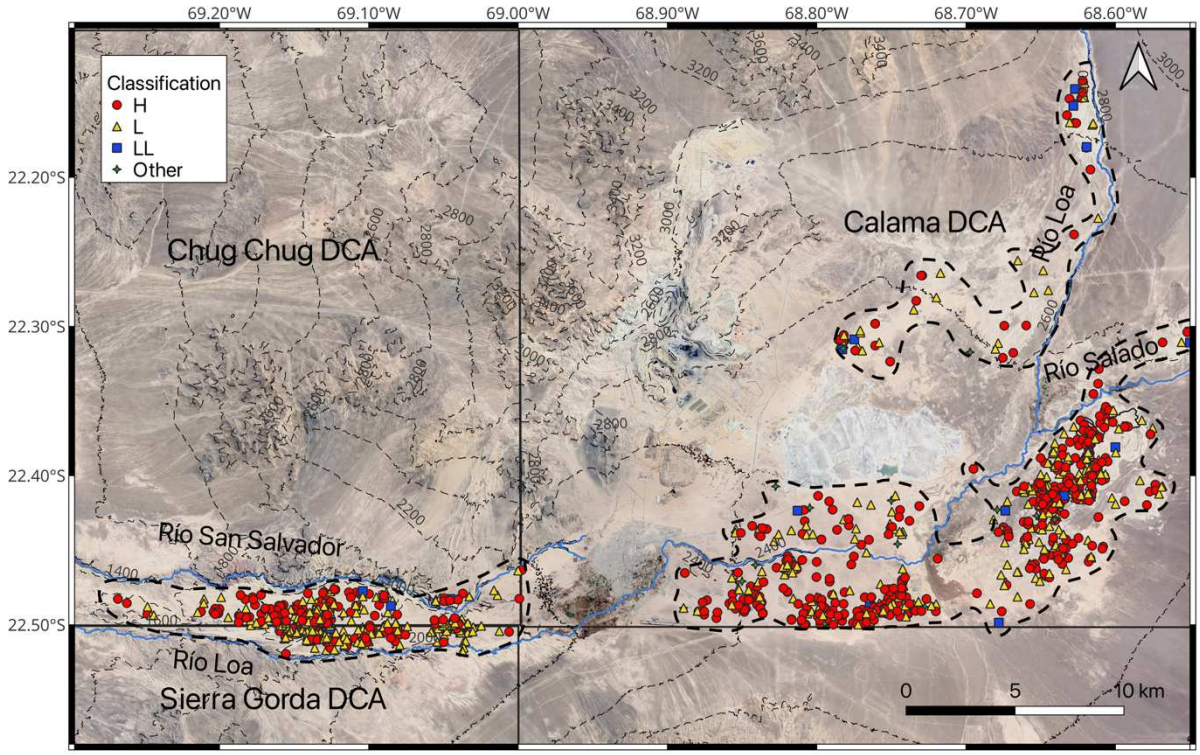

461

462 Fig. 2

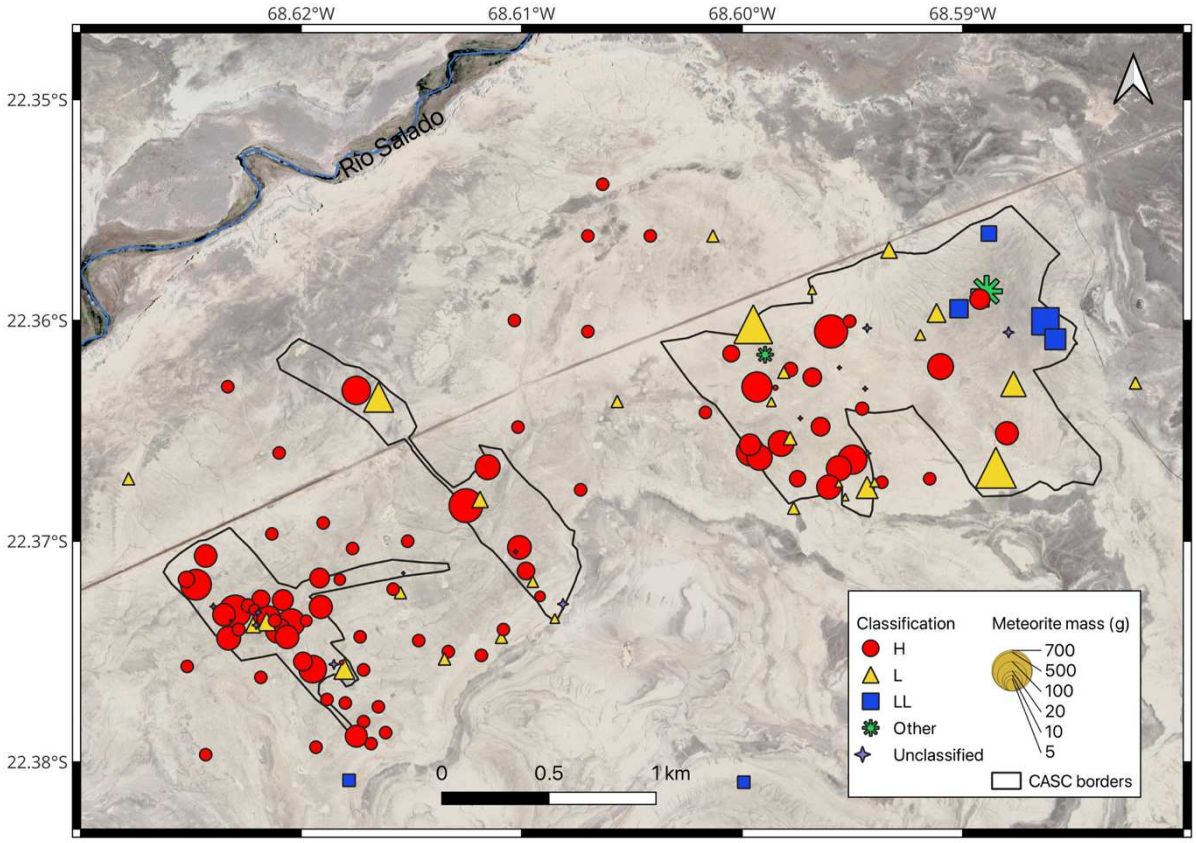

463

464 Fig. 3

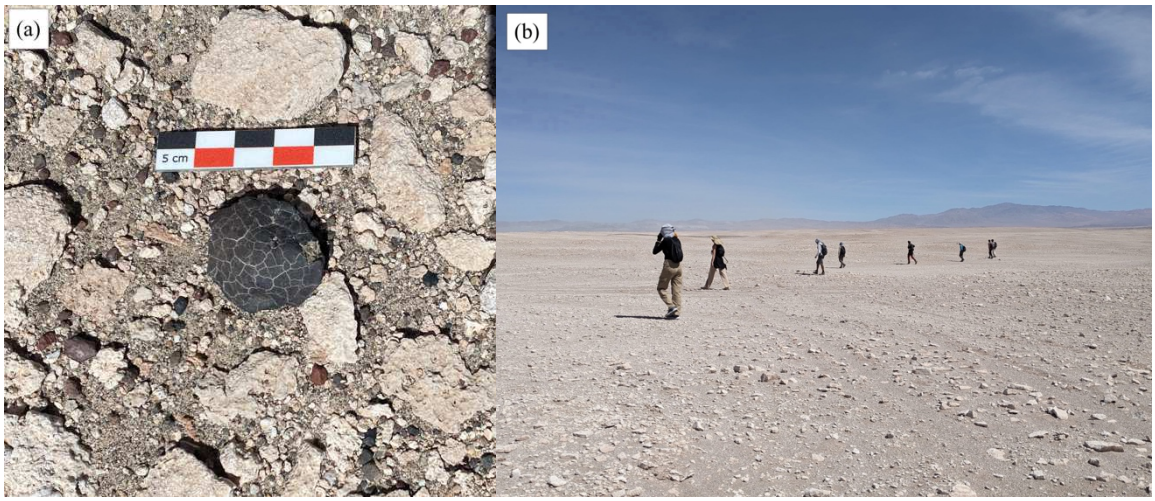
(a)
5 cm
(b)

Fig. 4

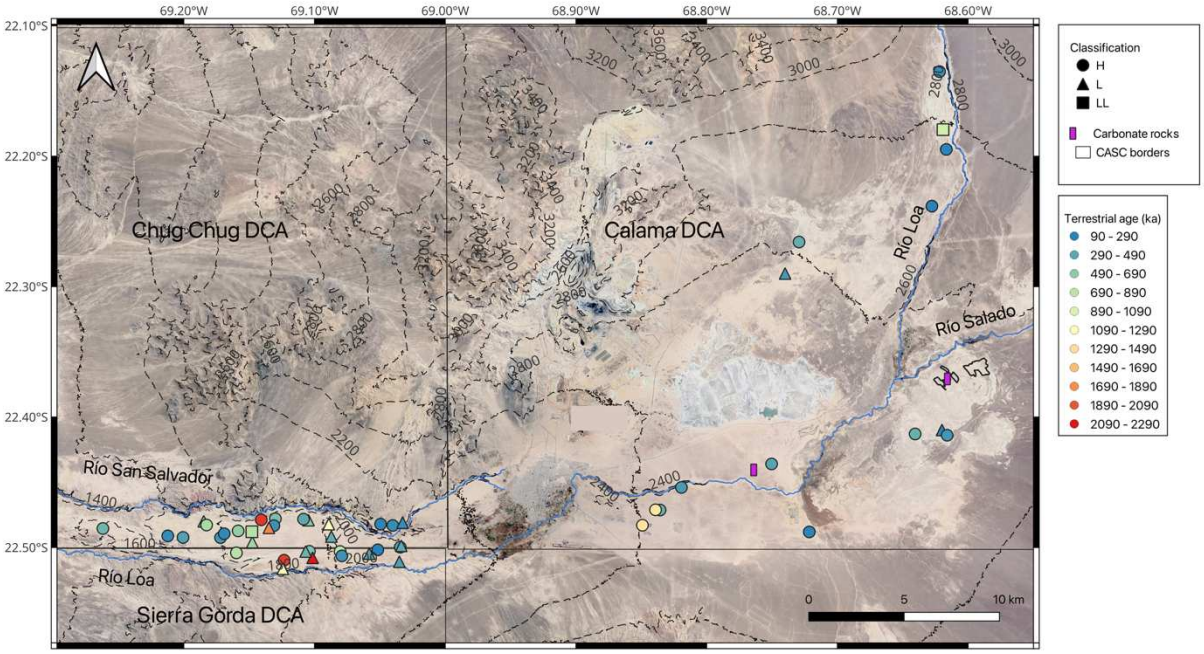
69.20°W
69.10°W
69.00°W
68.90°W
68.80°W
68.70°W
68.60°W
22.10°S
22.20°S
22.30°S
22.40°S
22.50°S
Chug-Chug DCA
Calama DCA
Sierra Gorda DCA
Río San Salvador
Río Loa
Río Salado
Río Loa
0
5
10 km
Classification
H
L
LL
Carbonate rocks
CASC borders
Terrestrial age (ka)
90 - 290
290 - 490
490 - 690
690 - 890
890 - 1090
1090 - 1290
1290 - 1490
1490 - 1690
1690 - 1890
1890 - 2090
2090 - 2290

Fig 5.

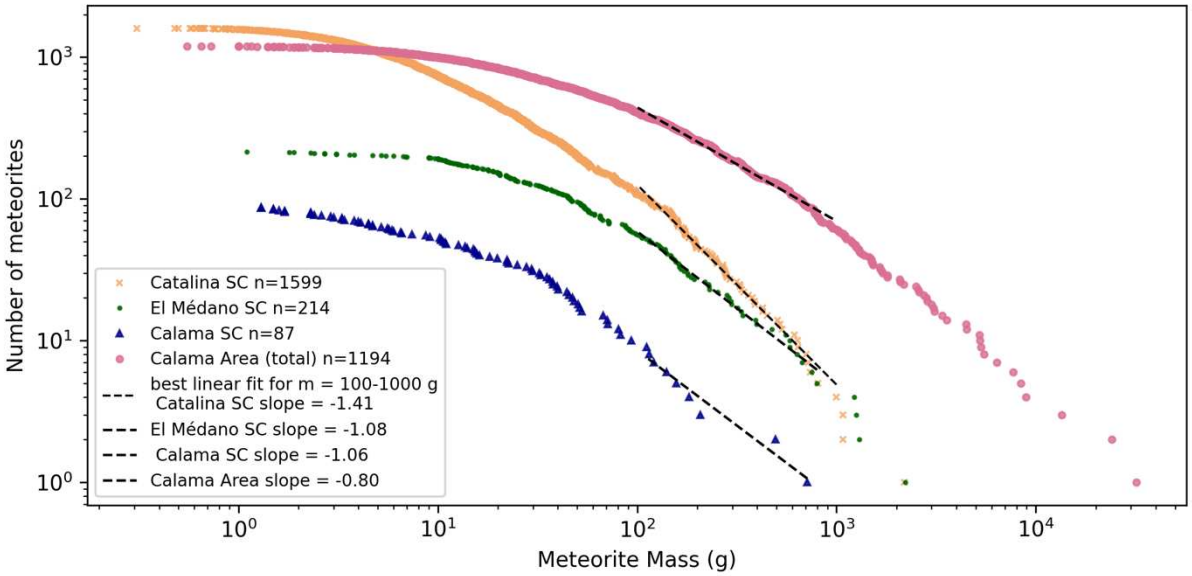

469

470 Fig 6.

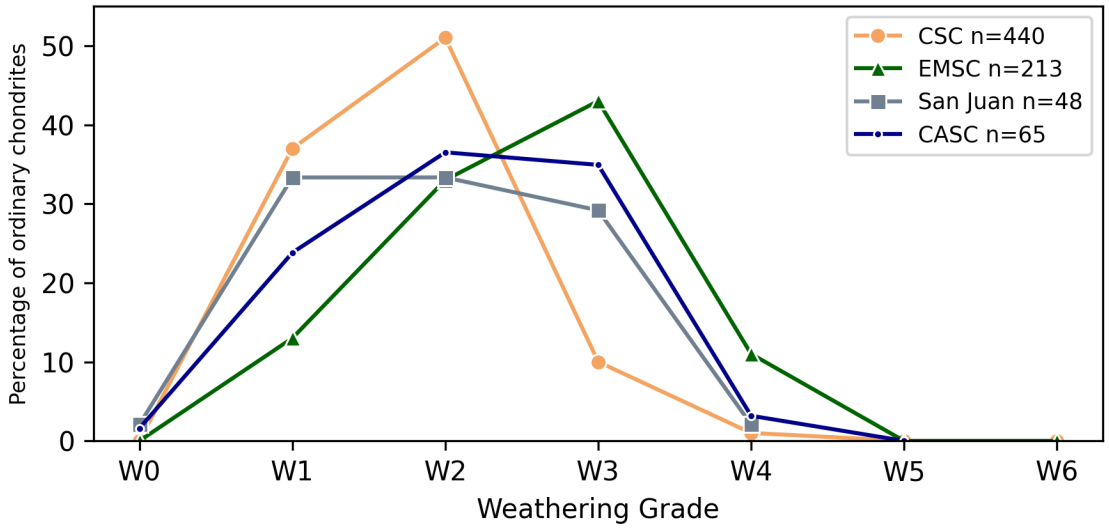

471

472 Fig. 7

473

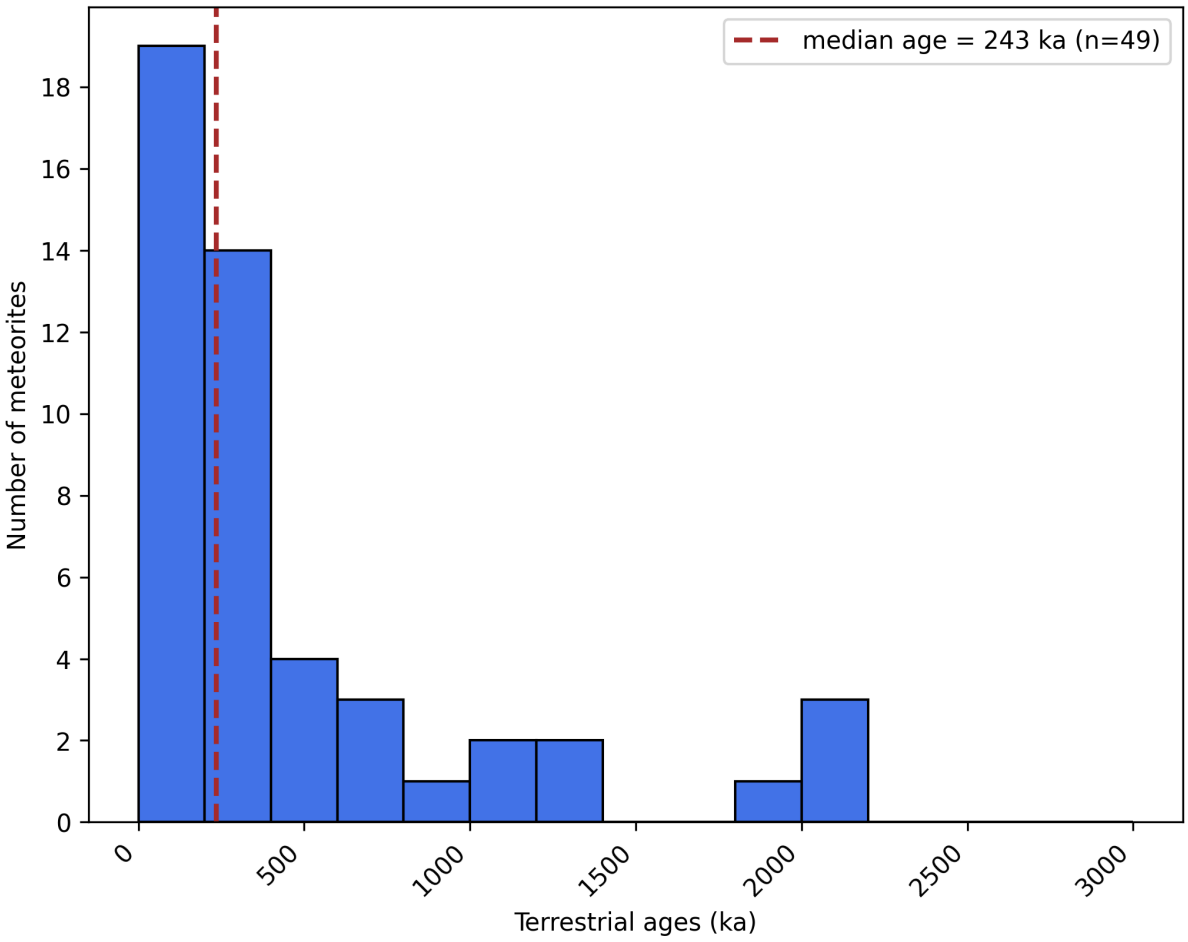
median age = 243 ka (n=49)
Number of meteorites
Terrestrial ages (ka)
0
2
4
6
8
10
12
14
16
18
0
500
1000
1500
2000
2500
3000

Fig. 8

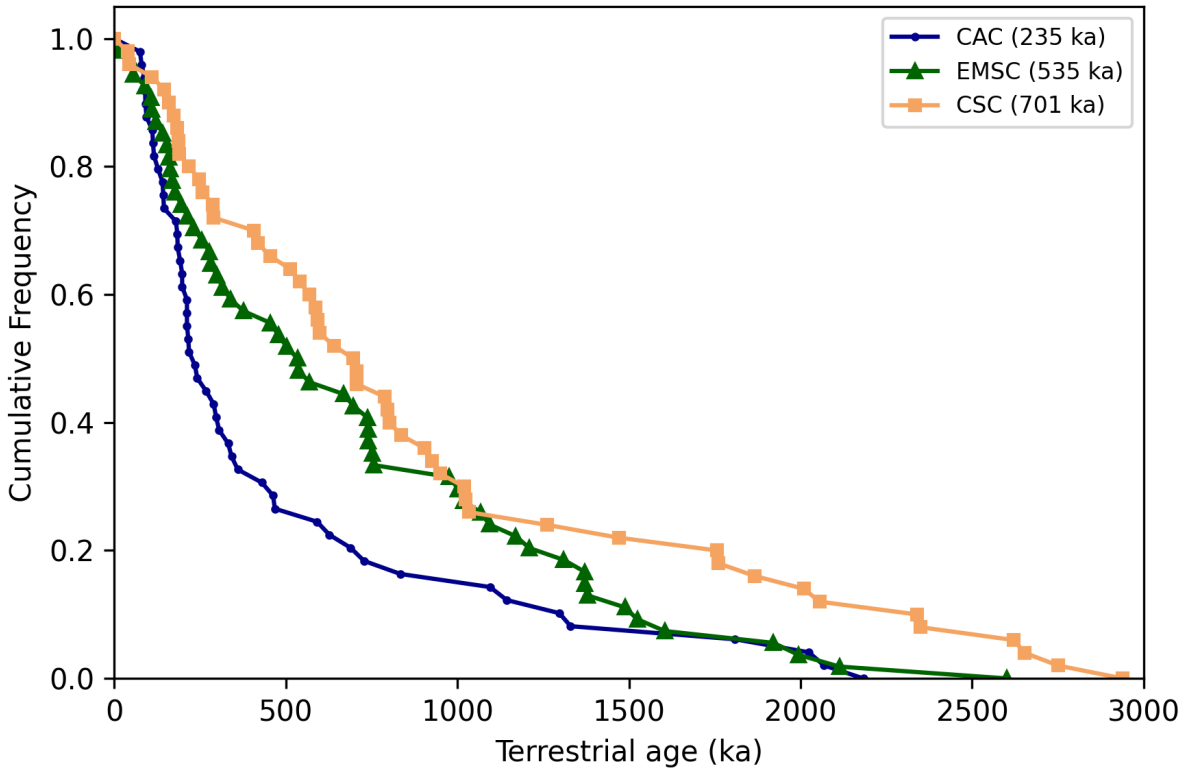
CAC (235 ka)
EMSC (535 ka)
CSC (701 ka)
Cumulative Frequency
Terrestrial age (ka)
0.0
0.2
0.4
0.6
0.8
1.0
0
500
1000
1500
2000
2500
3000

Fig. 9

TABLES

Table 1. Exposure ages of surface rocks from Calama DCA using ^{36}Cl measurements using the model of Schimmelpfennig et al. (2009).

Sample name	Rock type	Latitude	Longitude	Altitude (m)	[^{36}Cl] (atoms/g)	Exposure age (Ma)
497	Carbonate	-22.3708°	-68.6092°	2571	2.95×10^7	1.35±1.13
498	Carbonate	-22.4406°	-68.7574°	2500	3.57×10^7	0.983±0.51

Table 2. Climate, meteorite density and terrestrial ages statistics of the Calama Area Collection (CAC), Catalina Systematic Collection (CSC), and El Médano Systematic Collection (EMSC). For the CAC, precipitation and temperature were averaged on the three DCAs (Calama, Chug Chug, and Sierra Gorda).

Collection	CAC	CSC[+]	EMSC[†]	San Juan
Climate*				
Climatic regime	Arid	Hyperarid	Hypearid	Hyperarid
Precipitation (mm/year)	22	15	14	19
Temperature (°C)	15	16	15	17
Meteorite density				
N total	87	1599	213	48
Total surface (km^2)	2.5	6.8	1.5	3.9
Density (mets per km^2)	37	235	251	12
Density >20 g	15	67	181	11
Corrected density§ >20 g	18	71	123	9
Terrestrial ages (ka)				

Mean ± s.d.	491 ± 560	937 ± 802	706 ± 616	-
Range (min-max)	62 – 2183	39 - 2940	<60 - 2587	-
Median	243	705	526	-

* over the period 2001-2021 (data from Pinto et al., 2024).

§ corrected for recovery biases and pairing

+ Sadaka et al. (2025a,b)

† Hutzler et al. (2016); ages recalculated from Drouard et al. (2019)

Table 3. Calama Area Systematic Collection (CASC) meteorite statistics for meteorites >5 g and >20 g.

Type	N >5 g before pairing	N >20 g before pairing	N >20 g after pairing
H	45	29	12
L	14	6	2
LL	4	2	1
CC	1	1	1
EC	1	0	0
Total	65	38	16
Density (meteorites/km^2)	26	15	9

498 Table 4. Terrestrial ages of the Calama Area Collection (CAC) meteorites.

Official name	Meteorite mass (g)	Group	Petrographic Type	Weathering Grade	Dissolved metal mass (mg)	Ni/(Fe+Ni) %	Computed saturated activity (dpm/kg)	Measured activity (dpm/kg)	Terrestrial age (kyr)	Uncertainty (kyr)
Calama 003	5500	L	5	2	49	9.4	23.1	18.5	97	61
Calama 027	820	H	5	3	40	9.0	23.2	10.8	332	61
Calama 108	640	H	6	3	5	29.8	21.5	11.2	281	95
Calama 109	780	H	5	2	50	7.6	23.3	13.9	223	60
Calama 123	362	H	5	1	81	8.3	23.2	16.4	151	60
Calama 153	286	H	5	2	72	8.2	23.2	10.6	340	61
Calama 154	348	H	5	3	73	10.3	23.0	18.1	104	61
Calama 156	278	H	5	2	38	8.5	22.3	1.1	1312	65
Calama 159	2180	H	5	2	102	8.0	23.2	18.8	91	60
Calama 173	554	H	5	4	0	NA	23.1	1.1	1317	75
Calama 174	560	LL	6	3	2	10.2	23.1	3.2	858	224
Calama 247	128	H	4	3	91	9.0	23.2	14.6	202	60
Calama 273	255	L	6	1	33	13.5	22.8	13.8	216	64
Calama 279	2080	H	5	1	56	8.1	23.2	18.7	95	61
Calama 310	550	H	5	3	66	9.6	23.1	10.2	354	61
Chug Chug 002	388	H	5	1	48	7.8	23.2	16.7	145	61
Chug Chug 004	1080	L	5	2	3	16.3	22.6	7.2	496	105
Chug Chug 006	594	L	5	2	3	11.9	22.9	10.7	331	130

Official name	Meteorite mass (g)	Group	Petrographic Type	Weathering Grade	Dissolved metal mass (mg)	Ni/(Fe+Ni) %	Computed saturated activity (dpm/kg)	Measured activity (dpm/kg)	Terrestrial age (kyr)	Uncertainty (kyr)
Chug 007	Chug	345	H	5	2	62	9.2	23.2	14.5	206	63
Chug 011	Chug	2500	L	6	1	21	18.7	22.4	1.6	1139	65
Chug 016	Chug	1520	L	5	3	37	12.5	22.9	5.9	586	116
Chug 021	Chug	251	LL	5	3	2	5.8	23.4	4.8	686	69
Chug 026	Chug	361	H	5	1	12	10.1	23.1	17.2	127	62
Chug 028	Chug	324	H	5	1	35	7.3	23.3	11.5	307	61
Chug 031	Chug	1455	H	5	1	74	7.9	23.2	8.5	438	61
Chug 032	Chug	625	H	5	3	37	7.1	23.3	15.7	171	60
Chug 042	Chug	1080	L	5	2	25	5.8	23.4	0.4	1813	67
Chug 045	Chug	338	H	6	1	101	9.4	23.1	9.5	386	60
Chug 065	Chug	1712	H	5	1	94	8.2	23.2	16.7	144	60

Official name	Meteorite mass (g)	Group	Petrographic Type	Weathering Grade	Dissolved metal mass (mg)	Ni/(Fe+Ni) %	Computed saturated activity (dpm/kg)	Measured activity (dpm/kg)	Terrestrial age (kyr)	Uncertainty (kyr)
Chug 066	Chug 1528	L	6	2	99	10.2	23.1	16.2	152	61
Chug 067	Chug 3100	H	5	1	79	8.5	23.2	13.2	244	61
Chug 076	Chug 198	L	6	1	42	13.8	22.8	11.1	311	68
Chug 082	Chug 1650	H	5	1	89	8.1	23.2	18.5	99	60
Chug 084	Chug 580	L	6	1	45	12.8	22.8	7.6	476	62
Chug 094	Chug 1225	H	5	1	55	8.9	23.2	7.0	522	61
Chug 097	Chug 338	H	5	3	14	8.9	23.2	5.6	614	61
Chug 144	Chug 4470	H	6	3	98	7.9	23.2	0.2	2081	67
Chug 146	Chug 3000	H	5	2	12	8.5	23.2	12.6	265	70
Sierra 007	Gorda 502	H	5	3	39	9.2	23.1	0.2	2064	69
Sierra 026	Gorda 1800	H	4	2	133	7.4	23.3	8.2	454	60

Official name	Meteorite mass (g)	Group	Petrographic Type	Weathering Grade	Dissolved metal mass (mg)	Ni/(Fe+Ni) %	Computed saturated activity (dpm/kg)	Measured activity (dpm/kg)	Terrestrial age (kyr)	Uncertainty (kyr)
Sierra Gorda 033	322	H	5	2	66	9.2	23.1	18.8	90	60
Sierra Gorda 034	1125	H	6	2	71	9.5	23.1	4.3	733	62
Sierra Gorda 037	959	H	5	2	66	7.2	23.3	4.7	696	61
Sierra Gorda 042	260	L	6	1	46	12.6	22.9	1.8	1102	64
Sierra Gorda 047	242	L	5	1	56	12.6	22.9	12.8	252	62
Sierra Gorda 052	916	H	6	2	8	9.1	23.1	15.3	179	76
Sierra Gorda 057	790	L	5	2	45	11.8	22.9	11.8	290	61
Sierra Gorda 088	700	L	5	1	73	11.6	22.9	0.1	2198	78
Sierra Gorda 090	810	L	5	2	50	11.3	23.0	9.9	365	62

SUPPLEMENTARY MATERIAL

Table S1. Climatic characteristics of the Dense Collection Areas involved in this study.

DCA	Calama	Chug Chug	Sierra Gorda
Main morphotectonic unit	PRB/CD	CD/PRB	CD
Climate	Arid	Arid	Arid
Average annual cumulative precipitation*(mm/year)	~30	~18	~19
Average annual air temperature* (°C)	~13	~16	~15.5

* over the period 2001-2021 (from Pinto et al., 2024)

Table S2. Comparative characteristics of three Atacama DCAs

Parameter	Catalina (CSC)	Calama–Chug Chug–Sierra Gorda (CAC)	El Médano (EMSC)
Location	Central Depression (southern Atacama)	Central Depression (northern Atacama)	Coastal Atacama
Altitude	~2000 m a.s.l. (1900–2050 m)	2300–3200 m a.s.l.	1950–2400 m a.s.l.

Parameter	Catalina (CSC)	Calama–Chug Chug–Sierra Gorda (CAC)	El Médano (EMSC)
Geomorphology	Single continuous flat plain with gentle slope (~2°)	Heterogeneous: broad pampas, piedmont plains, fluvial terraces (Loa & Salado interfluve)	Fragmented surfaces in ~30 small zones; gentle slopes (<3°), local hills (~200 m)
Geology	Cretaceous–Jurassic volcanic and plutonic rocks (Augusta Victoria Fm., La Negra Fm., Cerro del Pingo plutonic group)	Neogene–Quaternary basin-fill sediments: Opache Fm. (7–3 Ma), Chiquicamata Form. + piedmont/alluvial fans, Quaternary fluvial terraces	Neogene–Quaternary surfaces with limited sediment cover; underlain by volcanic & sedimentary rocks of the Coastal Cordillera
Hydrology	No fluvial system	Río Loa and Río Salado (only perennial rivers of the Atacama)	No perennial rivers; local slope-driven clast movement
Climate	Hyperarid, ~16 °C mean annual temperature, ~15 mm yr^{-1} precipitation	Arid, ~15 °C mean annual temperature, ~22 mm yr^{-1} precipitation	Hyperarid, ~15 °C mean annual temperature, ~14 mm yr^{-1} precipitation
Surface stability	Continuous desert pavement over caliche/nitrate-rich layer	Wide pavements, stable pampas and terraces	Discontinuous but stable surfaces; local downslope creep
Cosmogenic nuclides / surface ages	--- *	Rocks ^{36}Cl ages up to 1.35 Ma	Quartz ^{10}Be exposure ages >1.5 Ma and up to >6 Ma

*No ages were measured in the Catalina DCA because of the lack of quartz or carbonate rocks in this area.

REFERENCES

Aboulahris, M., H. Chennaoui Aoudjehane, P. Rochette, J. Gattacceca, T. Jull, N. Laridhi Ouazaa, L. Folco, and S. Buhl. 2019. "Characteristics of the Sahara as a Meteorite Recovery Surface." *Meteoritics & Planetary Science* 54 (12): 2908–28. https://doi.org/10.1111/maps.13398.

Baroni, C., M. C. Salvatore, V. Vandelli, M. Marchetti, and M. Soldati. 2025. "Cosmogenic Dating Reveals the Timing of Glaciers Collapse in the High Dolomites Valleys (Northern Italy)." *Geomorphology* 474 (February): 109648. https://doi.org/10.1016/j.geomorph.2025.109648.

Barrat, J.-A., M. Chaussidon, A. Yamaguchi, P. Beck, J. Villeneuve, D. J. Byrne, M.l W. Broadley, and B. Marty. 2021. "A 4,565-My-Old Andesite from an Extinct Chondritic Protoplanet." *Proceedings of the National Academy of Sciences* 118 (11). https://doi.org/10.1073/pnas.2026129118.

Belhai, D. 2023. "Spatial Distribution and Classification of Algerian Meteorites: Qualitative and Quantitative Inventory." *Journal of African Earth Sciences* 207 (105058): 105058. doi:https://doi.org/10.1016/j.jafrearsci.2023.105058.

Benedix, G. K., K. Keil, and J. Y. Murakami. 1999. "Classification of Ten New Nullarbor Region Meteorites." *Meteoritics & Planetary Science* 34 (5): 813–15. https://doi.org/10.1111/j.1945-5100.1999.tb01395.x.

Cartwright, J.A., U. Ott, S. Herrmann, and C.B. Agee. 2014. "Modern Atmospheric Signatures in 4.4 Ga Martian Meteorite NWA 7034." *Earth and Planetary Science Letters* 400 (August): 77–87. https://doi.org/10.1016/j.epsl.2014.05.008.

Clarke, J.D.A. 2006. "Antiquity of Aridity in the Chilean Atacama Desert." *Geomorphology* 73 (1-2): 101–14. https://doi.org/10.1016/j.geomorph.2005.06.008.

Drouard, A., J. Gattacceca, A. Hutzler, P. Rochette, R. Braucher, D. Bourlès, M. Gounelle, et al. 2019. “The Meteorite Flux of the Past 2 M.y. Recorded in the Atacama Desert.” *Geology* 47 (7): 673–76. https://doi.org/10.1130/g45831.1.

Duhart, P., J. Muñoz, D. Quiroz, A. Mestre, and G. Varas. 2018. “Carta Sierra Gorda, Región de Antofagasta.” Carta Geológica de Chile, Serie Geología Básica 198. Santiago, Chile: Servicio Nacional de Geología y Minería (SERNAGEOMIN). ISSN 0717-7283.

Dunai, T. J., G. A. González López, and J. Juez-Larré. 2005. “Oligocene–Miocene Age of Aridity in the Atacama Desert Revealed by Exposure Dating of Erosion-Sensitive Landforms.” *Geology* 33 (4): 321. https://doi.org/10.1130/g21184.1.

Gattacceca, J., P. Eisenlohr, and P. Rochette. 2004. “Calibration of*in Situ*Magnetic Susceptibility Measurements.” *Geophysical Journal International* 158 (1): 42–49. https://doi.org/10.1111/j.1365-246x.2004.02297.x.

Gattacceca, J., M. Gounelle, B. Devouard, J.-A. Barrat, L. Bonal, A. J. King, C. Maurel, et al. 2025. “Oued Chebeika 002: A New CI1 Meteorite Linked to Outer Solar System Bodies.” *Meteoritics & Planetary Science* 60 (7): 1441–79. https://doi.org/10.1111/maps.14359.

Gattacceca, J., F. M. McCubbin, J. N. Grossman, D. L. Schrader, C. Cartier, G. Consolmagno, C. Goodrich, et al. 2025. “The Meteoritical Bulletin, No. 113.” *Meteoritics and Planetary Science* 60 (7): 1587–91. https://doi.org/10.1111/maps.14374.

Gattacceca, J., M. Valenzuela, M. Uehara, T. Jull, M. D. Giscard, P. Rochette, R. Braucher, et al. 2011. “The Densest Meteorite Collection Area in Hot Deserts: The San Juan Meteorite Field (Atacama Desert, Chile).” *Meteoritics & Planetary Science* 46 (9): 1276–87. https://doi.org/10.1111/j.1945-5100.2011.01229.x.

Hofmann, B. A., E. Gnos, T. Jull, S. Szidat, A. Majoub, K. Al Wagdani, S. N. Habibullah, et al. 2018. “Meteorite Reconnaissance in Saudi Arabia.” *Meteoritics & Planetary Science* 53 (11): 2372–94. https://doi.org/10.1111/maps.13132.

Hofmann, Beda A, and Edwin Gnos. 2024. “The Meteoritic Record of Arabia.” *Geological Society London Special Publications* 550 (1): SP550-20248. https://doi.org/10.1144/sp550-2024-8.

Hutzler, A., J. Gattacceca, P. Rochette, R. Braucher, B. Carro, E. Christensen, C. Cournede, et al. 2016. “Description of a Very Dense Meteorite Collection Area in Western Atacama: Insight into the Long-Term Composition of the Meteorite Flux to Earth.” *Meteoritics & Planetary Science* 51 (3): 468–82. https://doi.org/10.1111/maps.12607.

Jull, A. J. T., R. P. Binzel, R. M. Walker, and A. G. W. Cameron. 2006. “Terrestrial Ages of Meteorites.” In *Meteorites and the Early Solar System II,* edited by D. S. Lauretta and H. Y. McSween, 889–906. University of Arizona Press.

Jull, A. J. T., L. R. McHargue, P. A. Bland, R. C. Greenwood, A. W. R. Bevan, K. J. Kim, S. E. LaMotta, and J. A. Johnson. 2010. “Terrestrial Ages of Meteorites from the Nullarbor Region, Australia, Based on 14C and 14C-10Be Measurements.” *Meteoritics & Planetary Science* 45 (8): 1271–83. https://doi.org/10.1111/j.1945-5100.2010.01289.x.

Jungers, M. C., A. M. Heimsath, R. Amundson, G. Balco, D. Shuster, and G. Chong. 2013. “Active Erosion–Deposition Cycles in the Hyperarid Atacama Desert of Northern Chile.” *Earth and Planetary Science Letters* 371-372 (May): 125–33. https://doi.org/10.1016/j.epsl.2013.04.005.

Ladino, M., V. Maksaev, and N. Blanco. 2001. “Geología de La Precordillera Andina de Quebrada Blanca–Chuquicamata, Regiones I Y II (20°30′–22°30′S). Leyenda Para Los Cuadrángulos 1:50.000 Quebrada Chug-Chug Y Cerros de Montecristo, Región de Antofagasta.” Santiago, Chile: Servicio Nacional de Geología y Minería

(SERNAGEOMIN), Subdirección Nacional de Geología. Informe Registrado IR-01-20.

Leya, I., and J. Masarik. 2009. "Cosmogenic Nuclides in Stony Meteorites Revisited." *Meteoritics & Planetary Science* 44 (7): 1061–86. https://doi.org/10.1111/j.1945-5100.2009.tb00788.x.

Nica, N., J. Cameron, and B. Singh. 2012. "Nuclear Data Sheets for a = 36." *Nuclear Data Sheets* 113 (1): 1–155. https://doi.org/10.1016/j.nds.2012.01.001.

Pfeiffer, M., A. M. Morgan, A. M. Heimsath, T. E. Jordan, A. D. Howard, and R. Amundson. 2021. "Century Scale Rainfall in the Absolute Atacama Desert: Landscape Response and Implications for Past and Future Rainfall." *Quaternary Science Reviews* 254 (8): 106797–97. https://doi.org/10.1016/j.quascirev.2021.106797.

Pinto, G. A., A. Tavernier, J. Gattacceca, A. Corgne, M. Valenzuela, B. Luais, L. Flores, F. Olivares, and Y. Marrocchi. 2024. "Dense Collection Areas and Terrestrial Alteration of Meteorites in the Atacama Desert." *Meteoritics & Planetary Science* 59 (2): 351–67. https://doi.org/10.1111/maps.14125.

Pourkhorsandi, H., J. Gattacceca, P. Rochette, M. D'Orazio, H. Kamali, R. Avillez, S. Letichevsky, et al. 2019. "Meteorites from the Lut Desert (Iran)." *Meteoritics & Planetary Science* 54 (8): 1737–63. https://doi.org/10.1111/maps.13311.

Sadaka, C., J. Gattacceca, M. Gounelle, M. Roskosz, A. Lagain, R. Tartese, L. Bonal, C. Maurel, R. Martinez, and M. Valenzuela. 2025. "Systematic Meteorite Collection in the Catalina Dense Collection Area (Chile): Description and Statistics." *Meteoritics & Planetary Science*, no. 60 (January): 308–23. https://doi.org/10.1111/maps.14307.

Sadaka, C., J. Gattacceca, F. Dumas, et al. 2025. "Terrestrial ages of meteorites from the Atacama Desert (Chile) and insights into the past meteorite flux to Earth." *Meteoritics & Planetary Science*, doi: 10.1111/maps.70125.

Schimmelpfennig, I., L. Benedetti, R. Finkel, R. Pik, P.-H. Blard, D. Bourlès, P. Burnard, and A. Williams. 2009. “Sources of In-Situ 36Cl in Basaltic Rocks. Implications for Calibration of Production Rates.” *Quaternary Geochronology* 4 (6): 441–61. https://doi.org/10.1016/j.quageo.2009.06.003.

Schimmelpfennig, I., L. Benedetti, V. Garreta, R. Pik, P.-H. Blard, P. Burnard, D. Bourlès, R. Finkel, K. Ammon, and T. Dunai. 2011. “Calibration of Cosmogenic 36Cl Production Rates from ca and K Spallation in Lava Flows from Mt. Etna (38°N, Italy) and Payun Matru (36°S, Argentina).” *Geochimica et Cosmochimica Acta* 75 (10): 2611–32. https://doi.org/10.1016/j.gca.2011.02.013.

Schlüter, J. , L. Schultz, F. Thiedig, B. O. Al-Mahdi, and A. E. Abu Aghreb. 2002. “The Dar al Gani Meteorite Field (Libyan Sahara): Geological Setting, Pairing of Meteorites, and Recovery Density.” *Meteoritics & Planetary Science* 37 (8): 1079–93. https://doi.org/10.1111/j.1945-5100.2002.tb00879.x.

Tomlinson, A. J., N. Blanco, J. H. Dilles, V. Maksaev, and M. Ladino. 2018. “Carta Calama, Región de Antofagasta .” Carta Geológica de Chile, Serie Geología Básica. Servicio Nacional de Geología y Minería, Carta Geológica de Chile.

Zolensky, M. E., G. L. Wells, and H. M. Rendell. 1990. “The Accumulation Rate of Meteorite Falls at the Earth’s Surface: The View from Roosevelt County, New Mexico.” *Meteoritics* 25 (1): 11–17. https://doi.org/10.1111/j.1945-5100.1990.tb00965.x.

4.3. Conclusion

In summary, the Calama area collections provide complementary datasets to the Catalina and El Médano collections described in previous chapters. Despite being characterized by lower densities and younger terrestrial ages on average, these results are consistent with the slightly more humid climate and more dynamic geomorphology of the region. The high number of recovered meteorites and the presence of terrestrial ages exceeding 2 Ma demonstrate that long-term preservation is not restricted to a specific region of the Atacama but can be considered as a desert-wide feature. The systematic collection performed in a small zone of the Calama area also confirms the efficiency of such searches compared to random, non-systematic recoveries.

In conclusion, this study further confirms the unique ability of the Atacama Desert for hosting the densest and oldest meteorite collections in the world thus offering the opportunity to study the long-term variability of the meteorite flux to Earth.

Chapter 3

Chapter five

Cosmic-ray exposure ages of ordinary chondrites from the Atacama Desert: insights into the dynamics of meteoroid transfer from the Main Asteroid Belt to Earth



The Universe is under no obligation to make sense to you.
– Neil deGrasse Tyson

Chapter 5

Summary

5.1. Introduction 251

5.2. Methods 255

5.3. Results and discussion 255

5.3.1. Neon isotopic compositions 255

5.3.2. Cosmic-ray exposure ages and ejection ages 256

5.4. Conclusion 259

5.5. Chapter supplementary 260

5. Chapter 5

5.1. Introduction

Most meteorites are known to originate from the Main Asteroid Belt (Brož et al. 2024a; Brož et al. 2024b; Marsset et al. 2024; Anderson et al. 2025; Jenniskens et Devillepoix 2025). Meteoroid delivery is initiated with the ejection of fragments from parent bodies in the main belt due to collisional events, followed by slow dynamical evolution mainly under the influence of the Yarkovsky effect. This thermal effect is caused by the uneven heating of rotating meteoroids by solar radiation, which induces a small thrust that builds up slowly with time, changing the orbital parameters of those fragments (see Chapter 1). This relatively weak effect explains why some meteoroids stay up to tens of millions of years in the main belt before being pushed into powerful resonances, such as the 3:1 mean-motion resonance with Jupiter or the $\nu 6$ secular resonance, which inject fragments into Earth-crossing orbits in the Near-Earth space.

Near-Earth objects (NEOs) are thus a transient population that is continuously replenished from the main belt, acting as an intermediate stage in the delivery of meteoroids from their parent asteroids to Earth. While the typical dynamical lifetime of kilometer-sized NEOs is around 10 Myr (Gladman 2000), meter-sized meteoroids, which are the precursors of most meteorites on Earth, generally remain less than 1 Myr before falling on Earth (Gladman et al. 1997; Morbidelli and Gladman 1998; Bottke et al. 2002).

As introduced briefly in Chapter 1, cosmic-ray exposure (CRE) ages provide a direct measure of the time spent by meteoroids in the interplanetary space after ejection from their parent asteroids, while terrestrial ages record the time elapsed since a meteorite's fall on Earth. When combined, these two parameters yield ejection ages, representing the time since a meteoroid was excavated from its parent body to the present (Figure 5.1). Ejection age distributions thus provide clear insight into collisional events within the asteroid belt and the dynamical mechanisms of meteoroid delivery to Earth.

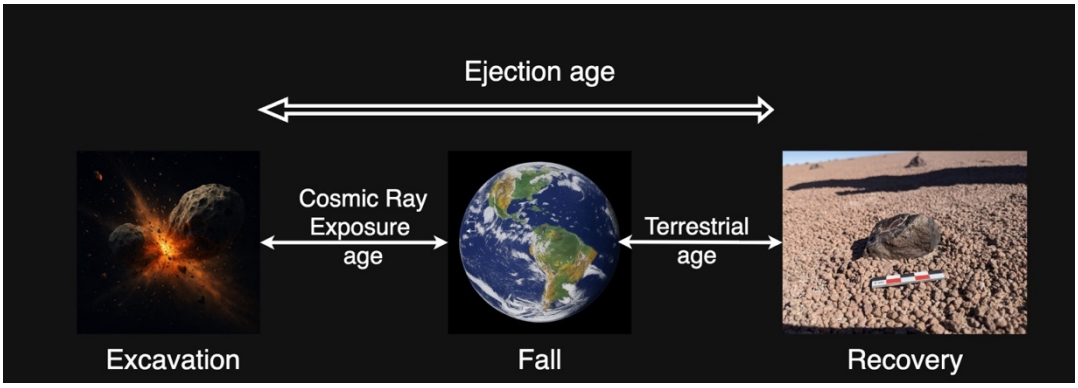

Figure 5.1. Schematic illustration of the different ages of a meteorite. The ejection age is the sum of the cosmic-ray exposure age (duration of exposure to cosmic rays in the interplanetary medium) and the terrestrial age (residence time on Earth).

For all meteorite collections, except those from the Atacama Desert, the terrestrial ages are negligible compared to the CRE ages, so that ejection ages are very well approximated by the CRE ages that can, therefore, be directly used to study the dynamics of meteorite delivery for the population currently falling on Earth or that fell over the last thousands to tens of thousands of years.

Compilations of CRE ages of ordinary chondrites (from falls, Antarctic, and hot desert meteorites) have revealed numerous well-defined clusters (Figure 5.2). For instance, H chondrites display a dominant peak between 5 and 7 Ma, interpreted as the result of major collisions linked to the formation of Karin and Koronis$_2$ asteroid families, considered as the main current sources of H chondrites (Brož et al. 2024b). Other major clusters, such as the 33 Ma peak in H chondrites, 40 Ma peak in L chondrites, and 15 Ma in LL chondrites, have been linked to major cratering or disruption events on their respective parent asteroids (Eugster et al. 2006; Herzog et al. 2007). These findings indicate that meteoroid delivery is not a continuous process but is rather shaped by intermittent collisional events.

Since most meteorites record CRE ages of only a few million years, their residence time as small meteoroids in near-Earth space must have been brief, suggesting that they were rapidly delivered to Earth soon after ejection from parent bodies (Gladman et al. 1997; Bottke et al. 2002).

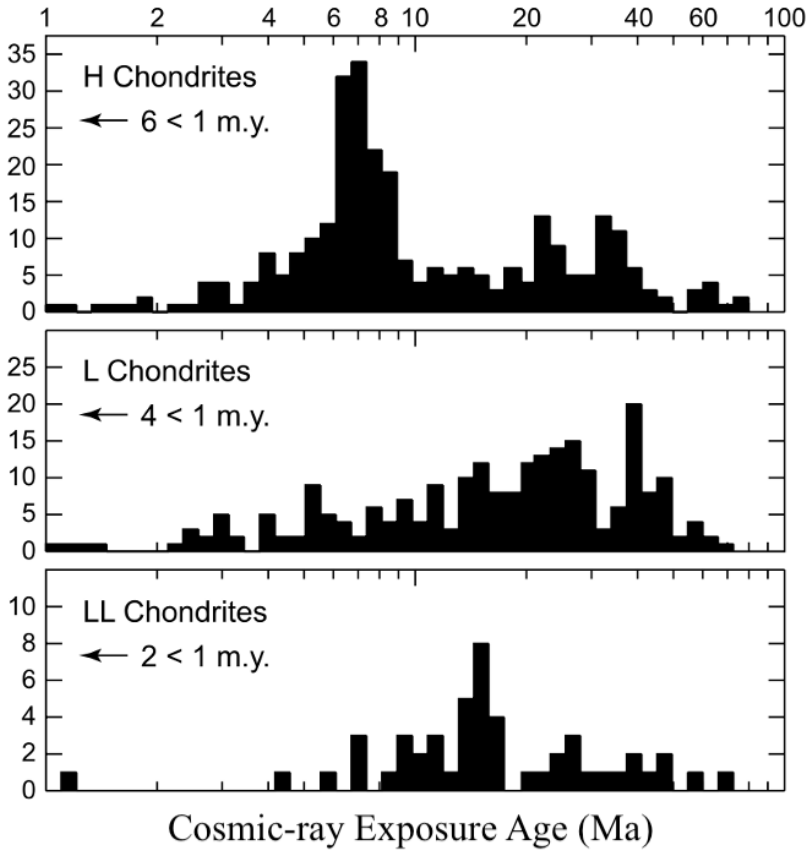

Figure 5.2. Distribution of cosmic-ray exposure ages of ordinary chondrites (H, L, and LL). Distinct peaks reflect major collisional events in the asteroid belt (From Eugster 2003).

Through the combination of dynamical modeling, asteroid surveys, and CRE age distributions, recent studies have significantly improved our understanding of meteorite source regions. For instance, young collisional families have been linked as the main source of ordinary chondrites. H chondrites are mainly derived from the Karin (~5.8 Ma) and Koronis$_2$ (~7.6 Ma) clusters (Brož et al. 2024b). However, the origin of L chondrites is still debated between the Massalia family (~40 Ma; Marsset et al. 2024) and the Hertha family at ~2.42 AU (Jenniskens and Devillepoix 2025). LL chondrites are thought to derive predominantly from the Flora and Nysa families (Brož et al. 2024b; Marsset et al. 2024). In parallel, CM chondrites have been linked to the Veritas family (~8.3 Ma), while CI chondrites are thought to derive from the Polana and Eusphrosyne families, consistent with their implantation from the outer Solar System at different times (Anderson et al. 2025; Brož, et al. 2024a). Based on these discoveries, the present meteorite flux appears to be strongly shaped by relatively recent collisional events, complemented with a continuous background from older families.

Despite these advances, many uncertainties remain. While dynamical models reproduce well the overall fall statistics, some discrepancies remain between meteorite collections and the populations of NEOs and asteroid populations (Figure 5.3). For example, a significant mismatch exists between the relative abundances of L and LL chondrites among the NEO population and meteorite falls (Vernazza et al. 2008; Binzel et al. 2015; Marsset et al. 2024; Brož et al. 2024b). This inconsistency between modeled and observed distributions illustrates the difficulty of reconciling asteroid family sources with the groups of meteorites found on Earth. In addition, the very low abundance of CO, CV, and CK chondrites among observed falls compared to their expected contribution from asteroid families also denotes biases linked to pre-atmospheric fragmentation or atmospheric filtering (Brož et al. 2024b; Shober et al. 2025).

Recent orbital reconstructions of meteorite falls also indicate that meter-sized meteoroids of a given type do not necessarily originate from the same source regions as kilometer-sized NEOs with similar taxonomic characteristics. Thus, the meteorite flux cannot be considered as a simple smaller-scale subset of the kilometer-sized NEO population (Jenniskens and Devillepoix 2025). Together, these observations highlight the intricacy of associating asteroid families with the meteorite flux to Earth.

While the size-dependence of the Yarkovsky effect helps explain both the compositional differences between kilometer-sized NEOs and meter-sized meteorites, as well as the observed well-defined clusters in CRE age distributions (Vernazza et al. 2008), it cannot, however, explain all discrepancies mentioned above. Additional factors must be influencing the meteorite flux reaching Earth, including collisional fragmentation within asteroid families, atmospheric filtering, different survival efficiencies among meteorite groups, and sampling biases (Brož, et al. 2024a; Jenniskens et Devillepoix 2025; Shober et al. 2025).

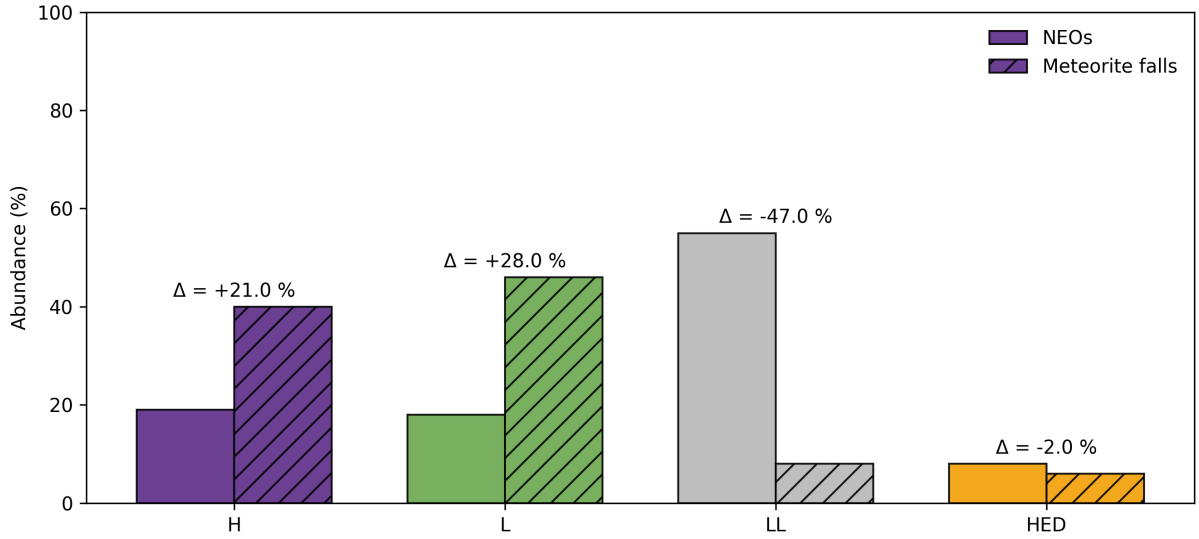

Figure 5.3. Abundance of different meteorite groups in the NEO vs meteorite falls populations and the difference between the two. Data from Brož, Vernazza, Marsset, DeMeo, et al. (2024b).

In world collections, Antarctic meteorites exhibit terrestrial ages of ~100 ka on average, while those from hot deserts such as the Arabian Peninsula, North African deserts or Australian deserts have average ages ~10 ka (Jull 2006; Drouard et al. 2019). Therefore, the CRE ages measured in these collections are effectively equivalent to ejection ages. This precludes the possibility of resolving Myr-scale variability in meteorite delivery sources. The Atacama Desert, however, offers a unique opportunity to overcome this limitation, owing to its hyperarid climate and long-term surface stability, which allows meteorites to reside up to over 2 Myr at the surface. These long residence times are not negligible any more relative to CRE ages. Therefore, the true ejection ages must combine ^{21}Ne-derived CRE ages with ^{36}Cl terrestrial ages, rather than relying solely on CRE ages as proxies. Earlier chapters (Chapters 3 and 4) presented the exceptionally long terrestrial ages of Atacama meteorites and provided robust datasets for the Catalina and Calama collections, which will serve as foundation for reconstructing ejection ages.

Our results from Chapter 3 indicate that the bulk flux of meteorites to Earth has remained roughly constant over the past 2 Myr. However, when investigating the compositional evolution of the flux, we find that the relative contribution of H chondrites to the total meteorite flux was higher between 1.2 and 0.4 Ma, before declining to present-day values. This temporal variation is not captured by current dynamical models of meteoroid transfer to Earth, which predict a constant H chondrite abundance over the last 3 Myr (Brož, Vernazza, Marsset, DeMeo, et al. 2024b). This discrepancy suggests that short-term changes in the meteorite flux may be influenced by other processes and/or events not accounted for in these models.

In this chapter, I build on the preliminary ^{21}Ne CRE ages introduced in Chapter 3, where they served primarily to verify ^{36}Cl saturation and validate terrestrial age determinations. Here, CRE ages are used as the main dataset and systematically combined with ^{36}Cl terrestrial ages of Atacama H chondrites. The objectives are to:

1. Examine the distribution of ejection ages of H chondrites that fell on Earth more than 0.5 million years ago
2. Assess the presence of a potential peak at ~3 Ma in H chondrites ejection ages, distinct from the well-established 5–7 Ma cluster
3. Improve our understanding of meteoroid transfer to Earth and the associated collisional processes within the asteroid belt

This approach provides deeper insight into short-term variability of meteoroid delivery to Earth and refines our understanding of the link between asteroid belt dynamics and changes in the meteorite flux to Earth.

5.2. Methods

Neon isotopic ratios were measured on 33 meteorites from the CSC (Catalina) and the EMSC (El Médano), selected for their ^{36}Cl terrestrial age >0.5 Ma, in two different noble gases facilities, the University of Bern, Switzerland, and the Centre de Recherches Pétrographiques et Géochimiques (CRPG), Nancy, France. The detailed analytical procedures for neon measurements are described in detail in Chapter 3. In brief, at the University of Bern, neon isotopes were measured in silicate fractions (~20 mg) following the protocol of (Leya et al. 2013) and (Tauseef et al. 2025; 2024) . Samples were degassed in a molybdenum crucible at 1750°C and released gases were purified with SAES getters and charcoal traps. Ne isotopes were then analyzed on a static sector field mass spectrometer with blanks and standards routinely conducted. At CRPG, smaller fragments (~1–2 mg) were melted with a CO_2 infrared laser in a dedicated chamber connected to a Helix MC Plus mass spectrometer. Extracted gases were purified using getters and charcoal traps, and Ne isotopes were measured in multicollection mode at high mass resolution, with blanks and standards used for correction and calibration.

We derive CRE ages using the $(^{22}Ne/^{21}Ne)_{cos}$–$^{21}Ne_{cos}$ method, the most widely used method for stony meteorites (Leya and Masarik 2009). Cosmogenic ^{21}Ne concentrations were derived by two-component deconvolution of neon isotopic ratios, using air and a cosmogenic endmember ($^{22}Ne/^{21}Ne = 0.82$; Dalcher et al. 2013). Production rates were calculated following Dalcher et al. (2013) with the appropriate chemical scaling for H, L, and LL chondrites. Ejection ages were then obtained by simply summing the ^{21}Ne-based CRE ages to ^{36}Cl terrestrial ages previously determined. Uncertainties were propagated from both CRE and terrestrial ages.

5.3. Results and discussion

5.3.1. Neon isotopic compositions

The measured $^{20}Ne/^{22}Ne$ and $^{21}Ne/^{22}Ne$ ratios define linear mixing trends between trapped atmospheric components and a cosmogenic endmember (Figure 5.4). Deconvolution with a cosmogenic $^{22}Ne/^{21}Ne$ ratio of 0.82 (Dalcher et al. 2013) allowed determination of the cosmogenic contribution (Table 5.1).

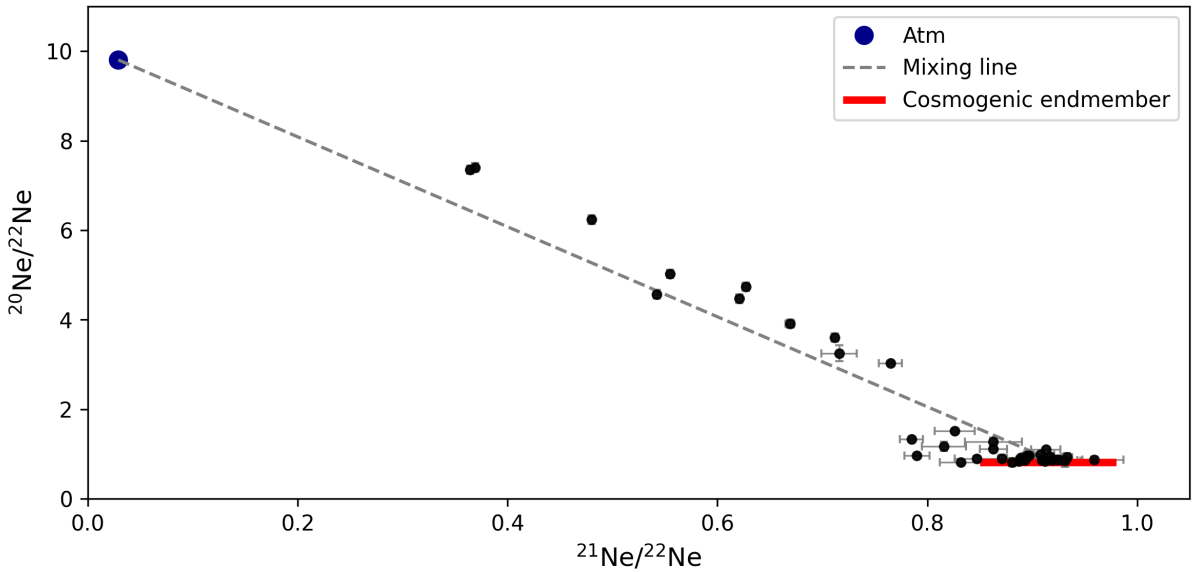

Figure 5.4. 20Ne/22Ne as a function of 21Ne/22Ne of H chondrites 33 (and replicas; n=39) from the Catalina Systematic Collection and the El Médano Systematic Collection. Also shown is the atmospheric component with 20Ne/22Ne = 9.80 and 21Ne/22Ne = 0.02904 (Ozima and Podosek 2002), and the cosmogenic component range (Dalcher et al. 2013; Leya and Masarik 2009).

The derived $(^{22}Ne/^{21}Ne)_{cos}$ range from 1.03 to 1.25 (average 1.11; Table 5.1), consistent with the values of ordinary chondrites in the literature (e.g., (Leya et al. 2013; Bekaert et al. 2022; Schultz et al. 2005). Duplicate analysis generally yielded consistent results, confirming the reproducibility of the measurements, except for two samples (El Médano 199 and Catalina 682), which showed discrepancies in $^{21}Ne_{cos}$ concentrations between aliquots, likely due to sample heterogeneity or analytical artifacts.

5.3.2. Cosmic-ray exposure ages and ejection ages

The 33 measured CRE ages range from 1.6 to 47.1 Myr, with a mean of 10.6 Myr and a median of 3.8 Myr (Figure 5.5), in broad agreement with the global ordinary chondrite record (Graf and Marti 1995; Eugster et al. 2006). Both datasets are displayed in Figure 5.5.

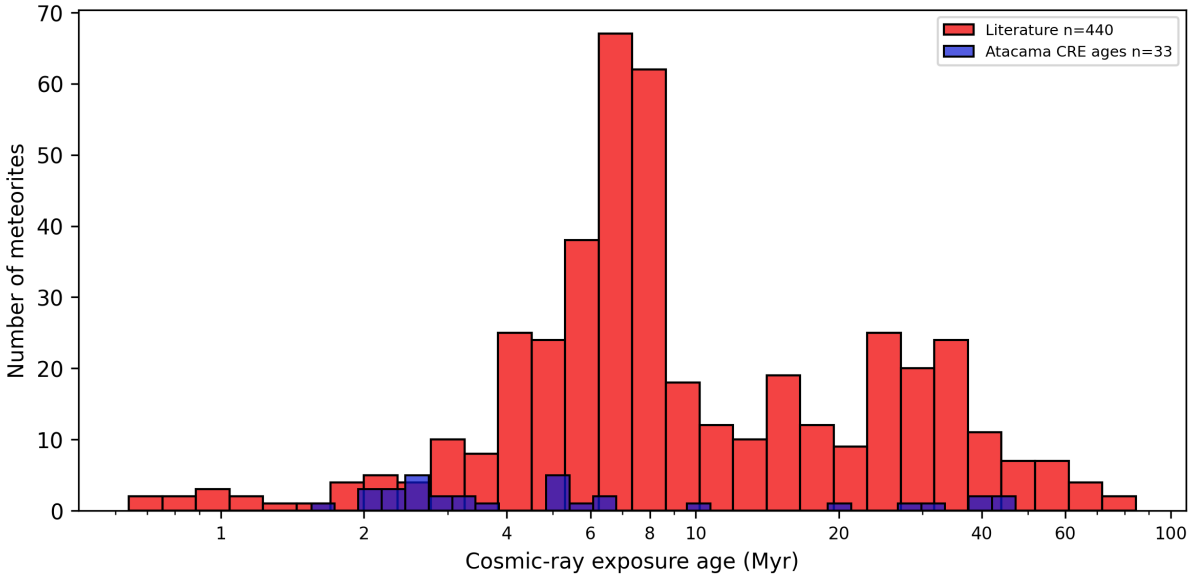

Figure 5.5. Distribution of cosmic-ray exposure (CRE) ages for H chondrites compiled from (Graf and Marti 1995), shown alongside CRE ages of H chondrites from the Atacama Desert determined in this study (n = 33).

Based on CRE ages results, the distribution of ejection ages of the studied H chondrites reveals two prominent features (Figure 5.6; Table 5.2). The first is a 5–7 Ma cluster, consistent with the well-established H chondrite peak associated with the Karin and Koronis$_2$ asteroid families (Brož et al. 2024b). The second is a faint peak around 3 Ma, apparently distinct from the well-established 5–7 Ma peak.

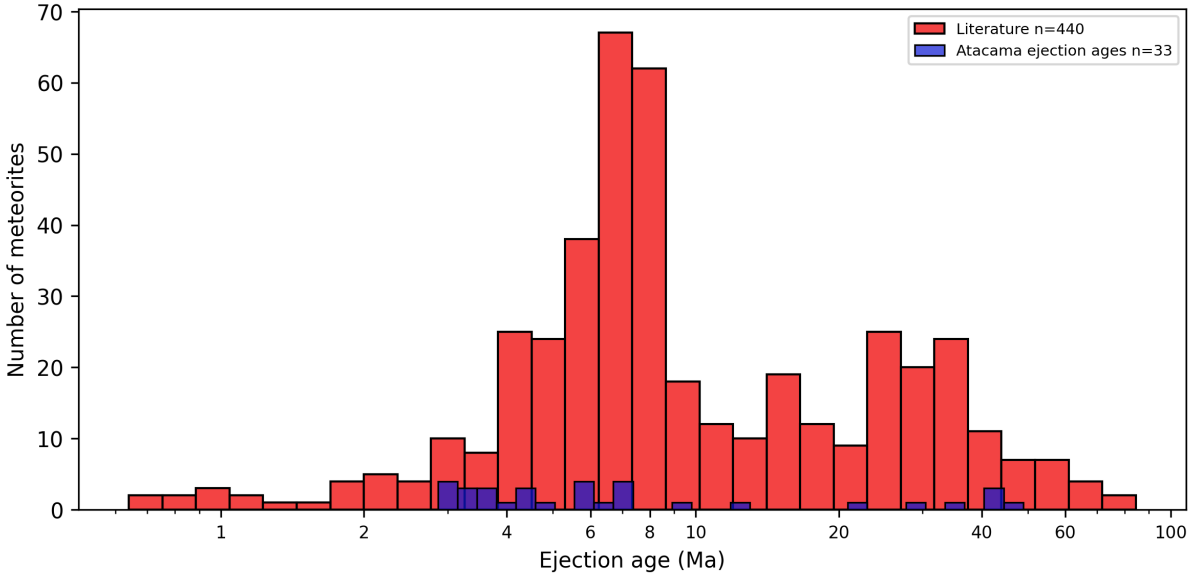

Figure 5.6. Distribution of cosmic-ray exposure (CRE) ages for H chondrites compiled from (Graf and Marti 1995), shown alongside ejection ages of H chondrites from the Atacama Desert with terrestrial ages > 0.5 Ma (this study, n = 33).

The 5–7 Ma cluster reinforces the global view that Karin and Koronis$_2$ families have supplied H chondrites to the meteorite flux over the past few million years, while the potential

~3 Ma peak suggests the contribution of an additional collisional event to the Atacama H chondrites population. This event may reflect either a smaller, undetected asteroid break up or a collisional cascade within the Karin/Koronis$_2$ population, temporarily increasing the influx of meteoroids to Earth.

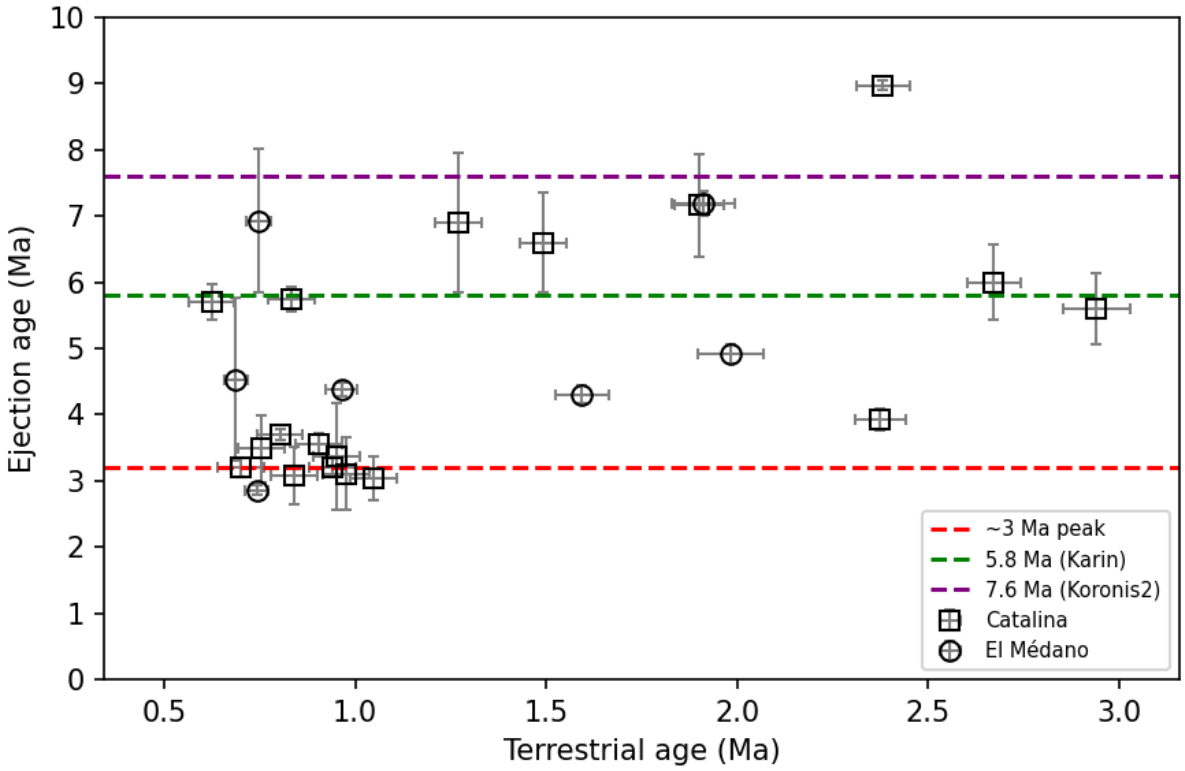

Figure 5.7. Ejection age as a function of the terrestrial age of the 33 H chondrites measured in this study from Catalina and El Médano collections, along with error bars. The dashed lines represent the main clusters of ejection ages: the ~3 Ma peak (red), the 5.8 Ma peak associated with the Karin cluster (green), and the 7.6 Ma peak linked to Koronis2 cluster (purple).

Figure 5.7 shows the ejection ages of the Atacama H chondrites as a function of their terrestrial ages. We notice that the previously identified cluster of meteorites that display ejection ages around 3 Ma have terrestrial ages exclusively in the 0.6–1.2 Ma range.

Interestingly, this ~3 Ma event corresponds to the transient increase in H chondrite relative abundance between 0.4 and 1.2 Ma documented in Atacama flux studies (Drouard et al. 2019; Sadaka et al., 2025b; Chapter 3; Figure 5.7). This suggests that this hypothetical collisional event produced a population of meteoroids that were in a favorable position that allowed their efficient delivery to Earth-crossing orbits within a short timescale (between 1.8 and 2.4 Ma), leading to a depletion of this reservoir after 0.6 Ma.

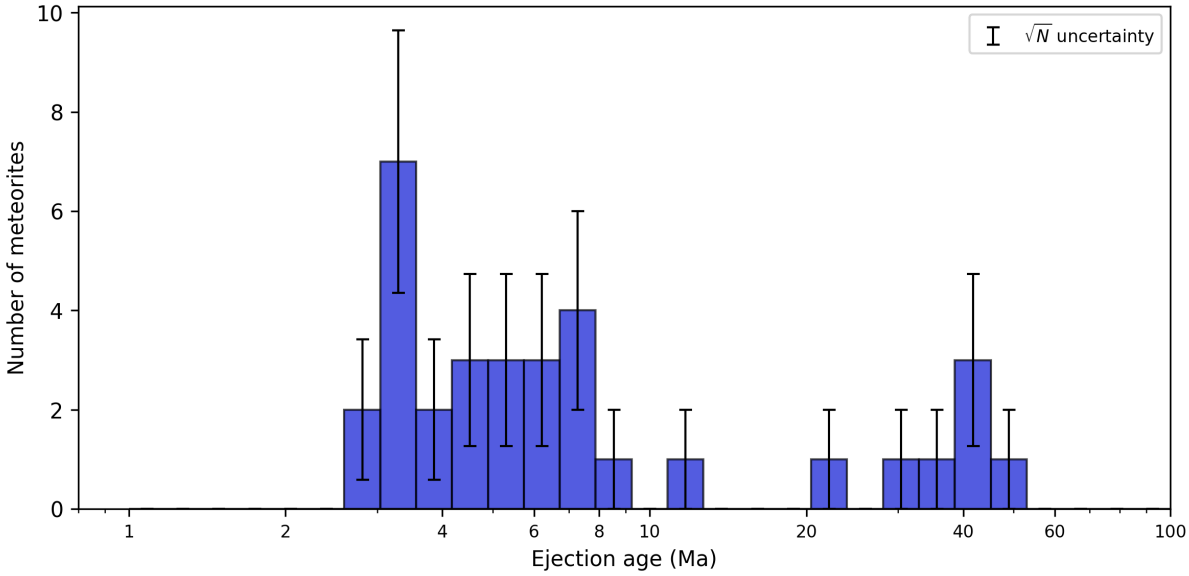

Figure 5.8. Distribution of ejection ages H chondrites with terrestrial age >0.5 Ma (n = 33). Error bars are uncertainties for a Poisson distribution (√N for N meteorites in a bin).

While the dataset is not yet large enough to confirm the statistical significance of this peak (Figure 5.8), this study highlights the unique potential of Atacama meteorites to resolve Myr-scale variations in meteoroid delivery. Expanding the dataset with additional CRE age measurements, specifically on H chondrites from the Atacama Desert with old terrestrial ages (> 0.5 Ma), will be essential to confirm or refute the observed ~3 Ma cluster.

With the constantly improving resolution of asteroid surveys (Kurlander et al. 2025), numerous smaller and younger asteroid families are now being identified, indicating that additional, previously undetected collisional events may have contributed to the recent meteorite flux to Earth. Together, these studies will help to refine models of meteoroid transfer and shed light on undetected collisional events.

5.4. Conclusion

This chapter presents ^{21}Ne-based cosmic-ray exposure (CRE) ages of ordinary chondrites from the Atacama Desert, which are combined with ^{36}Cl terrestrial ages to derive the ages of their ejection from their parent body. The results show the following key points:

1. ^{22}Ne/^{21}Ne ratios in the studied meteorite samples are consistent with those observed in global ordinary chondrite collections.
2. CRE ages range from 1.6 Myr to 47 Myr (n = 33), with most meteorites clustering between 5 and 15 Ma, in line with previously reported H chondrite distributions.
3. Ejection ages confirm the 5–7 Ma peak attributed to the Karin and Koronis$_2$ asteroid families. In addition, a possible ~3 Ma peak emerges, suggesting that more recent collisional activity, perhaps involving a small and currently undetected asteroid

family, may have be a major contribution to the H chondrite flux to Earth between 0.6 and 1.2 Ma.

These findings highlight the uniqueness of the Atacama meteorites, whose exceptionally long terrestrial ages allow to study the Myr-scale variability in ejection age distributions, which cannot be achieved with Antarctic or other hot-desert collections. While the dataset remains limited in size, the evidence for a ~3 Ma ejection peak emphasizes the need for additional CRE age measurements to fully capture the temporal variability of meteoroid delivery. This work reinforces the view that the meteorite flux to Earth is dominated by stochastic collisional events and raises the possibility that previously unrecognized collisional events may have influenced the meteorite flux within the past few million years.

5.5. Chapter supplementary

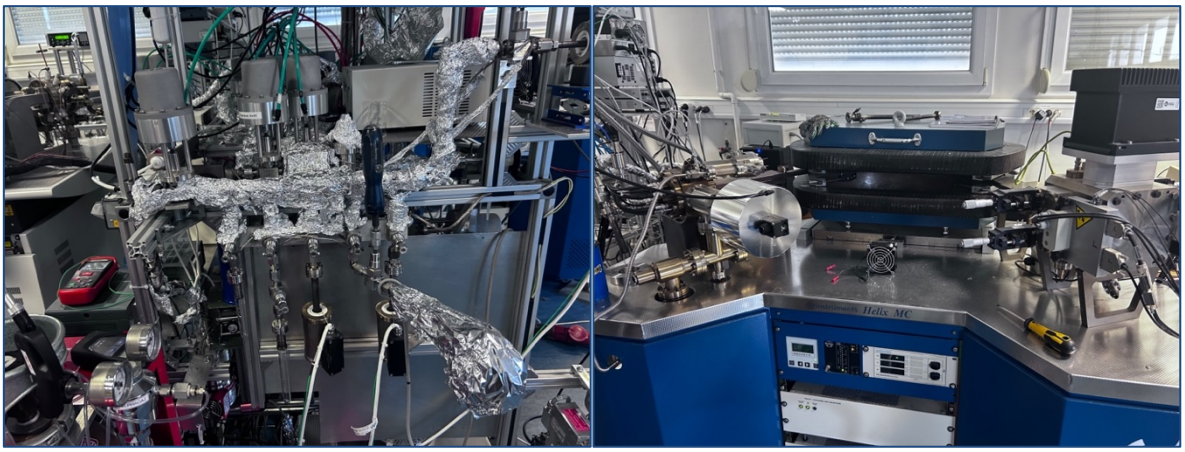

Figure 5.9. Extraction line and gas spectrometer for gas measurements at CRPG, Nancy.

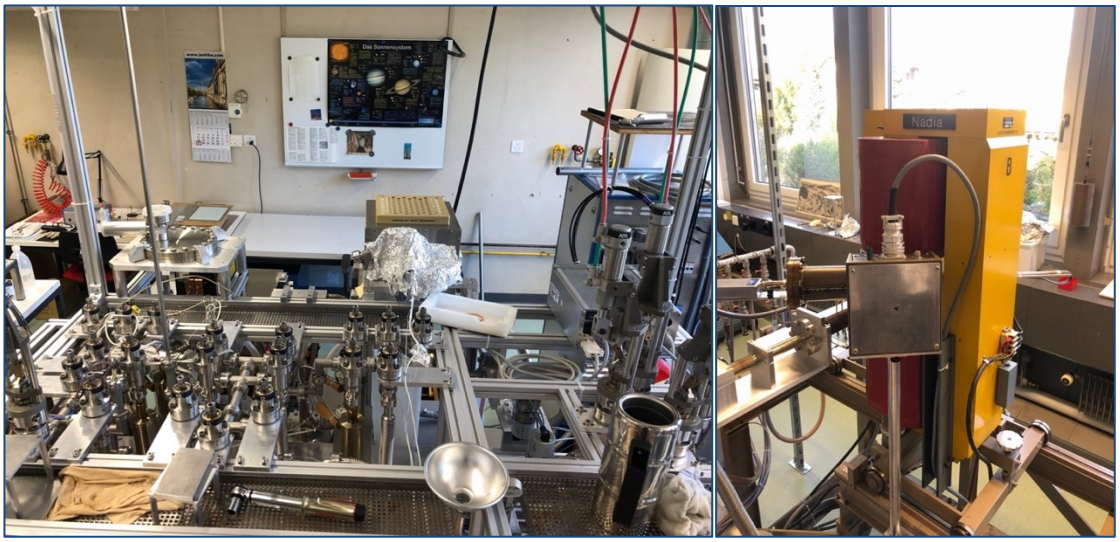

Figure 5.10. Extraction line and gas spectrometer at the University of Bern, Switzerland.

Table 5.1. Neon isotopic compositions, cosmogenic components, and Cosmic-Ray Exposure (CRE) ages of Atacama meteorites measured in this study.

Sample	Classification	F	$^{20}Ne/^{22}Ne$	+/-	$^{21}Ne21/^{2}2Ne$	+/-	$^{22}Ne/^{21}Ne_{(cos)}$	+/-	$^{21}Ne_{(cos)}$ (10-8 cm3 STP/g)	+/-	P(^{21}Ne) (10^{-8} cm^3 STP/g/Ma)	+/-	CRE age (Ma)	+/-
Catalina 229	H5	1.05	0.896	0.053	0.847	0.021	1.173	0.037	1.48	0.19	0.26	0.035	5.63	1.05
Catalina 474	H5	1.30	0.928	0.093	0.933	0.005	1.061	0.005	1.35	0.18	0.60	0.082	2.23	0.43
Catalina 476	H5	0.98	0.839	0.060	0.887	0.020	1.125	0.034	1.69	0.17	0.32	0.034	5.26	0.77
Catalina 477	H5	1.03	0.871	0.071	0.925	0.023	1.076	0.027	1.48	0.18	0.44	0.054	3.33	0.57
Catalina 480	H5	1.06	0.871	0.066	0.959	0.028	1.038	0.036	1.09	0.12	0.55	0.065	1.99	0.33
Catalina 481	H5	1.30	0.853	0.141	0.931	0.015	1.071	0.018	1.39	0.33	0.57	0.134	2.42	0.80
Catalina 494	H6	1.30	0.899	0.093	0.871	0.004	1.140	0.006	1.04	0.15	0.39	0.056	2.66	0.53
Catalina 517	H5	1.30	4.572	0.092	0.542	0.003	1.238	0.050	1.17	0.03	0.23	0.011	5.08	0.27
Catalina 524	H6	1.16	0.865	0.025	0.909	0.019	1.096	0.032	4.42	0.25	0.45	0.028	9.91	0.83
Catalina 535	H5	1.12	1.517	0.040	0.826	0.019	1.136	0.042	1.76	0.18	0.34	0.037	5.10	0.75
Catalina 538	H5	1.30	0.961	0.092	0.895	0.004	1.103	0.008	1.37	0.15	0.48	0.053	2.83	0.44
Catalina 538	H5	1.30	0.961	0.094	0.897	0.004	1.101	0.008	1.45	0.20	0.49	0.068	2.96	0.58
Catalina 548	H6	1.30	7.352	0.093	0.364	0.002	1.169	0.037	1.64	0.02	0.33	0.012	4.91	0.18
Catalina 551	H6	1.30	0.864	0.091	0.888	0.003	1.122	0.004	17.74	1.87	0.43	0.046	40.90	6.11
Catalina 555	H5	1.17	1.273	0.098	0.863	0.027	1.113	0.041	0.64	0.04	0.41	0.032	1.55	0.16
Catalina 600	H5	1.30	4.738	0.092	0.627	0.003	1.042	0.039	1.66	0.04	0.66	0.029	2.51	0.13
Catalina 637	H5	1.30	0.862	0.093	0.919	0.004	1.084	0.005	1.47	0.20	0.54	0.072	2.73	0.51

Sample	Classification	F	$^{20}Ne/^{22}Ne$	+/-	$^{21}Ne21/^{2}2Ne$	+/-	$^{22}Ne/^{21}Ne_{(cos)}$	+/-	$^{21}Ne_{(cos)}$ (10-8 cm3 STP/g)	+/-	P(^{21}Ne) (10^{-8} cm^3 STP/g/Ma)	+/-	CRE age (Ma)	+/-
Catalina 662	H5-6	1.30	3.606	0.092	0.712	0.003	1.060	0.049	1.61	0.05	0.61	0.033	2.64	0.16
Catalina 664	H5	1.30	5.024	0.092	0.555	0.002	1.135	0.040	2.65	0.05	0.40	0.016	6.59	0.29
Catalina 664	H5	1.30	7.404	0.093	0.369	0.002	1.137	0.038	2.64	0.04	0.40	0.014	6.60	0.25
Catalina 677	H5-6	1.30	0.864	0.091	0.893	0.003	1.116	0.004	18.94	2.00	0.45	0.048	42.04	6.28
Catalina 682	H5-6	1.30	6.235	0.092	0.480	0.002	1.088	0.035	1.41	0.02	0.53	0.019	2.67	0.10
Catalina 682	H5-6	1.30	3.911	0.093	0.669	0.004	1.087	0.058	0.84	0.03	0.53	0.034	1.59	0.12
Catalina 684	H6	1.30	4.469	0.092	0.621	0.003	1.092	0.042	1.17	0.03	0.52	0.023	2.27	0.12
Catalina 707	H6	1.30	0.818	0.091	0.881	0.003	1.136	0.004	18.93	2.11	0.40	0.045	47.09	7.43
Catalina 739	H6	1.30	0.870	0.091	0.924	0.003	1.078	0.003	17.83	1.87	0.55	0.058	32.16	4.77
El Médano 025	H6	1.30	0.867	0.005	0.930	0.013	1.070	0.015	16.45	4.28	0.58	0.150	28.54	10.51
El Médano 027	H5	1.30	0.993	0.006	0.908	0.013	1.084	0.016	1.83	0.03	0.54	0.012	3.41	0.09
El Médano 049	H4	1.30	0.967	0.008	0.790	0.012	1.250	0.019	1.14	0.02	0.22	0.005	5.28	0.16
El Médano 099	H5	1.30	1.110	0.010	0.863	0.013	1.129	0.017	1.22	0.03	0.42	0.012	2.93	0.11
El Médano 111	H5	1.30	0.842	0.005	0.912	0.013	1.094	0.015	9.86	0.16	0.51	0.011	19.39	0.52

Sample	Classification	F	$^{20}Ne/^{22}Ne$	+/-	$^{21}Ne21/^{2}2Ne$	+/-	$^{22}Ne/^{21}Ne_{(cos)}$	+/-	$^{21}Ne_{(cos)}$ (10-8 cm3 STP/g)	+/-	P(^{21}Ne) (10^{-8} cm^3 STP/g/Ma)	+/-	CRE age (Ma)	+/-
El Médano 115	H5	1.30	1.170	0.100	0.816	0.021	1.115	0.016	2.37	0.10	0.45	0.020	5.23	0.32
El Médano 115	H5	1.30	0.916	0.006	0.889	0.013	1.202	0.029	2.32	0.47	0.28	0.057	8.34	2.40
El Médano 115	H5	1.30	0.820	0.050	0.832	0.020	1.188	0.031	1.49	0.27	0.30	0.056	4.96	1.30
El Médano 199	H6	1.30	3.029	0.018	0.765	0.011	1.044	0.058	3.33	0.18	0.65	0.051	5.08	0.49
El Médano 199	H6	1.30	3.250	0.180	0.716	0.017	1.089	0.154	1.37	0.15	0.52	0.094	2.61	0.55
El Médano 236	H5	1.30	0.942	0.010	0.917	0.014	1.079	0.017	1.17	0.03	0.55	0.015	2.12	0.07
El Médano 245	H5-6	1.30	1.100	0.008	0.913	0.014	1.068	0.016	1.58	0.05	0.58	0.019	2.71	0.12
El Médano 261	H3	1.30	1.332	0.007	0.785	0.011	1.217	0.035	10.50	1.74	0.26	0.043	40.95	9.68

Table 5.2. Terrestrial ages, cosmic-ray exposure (CRE) ages, and ejection ages of H chondrites from the Atacama Desert (n = 33).

Sample	Classification	Terrestrial age (Ma)	CRE age (Ma)	Ejection age (Ma)	Laboratory
Catalina 229	H5	1.27 ± 0.06	5.63 ± 1.05	6.9 ± 1.05	Bern
Catalina 474	H5	0.84 ± 0.06	2.23 ± 0.43	3.07 ± 0.43	CRPG
Catalina 476	H5	1.9 ± 0.063	5.26 ± 0.77	7.16 ± 0.77	Bern
Catalina 477	H5	2.67 ± 0.069	3.33 ± 0.57	6 ± 0.57	Bern
Catalina 480	H5	1.05 ± 0.06	1.99 ± 0.33	3.04 ± 0.36	Bern
Catalina 481	H5	0.951 ± 0.062	2.42 ± 0.8	3.37 ± 0.80	CRPG
Catalina 494	H6	2.94 ± 0.089	2.66 ± 0.53	5.6 ± 0.54	CRPG
Catalina 517	H5	0.625 ± 0.059	5.08 ± 0.27	5.71 ± 0.28	CRPG
Catalina 524	H6	2.78 ± 0.069	9.91 ± 0.83	12.7 ± 0.83	Bern
Catalina 535	H5	1.49 ± 0.061	5.1 ± 0.75	6.59 ± 0.75	Bern
Catalina 538	H5	0.803 ± 0.059	2.9 ± 0.065	3.7 ± 0.09	CRPG
Catalina 548	H6	0.833 ± 0.06	4.91 ± 0.18	5.74 ± 0.19	CRPG
Catalina 551	H6	1.06 ± 0.063	40.9 ± 6.11	42 ± 6.11	CRPG
Catalina 555	H5	2.38 ± 0.066	1.55 ± 0.16	3.92 ± 0.17	Bern
Catalina 600	H5	0.701 ± 0.061	2.51 ± 0.13	3.21 ± 0.14	CRPG
Catalina 637	H5	0.755 ± 0.062	2.73 ± 0.51	3.48 ± 0.51	CRPG
Catalina 662	H5-6	0.905 ± 0.061	2.64 ± 0.16	3.54 ± 0.17	CRPG
Catalina 664	H5	2.38 ± 0.07	6.59 ± 0.005	8.98 ± 0.07	CRPG
Catalina 677	H5-6	0.749 ± 0.061	42.0 ± 6.28	42.8 ± 6.28	CRPG
Catalina 682	H5-6	0.977 ± 0.062	2.13 ± 0.54	3.11 ± 0.54	CRPG
Catalina 684	H6	0.942 ± 0.061	2.27 ± 0.12	3.21 ± 0.16	CRPG
Catalina 707	H6	1.8 ± 0.065	47.1 ± 7.43	48.9 ± 7.43	CRPG
Catalina 739	H6	1.8 ± 0.063	32.2 ± 4.77	34 ± 4.77	CRPG
El Médano 025	H6	0.993 ± 0.043	28.5 ± 10.5	29.5 ± 10.5	CRPG
El Médano 099	H5	1.98 ± 0.086	2.93 ± 0.11	4.91 ± 0.14	CRPG
El Médano 111	H5	1.51 ± 0.066	19.4 ± 0.52	20.9 ± 0.52	CRPG
El Médano 115	H5	0.746 ± 0.032	6.18 ± 1.08	6.92 ± 1.08	CRPG

Sample	Classification	Terrestrial age (Ma)	CRE age (Ma)	Ejection age (Ma)	Laboratory
El Médano 199	H6	0.687 ± 0.03	3.84 ± 1.24	4.53 ± 1.24	CRPG
El Médano 236	H5	0.742 ± 0.032	2.12 ± 0.07	2.86 ± 0.077	CRPG
El Médano 245	H5-6	1.59 ± 0.069	2.71 ± 0.12	4.3 ± 0.138	CRPG
El Médano 261	H3	0.493 ± 0.021	41.0 ± 9.68	41.4 ± 9.68	CRPG
El Médano 27	H5	0.965 ± 0.042	3.41 ± 0.09	4.38 ± 0.0993	CRPG
El Médano 49	H4	1.91 ± 0.083	5.28 ± 0.16	7.19 ± 0.18	CRPG

Chapter six

Conclusions and perspectives



We can judge our progress by the courage of our questions and the depth of our answers, our willingness to embrace what is true rather than what feels good.

– ***Carl Sagan***

6. Chapter 6

In this chapter, I will present the main conclusions of my thesis and propose potential perspectives for future studies.

6.1. Conclusions

This thesis retraces the history of ordinary chondrite precursors, from their extraction from parent asteroids to their recovery on Earth. The main objective is to investigate the intensity and composition of the long-term meteorite flux to Earth over the past 2 Myr, through systematic meteorite collections in the Atacama Desert, Chile and measurements of terrestrial ages and cosmic ray exposure ages.

6.1.1. Meteorite density

The Catalina Systematic Collection (CSC), located in the Central Depression of the Atacama Desert, has yielded the highest recovery density ever encountered in hot desert settings, with a density of 235 meteorites per km^2 before pairing (67 meteorites >20 g per km^2). The estimated pairing-corrected density estimate is 71 meteorites >20 g per km^2. This high density mirrors the long accumulation period under hyperarid conditions, with meteorites exhibiting relatively lower degrees of terrestrial weathering than other Atacama collections and other hot desert collections as well.

Further north in the desert, the Calama area also revealed high densities, with systematic searches yielding a recovery density of 37 meteorites per km^2 (15 meteorites per km^2 for meteorites > 20 g) and a pairing-corrected density of 18 meteorites > 20 g per km^2, higher than other hot deserts.

6.1.2. Terrestrial ages and past meteorite flux

Terrestrial ages measured using cosmogenic ^{36}Cl in the metal phase of the CSC meteorites reveal exceptionally old ages, with an average ~1 Ma (median 750 ka), making it the oldest known meteorite collection in the world. Meteorites from the Calama Area display younger terrestrial ages (median 331 ka) in line with a lower meteorite density, reflecting a slightly more humid climate and an active geomorphology, being close to the pre-Andean range. Nonetheless, all studied Atacama collections exceed other hot deserts in terms of density and terrestrial ages, indicating that this pattern spreads throughout the entire desert.

Given the uniquely old terrestrial ages of meteorites from the Atacama Desert, this region proves to be essential for studying the variability in meteoroid delivery

to Earth over the last 2 Myr. In the CSC, combining density estimates with measured terrestrial ages enabled to estimate a meteorite flux of 69 ± 8 meteorites per km^2 per Ma over the past 2 Myr. This value is broadly consistent with flux estimates from observed falls, Antarctic collections, and other hot deserts collections, suggesting that the long-term meteorite flux to Earth has remained roughly stable at the Myr timescale.

6.1.3. Composition of the meteorite flux

Investigating the composition of the meteorite flux using ordinary chondrites from the Atacama Desert revealed some temporal variations at the scale of a few hundreds of kyr. Notably, our results confirm an increase in H chondrite relative abundance between 1.2 and 0.4 Ma, a feature not reproduced by current dynamical models. This suggests that the short-term evolution of the meteorite flux may be influenced by processes not accounted for by these meteoroid delivery models.

6.1.4. Cosmic-ray exposure ages and ejection histories

We determined cosmic-ray exposure (CRE) ages from noble gas ^{21}Ne measurements on Atacama H chondrites with terrestrial ages >0.5 Ma. Their distribution is consistent with global datasets of CRE ages in the literature.

By combining CRE and terrestrial ages, we derive ejection ages from parent bodies. The resulting distribution confirms the existence of the 5–7 Ma peak in H chondrite ejection ages, associated with the Karin and $Koronis_2$ asteroid families. It also reveals a potential peak in H chondrite ejection ages around 3 Ma. Meteorites belonging to this peak fell between 0.6 and 1.1 Ma (Figure 5.7), which corresponds to the observed increase in H chondrites relative abundance between 0.4 and 1.2 Ma (Chapter 3). This peak is possibly linked to a more recent or smaller-scale collisional event, which provided additional H chondrites to the meteorite flux to Earth between 0.4 and 1.2 Ma, and which is no longer visible after 0.4 Ma.

Overall, these results bridge the gap between studies based on meteorite collections on Earth and those based on asteroid family observations and dynamical modeling.

6.2. Side projects

During my PhD, I had the opportunity to work on the classification of several rarer meteorite types from the Atacama and other collections, including R chondrites, lunar and Martian meteorites, CK, CV, eucrites, and diogenites. This has deepened my knowledge in meteorite classification and mineralogy, beyond ordinary chondrites and mesosiderites.

I also determined terrestrial ages using ^{36}Cl measurements for 22 Antarctic meteorites. Four of these were measured for the University of Manchester to assess pairing between meteorites collected in the framework of the Lost Meteorites of Antarctica project (Leverhulme Trust grant

RPG-2016-349; https://ukantarcticmeteorites.wordpress.com/; PI Geoff Evatt, School of Maths, University of Manchester).

The remaining 18 Antarctic samples were measured for the Vrije Universiteit Brussel (VUB) as part of the FROID project (Finding the world's oldest ice record around the Princess Elisabeth Station) with the aim to provide constraints on the age of Antarctic ice (https://www.vub.be/en/news/in-search-for-million-year-old-ice-belgian-scientists-return ; PIs Veronica Tollenaar (VUB), and Harry Zekollari (VUB)).

These studies highlight how the measurement of terrestrial ages of meteorites can serve as means to assess the climatic stability and surface processes of a region, beyond their use for extraterrestrial flux estimations.

6.3. Perspectives

6.3.1. On the future of hot desert meteorite collections

With tens of thousands of meteorite samples currently curated in world collections, an important question arises: what additional scientific knowledge can be gained through additional collections? Besides well-established studies, such as classification statistics, terrestrial ages, CRE ages, flux estimates, and weathering effects, the challenge lies in finding new research directions that would justify adding more samples to collections. For ordinary chondrites, already represented by tens of thousands of specimens in laboratories and museums, the scientific value of simply expanding collections has become limited, since their classification and properties have already been thoroughly investigated and are currently well established.

While the occasional discovery of rare types will always be impactful for the scientific community (e.g., NWA 7034 and paired stones, Erg Chech 002, Oued Chebeika 002, etc.), the broader scientific interest of large collections of ordinary chondrites is relatively reduced, therefore limiting the need for their additional recovery. For such field missions, it will become difficult to justify the financial and environmental costs (carbon footprint).

Antarctic meteorite collections remain, however, extremely important since they provide exceptionally fresh and well-preserved material due to cold and dry conditions. In contrast, many of the rare types discovered today come from Northwest Africa (NWA) meteorites, where 44% of classified meteorites are non-ordinary chondrites (Meteoritical Bulletin DataBase). In addition, among NWA ordinary chondrites, ~19% are of petrographic type 3, which are rarer among ordinary chondrite and represent only 5.8% of ordinary chondrite falls. In these regions, meteorites are mostly collected by private hunters and dealers who tend to perform a selective recovery, only collecting samples that seem special and rare.

These samples are then classified through the Nomenclature Committee of the Meteoritical Society, which requires that 20 g of the sample are given to a scientific

institution, a mass sufficient for classification and other analyses. This system creates a mutually beneficial situation between private collectors and the scientific community, while reducing the need for costly dedicated field missions in Antarctica or other hot deserts for meteorite collections.

Another important aspect in meteorite recovery in hot deserts is camera networks, which enable the recovery of freshly fallen samples with known orbits, such as the Desert Fireball Network (DFN) in Australia (Devillepoix et al. 2022) and the Global Fireball Observatory (GFO) in Oman (Zappatini et al. 2024).

Accordingly, since new and rare meteorites are added to the collections at almost no cost thanks to the classification of material found by private hunters, future meteorite recovery missions led by the scientific community will need to target questions that cannot be addressed with existing collections.

6.3.2. Towards confirming the 3 Ma peak in H chondrite ejection ages

A promising follow-up to this thesis would be to confirm the existence of the ~3 Ma peak in ejection ages of H chondrites that fell between, 0.4 and 1.2 Ma ago, suggested by our preliminary dataset. This could involve first expanding the dataset of H chondrite terrestrial ages from several Dense Collection Areas in the Atacama Desert, particularly targeting highly weathered samples that are more likely (though not necessarily) to terrestrial ages in the adequate range, and subsequently measuring their CRE ages to build a statistically robust dataset of ejection ages. Statistical approaches such as Monte Carlo resampling and goodness-of-fit tests (Kolmogorov-Smirnov, Anderson-Darling) could then be applied to evaluate the significance of the ~3 Ma peak. If confirmed, this population could be compared with the 5–7 Ma peak in terms of shock stages, mineralogy (olivine and low-Ca pyroxene compositions), and petrographic types, potentially linking the ~3 Ma population to a distinct collisional source from the Karin and Koronis$_2$ families.

6.3.3. Comparing meteorite and micrometeorite flux records

Another interesting perspective would be to compare the meteorite density to the micrometeorite density from the same collection sites. The Atacama Desert has proved to be valuable for micrometeorite recovery as well, with thousands of particles >200 µm already recovered (Van Ginneken et al. 2024) . A comparison between meteorite and micrometeorite records would shed light on whether different size populations show similar features in terms of compositions, preservation, and accumulation, thus offering an overall clearer picture on the extraterrestrial influx of material to Earth.

Bibliography

Abe, S. 2008. “Meteoroids and Meteors — Observations and Connection to Parent Bodies.” In *Small Bodies in Planetary Systems*, edited by Ingrid Mann, Akiko Nakamura, and Tadashi Mukai, vol. 758. Lecture Notes in Physics. Springer Berlin Heidelberg. https://doi.org/10.1007/978-3-540-76935-4_5.

Aboulahris, Maria, Hasnaa Chennaoui Aoudjehane, Pierre Rochette, et al. 2019. “Characteristics of the Sahara as a Meteorite Recovery Surface.” *Meteoritics & Planetary Science* 54 (12): 2908–28. https://doi.org/10.1111/maps.13398.

Alvarez, Luis W., Walter Alvarez, Frank Asaro, and Helen V. Michel. 1980. “Extraterrestrial Cause for the Cretaceous-Tertiary Extinction.” *Science* 208 (4448): 1095–108. https://doi.org/10.1126/science.208.4448.1095.

Anderson, Sarah E., Pierre Vernazza, and Miroslav Brož. 2025. “Different Arrival Times of CM and CI-like Bodies from the Outer Solar System to the Asteroid Belt.” Version 1. Preprint, arXiv. https://doi.org/10.48550/ARXIV.2507.22649.

Arnold, Maurice, Silke Merchel, Didier L. Bourlès, et al. 2010. “The French Accelerator Mass Spectrometry Facility ASTER: Improved Performance and Developments.” *Nuclear Instruments and Methods in Physics Research Section B: Beam Interactions with Materials and Atoms* 268 (11–12): 1954–59. https://doi.org/10.1016/j.nimb.2010.02.107.

Azua-Bustos, A., A. G. Fairén, C. González-Silva, et al. 2018. “Unprecedented Rains Decimate Surface Microbial Communities in the Hyperarid Core of the Atacama Desert.” *Scientific Reports* 8 (1): 16706. https://doi.org/10.1038/s41598-018-35051-w.

Bekaert, David V., Joshua Curtice, Matthias M. M. Meier, et al. 2022. “Determining the Noble Gas Cosmic Ray Exposure Ages of 23 Meteorites (8 Chondrites and 15 Achondrites) from Modeling and Empirical Methods.” *Meteoritics & Planetary Science* 57 (8): 1542–69. https://doi.org/10.1111/maps.13887.

Belhai, Djelloul. 2023. “Spatial Distribution and Classification of Algerian Meteorites: Qualitative and Quantitative Inventory.” *Journal of African Earth Sciences* 207 (November): 105058. https://doi.org/10.1016/j.jafrearsci.2023.105058.

Benedix, G. K., K. Keil, and J. Y. Murakami. 1999. “Classification of Ten New Nullarbor Region Meteorites.” *Meteoritics & Planetary Science* 34 (5): 813–15. https://doi.org/10.1111/j.1945-5100.1999.tb01395.x.

Binzel, R. P., V. Reddy, and T. L. Dunn. 2015. “The Near-Earth Object Population: Connections to Comets, Main-Belt Asteroids, and Meteorites.” In *Asteroids IV*. https://doi.org/10.2458/azu_uapress_9780816532131-ch013.

Bischoff, A., and T. Geiger. 1995. “Meteorites from the Sahara: Find Locations, Shock Classification, Degree of Weathering and Pairing.” *Meteoritics* 30 (1): 113–22. https://doi.org/10.1111/j.1945-5100.1995.tb01219.x.

References

Bischoff, A., E. R. D. Scott, K. Metzler, and C. A. Goodrich. 2006. "Nature and Origins of Meteoritic Breccias." In *Meteorites and the Early Solar System II*. https://ui.adsabs.harvard.edu/abs/2006mess.book..679B.

Bonal, Lydie, Eric Quirico, Laurène Flandinet, and Gilles Montagnac. 2016. "Thermal History of Type 3 Chondrites from the Antarctic Meteorite Collection Determined by Raman Spectroscopy of Their Polyaromatic Carbonaceous Matter." *Geochimica et Cosmochimica Acta* 189 (September): 312–37. https://doi.org/10.1016/j.gca.2016.06.017.

Bottke, W. 2000. "Dynamical Evolution of Main Belt Meteoroids: Numerical Simulations Incorporating Planetary Perturbations and Yarkovsky Thermal Forces." *Icarus* 145 (2): 301–31. https://doi.org/10.1006/icar.2000.6361.

Bottke, W. F., M. Brož, D. P. O'Brien, A. Campo Bagatin, A. Morbidelli, and S. Marchi. 2015. "The Collisional Evolution of the Main Asteroid Belt." In *Asteroids IV*, edited by Patrick Michel, Francesca E. DeMeo, and William F. Bottke. University of Arizona Press. https://doi.org/10.2458/azu_uapress_9780816532131-ch036.

Bottke, William F., David Vokrouhlický, David P. Rubincam, and David Nesvorný. 2006. "THE YARKOVSKY AND YORP EFFECTS: Implications for Asteroid Dynamics." *Annual Review of Earth and Planetary Sciences* 34 (1): 157–91. https://doi.org/10.1146/annurev.earth.34.031405.125154.

Brož, M., P. Vernazza, M. Marsset, R. P. Binzel, et al. 2024a. "Source Regions of Carbonaceous Meteorites and Near-Earth Objects." *Astronomy & Astrophysics* 689 (September): A183. https://doi.org/10.1051/0004-6361/202450532.

Brož, M., P. Vernazza, M. Marsset, F. E. DeMeo, et al. 2024b. "Young Asteroid Families as the Primary Source of Meteorites." *Nature* 634 (8034): 566–71. https://doi.org/10.1038/s41586-024-08006-7.

Brunetto, R., F. Romano, A. Blanco, et al. 2006. "Space Weathering of Silicates Simulated by Nanosecond Pulse UV Excimer Laser." *Icarus* 180 (2): 546–54. https://doi.org/10.1016/j.icarus.2005.10.016.

Buchwald, Vagn Fabritius. 2001. "Ancient Iron and Slags in Greenland." *Meddelelser Om Grønland. Man & Society* 26 (December). https://doi.org/10.7146/mog-ms.v26.146799.

Burbine, Thomas H. 2016. "Advances in Determining Asteroid Chemistries and Mineralogies." *Geochemistry* 76 (2): 181–95. https://doi.org/10.1016/j.chemer.2015.09.003.

Burbine, Thomas H., Iman Khanani, Deepika Kumawat, Ahlay Hussain, Sydney M. Wallace, and M. Darby Dyar. 2024. "Testing the Bus–DeMeo Asteroid Taxonomy Using Meteorite Spectra." *The Planetary Science Journal* 5 (9): 194. https://doi.org/10.3847/PSJ/ad57b6.

Carrillo-Sánchez, Juan Diego, Juan Carlos Gómez-Martín, David L. Bones, et al. 2020. "Cosmic Dust Fluxes in the Atmospheres of Earth, Mars, and Venus." *Icarus* 335 (January): 113395. https://doi.org/10.1016/j.icarus.2019.113395.

References

Carruba, V. 2003. “Orbital Evolution of the Gefion and Adeona Asteroid Families: Close Encounters with Massive Asteroids and the Yarkovsky Effect.” *Icarus* 162 (2): 308–27. https://doi.org/10.1016/S0019-1035(02)00062-3.

Carruba, V., S. Aljbaae, Á.L. Fazenda, et al. 2020. “Spin Pairs in the Koronis Asteroid Family.” *Planetary and Space Science* 193 (November): 105083. https://doi.org/10.1016/j.pss.2020.105083.

Chabrier, Gilles, and Isabelle Baraffe. 2000. “Theory of Low-Mass Stars and Substellar Objects.” *Annual Review of Astronomy and Astrophysics* 38 (1): 337–77. https://doi.org/10.1146/annurev.astro.38.1.337.

Chapman, Clark R., and John W. Salisbury. 1973. “Comparisons of Meteorite and Asteroid Spectral Reflectivities.” *Icarus* 19 (4): 507–22. https://doi.org/10.1016/0019-1035(73)90078-X.

Chesley, Steven R., Steven J. Ostro, David Vokrouhlický, et al. 2003. “Direct Detection of the Yarkovsky Effect by Radar Ranging to Asteroid 6489 Golevka.” *Science* 302 (5651): 1739–42. https://doi.org/10.1126/science.1091452.

Comelli, Daniela, Massimo D’orazio, Luigi Folco, et al. 2016. “The Meteoritic Origin of Tutankhamun’s Iron Dagger Blade.” *Meteoritics & Planetary Science* 51 (7): 1301–9. https://doi.org/10.1111/maps.12664.

Connelly, James N., Martin Bizzarro, Alexander N. Krot, Åke Nordlund, Daniel Wielandt, and Marina A. Ivanova. 2012. “The Absolute Chronology and Thermal Processing of Solids in the Solar Protoplanetary Disk.” *Science* 338 (6107): 651–55. https://doi.org/10.1126/science.1226919.

Dalcher, N., M. W. Caffee, K. Nishiizumi, et al. 2013. “Calibration of Cosmogenic Noble Gas Production in Ordinary Chondrites Based on^{36} Cl-^{36} Ar Ages. Part 1: Refined Produced Rates for Cosmogenic^{21} Ne and^{38} Ar.” *Meteoritics & Planetary Science* 48 (10): 1841–62. https://doi.org/10.1111/maps.12203.

Delbo, M., et al. “Identification of a Primordial Asteroid Family Constrains the Original Planetesimal Population.” *Science*, vol. 357, no. 6355, 3 Aug. 2017, pp. 1026–1029, https://doi.org/10.1126/science.aam6036.

DeMeo, F. E., C. M. O’D. Alexander, K. J. Walsh, C. R. Chapman, and R. P. Binzel. 2015. “The Compositional Structure of the Asteroid Belt.” In *Asteroids IV*, edited by Patrick Michel, Francesca E. DeMeo, and William F. Bottke. University of Arizona Press. https://doi.org/10.2458/azu_uapress_9780816532131-ch002.

DeMeo, F. E., and B. Carry. 2014. “Solar System Evolution from Compositional Mapping of the Asteroid Belt.” *Nature* 505 (7485): 629–34. https://doi.org/10.1038/nature12908.

DeMeo, Francesca E., Richard P. Binzel, Stephen M. Slivan, and Schelte J. Bus. 2009. “An Extension of the Bus Asteroid Taxonomy into the Near-Infrared.” *Icarus* 202 (1): 160–80. https://doi.org/10.1016/j.icarus.2009.02.005.

Desch, Steven J., Anusha Kalyaan, and Conel M. O’D. Alexander. 2018. “The Effect of Jupiter’s Formation on the Distribution of Refractory Elements and Inclusions in

Meteorites." *The Astrophysical Journal Supplement Series* 238 (1): 11. https://doi.org/10.3847/1538-4365/aad95f.

Devillepoix, Hadrien A. R., Eleanor K. Sansom, Patrick Shober, et al. 2022. "Trajectory, Recovery, and Orbital History of the Madura Cave Meteorite." *Meteoritics & Planetary Science* 57 (7): 1328–38. https://doi.org/10.1111/maps.13820.

Drouard, A., J. Gattacceca, A. Hutzler, et al. 2019. "The Meteorite Flux of the Past 2 m.y. Recorded in the Atacama Desert." *Geology* 47 (7): 673–76. https://doi.org/10.1130/G45831.1.

Dunai, Tibor J., Gabriel A. González López, and Joaquim Juez-Larré. 2005. "Oligocene–Miocene Age of Aridity in the Atacama Desert Revealed by Exposure Dating of Erosion-Sensitive Landforms." *Geology* 33 (4): 321. https://doi.org/10.1130/G21184.1.

Edwards, Graham H., and Terrence Blackburn. 2020. "Accretion of a Large LL Parent Planetesimal from a Recently Formed Chondrule Population." *Science Advances* 6 (16): eaay8641. https://doi.org/10.1126/sciadv.aay8641.

Esser, Bradley K., and Karl K. Turekian. 1988. "Accretion Rate of Extraterrestrial Particles Determined from Osmium Isotope Systematics of Pacific Pelagic Clay and Manganese Nodules." *Geochimica et Cosmochimica Acta* 52 (June): 1383–88. https://doi.org/10.1016/0016-7037(88)90209-8.

Eugster, O. 2003. "Cosmic-Ray Exposure Ages of Meteorites and Lunar Rocks and Their Significance." *Geochemistry* 63 (1): 3–30. https://doi.org/10.1078/0009-2819-00021.

Eugster, O., G.F. Herzog, K. Marti, and M. W. Caffee. 2006. "Irradiation Records, Cosmic-Ray Exposure Ages, and Transfer Times of Meteorites(Pp. 829-852) Irradiation Records, Cosmic-Ray Exposure Ages, and Transfer Times of Meteorites." In *Meteorites and the Early Solar System II*, edited by D. S. Lauretta. University of Arizona Press. https://doi.org/10.2307/j.ctv1v7zdmm.

Evatt, G W, A R D Smedley, K H Joy, L Hunter, W H Tey, and I D Abrahams. n.d. *1 The Spatial Flux of Earth's Meteorite Falls Found via Antarctic 2 Data: Supplementary Material*.

Evatt, G.W., A.R.D. Smedley, K.H. Joy, et al. 2020. "The Spatial Flux of Earth's Meteorite Falls Found via Antarctic Data." *Geology* 48 (7): 683–87. https://doi.org/10.1130/G46733.1.

Farinella, Paolo, David Vokrouhlický, and William K. Hartmann. 1998. "Meteorite Delivery via Yarkovsky Orbital Drift." *Icarus* 132 (2): 378–87. https://doi.org/10.1006/icar.1997.5872.

Farley, K.A., A. Montanari, and R. Coccioni. 2012. "A Record of the Extraterrestrial 3He Flux through the Late Cretaceous." *Geochimica et Cosmochimica Acta* 84 (May): 314–28. https://doi.org/10.1016/j.gca.2012.01.015.

Fénisse, G., D.V. Bekaert, P.-H. Blard, et al. 2025. "The Extraterrestrial Dust Accretion Rate on Earth at Dome C, Antarctica: A Fresh Look with 3He." *Earth and Planetary Science Letters* 663 (August): 119396. https://doi.org/10.1016/j.epsl.2025.119396.

References

Folco, Luigi, Pierre Rochette, Jérôme Gattacceca, and Natale Perchiazzi. 2006. “In Situ Identification, Pairing, and Classification of Meteorites from Antarctica through Magnetic Susceptibility Measurements.” *Meteoritics & Planetary Science* 41 (3): 343–53. https://doi.org/10.1111/j.1945-5100.2006.tb00467.x.

French, Bevan M. 1999. “Traces of Catastrophe: A Handbook of Shock-Metamorphic Effects in Terrestrial Meteorite Impact Structures.” *Choice Reviews Online* 36 (10): 36-5704-36–5704. https://doi.org/10.5860/CHOICE.36-5704.

Gaffey, Michael J., Jeffrey F. Bell, R.Hamilton Brown, et al. 1993. “Mineralogical Variations within the S-Type Asteroid Class.” *Icarus* 106 (2): 573–602. https://doi.org/10.1006/icar.1993.1194.

Gallardo, Tabare. 2018. “Resonances in the Asteroid and Trans-Neptunian Belts: A Brief Review.” *Planetary and Space Science* 157 (August): 96–103. https://doi.org/10.1016/j.pss.2018.03.007.

Ganguly, Jibamitra, Massimiliano Tirone, Sumit Chakraborty, and Kenneth Domanik. 2013. “H-Chondrite Parent Asteroid: A Multistage Cooling, Fragmentation and Re-Accretion History Constrained by Thermometric Studies, Diffusion Kinetic Modeling and Geochronological Data.” *Geochimica et Cosmochimica Acta* 105 (March): 206–20. https://doi.org/10.1016/j.gca.2012.11.024.

Gattacceca, J., L. Bonal, C. Sonzogni, and J. Longerey. 2020. “CV Chondrites: More than One Parent Body.” *Earth and Planetary Science Letters* 547 (October): 116467. https://doi.org/10.1016/j.epsl.2020.116467.

Gattacceca, J., M. Gounelle, B. Devouard, et al. 2025. “Oued Chebeika 002: A New CI1 Meteorite Linked to Outer Solar System Bodies.” *Meteoritics & Planetary Science* 60 (7): 1441–79. https://doi.org/10.1111/maps.14359.

Gattacceca, Jérôme, Millarca Valenzuela, Minoru Uehara, et al. 2011a. “The Densest Meteorite Collection Area in Hot Deserts: The San Juan Meteorite Field (Atacama Desert, Chile).” *Meteoritics & Planetary Science* 46 (9): 1276–87. https://doi.org/10.1111/j.1945-5100.2011.01229.x.

Gattacceca, Jérôme, Millarca Valenzuela, Minoru Uehara, et al. 2011b. “The Densest Meteorite Collection Area in Hot Deserts: The San Juan Meteorite Field (Atacama Desert, Chile).” *Meteoritics & Planetary Science* 46 (9): 1276–87. https://doi.org/10.1111/j.1945-5100.2011.01229.x.

Gattacceca, Francis M. McCubbin, Jeffrey N. Grossman, et al. 2025. “The Meteoritical Bulletin, No. 113.” *Meteoritics & Planetary Science* 60 (7): 1587–91. https://doi.org/10.1111/maps.14374.

Genge, Matthew J., Matthias Van Ginneken, and Martin D. Suttle. 2020. “Micrometeorites: Insights into the Flux, Sources and Atmospheric Entry of Extraterrestrial Dust at Earth.” *Planetary and Space Science* 187 (August): 104900. https://doi.org/10.1016/j.pss.2020.104900.

Gladman, B. 2000. “The Near-Earth Object Population.” *Icarus* 146 (1): 176–89. https://doi.org/10.1006/icar.2000.6391.

References

Gladman, Brett J., Fabbio Migliorini, Alessandro Morbidelli, et al. 1997. “Dynamical Lifetimes of Objects Injected into Asteroid Belt Resonances.” *Science* 277 (5323): 197–201. https://doi.org/10.1126/science.277.5323.197.

Glass, B.P. 2002. “Upper Eocene Impact Ejecta/Spherule Layers in Marine Sediments.” *Geochemistry* 62 (3): 173–96. https://doi.org/10.1078/0009-2819-00017.

Goldstein, G. 1966. “Partial Half-Life for β-Decay of 36Cl.” *Journal of Inorganic and Nuclear Chemistry* 28 (4): 937–39. https://doi.org/10.1016/0022-1902(66)80189-6.

Goldstein, J.I., E.R.D. Scott, and N.L. Chabot. 2009. “Iron Meteorites: Crystallization, Thermal History, Parent Bodies, and Origin.” *Geochemistry* 69 (4): 293–325. https://doi.org/10.1016/j.chemer.2009.01.002.

Gomes, R., H. F. Levison, K. Tsiganis, and A. Morbidelli. 2005. “Origin of the Cataclysmic Late Heavy Bombardment Period of the Terrestrial Planets.” *Nature* 435 (7041): 466–69. https://doi.org/10.1038/nature03676.

Graf, Thomas, and Kurt Marti. 1995. “Collisional History of H Chondrites.” *Journal of Geophysical Research: Planets* 100 (E10): 21247–63. https://doi.org/10.1029/95JE01903.

Grossman, Jeffrey N., and Adrian J. Brearley. 2005. “The Onset of Metamorphism in Ordinary and Carbonaceous Chondrites.” *Meteoritics & Planetary Science* 40 (1): 87–122. https://doi.org/10.1111/j.1945-5100.2005.tb00366.x.

Harvey, Ralph. 2003. “The Origin and Significance of Antarctic Meteorites.” *Geochemistry* 63 (2): 93–147. https://doi.org/10.1078/0009-2819-00031.

Hellmann, Jan L., Thomas S. Kruijer, James A. Van Orman, Knut Metzler, and Thorsten Kleine. 2019. “Hf-W Chronology of Ordinary Chondrites.” *Geochimica et Cosmochimica Acta* 258 (August): 290–309. https://doi.org/10.1016/j.gca.2019.05.040.

Herzog, G.F. 2007. “Cosmic-Ray Exposure Ages of Meteorites.” In *Treatise on Geochemistry*. Elsevier. https://doi.org/10.1016/B0-08-043751-6/01069-0.

Herzog, G.F., and M.W. Caffee. 2014. “Cosmic-Ray Exposure Ages of Meteorites.” In *Treatise on Geochemistry*. Elsevier. https://doi.org/10.1016/B978-0-08-095975-7.00110-8.

Hofmann, Beda A., and Edwin Gnos. 2025. “The Meteoritic Record of Arabia.” *Geological Society, London, Special Publications* 550 (1): 469–92. https://doi.org/10.1144/SP550-2024-8.

Hofmann, Beda A., Edwin Gnos, A. J. Timothy Jull, et al. 2018. “Meteorite Reconnaissance in Saudi Arabia.” *Meteoritics & Planetary Science* 53 (11): 2372–94. https://doi.org/10.1111/maps.13132.

Hopp, Timo, Nicolas Dauphas, Yoshinari Abe, et al. 2022. “Ryugu’s Nucleosynthetic Heritage from the Outskirts of the Solar System.” *Science Advances* 8 (46): eadd8141. https://doi.org/10.1126/sciadv.add8141.

Hutzler, A. 2015. “The Flux of Meteorites on Earth: Contribution of Measuring the Concentration of Multiple Cosmogenic Nuclides, and Collections in Arid Areas.” Aix-Marseille Université. https://theses.fr/2015AIXM4302.

References

Hutzler, A., J. Gattacceca, P. Rochette, R. Braucher, B. Carro, E. Christensen, C. Cournede, et al. 2016. “Description of a Very Dense Meteorite Collection Area in Western Atacama: Insight into the Long-Term Composition of the Meteorite Flux to Earth.” *Meteoritics & Planetary Science* 51 (3): 468–82. https://doi.org/10.1111/maps.12607.

Jenniskens, Peter, and Hadrien A. R. Devillepoix. 2025. “Review of Asteroid, Meteor, and Meteorite-type Links.” *Meteoritics & Planetary Science* 60 (4): 928–73. https://doi.org/10.1111/maps.14321.

Joy, Katherine H., Ian A. Crawford, Natalie M. Curran, Michael Zolensky, Amy F. Fagan, and David A. Kring. 2016. “The Moon: An Archive of Small Body Migration in the Solar System.” *Earth, Moon, and Planets* 118 (2–3): 133–58. https://doi.org/10.1007/s11038-016-9495-0.

Jull, A J Timothy. 2006. “Terrestrial Ages of Meteorites.” In *Meteorites and the Early Solar System II*.

Jull, A. J. Timothy, Lanny R. McHARGUE, Philip A. Bland, et al. 2010. “Terrestrial Ages of Meteorites from the Nullarbor Region, Australia, Based on^{14} C and^{14} C–^{10} Be Measurements.” *Meteoritics & Planetary Science* 45 (8): 1271–83. https://doi.org/10.1111/j.1945-5100.2010.01289.x.

Kirby, R. S., et al. “A Statistical Investigation into Relationships between the IIE Irons and the Ordinary, F and “ HH ” Chondrites.” *Meteoritics & Planetary Science*, vol. 60, no. 10, 5 Sept. 2025, pp. 2376–2400, https://doi.org/10.1111/maps.70040. Accessed 6 Mar. 2026.

Kleine, T., G. Budde, C. Burkhardt, et al. 2020. “The Non-Carbonaceous–Carbonaceous Meteorite Dichotomy.” *Space Science Reviews* 216 (4): 55. https://doi.org/10.1007/s11214-020-00675-w.

Kleine, Thorsten, Mathieu Touboul, James A. Van Orman, et al. 2008. “Hf–W Thermochronometry: Closure Temperature and Constraints on the Accretion and Cooling History of the H Chondrite Parent Body.” *Earth and Planetary Science Letters* 270 (1–2): 106–18. https://doi.org/10.1016/j.epsl.2008.03.013.

Korochantseva, Ekaterina V., Mario Trieloff, Cyrill A. Lorenz, et al. 2007. “L-chondrite Asteroid Breakup Tied to Ordovician Meteorite Shower by Multiple Isochron^{40} Ar-^{39} Ar Dating.” *Meteoritics & Planetary Science* 42 (1): 113–30. https://doi.org/10.1111/j.1945-5100.2007.tb00221.x.

Kruijer, Thomas S., Thorsten Kleine, and Lars E. Borg. 2019. “The Great Isotopic Dichotomy of the Early Solar System.” *Nature Astronomy* 4 (1): 32–40. https://doi.org/10.1038/s41550-019-0959-9.

Kurlander, Jacob A., Pedro H. Bernardinelli, Megan E. Schwamb, et al. 2025. “Predictions of the LSST Solar System Yield: Near-Earth Objects, Main Belt Asteroids, Jupiter Trojans, and Trans-Neptunian Objects.” Version 2. Preprint, arXiv. https://doi.org/10.48550/ARXIV.2506.02487.

Lagain, A., K. Servis, G. K. Benedix, C. Norman, S. Anderson, and P. A. Bland. 2021. “Model Age Derivation of Large Martian Impact Craters, Using Automatic Crater Counting

Methods." *Earth and Space Science* 8 (2): e2020EA001598. https://doi.org/10.1029/2020EA001598.

Lagain, Anthony, Mikhail Kreslavsky, David Baratoux, et al. 2022. "Has the Impact Flux of Small and Large Asteroids Varied through Time on Mars, the Earth and the Moon?" *Earth and Planetary Science Letters* 579 (February): 117362. https://doi.org/10.1016/j.epsl.2021.117362.

Lee, Martin R., Conel M. O'D. Alexander, Addi Bischoff, et al. 2025. "Low-Temperature Aqueous Alteration of Chondrites." *Space Science Reviews* 221 (1): 11. https://doi.org/10.1007/s11214-024-01132-8.

Leya, I., K. Ammon, M. Cosarinsky, et al. 2013. "Light Noble Gases in 12 Meteorites from the Omani Desert, Australia, Mauritania, Canada, and Sweden." *Meteoritics & Planetary Science* 48 (8): 1401–14. https://doi.org/10.1111/maps.12142.

Leya, Ingo, and Jozef Masarik. 2009. "Cosmogenic Nuclides in Stony Meteorites Revisited." *Meteoritics & Planetary Science* 44 (7): 1061–86. https://doi.org/10.1111/j.1945-5100.2009.tb00788.x.

Li, Ye, Yuting Wang, Haoxuan Jiang, et al. 2025. "The Geochronology and Cooling History of Type 7 Chondrites: Insights into the Early Impact Events on Chondritic Parent Body." *Geochimica et Cosmochimica Acta* 389 (January): 280–93. https://doi.org/10.1016/j.gca.2024.11.020.

Love, S. G., and D. E. Brownlee. 1993. "A Direct Measurement of the Terrestrial Mass Accretion Rate of Cosmic Dust." *Science* 262 (5133): 550–53. https://doi.org/10.1126/science.262.5133.550.

Lucas, Michael P., Nick Dygert, Jialong Ren, Marc A. Hesse, Nathaniel R. Miller, and Harry Y. McSween. 2020. "Evidence for Early Fragmentation-Reassembly of Ordinary Chondrite (H, L, and LL) Parent Bodies from REE-in-Two-Pyroxene Thermometry." *Geochimica et Cosmochimica Acta* 290 (December): 366–90. https://doi.org/10.1016/j.gca.2020.09.010.

Madeira, Gustavo, Sébastien Charnoz, and Ryuki Hyodo. 2023. "Dynamical Origin of Dimorphos from Fast Spinning Didymos." *Icarus* 394 (April): 115428. https://doi.org/10.1016/j.icarus.2023.115428.

Marsset, M., P. Vernazza, M. Brož, et al. 2024. "The Massalia Asteroid Family as the Origin of Ordinary L Chondrites." *Nature* 634 (8034): 561–65. https://doi.org/10.1038/s41586-024-08007-6.

Masiero, Joseph R., A. K. Mainzer, J. M. Bauer, T. Grav, C. R. Nugent, and R. Stevenson. 2013. "ASTEROID FAMILY IDENTIFICATION USING THE HIERARCHICAL CLUSTERING METHOD AND *WISE* /NEOWISE PHYSICAL PROPERTIES." *The Astrophysical Journal* 770 (1): 7. https://doi.org/10.1088/0004-637X/770/1/7.

Mazrouei, Sara, Rebecca R. Ghent, William F. Bottke, Alex H. Parker, and Thomas M. Gernon. 2019. "Earth and Moon Impact Flux Increased at the End of the Paleozoic." *Science* 363 (6424): 253–57. https://doi.org/10.1126/science.aar4058.

McSween, Harry Y. 1979. “Are Carbonaceous Chondrites Primitive or Processed? A Review.” *Reviews of Geophysics* 17 (5): 1059–78. https://doi.org/10.1029/RG017i005p01059.

Michel, Patrick, Derek C. Richardson, Daniel D. Durda, Martin Jutzi, and Erik Asphaug. 2015. *Collisional Formation and Modeling of Asteroid Families*. https://doi.org/10.2458/azu_uapress_9780816532131-ch018.

Minton, David A., and Renu Malhotra. 2010. “Dynamical Erosion of the Asteroid Belt and Implications for Large Impacts in the Inner Solar System.” *Icarus* 207 (2): 744–57. https://doi.org/10.1016/j.icarus.2009.12.008.

Morbidelli, A., and D. Vokrouhlický. 2003. “The Yarkovsky-Driven Origin of near-Earth Asteroids.” *Icarus* 163 (1): 120–34. https://doi.org/10.1016/S0019-1035(03)00047-2.

Morbidelli, Alessandro, Kevin J. Walsh, David P. O’Brien, David A. Minton, and William F. Bottke. 2015. *The Dynamical Evolution of the Asteroid Belt*. https://doi.org/10.2458/azu_uapress_9780816532131-ch026.

Nakamura, Tomoki, Takaaki Noguchi, Masahiko Tanaka, et al. 2011. “Itokawa Dust Particles: A Direct Link Between S-Type Asteroids and Ordinary Chondrites.” *Science* 333 (6046): 1113–16. https://doi.org/10.1126/science.1207758.

Nesvorný, D., M. Broz, and V. Carruba. 2015. “Identification and Dynamical Properties of Asteroid Families.” In *Asteroids IV*, edited by Patrick Michel, Francesca E. DeMeo, and William F. Bottke. University of Arizona Press. https://doi.org/10.2458/azu_uapress_9780816532131-ch016.

Nesvorný, D., S. Ferraz-Mello, M. Holman, and A. Morbidelli. 2002. “Regular and Chaotic Dynamics in the Mean-Motion Resonances: Implications for the Structure and Evolution of the Asteroid Belt.” In *Asteroids III*. https://ui.adsabs.harvard.edu/abs/2002aste.book..379N.

Nesvorný, David, William F. Bottke, David Vokrouhlický, Alessandro Morbidelli, and Robert Jedicke. 2005. “Asteroid Families.” *Proceedings of the International Astronomical Union* 1 (S229): 289–99. https://doi.org/10.1017/S1743921305006800.

Nesvorny, David, Nicolas Dauphas, David Vokrouhlicky, Rogerio Deienno, and Timo Hopp. 2023. “Isotopic Trichotomy of Main Belt Asteroids from Implantation of Outer Solar System Planetesimals.” arXiv:2311.16053. Preprint, arXiv, November 27. https://doi.org/10.48550/arXiv.2311.16053.

Nica, Ninel, John Cameron, and Balraj Singh. 2012. “Nuclear Data Sheets for A = 36.” *Nuclear Data Sheets* 113 (1): 1–155. https://doi.org/10.1016/j.nds.2012.01.001.

Ozima, M. and Podosek. 2002. *Noble Gas Geochemistry*. 2nd edition. Vol. 67. Cambridge University Press.

Pinto, Gabriel A., Adrien Tavernier, Jérôme Gattacceca, et al. 2024. “Dense Collection Areas and Terrestrial Alteration of Meteorites in the Atacama Desert.” *Meteoritics & Planetary Science* 59 (2): 351–67. https://doi.org/10.1111/maps.14125.

Piralla, Maxime, Johan Villeneuve, Nicolas Schnuriger, David V. Bekaert, and Yves Marrocchi. 2023. “A Unified Chronology of Dust Formation in the Early Solar System.” *Icarus* 394 (April): 115427. https://doi.org/10.1016/j.icarus.2023.115427.

Pitjeva, E. V., and N. P. Pitjev. 2018. “Masses of the Main Asteroid Belt and the Kuiper Belt from the Motions of Planets and Spacecraft.” *Astronomy Letters* 44 (8–9): 554–66. https://doi.org/10.1134/S1063773718090050.

Pourkhorsandi, Hamed, Jérôme Gattacceca, Pierre Rochette, et al. 2019. “Meteorites from the Lut Desert (Iran).” *Meteoritics & Planetary Science* 54 (8): 1737–63. https://doi.org/10.1111/maps.13311.

Pourkhorsandi, Hamed, Jérôme Gattacceca, Pierre Rochette, et al. 2022. “The Famenin Fall and Other Ordinary Chondrites Intermediate between H and L Groups.” *Meteoritics & Planetary Science* 57 (5): 1038–59. https://doi.org/10.1111/maps.13801.

Rochette, Pierre, Jérôme Gattacceca, Lydie Bonal, et al. 2008. “Magnetic Classification of Stony Meteorites: 2. Non-ordinary Chondrites.” *Meteoritics & Planetary Science* 43 (5): 959–80. https://doi.org/10.1111/j.1945-5100.2008.tb01092.x.

Rochette, Pierre, Leonardo Sagnotti, Michèle Bourot-Denise, et al. 2003. “Magnetic Classification of Stony Meteorites: 1. Ordinary Chondrites.” *Meteoritics & Planetary Science* 38 (2): 251–68. https://doi.org/10.1111/j.1945-5100.2003.tb00263.x.

Rojas, J., J. Duprat, C. Engrand, et al. 2021. “The Micrometeorite Flux at Dome C (Antarctica), Monitoring the Accretion of Extraterrestrial Dust on Earth.” *Earth and Planetary Science Letters* 560 (April): 116794. https://doi.org/10.1016/j.epsl.2021.116794.

Rubin, Alan E. 2018. “Mechanisms Accounting for Variations in the Proportions of Carbonaceous and Ordinary Chondrites in Different Mass Ranges.” *Meteoritics & Planetary Science* 53 (10): 2181–92. https://doi.org/10.1111/maps.13117.

Rubin, Alan, and Chi Ma. 2021a. *Meteorite Mineralogy*. 1st ed. Cambridge University Press. https://doi.org/10.1017/9781108613767.

Rubin, Alan, and Chi Ma. 2021b. *Meteorite Mineralogy*. 1st ed. Cambridge University Press. https://doi.org/10.1017/9781108613767.

Rubincam, David Parry. 2000. “Radiative Spin-up and Spin-down of Small Asteroids.” *Icarus* 148 (1): 2–11. https://doi.org/10.1006/icar.2000.6485.

Sadaka, Carine, Jérôme Gattacceca, Matthieu Gounelle, et al. 2025. “Systematic Meteorite Collection in the Catalina Dense Collection Area (Chile): Description and Statistics.” *Meteoritics & Planetary Science* 60 (2): 308–23. https://doi.org/10.1111/maps.14307.

Schlüter, J., L. Schultz, F. Thiedig, B. O. Al-Mahdi, and A. E. Abu Aghreb. 2002. “The Dar al Gani Meteorite Field (Libyan Sahara): Geological Setting, Pairing of Meteorites, and Recovery Density.” *Meteoritics & Planetary Science* 37 (8): 1079–93. https://doi.org/10.1111/j.1945-5100.2002.tb00879.x.

Schmieder, Martin, and David A. Kring. 2020. “Earth’s Impact Events Through Geologic Time: A List of Recommended Ages for Terrestrial Impact Structures and Deposits.” *Astrobiology* 20 (1): 91–141. https://doi.org/10.1089/ast.2019.2085.

Schmitz*, Birger, Martin Schmieder, Shiyong Liao, Ellinor Martin, and Fredrik Terfelt. 2022. “Impact-Crater Ages and Micrometeorite Paleofluxes Compared: Evidence for the Importance of Ordinary Chondrites in the Flux of Meteorites and Asteroids to Earth over the Past 500 Million Years.” In *From the Guajira Desert to the Apennines, and*

from Mediterranean Microplates to the Mexican Killer Asteroid: Honoring the Career of Walter Alvarez, edited by Christian Koeberl, Philippe Claeys, and Alessandro Montanari. Geological Society of America. https://doi.org/10.1130/2022.2557(18).

Schultz, L., L. Franke, and A. W. R. Bevan. 2005. "Noble Gases in Ten Nullarbor Chondrites: Exposure Ages, Terrestrial Ages, and Weathering Effects." *Meteoritics & Planetary Science* 40 (5): 659–64.

Scott, E. R. D., and A. N. Krot. 2003. "Chondrites and Their Components." *Treatise on Geochemistry* 1 (December): 711. https://doi.org/10.1016/B0-08-043751-6/01145-2.

Scott, Edward R.D., Tatiana V. Krot, Joseph I. Goldstein, and Shigeru Wakita. 2014. "Thermal and Impact History of the H Chondrite Parent Asteroid during Metamorphism: Constraints from Metallic Fe–Ni." *Geochimica et Cosmochimica Acta* 136 (July): 13–37. https://doi.org/10.1016/j.gca.2014.03.038.

Sears, D. W., J. N. Grossman, C. L. Melcher, L. M. Ross, and A. A. Mills. 1980. "Measuring Metamorphic History of Unequilibrated Ordinary Chondrites." *Nature* 287 (5785): 791–95. https://doi.org/10.1038/287791a0.

Sears, Derek W. G., Lu Jie, Paul H. Benoit, John M. DeHart, and Gary E. Lofgren. 1992. "A Compositional Classification Scheme for Meteoritic Chondrules." *Nature* 357 (6375): 207–10. https://doi.org/10.1038/357207a0.

Shober, Patrick M., Hadrien A. R. Devillepoix, Jeremie Vaubaillon, et al. 2025. "Perihelion History and Atmospheric Survival as Primary Drivers of the Earth's Meteorite Record." *Nature Astronomy* 9 (6): 799–812. https://doi.org/10.1038/s41550-025-02526-6.

Sliz, Malgorzata U., Beda A. Hofmann, Ingo Leya, et al. 2022. "Terrestrial Ages of Seven Meteorite Strewn Fields and Two Single Unpaired Meteorites from the Sultanate of Oman Determined Using^{14} C and^{10} Be." *Meteoritics & Planetary Science* 57 (12): 2170–91. https://doi.org/10.1111/maps.13922.

Spitzer, Fridolin, Thorsten Kleine, Christoph Burkhardt, et al. 2024. "The Ni Isotopic Composition of Ryugu Reveals a Common Accretion Region for Carbonaceous Chondrites." *Science Advances* 10 (39): eadp2426. https://doi.org/10.1126/sciadv.adp2426.

Spoto, Federica, Andrea Milani, and Zoran Knežević. 2015. "Asteroid Family Ages." *Icarus* 257 (September): 275–89. https://doi.org/10.1016/j.icarus.2015.04.041.

Stöffler, Dieter, Christopher Hamann, and Knut Metzler. 2018. "Shock Metamorphism of Planetary Silicate Rocks and Sediments: Proposal for an Updated Classification System." *Meteoritics & Planetary Science* 53 (1): 5–49. https://doi.org/10.1111/maps.12912.

Stöffler, Dieter, Klaus Keil, and Scott Edward R.D. 1991. "Shock Metamorphism of Ordinary Chondrites." *Geochimica et Cosmochimica Acta* 55 (12): 3845–67. https://doi.org/10.1016/0016-7037(91)90078-J.

Suttle, M. D., and L. Folco. 2020. "The Extraterrestrial Dust Flux: Size Distribution and Mass Contribution Estimates Inferred From the Transantarctic Mountains (TAM)

Micrometeorite Collection." *Journal of Geophysical Research: Planets* 125 (2): e2019JE006241. https://doi.org/10.1029/2019JE006241.

Svensson, Matthew J.O., Stephen A. Kissin, Marie-Claude Corbeil, Peter Whitridge, and James W. Helmer. 2021. "Methods for Determination of the Source of Iron in Precontact Inuit and Dorset Culture Artifacts from the Canadian Arctic." *Journal of Archaeological Science: Reports* 36 (April): 102814. https://doi.org/10.1016/j.jasrep.2021.102814.

Synal, Hans-Arno. 2013. "Developments in Accelerator Mass Spectrometry." *International Journal of Mass Spectrometry* 349–350 (September): 192–202. https://doi.org/10.1016/j.ijms.2013.05.008.

Tait, Alastair W., Andrew G. Tomkins, Bélinda M. Godel, Siobhan A. Wilson, and Pavlina Hasalova. 2014. "Investigation of the H7 Ordinary Chondrite, Watson 012: Implications for Recognition and Classification of Type 7 Meteorites." *Geochimica et Cosmochimica Acta* 134 (June): 175–96. https://doi.org/10.1016/j.gca.2014.02.039.

Tauseef, Mohammad, Ingo Leya, Jérôme Gattacceca, et al. 2024. "^{14}C and ^{14}C-^{10}Be Terrestrial Age Dating System for Meteorites—New Data for Four Recently Fallen Meteorites." *Meteoritics & Planetary Science* 59 (6): 1219–35. https://doi.org/10.1111/maps.14144.

Tauseef, Mohammad, Ingo Leya, Jérôme Gattacceca, et al. 2025. "Evaluating ^{14}C and ^{14}C / ^{10}Be Terrestrial Age Dating Systems for Meteorites Using Experimental Data and Model Calculations." *Meteoritics & Planetary Science* 60 (5): 1263–83. https://doi.org/10.1111/maps.14355.

Taylor, Susan, James H. Lever, and Ralph P. Harvey. 1998. "Accretion Rate of Cosmic Spherules Measured at the South Pole." *Nature* 392 (6679): 899–903. https://doi.org/10.1038/31894.

Terada, K., Y. Sano, N. Takahata, et al. 2018. "Thermal and Impact Histories of 25143 Itokawa Recorded in Hayabusa Particles." *Scientific Reports* 8 (1): 11806. https://doi.org/10.1038/s41598-018-30192-4.

Trieloff, Mario, Elmar K. Jessberger, Ingrid Herrwerth, et al. 2003. "Structure and Thermal History of the H-Chondrite Parent Asteroid Revealed by Thermochronometry." *Nature* 422 (6931): 502–6. https://doi.org/10.1038/nature01499.

Tsiganis, K., R. Gomes, A. Morbidelli, and H. F. Levison. 2005. "Origin of the Orbital Architecture of the Giant Planets of the Solar System." *Nature* 435 (7041): 459–61. https://doi.org/10.1038/nature03539.

Van Ginneken, Matthias, Penelope J. Wozniakiewicz, Donald E. Brownlee, et al. 2024. "Micrometeorite Collections: A Review and Their Current Status." *Philosophical Transactions of the Royal Society A: Mathematical, Physical and Engineering Sciences* 382 (2273): 20230195. https://doi.org/10.1098/rsta.2023.0195.

Van Schmus, W.R., and J.A. Wood. 1967. "A Chemical-Petrologic Classification for the Chondritic Meteorites." *Geochimica et Cosmochimica Acta* 31 (5): 747–65. https://doi.org/10.1016/S0016-7037(67)80030-9.

Vernazza, P., R. P. Binzel, A. Rossi, M. Fulchignoni, and M. Birlan. 2009. “Solar Wind as the Origin of Rapid Reddening of Asteroid Surfaces.” *Nature* 458 (7241): 993–95. https://doi.org/10.1038/nature07956.

Vernazza, P., R. P. Binzel, C. A. Thomas, et al. 2008. “Compositional Differences between Meteorites and Near-Earth Asteroids.” *Nature* 454 (7206): 858–60. https://doi.org/10.1038/nature07154.

Vernazza, P., M. Ferrais, L. Jorda, et al. 2021. “VLT/SPHERE Imaging Survey of the Largest Main-Belt Asteroids: Final Results and Synthesis.” *Astronomy & Astrophysics* 654 (October): A56. https://doi.org/10.1051/0004-6361/202141781.

Vernazza, P., B. Zanda, R. P. Binzel, et al. 2014. “MULTIPLE AND FAST: THE ACCRETION OF ORDINARY CHONDRITE PARENT BODIES.” *The Astrophysical Journal* 791 (2): 120. https://doi.org/10.1088/0004-637X/791/2/120.

Vernazza, P., B. Zanda, T. Nakamura, E. Scott, and S. Russell. 2015. “The Formation and Evolution of Ordinary Chondrite Parent Bodies.” In *Asteroids IV*, edited by Patrick Michel, Francesca E. DeMeo, and William F. Bottke. University of Arizona Press. https://doi.org/10.2458/azu_uapress_9780816532131-ch032.

Vernazza, Pierre, and Pierre Beck. 2017. “Composition of Solar System Small Bodies.” In *Planetesimals*, 1st ed., edited by Linda T. Elkins-Tanton and Benjamin P. Weiss. Cambridge University Press. https://doi.org/10.1017/9781316339794.013.

Vokrouhlický, D., W. F. Bottke, S. R. Chesley, D. J. Scheeres, and T. S. Statler. 2015. “The Yarkovsky and YORP Effects.” In *Asteroids IV*, edited by Patrick Michel, Francesca E. DeMeo, and William F. Bottke. University of Arizona Press. https://doi.org/10.2458/azu_uapress_9780816532131-ch027.

Vokrouhlický, D., and P. Farinella. 2000. “Efficient Delivery of Meteorites to the Earth from a Wide Range of Asteroid Parent Bodies.” *Nature* 407 (6804): 606–8. https://doi.org/10.1038/35036528.

Voldman, G. G., M. J. Genge, G. L. Albanesi, C.R. Barnes, and G. Ortega. 2013. “Cosmic Spherules from the Ordovician of Argentina.” *Geological Journal* 48 (2–3): 222–35. https://doi.org/10.1002/gj.2418.

Walsh, Kevin J., Alessandro Morbidelli, Sean N. Raymond, David P. O’Brien, and Avi M. Mandell. 2011. “A Low Mass for Mars from Jupiter’s Early Gas-Driven Migration.” *Nature* 475 (7355): 206–9. https://doi.org/10.1038/nature10201.

Wasson, J. T. “Formation of Non-Magmatic Iron-Meteorite Group IIE.” *Geochimica et Cosmochimica Acta*, vol. 197, Jan. 2017, pp. 396–416, https://doi.org/10.1016/j.gca.2016.09.043. Accessed 27 June 2020.

Warren, Paul H. 2011. “Stable-Isotopic Anomalies and the Accretionary Assemblage of the Earth and Mars: A Subordinate Role for Carbonaceous Chondrites.” *Earth and Planetary Science Letters* 311 (1–2): 93–100. https://doi.org/10.1016/j.epsl.2011.08.047.

Weirich, J. R., T. D. Swindle, and C. E. Isachsen. 2012. “^{40}Ar-^{39}Ar Age of Northwest Africa 091: More Evidence for a Link between L Chondrites and Fossil Meteorites.”

Meteoritics & Planetary Science 47 (8): 1324–35. https://doi.org/10.1111/j.1945-5100.2012.01397.x.

Weisberg, M. K., T. J. McCoy, and A. N. Krot. 2006. "Systematics and Evaluation of Meteorite Classification." In *Meteorites and the Early Solar System II*. https://ui.adsabs.harvard.edu/abs/2006mess.book...19W.

Wilkison, Sarah L., Mark S. Robinson, Peter C. Thomas, et al. 2002. "An Estimate of Eros's Porosity and Implications for Internal Structure." *Icarus* 155 (1): 94–103. https://doi.org/10.1006/icar.2001.6751.

Wimmer, Karl, Edwin Gnos, and Beda A. Hofmann. 2022. "Once in a Summer: Fall History of the J a H 073 Strewn Field, Sultanate of Oman." *Meteoritics & Planetary Science* 57 (12): 2216–28. https://doi.org/10.1111/maps.13924.

Wlotzka, F. 1993. "A Weathering Scale for the Ordinary Chondrites." *Meteoritics* 28 (July): 460–460.

Wlotzka, Frank. 2005. "Cr Spinel and Chromite as Petrogenetic Indicators in Ordinary Chondrites: Equilibration Temperatures of Petrologic Types 3.7 to 6." *Meteoritics & Planetary Science* 40 (11): 1673–702. https://doi.org/10.1111/j.1945-5100.2005.tb00138.x.

Wyatt, S. P., and F. L. Whipple. 1950. "The Poynting-Robertson Effect on Meteor Orbits." *The Astrophysical Journal* 111 (January): 134–41. https://doi.org/10.1086/145244.

Yoshida, Masaru. 2010. "Discovery of the Yamato Meteorites in 1969." *Polar Science* 3 (4): 272–84. https://doi.org/10.1016/j.polar.2009.11.001.

Zappatini, A., B. A. Hofmann, E. Gnos, et al. 2024. "Al-Khadhaf: A Camera-Observed H5–6 Fall from Oman." LPI Contribution, vol. 3036: 6140. https://www.hou.usra.edu/meetings/metsoc2024/pdf/6140.pdf.

Zekollari, Harry, Steven Goderis, Vinciane Debaille, et al. 2019. "Unravelling the High-Altitude Nansen Blue Ice Field Meteorite Trap (East Antarctica) and Implications for Regional Palaeo-Conditions." *Geochimica et Cosmochimica Acta* 248 (March): 289–310. https://doi.org/10.1016/j.gca.2018.12.035.

Zolensky, M., P. Bland, P. Brown, and I. Halliday. 2006. "Flux of Extraterrestrial Materials." In *Meteorites and the Early Solar System II*. https://ui.adsabs.harvard.edu/abs/2006mess.book..869Z.

Zolensky, Michael E., Gordon L. Wells, and Helen M. Rendell. 1990. "The Accumulation Rate of Meteorite Falls at the Earth's Surface: The View from Roosevelt County, New Mexico." *Meteoritics* 25 (1): 11–17. https://doi.org/10.1111/j.1945-5100.1990.tb00965.x.

Zurfluh, Florian J., Beda A. Hofmann, Edwin Gnos, Urs Eggenberger, and A. J. Timothy Jull. 2016. "Weathering of Ordinary Chondrites from Oman: Correlation of Weathering Parameters with^{14} C Terrestrial Ages and a Refined Weathering Scale." *Meteoritics & Planetary Science* 51 (9): 1685–700. https://doi.org/10.1111/maps.12690.

Image credits

Chapter one: Credits: NASA, ESA and the Hubble Heritage Team (STScI/AURA)
Chapter five: Credit: NASA, ESA, D. Jewitt (UCLA)

References

APPENCIDES

Appendices

A. Detailed protocol of ^{36}Cl extraction from meteorite samples

The protocol is based on the work of Hutzler (2016) and Drouard (2019).

I. Metal extraction

Chlorine isotopes are measured in the metallic phase of meteorites since ^{36}Cl is produced only by spallation reactions on the target element Fe by high-energy secondary neutrons. For this, we first begin with a metal extraction step, by following these steps:

1. A small piece of the initial meteorite sample is cut and crushed in a metal grinder first, and then with an agate mortar. We want to obtain around 100 mg of metal for each sample, so depending on the meteorite class (H, L, or LL chondrite), and knowing that the metal content of H, L, and LL fresh chondrites is ~18, 8, and 3 wt%, respectively. Additionally, the weathering grade can also help to estimate the initial meteorite mass needed; with increasing weathering grade, more metal is consumed, thus a greater initial mass is needed. For example, for a fresh H chondrite, ~0.6 g is initially needed, compared to ~1.3 and ~3.4 g for L and LL chondrites, respectively.

2. The crushing process is repeated as many times as necessary for the obtained powder to pass through a 400 µm sieve. The magnetic part is separated using a **hand magnet**. The silicates are kept for potential ^{10}Be measurements.

3. The powder is placed in an ultrasonic ethanol bath for 10 minutes to separate mineral grains and are then dried.

4. Another magnetic separation is done before placing the sample in an ultrasonic bath for 30 minutes with Hydrochloric acid HCl 0.2M to dissolve troilite.

5. Two to three ultrasonic baths with 67% ethanolamine thioglycolate (EATG) to remove rust. The sample is rinsed with milliQ water and ethanol before being dried. The purity of the metal grains is verified with inspection under a binocular.

Since magnetic particles clump, making it difficult to properly clean the metal grains, the sample is periodically demagnetized using a Molspin demagnetize using an applied alternative field of 30 mT.

The following steps allow the dissolution of the metal in acid followed by the formation of an AgCl precipitate which will be measured at ASTER by accelerator mass spectrometry.

Work was performed with gloves and under a fume hood when handling acids. The fume hood was thoroughly cleaned the fume hood before performing the experiments to avoid any potential contamination by chloroforms. Caution was taken as to avoid cross-sample contamination.

II. Metal dissolution

1. The tubes are placed to heat in the oven with the corresponding sample names. The tubes should be weighted with and without the cap.
2. The metal grains are added, and the tubes are weighed without the cap to estimate the mass of the added metal grains.
3. 340 µL of ^{36}Cl spike (Spike 261018, 6 mg/g, 19/12/2022) are added using an adjustable micropipette (caution should be taken as not to touch anything during the experiments to avoid contamination). Some bubbles should be observed. The chlorine is present is extremely small quantities in the metal grains (a few ppm), that's why it is necessary to add a chlorine solution with a known concentration (spike) which fixes the isotopic ratio.
4. Tubes are weighed after adding the spike (without cap).
5. Add around 10 mL of nitric acid HNO_3, 2M using a Pasteur pipette. 6. Close the tube and shake carefully. Wait until the metal is fully dissolved (1 to 2 days usually). If the metal is still resisting, add a few drops of pure HNO_3.

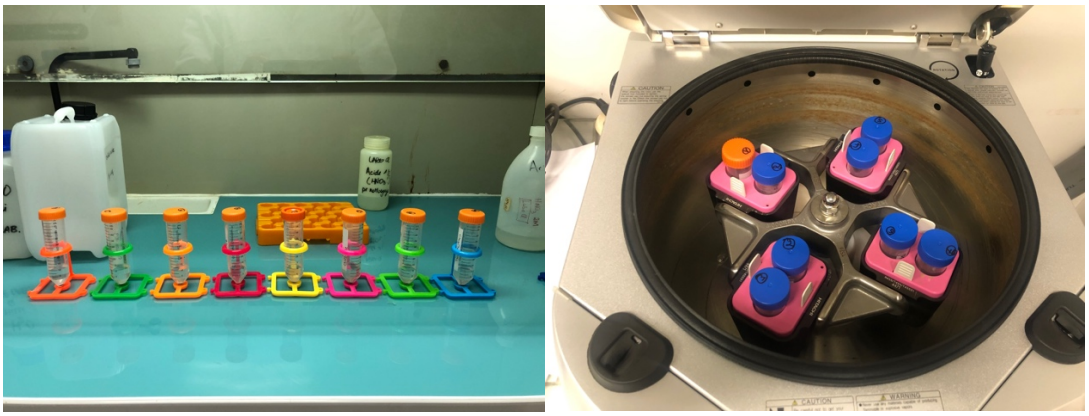

Figure A. 1. Dissolution of metal in nitric acid (left) and centrifuged in a Himac Eppendorf CT 6E centrifuge centrifuge (right).

III. Precipitation

- Once the metal is dissolved, the tubes are placed in a Himac Eppendorf CT 6E centrifuge (4000 tours for 5 minutes) to obtain a compact residue. The supernatant (containing chlorine) is recovered in a new tube on which we note "Cl" with the sample names.
- The remaining residues in the tubes are rinsed three times with 10 to 20 mL of milliQ water and centrifuged after each rinsing. The rinsing water is thrown

away in an acid waste container and the tubes with the residues are dried in the oven at 70 to 80°C for complete drying.

- The tubes and the residues are weighed to later estimate the mass of the metal dissolved.
- The residues are removed, and the tubes are rinsed the tube with MilliQ water and ethanol and then dried and weighed. Caution: the tubes should not be left to dry too long to avoid considerable mass loss due from excessive heating.

The precipitation of AgCl takes place in three different steps.

a. First precipitation

- In the supernatant solution containing chlorine**,** 1 mL of AgNO3 (10%) is added and the obtained solution is then vortexed for homogenization
- The solution is to rest overnight in the fridge in the dark due to the photosensitivity of AgCl.
- The next day, the tubes are centrifuged to separate the supernatant and the white precipitate.
- The supernatant is placed in a new tube labeled « other elements » for later measurements of Fe and Ni contents.

b. Second precipitation

- In the tubes containing the AgCl precipitates, 2 mL of $NH_{3(aq)}$ (25 %) are added then vortexed to dissolve the precipitate well, before adding 1 mL of milliQ water and 0.5 mL of saturated solution of $Ba(NO_3)_2$ to precipitate $Ba(SO_4)$ in order to get rid of sulfur. In a basic milieu, AgCl dissolves, the solution becomes red in the presence of sulfur (Figure A.2).

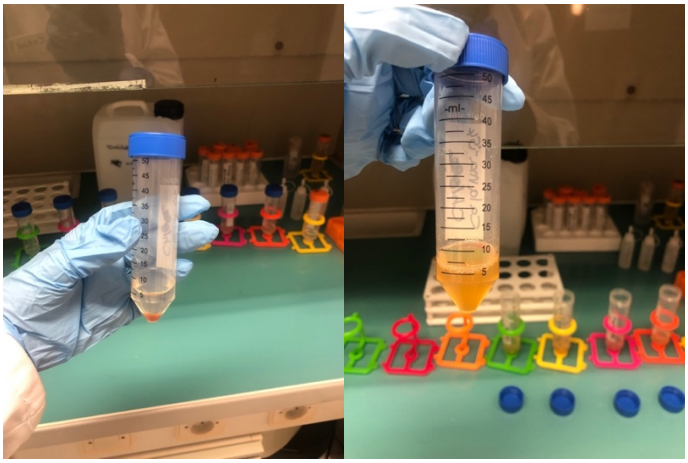

Figure A. 2. Elimination of isobars in a basic medium, the solution becomes orange.

- The tubes are vortexed and centrifuged for10 to 15 seconds at 1000 rotations so that the drops fall from the cap but be careful not to centrifuge for too long or the precipitate will compact.

- The cap is open (to let CO_2 penetrate et enhance the reaction) and the solution are left to rest overnight under the hood.
- Test the pH the next day or smell ammonia, if it becomes acid, a few drops of $(NH_3)_{aq}$ should be added.

1. The next day, the tubes are closed and centrifuged them for 5 minutes to obtain a pellet of Ba(SO)/Ba(CO) at the bottom of the tube.
2. The supernatant is poured into a PTFE syringe with a 0.45 µm filter attached to the end, then into a small centrifuge tube. This step serves to retain any $BaSO_4$ that may not have been properly centrifuged.
3. In the tube containing the Ba pellet, two drops of $(NH_{3(aq)})$ are added to rinse the remaining sample.
4. The rinsing solution is added to the chlorine solution (supernatant) in the syringe. The syringe is held in a clean beaker previously rinsed with milliQ water.

c. Third precipitation

- In this step, 1 mL of pure HNO_3 is added to the chlorine solution. A white precipitate and white smoke should appear, and the tube becomes hot (exothermic reaction).
- The solution is vortexed and set aside to rest for at least one hour in the dark.

A few hours later:

1. The precipitates are centrifuged for 3 minutes, and the supernatant is discarded.
2. The precipitates are rinsed twice with 5 mL of milliQ water.
3. The tubes are opened and wrapped with an aluminum foil before being placed in the oven at 80°C for at least 48 hours to complete drying. The target precipitates are ready to be inserted in cathodes and measured using AMS.

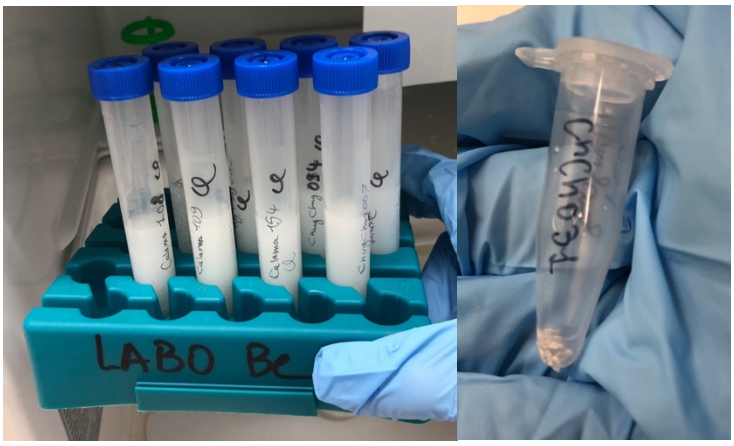

Figure A. 3. Precipitation of AgCl in an acid medium (left).

Preparation of solutions:

- 10 % $AgNO_3$: 3g of $AgNO_3$ powder to complete to 30g with milliQ water.
- $Ba(NO_3)_{sat}$: milliQ water + NH_3 to be in a basic medium + a significant amount of $Ba(NO_3)_2$ powder to be saturated. This solution should be prepared ahead.
- HNO_3 2M: pure HNO_3 (65 %) is of molarity 15M. To dilute to 2M: 2/15 liters of pure HNO_3 + 13/15 liters of milliQ water, equivalent to 15 vol% of HNO_3 for 85% H_2O.

B. Uncertainty on terrestrial age

Based on Drouard, 2019 (thesis) and considering the production of ^{36}Cl on Earth negligible (see article), the terrestrial age is calculated as:

$$T_{terr} = \frac{1}{\lambda^{36Cl}} ln\left(\frac{P_{sat}}{P_{meas}}\right) = \frac{1}{\lambda^{36Cl}} ln\left(\frac{P_{sat}}{\lambda^{36Cl} N_{meas}}\right)$$

Constants:

- $\lambda^{36Cl} = \frac{ln(2)}{T_{36}}$; with half-life of ^{36}Cl: T_{36} = 301 000 years (Nica 2012, Goldstein, 1966)
- Avogadro's number: $N_A = 6.022 \times 10^{23}$ mol^{-1}
- The molar mass of ^{36}Cl: M_{Cl} = 35.968 g/mol
- The chlorine concentration of the spike solution: C_{spike} = 6.0 mg Cl per g solution; ASTER)
- P_{sat} saturated production rate in space in the metal (dpm/kg)

Variables:

- mass of the metal dissolved in grams
- mass of the spike solution added in g
- measured isotopic ratio *R* with a relative uncertainty *dR* (given by AMS measurements)
- calculated saturated production rate P_{sat} (see text for details)

Adopted instrument/constant uncertainties are:

- σ_{Psat} = 3.1 dpm/kg (Scherer et al., 1997)
- σ_m = 0.001 g
- σ_{spike} = 0.0001 g
- σ_{Cspike} = 0.01 mg/g
- σ_{T36} = 2000 years (Goldstein 1966)

Calculations:

- The number of stable chlorine atoms added by the spike:

$$N_{spike} = \frac{m_{spike} \times C_{spike} \times N_A}{1000 \times M_{Cl}}$$

- the number of ^{36}Cl atoms in the metal is

$$N_{Cl} = N_{spike} \times R$$

- The measured activity of the metal (in dpm/kg) is

$$N_{meas} = \frac{N_{Cl} \times ln(2) \times 1000}{(365 \times 24 \times 60) \times T_{36} \times m_{metal}}$$

- The age equation becomes:

$$T_{terr} = \frac{T_{36}}{ln(2)} ln \times \left(\frac{P_{sat} \times M_{Cl} \times T_{36}}{ln(2) \times R \times m_{spike} \times C_{spike} \times N_A \times m_{metal}} \right)$$

- The 1σ uncertainty is propagated in quadrature as:

$$\sigma^2_{Tterr} = [(\frac{\sigma Psat}{Psat})^2 + (\frac{\sigma R}{R})^2 + (\frac{\sigma m_{metal}}{m_{metal}})^2 + (\frac{\sigma mspike}{mspie})^2 + (\frac{\sigma C}{Cspike})^2] + (\frac{1}{ln(2)} + \frac{Tterr}{T_{36}})^2 \times \sigma^2_{T36}$$

C. Uncertainty on H chondrite relative abundance

H chondrite relative abundance calculated as a H/ (H+L+LL).

H = number of H chondrites; L = number of L chondrites; LL = number of LL chondrites.

Error bars were estimated using a Poisson distribution on the number of chondrites:

dH = √H; dL = √L; dLL = √LL.

The number of H chondrites is corrected by a factor calculated for each meteorite collection.

i. Factor

First, we consider the number of each ordinary chondrite group in the whole collection (from MBDB):

$$f_{collection} = \frac{H_c}{H_c + L_c + LL_c}$$

Second, we take the number of each ordinary chondrite group in the subset:

$$f_{subset} = \frac{H_s}{H_s + L_s + LL_s}$$

Then the factor is simply calculated as:

$$factor = \frac{f_{collection}}{f_{subset}}$$

ii. Ratio

The corrected H chondrite count is H_{corr} = H × factor.

We consider N = H + L + LL and $\mathbf{r} = \frac{H}{H+L+LL}$

$$\frac{\partial r}{\partial H} = \frac{L + LL}{N^2}$$

$$\frac{\partial r}{\partial L} = \frac{-H_{corr}}{N^2}$$

$$\frac{\partial r}{\partial LL} = \frac{-H_{corr}}{N^2}$$

Thus, the final uncertainty on the ratio is:

$$dr^2 = (\frac{\partial r}{\partial H}\, dH)^2 + (\frac{\partial r}{\partial L}\, dL)^2 + (\frac{\partial r}{\partial LL}\, dLL)^2$$

Or

$$dr = \sqrt{[(\frac{\partial r}{\partial H}\, dH)^2 + (\frac{\partial r}{\partial L}\, dL)^2 + (\frac{\partial r}{\partial LL}\, dLL)^2]}$$

D. Repositories and projects

The pairing code was based on the one developed by Hutzler et al. (2016), it was adapted from Matlab to Python with the help of data scientist Pierre Sempéré (https://github.com/Psemp).

Link to the pairing code: https://github.com/csadaka2/ordinary_chondrites_pairing .

P. Sempéré also developed an ML code for classification of ordinary chondrites with digital microscope images, for which I provided >700 images taken with the Keyence microscope at CEREGE. This model is still preliminary but had already yielded encouraging results.

Link to project: https://github.com/Psemp/MeteorID

Link to images used: https://doi.org/10.34740/kaggle/dsv/9559927

E. Additional terrestrial ages

Table A. 1. Terrestrial ages of three mesosiderites from the Catalina Systematic Collection.

Sample	Mass (g)	Magnetic Susceptibility	Petrographic Type	Weathering Grade	% Fe	% Ni	Saturated activity (dpm/kg)	Terrestrial age (ka)	Uncertainty (ka)	Measured activity (dpm/kg)
Catalina 399	30.4	5.60	Meso-B2	low	98.4	1.6	24.33	1068	61	2.01
Catalina 500	999	5.25	Meso-B3	moderate	98.3	1.7	24.32	1072	61	1.99
Catalina 581	136	5.38	Meso-A3	low	97.8	2.2	24.28	1077	61	1.95

F. Additional neon analysis and CRE ages

Table A. 2. Neon isotopic compositions, cosmogenic components, and Cosmic-Ray Exposure (CRE) ages of meteorites from the Calama area.

Sample	Classification	F	$^{20}Ne/^{22}Ne$	+/-	$^{21}Ne/^{22}Ne$	+/-	$^{22}Ne/^{21}Ne_{(cos)}$	+/-	$^{21}Ne_{(cos)}$ (10^{-8} cm^3 STP/g)	+/-	P(^{21}Ne) (10^{-8} cm^3 STP/g/Ma)	+/-	CRE age (Ma)	+/-
Calama 123	H5	1.30	1.070	0.092	0.840	0.003	1.218	0.017	1.56	0.159	0.25	0.026	6.12	0.89
Calama 173	H5	1.09	2.337	0.064	0.754	0.017	1.149	0.102	1.21	0.086	0.27	0.030	4.54	0.61
Sierra Gorda 007	H5	1.09	1.032	0.059	0.934	0.030	1.051	0.040	0.78	0.057	0.45	0.037	1.72	0.19
Sierra Gorda 088	L5	1.29	0.853	0.091	0.870	0.003	1.146	0.004	11.34	1.217	0.37	0.040	30.3	4.59